

**MODELING AND SIMULATION OF A COMBINED  
ISOMERIZATION REACTOR/PRESSURES SWING  
ADSORPTION/ MEMBRANE UNIT.**

BY

**Tareg Mohammed Al-Soudani**

A Thesis Presented to the  
DEANSHIP OF GRADUATE STUDIES

**KING FAHD UNIVERSITY OF PETROLEUM & MINERALS**  
DHAHRAN, SAUDI ARABIA

In Partial Fulfillment of the  
Requirements for the Degree of

**MASTER OF SCIENCE**

In

**CHEMICAL ENGINEERING**

**JUNE 2004**

UMI Number: 1420772

## INFORMATION TO USERS

The quality of this reproduction is dependent upon the quality of the copy submitted. Broken or indistinct print, colored or poor quality illustrations and photographs, print bleed-through, substandard margins, and improper alignment can adversely affect reproduction.

In the unlikely event that the author did not send a complete manuscript and there are missing pages, these will be noted. Also, if unauthorized copyright material had to be removed, a note will indicate the deletion.

**UMI<sup>®</sup>**

---

UMI Microform 1420772

Copyright 2004 by ProQuest Information and Learning Company.

All rights reserved. This microform edition is protected against unauthorized copying under Title 17, United States Code.

ProQuest Information and Learning Company  
300 North Zeeb Road  
P.O. Box 1346  
Ann Arbor, MI 48106-1346

**KING FAHD UNIVERSITY OF PETROLEUM & MINERALS  
DHAHRAN 31261, SAUDI ARABIA  
DEANSHIP OF GRADUATE STUDIES**

*This thesis, written by*

**Tareg M. Al-Soudani**

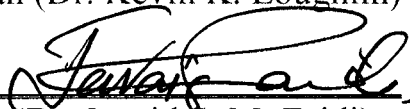
*Under the direction of his thesis advisor and approved by his thesis committee. Has been presented to and accepted by the Dean of Graduate Studies, in partial fulfillment of the requirements for the degree of*

**MASTER OF SCIENCE IN CHEMICAL ENGINEERING.**

***Thesis Committee:***



Chairman (Dr. Kevin K. Loughlin)



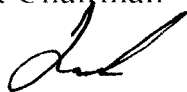
Member (Dr. Javaid S. M. Zaidi)



Member (Dr. Ashraf I. Fatehi)



Prof. Mohamed B. Amin  
Department Chairman



Prof. Osama Ahmad Jannadi  
Dean of Graduate Studies



Date: 06/01/2004

## **DEDICATION**

**I dedicate this thesis to:**

**the memory of my father who taught me a lot on his presence and absence. May God have mercy on him.**

**my beloved mother. I can say so much. I still owe her a lot.**

**my lovely wife who shares me my happiness and stands by me on my sorrows.**

**my son Ziyad who has seen light four months before the defense of this Thesis.**



## **ACKNOWLEDGEMENT**

Acknowledgement is due to King Fahd University of Petroleum & Minerals for supporting this research.

I wish to express my appreciation to Dr. Kevin K. Loughlin who served as my major advisor. I also wish to thank the other members of my thesis committee Dr. Jawaid S. M. Zaidi and Dr. Ashraf I. Fatehi.

## TABLE OF CONTENTS

DEDICATION .....	ii
ACKNOWLEDGEMENT .....	iii
TABLE OF CONTENTS .....	iv
LIST OF FIGURES .....	vi
LIST OF TABLES .....	xiv
ABSTRACT (English).....	xv
ABSTRACT (Arabic) .....	xvi
CHAPTER 1 .....	1
1.1 INTRODUCTION .....	1
1.2 n-PARAFFINS ISOMERIZATION REACTION .....	5
1.3 PRESSURE SWING ADSORPTION (PSA) AND SEPARATION OF n/i- PARAFFINS MIXTURE.....	9
1.3.1 EQUILIBRIUM ADSORPTION ISOTHERMS .....	9
1.3.2 KINETICS OF SORPTION.....	11
1.3.3 HYDROGEN MEMBRANE.....	12
1.3.4 PSA PROCESS AND MODELING.....	15
1.4 PRESURE SWING ADSORPTION REACTOR (PSAR).....	20
1.5 OBJECTIVES OF THE PRESENT RESEARCH.....	24
CHAPTER 2 .....	25
2.1 MODEL ASSUMPTIONS.....	25
2.2 MODEL EQUATIONS .....	28
2.3 NUMERICAL METHODS .....	38
2.4 PARAMETERS ESTIMATIONS .....	51
2.5 RESULTS AND DISCUSSION.....	53
Nomenclature.....	60
CHAPTER 3 .....	62
3.1 MODEL ASSUMPTIONS.....	62
3.2 PSAR PROCESS DESCRIPTION .....	62
3.3 MODEL EQUATIONS .....	66
3.4 HANDLING RECYCLE STREAM.....	79
3.5 NUMERICAL METHODS .....	83
3.6 RESULTS AND DISCUSSION.....	88
3.6.1 Conventional PSAR Cyclic Process .....	88
3.6.1.1 Conventional PSAR Cyclic Process with hydrogen purge .....	88
3.6.1.2 Conventional PSAR Cyclic Process with Self Regeneration .....	102
3.6.2 PSAR Cyclic Process with Waste Stream Recycled to Feed.....	111
3.6.2.1 PSAR Cyclic Process with Waste Stream Recycled to Feed (Hydrogen Purge).....	111
3.6.2.2 PSAR Cyclic Process with Waste Stream Recycled to feed (Self Regeneration).....	120
3.6.3 Overall Comparison of PSAR Systems .....	129
Nomenclature.....	133

CHAPTER 4 .....	136
4.1 MODEL ASSUMPTIONS.....	136
4.2 PSARM PROCESS DESCRIPTION.....	136
4.3 MODEL EQUATIONS .....	142
4.4 HANDLING RECYCLE STREAM.....	154
4.5 PARAMETERS ESTIMATIONS .....	157
4.6 NUMERICAL METHODS .....	159
4.7 RESULTS AND DISCUSSION .....	159
4.7.1 Conventional PSARM Cyclic Process.....	159
4.7.1.1 Conventional PSARM Cyclic Process with Hydrogen Purge .....	160
4.7.1.2 Conventional PSARM Cyclic Process with Self Regeneration.....	173
4.7.2 PSARM Cyclic Process with Waste Stream Recycled to feed.....	183
4.7.2.1 PSARM Cyclic Process with Waste Stream Recycled to feed (Hydrogen Purge).....	183
4.7.2.2 PSARM Cyclic Process with Waste Stream Recycled to feed (Self Regeneration).....	192
4.7.3 Overall Comparison of PSARM Systems.....	201
Nomenclature.....	204
CHAPTER 5 .....	207
5.1 CONCLUSIONS.....	207
5.2 RECOMMENDATIONS FOR FUTURE WORK .....	209
References.....	212
APPENDICES .....	222
APPENDIX A.....	223
APPENDIX B.....	231
APPENDIX C .....	238
APPENDIX D.....	245
APPENDIX E .....	252
APPENDIX F.....	260
APPENDIX G.....	267
APPENDIX H.....	274
VITA.....	281

## LIST OF FIGURES

Figure 1.1:	Flowsheet diagram for the Total Isomerization Process (TIP) .....	4
Figure 1.2:	Weisz Bifunctional Mechanism .....	8
Figure 1.3:	Steps for $nC_5/nC_6$ , $iC_5/iC_6$ separation based on Skarstrom Cycle [80]. ....	18
Figure 1.4:	Summary for PSA models' development. ....	19
Figure 1.5:	Flow diagram for the Combined Isomerization Reactor/Adsorber Process. ....	23
Figure 2.1:	Steps for $n-C_5/n-C_6/i-C_5/i-C_6$ PSA separation based on Skarstrom Cycle. ....	26
Figure 2.2:	Solution Flow Diagram for a single PSA step. ....	39
Figure 2.3:	Optimum values of alpha and beta corresponding to minimum Re for $N=20$ . ....	44
Figure 2.4a:	Selected profiles for the first cycle for $N = 10$ . ....	45
Figure 2.4b:	Selected profiles for the first cycle for $N = 15$ . ....	46
Figure 2.4c:	Selected profiles for the first cycle for $N = 19$ . ....	47
Figure 2.4d:	Selected profiles for the first cycle for $N = 20$ . ....	48
Figure 2.5a:	Absolute interpolation error introduced with $N=10$ , assuming $N=20$ is the exact solution. ....	49
Figure 2.5b:	Absolute interpolation error introduced with $N=19$ , assuming $N=20$ is the exact solution. ....	50
Figure 2.6:	Gas Phase concentration profiles of $n-C_5$ , $n-C_6$ and Temperature profile at the end of the cyclic steady state (Pressurization Step). ....	55
Figure 2.7:	Gas Phase concentration profiles of $n-C_5$ , $n-C_6$ and Temperature profile at the end of the cyclic steady state (Adsorption Step) .....	56
Figure 2.8:	Gas Phase concentration profiles of $n-C_5$ , $n-C_6$ and Temperature profile at the end of the cyclic steady state (Blow down Step) .....	57
Figure 2.9:	Gas Phase concentration profiles of $n-C_5$ , $n-C_6$ and Temperature profile at the end of the cyclic steady state (Desorption Step) .....	58
Figure 2.10:	Approach to cyclic steady state, illustrating exit concentration of $n-C_5$ , $n-C_6$ at end of blowdown step .....	59
Figure 3.1:	Flow diagram for the Combined Isomerization Reactor/Adsorber Process. ....	64
Figure 3.2:	Proposed Cyclic Steps for PSAR Unit. ....	65
Figure 3.3a:	Mathematical Representation for the PSAR Unit (Steps 1, 2 and 3) .....	67
Figure 3.3b:	Mathematical Representation for the PSAR Unit (Step 4) .....	67
Figure 3.4:	Connectivity diagram for handling recycle to feed in all four cyclic steps. ....	81
Figure 3.5:	Conversion versus reactor length at $300^\circ\text{C}$ : a: $n$ -Pentane, b: $n$ -Hexane ...	85
Figure 3.6:	Gas phase concentration profiles for reactive components in the PSAR bed at the end of cyclic steady state .....	95

Figure 3.7:	Gas phase concentration profiles for H <sub>2</sub> in the PSAR bed at the end of cyclic steady state .....	96
Figure 3.8:	Temperature Profiles in the bed at the end of cyclic steady state .....	97
Figure 3.9:	Velocity Profiles in the bed at the end of cyclic steady state .....	98
Figure 3.10:	Solid phase capacitance profiles for reactive components in the PSAR bed at the end of cyclic steady state .....	99
Figure 3.11:	Approach to cyclic steady state, showing exit concentrations of reactants and products at end of Blowdown/Reaction step .....	100
Figure 3.12:	Gas phase concentration profiles for reactive components in the PSAR bed at the end of cyclic steady state .....	104
Figure 3.13:	Gas phase concentration profiles for H <sub>2</sub> in the PSAR bed at the end of cyclic steady state .....	105
Figure 3.14:	Temperature Profiles in the bed at the end of cyclic steady state .....	106
Figure 3.15:	Velocity Profiles in the bed at the end of cyclic steady state .....	107
Figure 3.16:	Solid phase capacitance profiles for reactive components in the PSAR bed at the end of cyclic steady state .....	108
Figure 3.17:	Approach to cyclic steady state, showing exit concentrations of reactants and products at end of Blowdown/Reaction step .....	109
Figure 3.18:	Gas phase concentration profiles for reactive components in the PSAR bed at the end of cyclic steady state .....	113
Figure 3.19:	Gas phase concentration profiles for H <sub>2</sub> in the PSAR bed at the end of cyclic steady state .....	114
Figure 3.20:	Temperature Profiles in the bed at the end of cyclic steady state .....	115
Figure 3.21:	Velocity Profiles in the bed at the end of cyclic steady state .....	116
Figure 3.22:	Solid phase capacitance profiles for reactive components in the PSAR bed at the end of cyclic steady state .....	117
Figure 3.23:	Approach to cyclic steady state, showing exit concentrations of reactants and products at end of Blowdown/Reaction step .....	118
Figure 3.24:	Gas phase concentration profiles for reactive components in the PSAR bed at the end of cyclic steady state .....	122
Figure 3.25:	Gas phase concentration profiles for H <sub>2</sub> in the PSAR bed at the end of cyclic steady state .....	123
Figure 3.26:	Temperature Profiles in the bed at the end of cyclic steady state .....	124
Figure 3.27:	Velocity Profiles in the bed at the end of cyclic steady state .....	125
Figure 3.28:	Solid phase capacitance profiles for reactive components in the PSAR bed at the end of cyclic steady state .....	126
Figure 3.29:	Approach to cyclic steady state, showing exit concentrations of reactants and products at end of Blowdown/Reaction step .....	127
Figure 3.30:	Products' profiles for all models at the end of cyclic steady state reaction/adsorption step .....	131
Figure 4.1:	Flow diagram for the Combined Isomerization Reactor/Adsorber /Membrane Process. ....	139
Figure 4.2:	Cross sectional and isometric views of the PSARM vessel topology .....	140
Figure 4.3:	Proposed Cyclic Steps for PSARM Unit .....	141
Figure 4.4:	Connectivity diagram for handling recycle to feed in all four cyclic steps .....	156

Figure 4.5:	Gas phase concentration profiles for reactive components in the PSARM bed at the end of cyclic steady state.....	166
Figure 4.6:	Gas phase concentration profiles for H <sub>2</sub> in the PSARM bed at the end of cyclic steady state.....	167
Figure 4.7:	Temperature Profiles in the bed at the end of cyclic steady state .....	168
Figure 4.8:	Velocity Profiles in the bed at the end of cyclic steady state.....	169
Figure 4.9:	Solid phase capacitance profiles for reactive components in the PSARM bed at the end of cyclic steady state.....	170
Figure 4.10:	Approach to cyclic steady state, showing exit concentrations of reactants and products at end of Blowdown/Reaction step .....	171
Figure 4.11:	Gas phase concentration profiles for reactive components in the PSAR bed at the end of cyclic steady state .....	176
Figure 4.12:	Gas phase concentration profiles for H <sub>2</sub> in the PSARM bed at the end of cyclic steady state.....	177
Figure 4.13:	Temperature Profiles in the bed at the end of cyclic steady state .....	178
Figure 4.14:	Velocity Profiles in the bed at the end of cyclic steady state.....	179
Figure 4.15:	Solid phase capacitance profiles for reactive components in the PSAR bed at the end of cyclic steady state .....	180
Figure 4.16:	Approach to cyclic steady state, showing exit concentrations of reactants and products at end of Blowdown/Reaction step .....	181
Figure 4.17:	Gas phase concentration profiles for reactive components in the PSARM bed at the end of cyclic steady state.....	185
Figure 4.18:	Gas phase concentration profiles for H <sub>2</sub> in the PSARM bed at the end of cyclic steady state.....	186
Figure 4.19:	Temperature Profiles in the bed at the end of cyclic steady state .....	187
Figure 4.20:	Velocity Profiles in the bed at the end of cyclic steady state.....	188
Figure 4.21:	Solid phase capacitance profiles for reactive components in the PSAR bed at the end of cyclic steady state .....	189
Figure 4.22:	Approach to cyclic steady state, showing exit concentrations of reactants and products at end of Blowdown/Reaction step .....	190
Figure 4.23:	Gas phase concentration profiles for reactive components in the PSAR bed at the end of cyclic steady state .....	194
Figure 4.24:	Gas phase concentration profiles for H <sub>2</sub> in the PSARM bed at the end of cyclic steady state.....	195
Figure 4.25:	Temperature Profiles in the bed at the end of cyclic steady state .....	196
Figure 4.26:	Velocity Profiles in the bed at the end of cyclic steady state.....	197
Figure 4.27:	Solid phase capacitance profiles for reactive components in the PSAR bed at the end of cyclic steady state .....	198
Figure 4.28:	Approach to cyclic steady state, showing exit concentrations of reactants and products at end of Blowdown/Reaction step .....	199
Figure 4.29:	Products' profiles for all models at the end of cyclic steady state reaction/adsorption step.....	202

Figure A.1:	Three dimensional drawing illustrating the transient and spatial change in n-C <sub>5</sub> concentration with respect to time and axial distance for the four basic steps at the steady state cycle. (Conventional PSAR Unit/Hydrogen Purge).....	224
Figure A.2:	Three dimensional drawing illustrating the transient and spatial change in n-C <sub>6</sub> concentration with respect to time and axial distance for the four basic steps at the steady state cycle. (Conventional PSAR Unit/Hydrogen Purge).....	225
Figure A.3:	Three dimensional drawing illustrating the transient and spatial change in i-C <sub>5</sub> concentration with respect to time and axial distance for the four basic steps at the steady state cycle. (Conventional PSAR Unit/Hydrogen Purge).....	226
Figure A.4:	Three dimensional drawing illustrating the transient and spatial change in i-C <sub>6</sub> concentration with respect to time and axial distance for the four basic steps at the steady state cycle. (Conventional PSAR Unit/Hydrogen Purge).....	227
Figure A.5:	Three dimensional drawing illustrating the transient and spatial change in H <sub>2</sub> concentration with respect to time and axial distance for the four basic steps at the steady state cycle. (Conventional PSAR Unit/Hydrogen Purge).....	228
Figure A.6:	Three dimensional drawing illustrating the transient and spatial change in Temperature with respect to time and axial distance for the four basic steps at the steady state cycle. (Conventional PSAR Unit/Hydrogen Purge).....	229
Figure A.7:	Three dimensional drawing illustrating the transient and spatial change in Velocity with respect to time and axial distance for the four basic steps at the steady state cycle. (Conventional PSAR Unit/Hydrogen Purge).....	230
Figure B.1:	Three dimensional drawing illustrating the transient and spatial change in n-C <sub>5</sub> concentration with respect to time and axial distance for the four basic steps at the steady state cycle. (Conventional PSAR Unit/Self Regeneration) .....	232
Figure B.2:	Three dimensional drawing illustrating the transient and spatial change in n-C <sub>6</sub> concentration with respect to time and axial distance for the four basic steps at the steady state cycle. (Conventional PSAR Unit/Self Regeneration) .....	233
Figure B.3:	Three dimensional drawing illustrating the transient and spatial change in i-C <sub>5</sub> concentration with respect to time and axial distance for the four basic steps at the steady state cycle. (Conventional PSAR Unit/Self Regeneration) .....	234
Figure B.4:	Three dimensional drawing illustrating the transient and spatial change in i-C <sub>6</sub> concentration with respect to time and axial distance for the four basic steps at the steady state cycle. (Conventional PSAR Unit/Self Regeneration) .....	235

Figure B.5:	Three dimensional drawing illustrating the transient and spatial change in $H_2$ concentration with respect to time and axial distance for the four basic steps at the steady state cycle. (Conventional PSAR Unit/Self Regeneration) .....	236
Figure B.6:	Three dimensional drawing illustrating the transient and spatial change in Temperature with respect to time and axial distance for the four basic steps at the steady state cycle. (Conventional PSAR Unit/Self Regeneration) .....	237
Figure C.1:	Three dimensional drawing illustrating the transient and spatial change in n- $C_5$ concentration with respect to time and axial distance for the four basic steps at the steady state cycle. (PSAR Unit with Waste Recycled to Feed/Hydrogen Purge) .....	239
Figure C.2:	Three dimensional drawing illustrating the transient and spatial change in n- $C_6$ concentration with respect to time and axial distance for the four basic steps at the steady state cycle. (PSAR Unit with Waste Recycled to Feed/Hydrogen Purge) .....	240
Figure C.3:	Three dimensional drawing illustrating the transient and spatial change in i- $C_5$ concentration with respect to time and axial distance for the four basic steps at the steady state cycle. (PSAR Unit with Waste Recycled to Feed/Hydrogen Purge) .....	241
Figure C.4:	Three dimensional drawing illustrating the transient and spatial change in i- $C_6$ concentration with respect to time and axial distance for the four basic steps at the steady state cycle. (PSAR Unit with Waste Recycled to Feed/Hydrogen Purge) .....	242
Figure C.5:	Three dimensional drawing illustrating the transient and spatial change in $H_2$ concentration with respect to time and axial distance for the four basic steps at the steady state cycle. (PSAR Unit with Waste Recycled to Feed/Hydrogen Purge) .....	243
Figure C.6:	Three dimensional drawing illustrating the transient and spatial change in Temperature with respect to time and axial distance for the four basic steps at the steady state cycle. (PSAR Unit with Waste Recycled to Feed/Hydrogen Purge) .....	244
Figure D.1:	Three dimensional drawing illustrating the transient and spatial change in n- $C_5$ concentration with respect to time and axial distance for the four basic steps at the steady state cycle. (PSAR Unit with Waste Recycled to Feed/Self Regeneration) .....	246
Figure D.2:	Three dimensional drawing illustrating the transient and spatial change in n- $C_6$ concentration with respect to time and axial distance for the four basic steps at the steady state cycle. (PSAR Unit with Waste Recycled to Feed/Self Regeneration) .....	247
Figure D.3:	Three dimensional drawing illustrating the transient and spatial change in i- $C_5$ concentration with respect to time and axial distance for the four basic steps at the steady state cycle. (PSAR Unit with Waste Recycled to Feed/Self Regeneration) .....	248



Figure D.4:	Three dimensional drawing illustrating the transient and spatial change in i-C <sub>6</sub> concentration with respect to time and axial distance for the four basic steps at the steady state cycle. (PSAR Unit with Waste Recycled to Feed/Self Regeneration) .....	249
Figure D.5:	Three dimensional drawing illustrating the transient and spatial change in H <sub>2</sub> concentration with respect to time and axial distance for the four basic steps at the steady state cycle. (PSAR Unit with Waste Recycled to Feed/Self Regeneration) .....	250
Figure D.6:	Three dimensional drawing illustrating the transient and spatial change in Temperature with respect to time and axial distance for the four basic steps at the steady state cycle. (PSAR Unit with Waste Recycled to Feed/Self Regeneration) .....	251
Figure E.1:	Three dimensional drawing illustrating the transient and spatial change in n-C <sub>5</sub> concentration with respect to time and axial distance for the four basic steps at the steady state cycle. (Conventional PSARM Unit/Hydrogen Purge) .....	253
Figure E.2:	Three dimensional drawing illustrating the transient and spatial change in n-C <sub>6</sub> concentration with respect to time and axial distance for the four basic steps at the steady state cycle. (Conventional PSARM Unit/Hydrogen Purge) .....	254
Figure E.3:	Three dimensional drawing illustrating the transient and spatial change in i-C <sub>5</sub> concentration with respect to time and axial distance for the four basic steps at the steady state cycle. (Conventional PSARM Unit/Hydrogen Purge) .....	255
Figure E.4:	Three dimensional drawing illustrating the transient and spatial change in i-C <sub>6</sub> concentration with respect to time and axial distance for the four basic steps at the steady state cycle. (Conventional PSARM Unit/Hydrogen Purge) .....	256
Figure E.5:	Three dimensional drawing illustrating the transient and spatial change in H <sub>2</sub> concentration with respect to time and axial distance for the four basic steps at the steady state cycle. (Conventional PSARM Unit/Hydrogen Purge) .....	257
Figure E.6:	Three dimensional drawing illustrating the transient and spatial change in Temperature with respect to time and axial distance for the four basic steps at the steady state cycle. (Conventional PSARM Unit/Hydrogen Purge) .....	258
Figure E.7:	Three dimensional drawing illustrating the transient and spatial change in Velocity with respect to time and axial distance for the four basic steps at the steady state cycle. (Conventional PSARM Unit/Hydrogen Purge) .....	259
Figure F.1:	Three dimensional drawing illustrating the transient and spatial change in n-C <sub>5</sub> concentration with respect to time and axial distance for the four basic steps at the steady state cycle. (Conventional PSARM Unit/Self Regeneration) .....	261

Figure F.2:	Three dimensional drawing illustrating the transient and spatial change in n-C <sub>6</sub> concentration with respect to time and axial distance for the four basic steps at the steady state cycle. (Conventional PSARM Unit/Self Regeneration).....	262
Figure F.3:	Three dimensional drawing illustrating the transient and spatial change in i-C <sub>5</sub> concentration with respect to time and axial distance for the four basic steps at the steady state cycle. (Conventional PSARM Unit/Self Regeneration).....	263
Figure F.4:	Three dimensional drawing illustrating the transient and spatial change in i-C <sub>6</sub> concentration with respect to time and axial distance for the four basic steps at the steady state cycle. (Conventional PSARM Unit/Self Regeneration).....	264
Figure F.5:	Three dimensional drawing illustrating the transient and spatial change in H <sub>2</sub> concentration with respect to time and axial distance for the four basic steps at the steady state cycle. (Conventional PSARM Unit/Self Regeneration).....	265
Figure F.6:	Three dimensional drawing illustrating the transient and spatial change in Temperature with respect to time and axial distance for the four basic steps at the steady state cycle. (Conventional PSARM Unit/Self Regeneration).....	266
Figure G.1:	Three dimensional drawing illustrating the transient and spatial change in n-C <sub>5</sub> concentration with respect to time and axial distance for the four basic steps at the steady state cycle. (PSARM Unit with Waste Recycled to Feed/Hydrogen Purge).....	268
Figure G.2:	Three dimensional drawing illustrating the transient and spatial change in n-C <sub>6</sub> concentration with respect to time and axial distance for the four basic steps at the steady state cycle. (PSARM Unit with Waste Recycled to Feed/Hydrogen Purge).....	269
Figure G.3:	Three dimensional drawing illustrating the transient and spatial change in i-C <sub>5</sub> concentration with respect to time and axial distance for the four basic steps at the steady state cycle. (PSARM Unit with Waste Recycled to Feed/Hydrogen Purge).....	270
Figure G.4:	Three dimensional drawing illustrating the transient and spatial change in i-C <sub>6</sub> concentration with respect to time and axial distance for the four basic steps at the steady state cycle. (PSARM Unit with Waste Recycled to Feed/Hydrogen Purge).....	271
Figure G.5:	Three dimensional drawing illustrating the transient and spatial change in H <sub>2</sub> concentration with respect to time and axial distance for the four basic steps at the steady state cycle. (PSARM Unit with Waste Recycled to Feed/Hydrogen Purge).....	272
Figure G.6:	Three dimensional drawing illustrating the transient and spatial change in Temperature with respect to time and axial distance for the four basic steps at the steady state cycle. (PSARM Unit with Waste Recycled to Feed/Hydrogen Purge).....	273

Figure H.1:	Three dimensional drawing illustrating the transient and spatial change in n-C <sub>5</sub> concentration with respect to time and axial distance for the four basic steps at the steady state cycle. (PSARM Unit with Waste Recycled to Feed/Self Regeneration) .....	275
Figure H.2:	Three dimensional drawing illustrating the transient and spatial change in n-C <sub>6</sub> concentration with respect to time and axial distance for the four basic steps at the steady state cycle. (PSARM Unit with Waste Recycled to Feed/Self Regeneration) .....	276
Figure H.3:	Three dimensional drawing illustrating the transient and spatial change in i-C <sub>5</sub> concentration with respect to time and axial distance for the four basic steps at the steady state cycle. (PSARM Unit with Waste Recycled to Feed/Self Regeneration) .....	277
Figure H.4:	Three dimensional drawing illustrating the transient and spatial change in i-C <sub>6</sub> concentration with respect to time and axial distance for the four basic steps at the steady state cycle. (PSARM Unit with Waste Recycled to Feed/Self Regeneration) .....	278
Figure H.5:	Three dimensional drawing illustrating the transient and spatial change in H <sub>2</sub> concentration with respect to time and axial distance for the four basic steps at the steady state cycle. (PSARM Unit with Waste Recycled to Feed/Self Regeneration) .....	279
Figure H.6:	Three dimensional drawing illustrating the transient and spatial change in Temperature with respect to time and axial distance for the four basic steps at the steady state cycle. (PSARM Unit with Waste Recycled to Feed/Self Regeneration) .....	280

## LIST OF TABLES

Table 1.1:	Typical Properties of the Total Isomerization Process .....	3
Table 1.2:	Properties of Isomerization Catalysts .....	7
Table 2.1:	<i>Re</i> Values at $\alpha=\beta=0$ and at optimum $\alpha$ and $\beta$ .....	42
Table 2.2:	First cycle time for $\alpha=\beta=0$ and for optimum values of $\alpha$ and $\beta$ . ....	43
Table 2.3:	Data for the base case system .....	52
Table 2.4:	Parametric Values used for simulation of the base case of the n-C <sub>5</sub> /n-C <sub>6</sub> /N <sub>2</sub> system. ....	54
Table 3.1:	Reaction & Adsorption Parameters for Reactor Section .....	84
Table 3.2:	First cycle time for $\alpha=\beta=0$ and for optimum values of $\alpha$ and $\beta$ . ....	86
Table 3.3:	Parametric Values used for simulation of PSARM systems.....	87
Table 3.4:	Percentage Relative Occupation for reactive components of the solid phase for both catalyst and adsorber sections (Conventional PSAR unit/H <sub>2</sub> purge).....	101
Table 3.5:	Percentage Relative Occupation for reactive components of the solid phase for both catalyst and adsorber sections (Conventional PSAR unit/Self Regeneration). ....	110
Table 3.6:	Percentage Relative Occupation for reactive components of the solid phase for both catalyst and adsorber sections (PSAR with waste recycled to feed/H <sub>2</sub> Purge) .....	119
Table 3.7:	Percentage Relative Occupation for reactive components of the solid phase for both catalyst and adsorber sections (PSAR with waste recycled to feed/Self Regeneration) .....	128
Table 3.8:	Exit concentrations of iso-pentane and iso-hexane and process yields for each of the models at the end of steady state cyclic reaction/adsorption step .....	132
Table 4.1:	Parametric Values used for simulation of conventional PSAR system ..	158
Table 4.2:	Percentage occupation for reactive components of the solid phase for both catalyst and adsorber sections (Conventional PSARM unit/H <sub>2</sub> purge) .....	172
Table 4.3:	Percentage Occupation for reactive components of the solid phase for both catalyst and adsorber sections (Conventional PSARM unit/Self Regeneration).....	182
Table 4.4:	Percentage Occupation for reactive components of the solid phase for both catalyst and adsorber sections (PSARM with waste recycled to feed/H <sub>2</sub> Purge).....	191
Table 4.5:	Percentage Occupation for reactive components of the solid phase for both catalyst and adsorber sections (PSARM with waste recycled to feed/Self Regeneration).....	200
Table 4.6:	Exit concentrations of iso-pentane and iso-hexane at the end of steady state cyclic reaction/adsorption step.....	203

## ABSTRACT

In this work, a novel process for isomerizing and separating n-pentane and n-hexane to their branched isomers is proposed. Both reactor and separation units are combined in one vessel. The vessel is divided into two sections: a reactor section and a PSA separation section. The reactor section is packed with Pt/Y-zeolite catalyst. The PSA separation section is equipped with a 5A zeolite adsorbent. Also, to facilitate separation, the addition of hydrogen membrane to the adsorber section is studied in this work.

A dispersed plug flow mathematical model of the entire process is developed. The model links both reactor and separation sections. The model is used to investigate the dynamics of a PSAR and PSARM units. Different operating modes of both models are studied.

For a feed to a conventional PSAR unit, containing an equimolar fractions of 0.03 for each of n-C<sub>5</sub>, n-C<sub>6</sub>, i-C<sub>5</sub> and i-C<sub>6</sub>, the molar fractions of i-C<sub>5</sub> and i-C<sub>6</sub> rise to values of 0.0439 and 0.045 after reaching equilibrium conversion at the end of the reactor section. The PSA section allows for complete separation of n-C<sub>5</sub> and n-C<sub>6</sub> from the reactor section effluent stream. The addition of a membrane to this section raises the concentration of i-C<sub>5</sub> and i-C<sub>6</sub> in the product stream to 0.1 and 0.09, respectively. Recycling of waste streams back to the process allows for recovery of valuable hydrocarbon material. Eight models are developed to investigate the behavior of conventional PSAR and PSARM models in addition to models containing recycling of waste to feed and to the adsorber section. The study revealed that the system achieving the highest yield of isomers, for both PSAR and PSARM systems is the one that recycles the waste stream to the feed and utilizes part of the product stream as a purge stream.

## الملخص

في هذا العمل عملية مبتكرة لتحويل وفصل البنتان و الهكسان الطبيعي الي مركباتهم التفرعية. وحدتي التفاعل والفصل مدمجتين في حاوية واحدة. الحاوية مجزأة الى قسمين: قسم للمفاعل وآخر للامتصاص. قسم المفاعل مكتظ بزيولايت البلاينيوم واي. قسم الفصل يكتظ بزيولايت 5A الممتص للبنتان و الهكسان الطبيعيان. أيضا ، لتسهيل عملية الفصل ، إضافة غشاء الهيدروجين الى قسم الفصل درست في هذا العمل.

نموذج التدفق الرياضي طور لمحاكاة كل العمليات. استخدم هذا النموذج لدراسة الديناميكا لوحدة التفاعل والامتصاص بالإضافة الى وحدة التفاعل والامتصاص و فصل الهيدروجين.

بالنسبة الى المدخل الى وحدة التفاعل والامتصاص والذي يحتوي على نسب مولية متساوية من البنتان والهكسان الطبيعيين والمتفرعين تقدر ب 0.05 من اجمالي المدخل لكل من المركبات السابقة الذكر، فان الكسر المولي يرتفع الى 0.0439 بالنسبة الى متفرع البنتان والى 0.045 بالنسبة الى متفرع الهكسان بعد الوصول الى التحول المتوازن في نهاية قسم المفاعل . قسم الامتصاص يسمح بامتصاص كل الكميات المتبقية من البنتان والهكسان الطبيعيين بعد خروجهما من المفاعل . إضافة الغشاء الهيدروجيني يرفع تركيز البنتان المتفرع الى 0.1 كما يرفع نسبة الهكسان المتفرع الى 0.09. ارجاع المنتج الغير مرغوب فيه ودمجه مع المدخل الاساس يسمح باحتواء المركبات الهيدروكربونية الثمينة. ثمانية نماذج طورت لدراسة سلوك وحدات التفاعل والفصل التقليدية بالإضافة الى الوحدات اللتي تعيد استخدام المنتج الغير مرغوب فيه . اظهرت الدراسة ان افضل الانظمة هو ذلك الذي يعيد استخدام المنتج الغير مرغوب فيه كما يستخدم جزء من الناتج الثمين لتطهير الحاوية .

# CHAPTER 1

## INTRODUCTION AND BACKGROUND

In this chapter a brief introduction to the topics discussed in this research thesis is given and the relevant literature on these topics is summarized.

### 1.1 INTRODUCTION

The Hydroisomerization of low molecular weight paraffins has become an increasingly important conversion process in recent years. This is due to phase-out of Tetra Ethyl Lead (TEL) and to the constraints imposed on the use of Methyl Tertiary Butyle Ether (MTBE) as octane boosters. The research octane number of streams containing mostly straight-chain hydrocarbons ( $C_5$  and  $C_6$ ) can be boosted from 70 to over 80 with the extent of improvement depending on the isomerization temperature and  $C_5/C_6$  ratio [81]. The unleaded research octane number for isopentane is 93 compared with 62 for n-pentane [38].

Zeolite catalysts have been employed almost exclusively in new efforts in this area. Paraffin isomerization requires a stable catalyst with high activity to take advantage of the higher equilibrium conversions to branched isomers at low temperature. Zeolites are known to be highly active for this type of reaction, and have additional advantages such as relative insensitivity to moisture, sulfur and nitrogen.

Light straight-run naphtha, consisting mainly of n-pentane and n-hexane, is partially isomerized via an isomerization reactor. It is necessary to recycle the unreacted n-paraffins to the reactor. Separation by distillation is difficult and energy consuming because the n-/isoparaffins mixture is composed of components with close-boiling points. Alternatively, the separation is better done by selective adsorption using molecular sieves such as 5A zeolite, where the n-paraffins are adsorbed and the iso-paraffins are excluded [48,49].

This separation method is widely used in industry. An example is the Total Isomerization Process (TIP) developed by Union Carbide in 1970 [25]. The flow sheet for the TIP process is shown in Figure 1.1. In the flow sheet diagram, the reactor (vessel 22) is typically operated most efficiently at high pressures (200-400 psia). The reaction must be conducted in the presence of hydrogen to avoid deactivation of the catalyst. Depending on the particular catalyst composition employed, the operating temperature of the isomerization reactor is generally within the range of 200 to 390° C. The TIP process employs a bi-functional catalyst, which consists of a noble metal such as platinum deposited on an acidic media such as Y-Zeolite. The minimum hydrogen partial pressure required is also dependent on the catalyst used, and is usually in the range of 100 to 250 psia. Adsorber units (vessels 44, 46, 48, 50), however, have typically operated more efficiently at lower pressures (200-300 psia) than the reactor. Typical properties of the TIP process, as in the patent published by Gary [25], are summarized in Table 1.1.

Selective permeation through a membrane has become a recognized chemical engineering process for separation of fluid mixtures. During the past two decades, considerable attention has been paid to the integration of the membrane process to chemical reactors. Membrane reactors, which combine reaction and separation or combine mixing/distribution and reaction in one-unit operation, are the result of this integration. These reactors have been used to enhance the reaction yield and conversion of thermodynamically limited reactions or to control the reaction pathway by introducing a reactant into the reaction zone in a controlled manner [44].



Table 1.1: Typical Properties of the Total Isomerization Process [25]

<b><i>Fresh Feedstock Composition:</i></b>	
<b>Component</b>	<b>Weight%</b>
C <sub>4</sub> and lower	4.1
i-C <sub>5</sub>	24.5
n-C <sub>5</sub>	27.8
i-C <sub>6</sub>	14.7
n-C <sub>6</sub>	27.4
C7 and Higher	1.5
<b><i>Reactor Condition:</i></b>	
• Catalyst	0.1-1.0 %wt Pt (Pd) / Y-zeolite
• Pressure (bar)	14-28
• Temperature(°C)	200-390
• H <sub>2</sub> Partial Pressure (bar)	7-14
• H <sub>2</sub> Feed Composition (mol %)	50-70
<b><i>Adsorbers Condition:</i></b>	
• Adsorbent	5A zeolite
• No. of beds	4
• No. of steps / bed	4 (Basic Skarstrom Cycle)
• Pressure at adsorption step	14-20 bar
• Temperature	200 – 390 °C

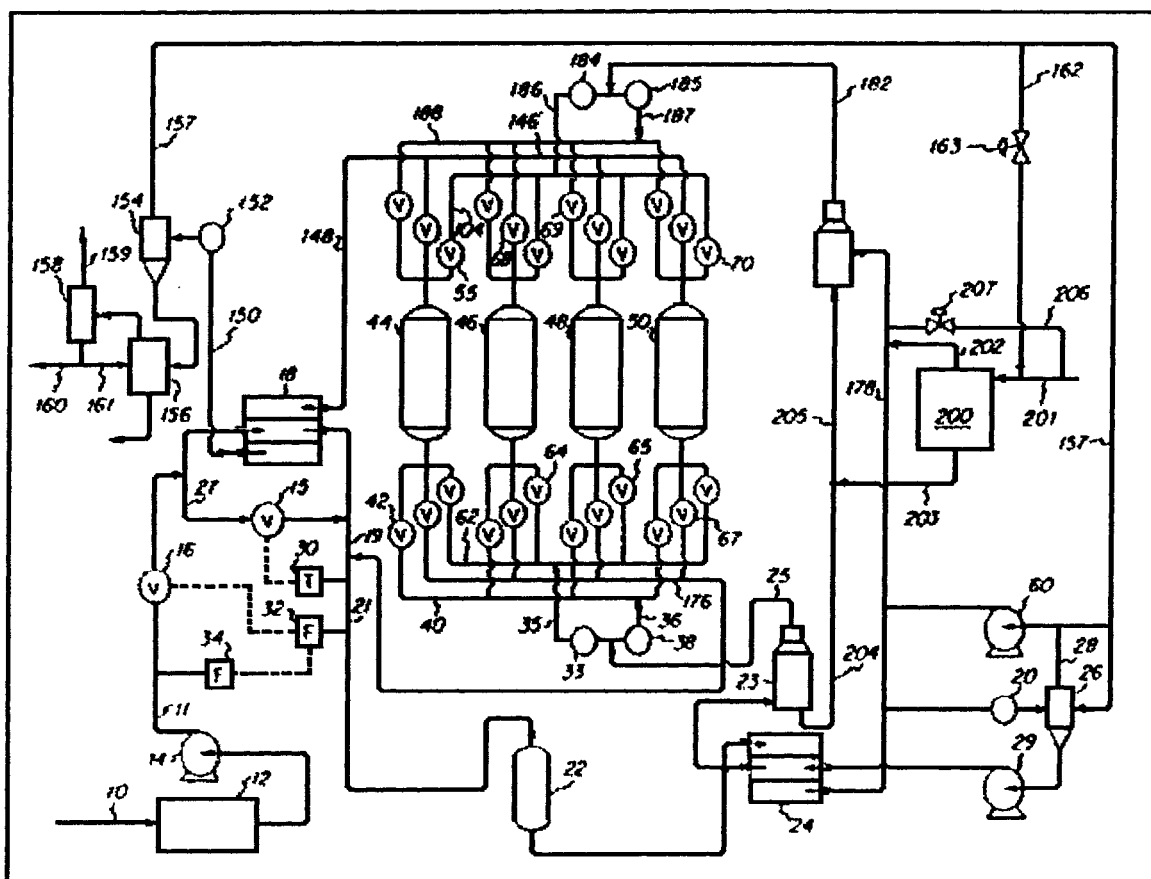


Figure 1.1: Flowsheet diagram for the Total Isomerization Process (TIP). [25]

## **1.2 n-PARAFFINS ISOMERIZATION REACTION**

Paraffin isomerization requires a stable catalyst with high activity to take advantages of the higher equilibrium conversions to branched products at lower temperatures [38]. Selectivity is another important property for the catalyst where the undesired reaction is the cracking of alkanes [9]. Different isomerization catalyst systems have been developed. Fujimoto, et al [24] presented a good summary of these systems. The catalyst systems can be classified into three groups: Friedel-Craft, bi-functional, and solid super-acid catalysts. Up to 1956, commercial processes for the isomerization of light paraffins employed anhydrous aluminum chloride as the catalyst, which is known as Friedel-Craft catalyst. It possesses high activity for n-butane isomerization at low temperature, below 90°C. However, because of its low selectivity, especially for n-C<sub>5</sub> and n-C<sub>6</sub> isomerization, poor structure stability, and strong corrosivity, it is out of favor today.

Then, bi-functional catalysts with a hydrogenation-dehydrogenation function (e.g., Pt or Pd) and an acid function (e.g., alumina, silica-alumina, or zeolites) were used. It is known that Pt-alumina is effective for the isomerization of n-C<sub>5</sub> and n-C<sub>6</sub>, but it has to be used at high reaction temperatures, usually between 455 and 510 °C. To improve the performance and to lower the operating temperature, low temperature type bifunctional catalysts, which were Pt-alumina treated by AlCl<sub>3</sub> or organic chlorides, were developed and they have been widely used in the industry. Later, in 1983, Ribeiro developed new kinds of bifunctional catalysts of noble metal/aluminosilicate and noble metal/zeolite, which produced a high conversion near to the equilibrium value in a medium temperature of 260 to 314°C [59].

The third group is solid super-acid catalysts such as sulfated zirconia, which have been developed in recent years and are still under study. Most of these studies are for n-butane isomerization. Gates and Ryu published a recent study in 1998 for n-hexane isomerization via sulfated zirconia [26].

Sulfated zirconia is shown to compromise the positive properties of the other two groups of catalysts. A summary comparing the three groups of catalysts is presented in Table 1.2.

Hydroisomerization of n-paraffin on a bifunctional catalyst is considered to proceed through a mechanism whereby olefins are formed at the metallic site by dehydrogenation of the normal paraffin feed and are then adsorbed at an acidic site. At this acidic site, a carbonium ion is formed which undergoes skeletal rearrangement. The resulting isocarbonium ion is converted to an iso-olefin, which is then hydrogenated at the metallic site and desorbed. This is known as the classical Weisz bifunctional mechanism, which was first established by Weisz in 1962 [89]. This mechanism, shown schematically in Figure 1.2, dominated the explanation for hydroisomerization of n-paraffins for a long period. Different authors have proved that the skeletal isomerization of the reactive intermediate (the carbonium ion) is the rate-controlling step [9,12,13].

In 1956, Barrer and Sutherland studied experimentally the hydroisomerization of n-C<sub>5</sub>/n-C<sub>6</sub> mixtures on a 0.5 wt % Pt/H-mordenite and a 0.5 wt% Pd/H-faujasite catalysts [8]. The rate constant values for a temperature range of 506 to 533 K have been published for the two catalyst systems. In 1982, Bryant and Spivey [13] have shown that mordenite is more active than faujasite. However, mordenite suffers from a high rate of deactivation [15,63,64]. Thus, faujasite is chosen as the catalyst for the present study because catalyst deactivation is assumed negligible when modeling the process.

Table 1.2: Properties of Isomerization Catalysts.

<b>CATALYST</b>	<b>Pt/Cl-Alumina</b>	<b>Pt/Zeolite</b>	<b>Solid Super-acid</b>
<i>Reaction temperature (°C)</i>	Low (120-180)	High (250-280)	Low (180-220)
<i>Tolerance to feed contaminants (S, N<sub>2</sub>, water, oxygenates )</i>	Low	High	High
<i>Corrosion problem.</i>	High	Low	Low
<i>Auxiliary equipment needed:</i> <ul style="list-style-type: none"> <li>• <i>Cl injection</i></li> <li>• <i>HCl scrubber</i></li> <li>• <i>Feed dryers</i></li> <li>• <i>H<sub>2</sub> recycle</i></li> </ul>	Yes Yes Yes No	No No No Yes	No No No Yes

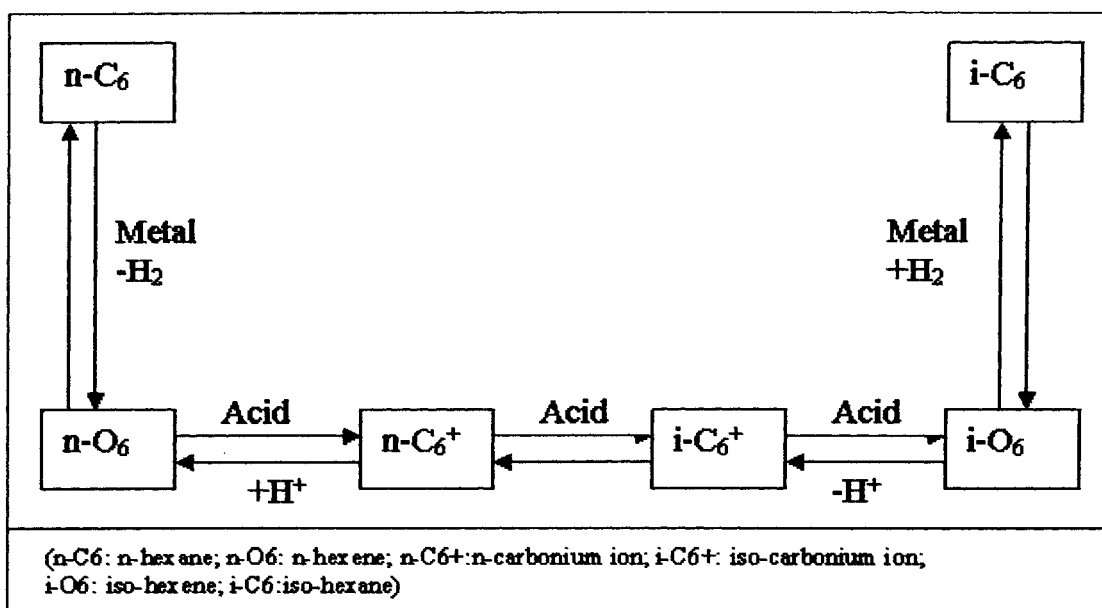


Figure 1.2: Weisz Bifunctional Mechanism [89]

### 1.3 PRESSURE SWING ADSORPTION (PSA) AND SEPARATION OF n/i-PARAFFINS MIXTURE

Pressure swing adsorption (PSA) is a process where one or more fixed beds are used to separate a gas mixture based on the differing affinities of individual components for a selected adsorbent. The selectivity may depend on a difference in adsorption equilibrium (equilibrium-based separation) or on a difference in sorption rates (kinetic-based separation). An example for the former is the production of oxygen by air separation on CaX zeolite, and an example for the latter is the production of nitrogen by air separation on 4A zeolite.

Modeling of PSA system is actually a process of linking up several models for sub-processes in the system. The PSA model should consider mass transfer, heat transfer, and physical equilibrium models. Reviews of these concepts are presented below.

#### 1.3.1 EQUILIBRIUM ADSORPTION ISOTHERMS

Adsorption equilibria are described by isotherms, a relationship between adsorbed and bulk phase concentrations at constant temperatures. Different approaches are used to study the adsorption equilibrium isotherms on molecular sieve zeolites. The phenomena can be treated by thermodynamic means using virial isotherms (e.g. Ruthven and Kaul [67]), by molecular models based on localized adsorption (e.g. Langmuir [40]; Nitta *et al* [52], or by empirical correlations (e.g. Yang [90]). Although a virial isotherm interprets data well from a thermodynamic point of view, it is unable to give insight into sorption events at the molecular level [7].

Sorption isotherms in zeolites generally follow type I in IUPAC classification. A representative and very well known isotherm for type I is Langmuir Isotherm [40], which is given by:

$$\theta = \frac{q}{q_{\max}} = \frac{K_{ads}P}{1 + K_{ads}P} \quad (1.1a)$$

$$\text{or alternatively: } K_{ads} = \frac{1}{P} \frac{\theta}{1 - \theta} \quad (1.1b)$$

Nomenclature of the above expressions is presented at end of Chapter 2. In the above expression, Langmuir assumed that each adsorbed molecule occupies one active site, the surface is homogeneous, and no interaction exists between adsorbed molecules.

Based on Langmuir isotherm, Nitta *et al.* [52] developed a Multisite Langmuir (MSL) model, which is more reliable and accurate. Nitta *et al.* assumed that localized adsorption takes place where the adsorbed molecule occupies a certain number of active sites,  $n$ . They presented two types of isotherms for both homogeneous and heterogeneous surfaces. The expression for homogeneous surface is:

$$K_{ads} = \frac{1}{P} \frac{\theta}{(1-\theta)^n} \quad (1.2)$$

In the above expression, the interaction term between sorbed molecules is neglected. Also, if  $n$  equals 1, the expression reduces to Langmuir isotherm. In 1997, Silva and Rodrigues proved experimentally that the Nitta *et al.* isotherm provides a good description of sorption of  $n$ -pentane and  $n$ -hexane in 5A zeolite. They found that  $n$  equals 5 and 6 for  $n$ -pentane and  $n$ -hexane, respectively [75,77].

The two models can be discriminated experimentally by plotting experimental data  $\frac{1}{P} \frac{\theta}{(1-\theta)^n}$  against  $\theta$  at different temperatures. The appropriate model is the one that gives straight lines parallel to the  $\theta$ -axis.



### 1.3.2 KINETICS OF SORPTION

Zeolite molecular sieves consist of small microporous crystals formed in a macroporous pellet, as represented schematically in Figure 1.4. Therefore, there are three diffusion mechanisms: the gas-film diffusion around the pellet, the macropore diffusion into the pellets, and the micropore diffusions into the crystals. Under practical conditions of operation the external film resistance is negligible [68, 69]. Thus, the sorption rate is generally controlled by either macropore or micropore diffusion or by the combined effects of these resistances. Ruckenstein *et al* in 1971 proposed a bi-disperse pore model for transient diffusion in bi-disperse porous adsorbents, based on the assumption that the two mechanisms are in series [61]. Based on that model, Ruthven and Loughlin [66] developed a criterion for the relative importance of the diffusion mechanisms which is given by:

$$\gamma = \frac{(1+K)(D_c/r_c^2)}{(D_p/R_p^2)} \quad (1.3)$$

where  $(1+K)R_p^2/D_p$  is the time constant for macropore diffusion,  $r_c^2/D_c$  is the time constant for micropore diffusion,  $K$  is the capacity factor given by  $(1-\varepsilon_p)H_{ad}/\varepsilon_p$ , and  $H_{ad}$  is the dimensionless Henry's constant given by  $\rho_s RTH/M_w$ . Description of other notations is presented at end of Chapter 2. In the above expression, macropore diffusion is the controlling mechanism for  $\gamma > 10$ ; crystal diffusion is the controlling mechanism for  $\gamma < 0.1$ . Between these limits, both mechanisms are important and should be taken into consideration.

The controlling diffusion mechanisms in zeolite molecular sieves can be determined experimentally by carrying out experiments in pellets with different sizes but with the same crystal size or pellets with the same size but with different crystals. If it is found that time constants for diffusion depend directly on pellet size and independent of crystal size, it can be concluded that macropore diffusion is the controlling mechanism. If the reverse is observed, micropore diffusion is the controlling mechanism. Other options to determine the controlling mechanism experimentally are by studying the effects of purge gas, purge flow rate, and temperature on the desorption curves [75,77].

In 1997, Silva and Rodrigues [75] made a detailed experimental study on adsorption and diffusion of n-pentane in pellets of 5A zeolite. They made also a similar study for n-hexane [77]. They found that, in both cases, macropore diffusion is the controlling mass transfer mechanism for the pellets they were using. Diffusion and equilibrium sorption data were obtained from these experiments, including the pore diffusivity of n-pentane, the pore diffusivity of n-hexane, the isosteric heat of adsorption for n-pentane and n-hexane, and the Henry constants.

### 1.3.3 HYDROGEN MEMBRANE

A membrane is a physical barrier between two fluids. In over 99% of the cases of current industrial interest the membrane is made of a polymer. This polymer is a cast or spun or extruded to form a continuous film without holes in the desired geometry [55].

A variety of membrane separation processes such as reverse osmosis; ultra filtration, gas permeation, and electro-dialysis are becoming increasingly popular in industry. This popularity is due to the simplicity of the processes, the gentle nature of the separation (high temperatures and phase changes are not required), the low energy requirements, and frequently low capital and operating costs.

In gas permeation, two or more gas species are separated based on different permeabilities in a membrane. Although a variety of devices could be used, hollow fiber and spiral wound systems are used commercially. The hollow fiber systems have the advantage of very large surface to volume ratios. The hollow fibers can have an ID up to 200 microns in diameter. The larger the ID, the lower the pressure drop inside the tubes (a surprisingly important design consideration), but the lower the area/volume ratio. The wall thickness can be from 25 to 250 microns depending on the pressure that must be withstood. The skin is from 0.1 to 1.0 micron thick and is formed on the outside of the hollow fiber. Thus the flow is radially inward since this allows the fiber to withstand much higher pressures. The hollow fiber systems are currently being used commercially for recovering hydrogen, carbon dioxide and nitrogen generation from air.

The basic flux equation is

$$N_A = \frac{F_{P,A}}{A} = \frac{P_A \Delta \bar{p}_A}{t_m} \quad (1.4)$$

where  $N_A$  is the volumetric flux,  $F_{P,A}$  is the steady state volumetric transfer rate of species A through the membrane, A is the membrane area,  $P_A$  is the permeability of the membrane for species A, the driving force  $\Delta \bar{p}_A$  is the change in the partial pressure of the species across the membrane, and  $t_m$  is the thickness of the membrane skin. Since the partial pressure is the mole fraction times the total pressure,  $\bar{p}_A = y_A p_{tot}$ , the above equation can also be written as

$$N_A = \frac{F_{P,A}}{A} = \frac{P_A (p_h y_{h,A} - p_p y_{p,A})}{t_m} \quad (1.5)$$

In this equation  $p_p$  is the total permeate pressure,  $p_h$  is the pressure on high pressure side,  $y_{h,A}$  is mole fraction A on high pressure side and  $y_{p,A}$  is mole fraction A in the permeate. Since y and p can vary along the membrane, this equation will need to be incorporated into a model for the membrane [55].

In order for permeation to take place, the feed side pressure should be higher than the permeate side pressure. This can be accomplished, in principle, by either compressing the feed gas to an elevated pressure level or maintaining the permeate side to sub-atmospheric pressure, or a combination of both [22].

Membrane gas separation processes are operated conventionally in a steady state fashion. Both the feed pressure and the permeate pressure are maintained at constant levels, and the permeation rate and permeate concentration do not change with time, except in the initial start up period. The steady state operation has the advantages of ease of startup and shutdown, simplicity of pressure and flow controls, large throughput of permeation, and low maintenance requirements. However, there have been a few patent disclosures that suggest and demonstrate the benefits of operating membrane gas separations in unsteady state fashion for some applications.

Pressure swing permeation is analogous to pressure swing adsorption and has the potential to be synergistically integrated with the pressure swing adsorption process for enhanced separation of gases [22].

Ueda et al [83] proposed a cyclic process for air separation that comprises repetition of the steps of pressurization of feed and evacuation of permeate. LaPack and Dupius [41] described another unsteady state process to improve permeation selectivity by operating the membrane permeation system dynamically. Their process is primarily based on the differences in the diffusivities of different permeating components through the membrane. From the instance that feed gas is admitted to the upstream side of the membrane and before the slow diffusing component reaches steady state permeation, the rate of mass transport through the membrane varies with time. During this period of transient permeation, the faster diffusing gas component is enriched in the permeate side. In a continuous operation, the feed can be introduced intermittently at appropriate time intervals such that steady state permeation is never reached. Alternatively, the difference in the desorption falloff rates due to the difference in the diffusivities can also be utilized to affect the separation, and the collected permeate will be a mixture enriched in the slower diffusing component [41].

Because of the nature of pressure-driven permeation, the permeate stream from the membrane system is collected at a pressure significantly lower than the feed-gas pressure, and recompression of permeate product is often required. In his paper, Feng, presented a novel unsteady state permeation for gas separation. The objective of his study is to produce a permeate stream at a pressure as high as the feed pressure without using a compressor. The idea is to elevate the relatively low permeate pressure by periodically pressurizing, or “pushing” the permeate with the high pressure feed gas [22].

#### 1.3.4 PSA PROCESS AND MODELING

The unit operations of PSA process are operated in a cyclic manner by a combination of adsorption and desorption steps. High pressure favors adsorption and low pressure favors desorption. Therefore, the starting step in a PSA cycle is pressurization of the bed from low pressure of desorption step to a higher pressure. In the next step, feed gas passes through the column and preferential retention of the strongly adsorbed component takes place and the weakly adsorbed component is collected at the other end of the column.

When a specified saturation of the bed has occurred, feed is shut off, and pressure reduction is accomplished. This is known as the blowdown step and prepares the bed for the subsequent desorption of the adsorbed component. This desorption is carried out using a purge gas flowing counter-currently in the column, thus purging the solid phase. The bed is then re-pressurized. These four steps constitute the most rudimentary cycle developed by Skarstrom in the 1960's [80], which is based on two beds operating synchronously as shown in Figure 1.4.

To increase the efficiency of PSA separation several modifications of the Skarstrom cycle have been developed. Most of the differences are associated with cycles designed to conserve compression energy. In multiple bed systems, for example, beds are connected such that pressurization and depressurization occur in stages through equalization with other beds. A review of PSA modification can be found in references [69, 90].

Theoretical modeling of a PSA system has been widely studied in the literature. The growth in PSA modeling has followed the route of gradual development by progressive elimination of the simplifying assumptions. A chronological summary for PSA models development is shown in Figure 1.5.

The first and simplest approach is by the equilibrium theory model, which is based on the assumption that local equilibrium always exists between the bulk and gas phases and hence mass transfer resistance is negligible. The concept was first published by Shendalman and Mitchell in 1972 [73]. An advantage of this approach is that it allows for analytical solution of the

governing mass balance equation by the method of characteristics. However, the predictions by the equilibrium model are not accurate for real systems where the mass transfer resistance is considerable, especially for kinetic-based separations.

Dynamic modeling, the other approach of PSA modeling, allows for mass transfer resistance in the system, and the governing equations can be solved only by numerical methods. In 1983, Chihara and Suzuki developed a dynamic model based on the assumption that the velocity is constant along the column in adsorption and desorption steps [17]. They also assumed that mass transfer between bulk and solid phases is negligible during pressurization and blowdown steps. The second assumption is well known in literature as the frozen solid approximation. Constant velocity models are most useful for liquid systems or gaseous purification-systems where the adsorbable components exist in the feed in trace amount. However, for bulk gas separation, where the change in flow rate due to adsorption-desorption is significant, this assumption is clearly inappropriate.

Later on, Ruthven and Raghavan developed a variable velocity model in 1985, where they allowed for velocity change in all steps [71]. However, they retained the frozen solid approximation. For purification processes, the frozen solid approximation is acceptable. For bulk-separation processes, however, mass transfer between gas and solid phases during pressurization and blowdown steps is significant to the extent that the frozen solid approximation is not accurate, especially for equilibrium-based separation [69].

Modeling by the equilibrium theory and the frozen solid approximation can be regarded as two extreme cases relative to the real situation. The former always gives predictions higher than reality; while the later always gives predictions lower than reality [90]. The first isothermal full solution model, which includes the dispersion term in the mass balance equation, allows for variable velocity during adsorption-desorption steps, and relaxes the frozen solid approximation, is the one published by Shin and Knaebel in 1987 [74]. Limited works have been published for developing the nonisothermal full solution model.

Both plug-flow and axially dispersed plug-flow conditions, isothermal and nonisothermal PSA systems are considered in PSA modeling development, as shown in Figure 1.5.

In pressurization and blowdown steps, the column pressure changes with time. One approach to account for this change in modeling is to assume that the pressure varies either linearly or exponentially over the period of the pressurization or blowdown step. An alternative approach is to assume instantaneous change of pressure followed by mass transfer (at constant high or low pressure) between the bulk and solid phases. The former is a good approximation for an equilibrium-based separation, while the latter is more appropriate for kinetic separation [69].

In order to determine the cyclic steady state, cycles are repeated until very minor differences are noticed in concentration profiles for all steps. This is called the successive substitution method, and used by most authors because of its simplicity, although in some cases the computation time is high. A new method is suggested by Alpay and co-workers in 1998, which is called the simultaneous discretization method seems to be more efficient [4]. However, a sophisticated mathematical background is needed in order to apply it. Most dynamic models developed so far have been solved numerically by either finite difference or orthogonal collocation techniques. The latter method has been shown to be, computationally, much superior than the former [71]. Also, for the previous works all computer simulation codes have been developed in FORTRAN language. Nowadays there is a tendency in engineering applications to shift from FORTRAN to the more sophisticated language, MATLAB. This is because MATLAB is much easier and is user friendly, and the output can be directly visualized graphically [10]. Therefore, there is a need to develop a MATLAB computer simulation code that solves both isothermal and nonisothermal full solution PSA models.

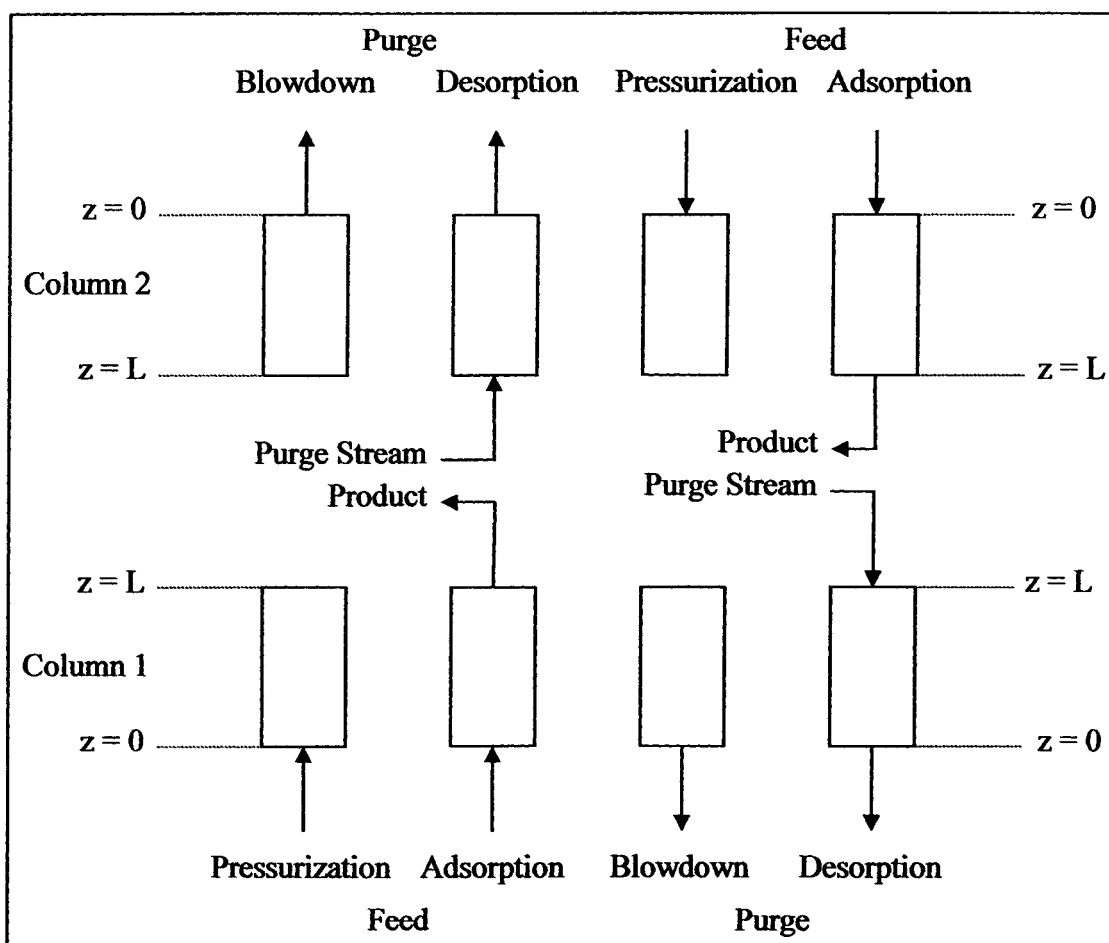


Figure 1.3: Steps for  $nC_5/nC_6$ ,  $iC_5/iC_6$  separation based on Skarstrom Cycle [80].



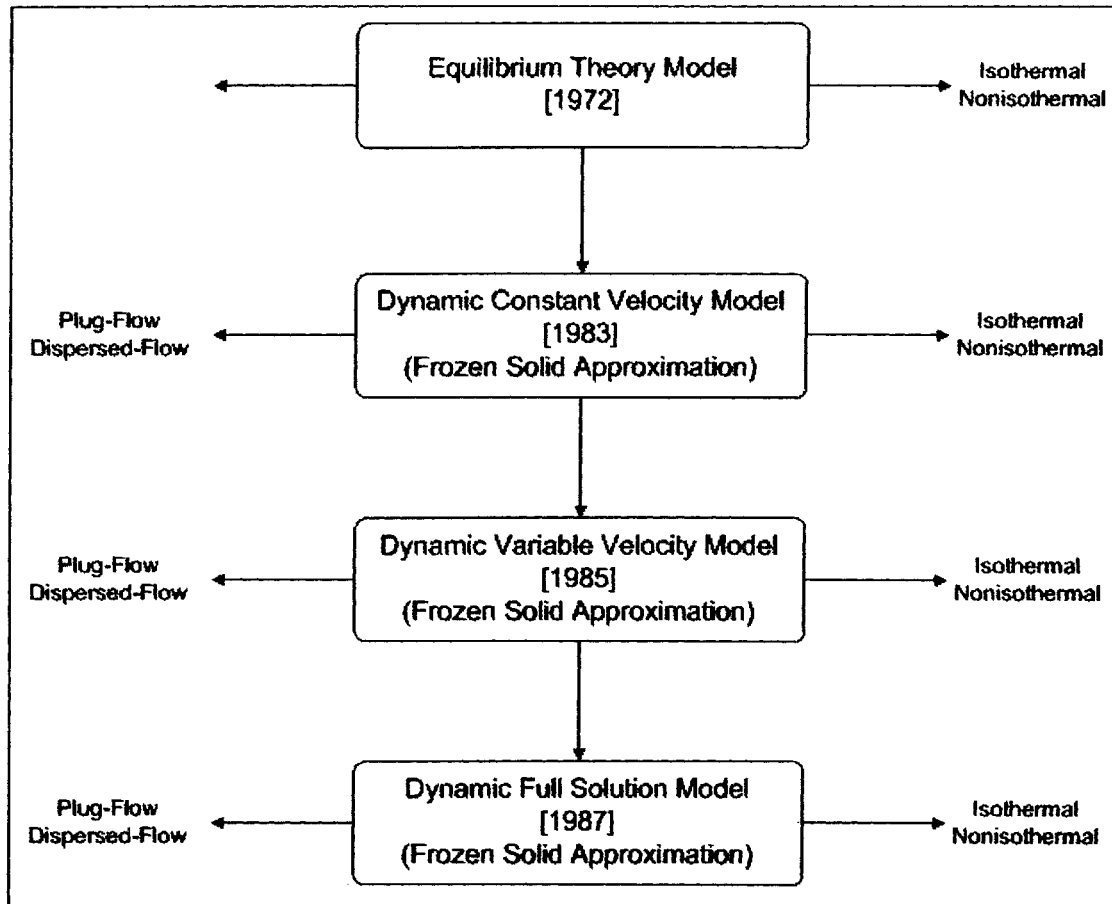


Figure 1.4: Summary for PSA models' development.

## **1.4 PRESURE SWING ADSORPTION REACTOR (PSAR)**

In conventional chemical reaction processes, the conversion is often limited by chemical equilibrium. In order to achieve higher conversions and improved overall energy efficiency, new chemical reactor configurations have been studied. In one, a conventional reactor is operated in a periodic mode [20]; other novel reactors can achieve simultaneous reaction and separation. The concept of combining reaction with separation is based on Le Chatelier's principle relating the conversion of reactants to products. The rate of forward reaction in an equilibrium-limited reaction can be increased by selectively removing some of the reaction products from the reaction zone [79]. Thus, a better conversion can be achieved. Another advantage of applying this concept is that both capital and operating cost may be reduced because the downstream separation section can be minimized or eliminated from the conventional process.

Numerous applications of this concept have been published, such as membrane reactors, reactive distillation units, and others [23]. The pressure-swing reactor is a relatively new and untested device that combines reaction and product separation in a plant resembling a pressure swing adsorption (PSA) system [2,16,28,36]. In this device, a mixture of a catalyst and an adsorbent is filled in a chemical reactor. Mixing of the sorbent with the catalyst can be done in either a homogeneous or heterogeneous way [42]. In homogeneous units, the catalyst and the adsorbent are mixed uniformly, and one of the reaction products should be the strongly adsorbed component in order to get higher conversion by shifting the conversion to the right.

Heterogeneous units are formed by dividing the unit into two separate regions: the catalyst-packed bed region followed by the adsorbent-packed bed region. In such units, the strongly adsorbed component can be either the reactant or the product.

Combining reaction with pressure swing adsorption process is relatively a new area of interest and very limited works have been published. A good literature review on PSR systems was done by Sircar et al. [79], and some outlines of the works done are briefly presented here. The first theoretical investigation of the PSR system is the one published by Vaporciyan and Kadlec in 1987 [84]. They considered a single rapid PSR column with

extremely fast reaction and they applied the equilibrium theory model for adsorption. Two years later, they performed the first experimental evaluation of the PSR systems using Pt/alumina as the catalyst and 5A zeolite as the adsorbent in a rapid PSR process for oxidation of carbon monoxide [85]. Their patent was approved in 1993, which is the first patent in PSR systems [32]. They found that under certain operating conditions carbon dioxide production could be increased by up to 2 times the conventional reactor production. In 1994, Lu and Rodrigues proposed another mathematical model for the PSR system, and applied it on the dehydrogenation reaction of ethane [46]. However, they also used the equilibrium theory for their model.

Dehydrogenation reaction of methylcyclohexane to toluene in a PSR unit has been studied experimentally by Alpay and co-workers in 1995 [3]. Also, Sircar *et al* [79] applied the PSR concept to the water-gas shift reaction in an experiment. Both experimental studies have shown that equilibrium yields could exceed the values achieved by a conventional reactor. In a recent publication in 1998, Alpay et al. have studied theoretically the rapid PSR concept, and applied it for a hypothetical dissociation reaction [4]. They made detailed parametric studies, and applied the simultaneous discretisation method for determining the cyclic steady state. However, they retained the equilibrium theory assumption.

Isomerization process is a good example for applying the PSR concept for two reasons. First, the operating temperature and pressure for the reactor and the adsorber are similar. Second, both the reactor and the adsorber operate under hydrogen environment. To date, all the previous studies considered homogeneous mixing of adsorbent and catalyst in the PSR unit. In these studies, the main objective of applying the homogeneous PSR concept is to increase the conversion to a value higher than the equilibrium value by shifting the equilibrium reaction to the right. For the current study, however, the heterogeneous PSR concept will be applied because the main objective here is to reduce the required unit operation equipment. Also, most previous PSR models have applied the equilibrium theory concept for adsorption. However, separation of n/i-paraffins mixture is an example of a bulk-separation process. As mentioned before, the equilibrium theory model is not appropriate for this type of separation. Thus, there is a need to develop a full solution model for the PSAR system.

The performance of a PSAR unit can be affected by a number of design parameters, such as the bed length and the adsorbent/catalyst size; operating

parameters, such as the duration of the various steps and the pressure level in each step; and physical/chemical parameters, such as adsorption isotherm relationship and reaction rate constant. The effects of these parameters are coupled so that it is difficult to arrive at an optimal design only by experimentation. Therefore, reliable mathematical modeling and computer simulations are required to obtain preliminary information about the performance of the PSAR process in order to ensure that the capital and/or operating costs are minimized while satisfying technical specifications such as conversion, yield, and product purity.

The block-flow diagram of the PSAR system, taking the example of n-paraffins isomerization reaction, is shown in Figure 1.6. In this figure, the heterogeneous mixing system is employed and the reactant is the strongly adsorbed component. This flow diagram will be described in detail in Chapter 3.

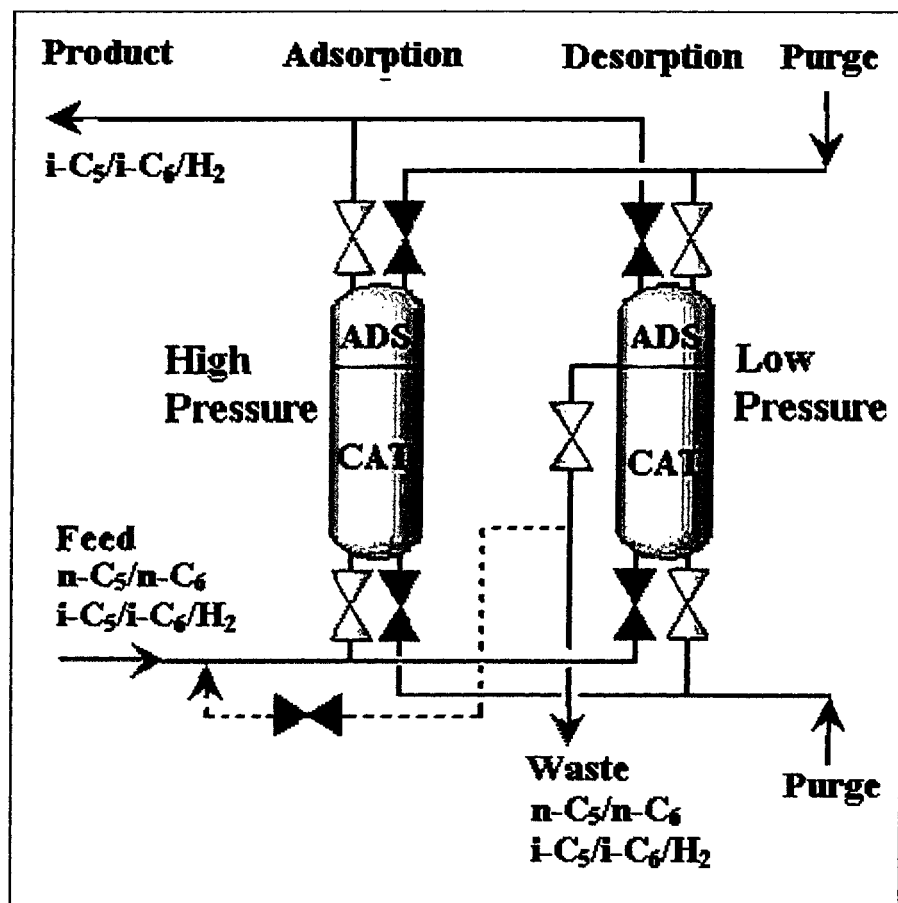


Figure 1.5: Flow diagram for the Combined Isomerization Reactor/Adsorber Process.

## **1.5 OBJECTIVES OF THE PRESENT RESEARCH**

The objectives of this research work are to:

1. Develop a nonisothermal PSA model for separation of  $iC_5/iC_6/H_2$  from a mixture containing  $nC_5/nC_6/iC_5/iC_6/H_2$ . Results of this model are to be compared with those obtained by Silva and Rodrigues.
2. Develop and establish a model that describes a combined reactor pressure swing adsorber unit (PSAR), for isomerizing n-pentane/n-hexane to their branched isomers. The PSAR model is to be full solution model; that is, most simplified assumptions are relaxed.
3. Introduce a  $H_2$  membrane to the separation section of the PSAR model. The introduction of the membrane will complete the separation process and make it possible to achieve pure isoalkanes production.
4. Study various operating scenarios of the PSAR and PSAR with membrane processes.

## CHAPTER 2

### MODELING AND SIMULATION OF THE BASE CASE

In order to compare the performance of the new PSAR process to that of a conventional PSA process, a base case consisting of a PSA unit is first simulated. The configuration of a PSA cycle is illustrated in Figure 2.1. The system is modeled as a non-isothermal process containing only five components ( $n\text{-C}_5/i\text{-C}_5/n\text{-C}_6/I\text{-C}_6/\text{H}_2$ ). Model Results are verified against those obtained by Silva and Rudrigues [78].

#### 2.1 MODEL ASSUMPTIONS

The dispersed PFR model is applied to describe the dynamic behavior of the PSA unit. Similarly, mass and energy balances are required for the adsorbent-packed region plus an investigation on the equilibrium and kinetics of sorption of  $n\text{-C}_5/\text{C}_6$  in 5A zeolites. The following additional assumptions are made:

- a) The gas is ideal. Although in some simulation runs, the pressure is high (15 bars and above), the gas is still an ideal system for two reasons: the temperature is high (500 K and above), and the hydrogen content is high (above 70%). To validate this assumption, the compressibility factor at high pressure is calculated to be close to unity using Peng Robinson Equation of State.
- b) The axial dispersed plug flow model describes the flow pattern.
- c) The main resistances to mass transfer in the adsorbent region are external fluid film resistance and macropore diffusion in series. These two resistances can be combined in a global resistance according to a lumped model suggested by Morbidelli et al [50].
- d) A resistance to heat transfer exists in the external fluid film around the adsorbent.

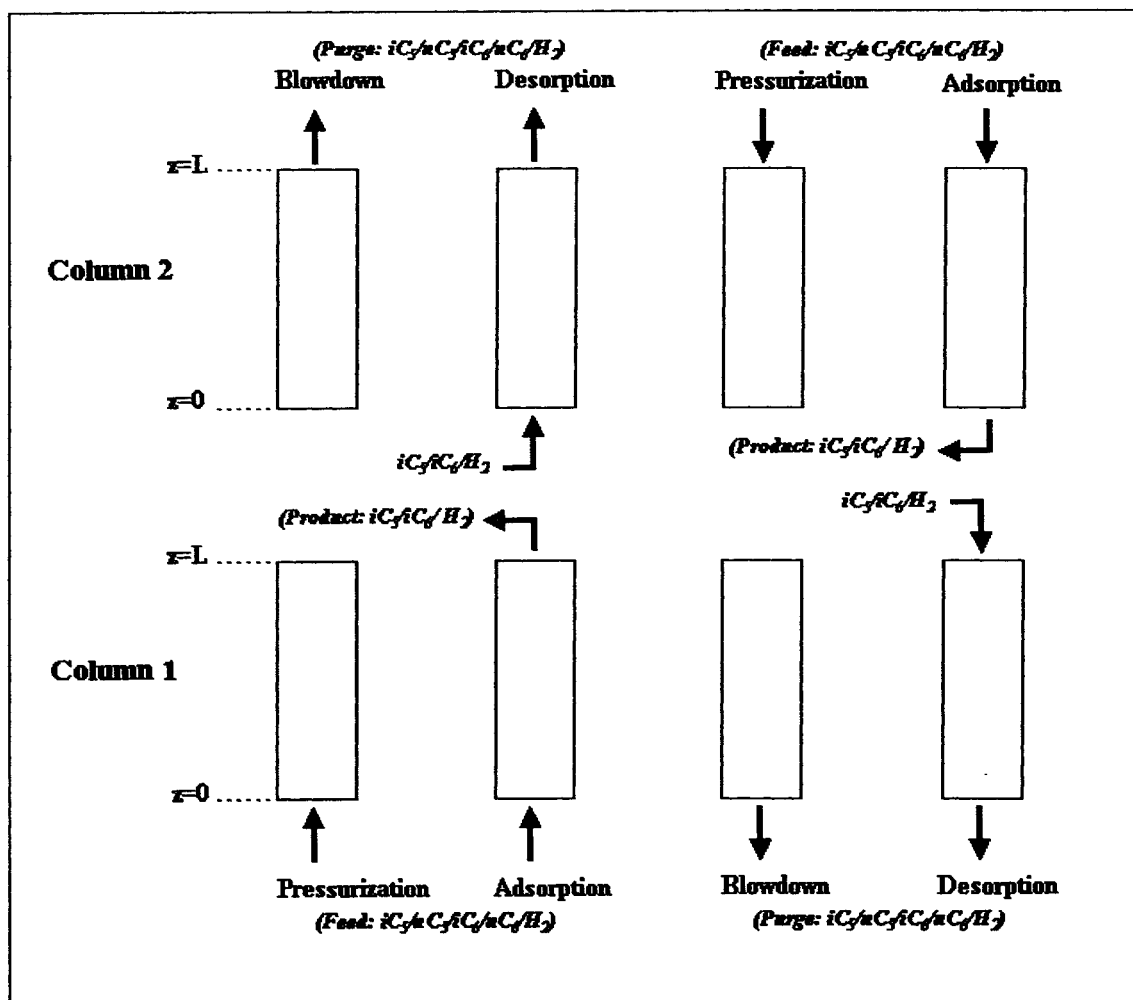


Figure 2.1: Steps for n-C<sub>5</sub>/n-C<sub>6</sub>/i-C<sub>5</sub>/i-C<sub>6</sub> PSA separation based on Skarstrom Cycle [80].



- e) Gas and solids properties are independent of temperature.
- f) Adsorption equilibrium is described by Nitta et al. model [53].
- g) Mass and energy balances are executed for the whole column in order to obtain a comprehensive model linking the catalyst region to the adsorbent region.
- h) The adsorption equilibrium constant is the most sensitive temperature-dependent term, and is assumed to follow the normal exponential temperature dependence  $K_{ads} = K_0 \exp[(-\Delta H_{ads})/RT]$ .
- i) Effective thermal conductivities of commercial adsorbents are relatively high, and therefore intraparticle temperature gradients can be neglected [68,90].
- j) Thermal equilibrium is assumed to exist between the fluid and the adsorbent particles. According to Ruthven and co-workers, this is a very common practical assumption in adsorber calculations [68]. This reduces the computational effort to a large extent since an energy balance for the solid phase is not required.
- k) An overall heat transfer coefficient is used to account for heat loss from the system to the surroundings.
- l) The temperature of the column wall is taken to be equal to that of the feed temperature.
- m) The boundary conditions for the heat balance equation are written assuming the heat-mass transfer analogy for a dispersed plug flow system.

## 2.2 MODEL EQUATIONS

Subject to the above assumptions, the model equations for the base case system are as follows: [A=n-pentane, B=n-hexane, C=isopentane, D=isoheptane, I=inert (H<sub>2</sub>), 1=reactor, 2=adsorber]

### Step 1 (Pressurization)

Fluid Phase mass balances are

$$-D_L \frac{\partial^2 c_{A2}}{\partial z^2} + \frac{\partial(Uc_{A2})}{\partial z} + \frac{\partial c_{A2}}{\partial t} + \frac{c_{A2}}{c_{T1}} \frac{\partial c_{T1}}{\partial t} + \frac{(1-\varepsilon)}{\varepsilon} \rho_s \frac{\partial \langle q_{A2} \rangle}{\partial t} = 0 \quad (2.11)$$

$$-D_L \frac{\partial^2 c_{B2}}{\partial z^2} + \frac{\partial(Uc_{B2})}{\partial z} + \frac{\partial c_{B2}}{\partial t} + \frac{c_{B2}}{c_{T1}} \frac{\partial c_{T1}}{\partial t} + \frac{(1-\varepsilon)}{\varepsilon} \rho_s \frac{\partial \langle q_{B2} \rangle}{\partial t} = 0 \quad (2.12)$$

$$-D_L \frac{\partial^2 c_{C2}}{\partial z^2} + \frac{\partial(Uc_{C2})}{\partial z} + \frac{\partial c_{C2}}{\partial t} + \frac{c_{C2}}{c_{T1}} \frac{\partial c_{T1}}{\partial t} + \frac{(1-\varepsilon)}{\varepsilon} \rho_s \frac{\partial \langle q_{C2} \rangle}{\partial t} = 0 \quad (2.13)$$

$$-D_L \frac{\partial^2 c_{D2}}{\partial z^2} + \frac{\partial(Uc_{D2})}{\partial z} + \frac{\partial c_{D2}}{\partial t} + \frac{c_{D2}}{c_{T1}} \frac{\partial c_{T1}}{\partial t} + \frac{(1-\varepsilon)}{\varepsilon} \rho_s \frac{\partial \langle q_{D2} \rangle}{\partial t} = 0 \quad (2.14)$$

$$\frac{\partial c_{A2}}{\partial t} + \frac{\partial c_{B2}}{\partial t} + \frac{\partial c_{C2}}{\partial t} + \frac{\partial c_{D2}}{\partial t} + \frac{\partial c_{I2}}{\partial t} = \frac{\partial c_T}{\partial t} \quad (2.15)$$

The overall material balance is obtained by adding equations (2.11), (2.12), (2.13), (2.14) and (2.15), recognizing that the total concentration  $c_{T2}$  defined as  $c_{T2} = c_{A2} + c_{B2} + c_{C2} + c_{D2} + c_{I2}$  is a function of time and is not a function of distance (due to negligible pressure drop in the bed)

$$c_{T2} \frac{\partial u}{\partial z} + \frac{\partial c_{T2}}{\partial t} + \rho_s \sum_i \frac{(1-\varepsilon)}{\varepsilon} \frac{\partial \langle q_i \rangle}{\partial t} = 0 \quad (2.16)$$

The mass transfer rate is defined by the LDF expression

$$\rho_s \frac{\partial \langle q_A \rangle}{\partial t} = a_p k_{gt} (c_{A2} - \langle c_{A2} \rangle) \quad (2.17)$$

The adsorption equilibrium isotherm is

$$\langle c_{i2} \rangle RT = \frac{1}{K_{ads,i}} \frac{\theta_i}{\left(1 - \sum_j \theta_j\right)^{n_i}} \quad (2.18)$$

where  $K_{ads,i}$  is the equilibrium isotherm constant, calculated by

$$K_{ads,i} = K_{o,i} e^{\left[\frac{(-\Delta H_{ads,i})}{RT}\right]} \quad (2.19)$$

The boundary conditions are Danckwert's boundary conditions

$$-D_L \frac{\partial c_{A2}}{\partial z} \Big|_{z=0} = u_f (c_{A2f} - c_{A2} \Big|_{z=0}) \quad (2.20a)$$

$$\frac{\partial c_{A2}}{\partial z} \Big|_{z=L} = 0 \quad (2.20b)$$

Similar boundary conditions apply to all other components.

Boundary condition for velocity

$$u \Big|_{z=L} = 0 \quad (2.21)$$

Note that  $c_{A2,f}$  appearing in equation (2.20a) is the exit concentration of the reactor.

## Step 2 (Adsorption)

Fluid phase mass balances are

$$-D_L \frac{\partial^2 c_{A2}}{\partial z^2} + \frac{\partial(Uc_{A2})}{\partial z} + \frac{\partial c_{A2}}{\partial t} + \frac{c_{A2}}{c_{T1}} \frac{\partial c_{T1}}{\partial t} + \frac{(1-\varepsilon)}{\varepsilon} \rho_s \frac{\partial \langle q_{A2} \rangle}{\partial t} = 0 \quad (2.22)$$

$$-D_L \frac{\partial^2 c_{B2}}{\partial z^2} + \frac{\partial(Uc_{B2})}{\partial z} + \frac{\partial c_{B2}}{\partial t} + \frac{c_{B2}}{c_{T1}} \frac{\partial c_{T1}}{\partial t} + \frac{(1-\varepsilon)}{\varepsilon} \rho_s \frac{\partial \langle q_{B2} \rangle}{\partial t} = 0 \quad (2.23)$$

$$-D_L \frac{\partial^2 c_{C2}}{\partial z^2} + \frac{\partial(Uc_{C2})}{\partial z} + \frac{\partial c_{C2}}{\partial t} + \frac{c_{C2}}{c_{T1}} \frac{\partial c_{T1}}{\partial t} + \frac{(1-\varepsilon)}{\varepsilon} \rho_s \frac{\partial \langle q_{C2} \rangle}{\partial t} = 0 \quad (2.24)$$

$$-D_L \frac{\partial^2 c_{D2}}{\partial z^2} + \frac{\partial(Uc_{D2})}{\partial z} + \frac{\partial c_{D2}}{\partial t} + \frac{c_{D2}}{c_{T1}} \frac{\partial c_{T1}}{\partial t} + \frac{(1-\varepsilon)}{\varepsilon} \rho_s \frac{\partial \langle q_{D2} \rangle}{\partial t} = 0 \quad (2.25)$$

$$\frac{\partial c_{A2}}{\partial t} + \frac{\partial c_{B2}}{\partial t} + \frac{\partial c_{C2}}{\partial t} + \frac{\partial c_{D2}}{\partial t} + \frac{\partial c_{I2}}{\partial t} = 0 \quad (2.26)$$

The overall material balance is obtained by adding equations (2.22), (2.23), (2.24), (2.25) and (2.26), recognizing that the total concentration  $c_{T2}$  does not change with time.

$$c_{T2} \frac{\partial u}{\partial z} + \frac{\partial c_{T2}}{\partial t} + \rho_s \sum_i \frac{(1-\varepsilon)}{\varepsilon} \frac{\partial \langle q_i \rangle}{\partial t} = 0 \quad (2.27)$$

The mass transfer rate is defined by the LDF expression

$$\rho_s \frac{\partial \langle q_A \rangle}{\partial t} = a_p k_{gl} (c_{A2} - \langle c_{A2} \rangle) \quad (2.28)$$

The adsorption equilibrium isotherm is

$$\langle c_{i2} \rangle RT = \frac{1}{K_{ads,i}} \frac{\theta_i}{\left(1 - \sum_j \theta_j\right)^{n_i}} \quad (2.29)$$

where  $K_{ads,i}$  is the equilibrium isotherm constant, calculated by

$$K_{ads,i} = K_{o,i} e^{\left[\frac{(-\Delta H_{ads,i})}{RT}\right]} \quad (2.30)$$

The boundary conditions are Danckwert's boundary conditions

$$-D_L \frac{\partial c_{A2}}{\partial z} \Big|_{z=0} = u_f (c_{A2f} - c_{A2} \Big|_{z=0}) \quad (2.31a)$$

$$\frac{\partial c_{A2}}{\partial z} \Big|_{z=L} = 0 \quad (2.31b)$$

Similar boundary conditions apply to all other components.

Boundary condition for velocity

$$u|_{z=0} = u_f \quad (2.32)$$

Note that  $c_{A2,f}$  appearing in equation (2.31a) is the exit concentration of the reactor.

Step 3 (Counter-current Blowdown)

Fluid phase mass balances are

$$-D_L \frac{\partial^2 c_{A2}}{\partial z^2} + \frac{\partial(Uc_{A2})}{\partial z} + \frac{\partial c_{A2}}{\partial t} + \frac{c_{A2}}{c_{T1}} \frac{\partial c_{T1}}{\partial t} + \frac{(1-\varepsilon)}{\varepsilon} \rho_s \frac{\partial \langle q_{A2} \rangle}{\partial t} = 0 \quad (2.33)$$

$$-D_L \frac{\partial^2 c_{B2}}{\partial z^2} + \frac{\partial(Uc_{B2})}{\partial z} + \frac{\partial c_{B2}}{\partial t} + \frac{c_{B2}}{c_{T1}} \frac{\partial c_{T1}}{\partial t} + \frac{(1-\varepsilon)}{\varepsilon} \rho_s \frac{\partial \langle q_{B2} \rangle}{\partial t} = 0 \quad (2.34)$$

$$-D_L \frac{\partial^2 c_{C2}}{\partial z^2} + \frac{\partial(Uc_{C2})}{\partial z} + \frac{\partial c_{C2}}{\partial t} + \frac{c_{C2}}{c_{T1}} \frac{\partial c_{T1}}{\partial t} + \frac{(1-\varepsilon)}{\varepsilon} \rho_s \frac{\partial \langle q_{C2} \rangle}{\partial t} = 0 \quad (2.35)$$

$$-D_L \frac{\partial^2 c_{D2}}{\partial z^2} + \frac{\partial(Uc_{D2})}{\partial z} + \frac{\partial c_{D2}}{\partial t} + \frac{c_{D2}}{c_{T1}} \frac{\partial c_{T1}}{\partial t} + \frac{(1-\varepsilon)}{\varepsilon} \rho_s \frac{\partial \langle q_{D2} \rangle}{\partial t} = 0 \quad (2.36)$$

$$\frac{\partial c_{A2}}{\partial t} + \frac{\partial c_{B2}}{\partial t} + \frac{\partial c_{C2}}{\partial t} + \frac{\partial c_{D2}}{\partial t} + \frac{\partial c_{I2}}{\partial t} = 0 \quad (2.37)$$

The overall material balance is obtained by adding equations (2.33), (2.34), (2.35), (2.36) and (2.37), recognizing that the total concentration  $c_{T2}$  defined as  $c_{T2} = c_{A2} + c_{B2} + c_{C2} + c_{D2} + c_{I2}$  is a function of time and is not a function of  $z$  (due to negligible pressure drop in the bed)

$$c_{T2} \frac{\partial u}{\partial z} + \frac{\partial c_{T2}}{\partial t} + \rho_s \sum_i \frac{(1-\varepsilon)}{\varepsilon} \frac{\partial \langle q_i \rangle}{\partial t} = 0 \quad (2.38)$$

The mass transfer rate is defined by the LDF expression

$$\rho_s \frac{\partial \langle q_A \rangle}{\partial t} = a_p k_{gl} (c_{A2} - \langle c_{A2} \rangle) \quad (2.39)$$

The adsorption equilibrium isotherm is

$$\langle c_{i2} \rangle RT = \frac{1}{K_{ads,i}} \frac{\theta_i}{\left(1 - \sum_j \theta_j\right)^{n_i}} \quad (2.40)$$

where  $K_{ads,i}$  is the equilibrium isotherm constant, calculated by

$$K_{ads,i} = K_{o,i} e^{\left[\frac{(-\Delta H_{ads,i})}{RT}\right]} \quad (2.41)$$

The boundary conditions are Danckwert's boundary conditions

$$-D_L \frac{\partial c_{A2}}{\partial z} \Big|_{z=0} = u_f (c_{A2,f} - c_{A2} \Big|_{z=0}) \quad (2.42)$$

But since  $u=0$  at the inlet of the column,  $z=0$ , we have

$$\frac{\partial c_{A2}}{\partial z} \Big|_{z=0} = 0 \quad (2.43a)$$

$$\frac{\partial c_{A2}}{\partial z} \Big|_{z=L} = 0 \quad (2.43b)$$

Similar boundary conditions apply to all other components.

Boundary condition for velocity

$$u \Big|_{z=0} = 0 \quad (2.44)$$

Step 4 (Counter-current Desorption)

Fluid phase mass balances are

$$-D_L \frac{\partial^2 c_{A2}}{\partial z^2} + \frac{\partial(Uc_{A2})}{\partial z} + \frac{\partial c_{A2}}{\partial t} + \frac{c_{A2}}{c_{T1}} \frac{\partial c_{T1}}{\partial t} + \frac{(1-\varepsilon)}{\varepsilon} \rho_s \frac{\partial \langle q_{A2} \rangle}{\partial t} = 0 \quad (2.45)$$

$$-D_L \frac{\partial^2 c_{B2}}{\partial z^2} + \frac{\partial(Uc_{B2})}{\partial z} + \frac{\partial c_{B2}}{\partial t} + \frac{c_{B2}}{c_{T1}} \frac{\partial c_{T1}}{\partial t} + \frac{(1-\varepsilon)}{\varepsilon} \rho_s \frac{\partial \langle q_{B2} \rangle}{\partial t} = 0 \quad (2.46)$$

$$-D_L \frac{\partial^2 c_{C2}}{\partial z^2} + \frac{\partial(Uc_{C2})}{\partial z} + \frac{\partial c_{C2}}{\partial t} + \frac{c_{C2}}{c_{T1}} \frac{\partial c_{T1}}{\partial t} + \frac{(1-\varepsilon)}{\varepsilon} \rho_s \frac{\partial \langle q_{C2} \rangle}{\partial t} = 0 \quad (2.47)$$

$$-D_L \frac{\partial^2 c_{D2}}{\partial z^2} + \frac{\partial(Uc_{D2})}{\partial z} + \frac{\partial c_{D2}}{\partial t} + \frac{c_{D2}}{c_{T1}} \frac{\partial c_{T1}}{\partial t} + \frac{(1-\varepsilon)}{\varepsilon} \rho_s \frac{\partial \langle q_{D2} \rangle}{\partial t} = 0 \quad (2.48)$$

$$\frac{\partial c_{A2}}{\partial t} + \frac{\partial c_{B2}}{\partial t} + \frac{\partial c_{C2}}{\partial t} + \frac{\partial c_{D2}}{\partial t} + \frac{\partial c_{I2}}{\partial t} = 0 \quad (2.49)$$

The overall material balance is obtained by adding equations (2.45), (2.46), (2.47), (2.48) and (2.49), recognizing that the total concentration  $c_{T2}$  defined as  $c_{T2} = c_{A2} + c_{B2} + c_{C2} + c_{D2} + c_{I2}$  is a function of time and is not a function of  $z$  (due to negligible pressure drop in the bed)

$$c_{T2} \frac{\partial u}{\partial z} + \frac{\partial c_{T2}}{\partial t} + \rho_s \sum_i \frac{(1-\varepsilon)}{\varepsilon} \frac{\partial \langle q_i \rangle}{\partial t} = 0 \quad (2.50)$$

The mass transfer rate is defined by the LDF expression

$$\rho_s \frac{\partial \langle q_A \rangle}{\partial t} = a_p k_{gl} (c_{A2} - \langle c_{A2} \rangle) \quad (2.51)$$

The adsorption equilibrium isotherm is

$$\langle c_{i2} \rangle RT = \frac{1}{K_{ads,i}} \frac{\theta_i}{\left(1 - \sum_j \theta_j\right)^{n_i}} \quad (2.52)$$

where  $K_{ads,i}$  is the equilibrium isotherm constant, calculated by

$$K_{ads,i} = K_{o,i} e^{\left[\frac{(-\Delta H_{ads,i})}{RT}\right]} \quad (2.53)$$

The boundary conditions are Danckwert's boundary conditions

$$-D_L \frac{\partial c_{A2}}{\partial z} \Big|_{z=0} = u_f (c_{A2f} - c_{A2} \Big|_{z=0}) \quad (2.54)$$

A purge inert stream of pure hydrogen is being employed, giving

$$-D_L \frac{\partial c_{A2}}{\partial z} \Big|_{z=0} = -u \Big|_{z=0} c_{A2} \Big|_{z=0} \quad (2.55a)$$

$$\frac{\partial c_{A2}}{\partial z} \Big|_{z=L} = 0 \quad (2.55b)$$

Similar boundary conditions apply to all other components.

Boundary condition for velocity

$$u \Big|_{z=0} = u_p \quad (2.56)$$

In the PSA simulations, the initial conditions are taken to be clean adsorbent bed and gas phase of pure hydrogen.

$$c_{A2}(z, t = 0) = 0 \quad (2.57a)$$

$$c_{B2}(z, t = 0) = 0 \quad (2.57b)$$

$$c_{C2}(z, t = 0) = 0 \quad (2.57c)$$

$$c_{D2}(z, t = 0) = 0 \quad (2.57d)$$

$$c_{I2}(z, t = 0) = c_{I0} \quad (2.57f)$$

where  $c_{I0}$  is the initial concentration of inert inside the bed.

The above set of equations is written in normalized form using the following dimensionless variables:

$$\begin{aligned} y_{Ai} &= \frac{c_{Ai}}{c_{Ti}} & y_{Bi} &= \frac{c_{Bi}}{c_{Ti}} & y_{Ci} &= \frac{c_{Ci}}{c_{Ti}} & y_{Di} &= \frac{c_{Di}}{c_{Ti}} \\ y_{Ii} &= \frac{c_{Ii}}{c_{Ti}} & x &= \frac{z}{L} & \tau &= \frac{tu_f}{L} & Q_i &= \frac{q_i}{q_{i,ref}} \\ C_{Ti} &= \frac{C_{Ti}}{C_{Tf}} & U &= \frac{u}{u_f} & & & & \end{aligned} \quad (2.58)$$

where  $q_{i,ref}$  represents the solid phase concentration of component  $i$  in equilibrium with  $y_{i2,f}$  at  $P_H$  and  $T_f$  ( $i = A, B, C$  or  $D$ ), calculated by



$$y_{A2,f} P_H = \frac{1}{K_{ads}} \frac{(q_{A,ref} / q_{\max})}{\left[1 - \sum_i (q_{i,ref} / q_{\max})\right]^{n_A}} \quad (2.59)$$

Thus, the model equations become:

### Step 1 (Pressurization)

$$-\frac{1}{Pe} \frac{\partial^2 y_{A2}}{\partial x^2} + \frac{\partial(Uy_{A2})}{\partial x} + \frac{\partial y_{A2}}{\partial \tau} + \frac{y_{A2}}{C_{T2}} \frac{\partial C_{T2}}{\partial \tau} + \zeta_{m,A} \frac{\partial Q_A}{\partial \tau} = 0 \quad (2.60)$$

$$-\frac{1}{Pe} \frac{\partial^2 y_{B2}}{\partial x^2} + \frac{\partial(Uy_{B2})}{\partial x} + \frac{\partial y_{B2}}{\partial \tau} + \frac{y_{B2}}{C_{T2}} \frac{\partial C_{T2}}{\partial \tau} + \zeta_{m,B} \frac{\partial Q_B}{\partial \tau} = 0 \quad (2.61)$$

$$-\frac{1}{Pe} \frac{\partial^2 y_{C2}}{\partial x^2} + \frac{\partial(Uy_{C2})}{\partial x} + \frac{\partial y_{C2}}{\partial \tau} + \frac{y_{C2}}{C_{T1}} \frac{\partial C_{T2}}{\partial \tau} + \zeta_{m,C} \frac{\partial Q_C}{\partial \tau} = 0 \quad (2.62)$$

$$-\frac{1}{Pe} \frac{\partial^2 y_{D2}}{\partial x^2} + \frac{\partial(Uy_{D2})}{\partial x} + \frac{\partial y_{D2}}{\partial \tau} + \frac{y_{D2}}{C_{T1}} \frac{\partial C_{T2}}{\partial \tau} + \zeta_{m,D} \frac{\partial Q_D}{\partial \tau} = 0 \quad (2.63)$$

$$\frac{\partial y_{A2}}{\partial t} + \frac{\partial y_{B2}}{\partial t} + \frac{\partial y_{C2}}{\partial t} + \frac{\partial y_{D2}}{\partial t} + \frac{\partial y_{I2}}{\partial t} = 0 \quad (2.64)$$

$$-\frac{1}{Pe} \frac{\partial y_A}{\partial x} \Big|_{x=0} = (y_{Af} - y_{A1}|_{x=0}) \quad (2.65a)$$

$$\frac{\partial y_A}{\partial x} \Big|_{x=1} = 0 \quad (2.65b)$$

$$U|_{x=1} = 0 \quad (2.66)$$

### Step 2 (Adsorption)

$$-\frac{1}{Pe} \frac{\partial^2 y_{A2}}{\partial x^2} + \frac{\partial(Uy_{A2})}{\partial x} + \frac{\partial y_{A2}}{\partial \tau} + \frac{y_{A2}}{C_{T2}} \frac{\partial C_{T2}}{\partial \tau} + \zeta_{m,A} \frac{\partial Q_A}{\partial \tau} = 0 \quad (2.67)$$

$$-\frac{1}{Pe} \frac{\partial^2 y_{B2}}{\partial x^2} + \frac{\partial(Uy_{B2})}{\partial x} + \frac{\partial y_{B2}}{\partial \tau} + \frac{y_{B2}}{C_{T2}} \frac{\partial C_{T2}}{\partial \tau} + \zeta_{m,B} \frac{\partial Q_B}{\partial \tau} = 0 \quad (2.68)$$

$$-\frac{1}{Pe} \frac{\partial^2 y_{C2}}{\partial x^2} + \frac{\partial(Uy_{C2})}{\partial x} + \frac{\partial y_{C2}}{\partial \tau} + \frac{y_{C2}}{C_{T1}} \frac{\partial C_{T2}}{\partial \tau} + \zeta_{m,C} \frac{\partial Q_C}{\partial \tau} = 0 \quad (2.69)$$

$$-\frac{1}{Pe} \frac{\partial^2 y_{D2}}{\partial x^2} + \frac{\partial(Uy_{D2})}{\partial x} + \frac{\partial y_{D2}}{\partial \tau} + \frac{y_{D2}}{C_{T1}} \frac{\partial C_{T2}}{\partial \tau} + \zeta_{m,D} \frac{\partial Q_D}{\partial \tau} = 0 \quad (2.70)$$

$$\frac{\partial y_{A2}}{\partial t} + \frac{\partial y_{B2}}{\partial t} + \frac{\partial y_{C2}}{\partial t} + \frac{\partial y_{D2}}{\partial t} + \frac{\partial y_{I2}}{\partial t} = 0 \quad (2.71)$$

$$-\frac{1}{Pe} \frac{\partial y_A}{\partial x} \Big|_{x=0} = (y_{Af} - y_{A1} \Big|_{x=0}) \quad (2.72a)$$

$$\frac{\partial y_A}{\partial x} \Big|_{x=1} = 0 \quad (2.73b)$$

$$U \Big|_{x=1} = 1 \quad (2.74)$$

### Step 3 (Counter-Current Blow down)

$$-\frac{1}{Pe} \frac{\partial^2 y_{A2}}{\partial x^2} + \frac{\partial(Uy_{A2})}{\partial x} + \frac{\partial y_{A2}}{\partial \tau} + \frac{y_{A2}}{C_{T2}} \frac{\partial C_{T2}}{\partial \tau} + \zeta_{m,A} \frac{\partial Q_A}{\partial \tau} = 0 \quad (2.75)$$

$$-\frac{1}{Pe} \frac{\partial^2 y_{B2}}{\partial x^2} + \frac{\partial(Uy_{B2})}{\partial x} + \frac{\partial y_{B2}}{\partial \tau} + \frac{y_{B2}}{C_{T2}} \frac{\partial C_{T2}}{\partial \tau} + \zeta_{m,B} \frac{\partial Q_B}{\partial \tau} = 0 \quad (2.76)$$

$$-\frac{1}{Pe} \frac{\partial^2 y_{C2}}{\partial x^2} + \frac{\partial(Uy_{C2})}{\partial x} + \frac{\partial y_{C2}}{\partial \tau} + \frac{y_{C2}}{C_{T1}} \frac{\partial C_{T2}}{\partial \tau} + \zeta_{m,C} \frac{\partial Q_C}{\partial \tau} = 0 \quad (2.77)$$

$$-\frac{1}{Pe} \frac{\partial^2 y_{D2}}{\partial x^2} + \frac{\partial(Uy_{D2})}{\partial x} + \frac{\partial y_{D2}}{\partial \tau} + \frac{y_{D2}}{C_{T1}} \frac{\partial C_{T2}}{\partial \tau} + \zeta_{m,D} \frac{\partial Q_C}{\partial \tau} = 0 \quad (2.78)$$

$$\frac{\partial y_{A2}}{\partial t} + \frac{\partial y_{B2}}{\partial t} + \frac{\partial y_{C2}}{\partial t} + \frac{\partial y_{D2}}{\partial t} + \frac{\partial y_{I2}}{\partial t} = 0 \quad (2.79)$$

$$\frac{\partial y_A}{\partial x} \Big|_{x=0} = 0 \quad (2.80a)$$

$$\frac{\partial y_A}{\partial x} \Big|_{x=1} = 0 \quad (2.80b)$$

$$U \Big|_{x=1} = 0 \quad (2.81)$$

### Step 4 (Counter-Current Desorption)

$$-\frac{1}{Pe} \frac{\partial^2 y_{A2}}{\partial x^2} + \frac{\partial(Uy_{A2})}{\partial x} + \frac{\partial y_{A2}}{\partial \tau} + \frac{y_{A2}}{C_{T2}} \frac{\partial C_{T2}}{\partial \tau} + \zeta_{m,A} \frac{\partial Q_A}{\partial \tau} = 0 \quad (2.82)$$

$$-\frac{1}{Pe} \frac{\partial^2 y_{B2}}{\partial x^2} + \frac{\partial(Uy_{B2})}{\partial x} + \frac{\partial y_{B2}}{\partial \tau} + \frac{y_{B2}}{C_{T2}} \frac{\partial C_{T2}}{\partial \tau} + \zeta_{m,B} \frac{\partial Q_B}{\partial \tau} = 0 \quad (2.83)$$

$$-\frac{1}{Pe} \frac{\partial^2 y_{C2}}{\partial x^2} + \frac{\partial(Uy_{C2})}{\partial x} + \frac{\partial y_{C2}}{\partial \tau} + \frac{y_{C2}}{C_{T1}} \frac{\partial C_{T2}}{\partial \tau} + \zeta_{m,C} \frac{\partial Q_C}{\partial \tau} = 0 \quad (2.84)$$

$$-\frac{1}{Pe} \frac{\partial^2 y_{D2}}{\partial x^2} + \frac{\partial(Uy_{D2})}{\partial x} + \frac{\partial y_{D2}}{\partial \tau} + \frac{y_{D2}}{C_{T1}} \frac{\partial C_{T2}}{\partial \tau} + \zeta_{m,D} \frac{\partial Q_C}{\partial \tau} = 0 \quad (2.85)$$

$$\frac{\partial y_{A2}}{\partial t} + \frac{\partial y_{B2}}{\partial t} + \frac{\partial y_{C2}}{\partial t} + \frac{\partial y_{D2}}{\partial t} + \frac{\partial y_{I2}}{\partial t} = 0 \quad (2.86)$$

$$-\frac{1}{Pe} \frac{\partial y_A}{\partial x} \Big|_{x=0} = (y_{Af} - y_{A1} \Big|_{x=1}) \quad (2.87a)$$

$$\frac{\partial y_A}{\partial x} \Big|_{x=1} = 0 \quad (2.88b)$$

$$U \Big|_{x=1} = u_p / u_f \quad (2.89)$$

In all the four steps, the normalized form of the mass transfer rate and the adsorption equilibrium isotherm are

$$\zeta_m \frac{\partial Q_A}{\partial \tau} = N_f C_{T2} (y_{A2} - \langle y_{A2} \rangle) \quad (2.90)$$

$$\langle y_{A2} \rangle P_2 = \frac{1}{K_{ads,A}} \frac{\theta_{ref,A} Q_A}{\left(1 - \sum_j \theta_{ref,j} Q_j\right)^{n_A}} \quad (2.91)$$

The initial conditions are

$$y_{A2}(x, \tau = 0) = 0 \quad (2.92a)$$

$$y_{B2}(x, \tau = 0) = 0 \quad (2.92b)$$

$$y_{C2}(x, \tau = 0) = 0 \quad (2.92c)$$

$$y_{D2}(x, \tau = 0) = 0 \quad (2.92d)$$

$$y_{I2}(x, \tau = 0) = 1 \quad (2.92f)$$

$$Q_{A2}(x, \tau = 0) = 0 \quad (2.92g)$$

$$Q_{B2}(x, \tau = 0) = 0 \quad (2.92h)$$

In the above dimensionless equations, model parameters are defined as follows:

Damköhler Number:

$$Da = \frac{k_1 L}{u_f}$$

Mass Peclet Number:

$$Pe = \frac{u_f L}{D_L}$$

Mass Capacity Factor:

$$\zeta_m = \frac{1 - \varepsilon}{\varepsilon} \frac{\rho_s Q_{A,ref}}{C_{Tf}}$$

Number of Film Mass-Transfer Units:

$$N_f = \frac{1 - \varepsilon}{\varepsilon} \frac{a_p k_{gl} L}{u_f}$$

Nonlinearity Parameter of Isotherm:

$$\theta_{ref} = \frac{Q_{A,ref}}{Q_{max}}$$

There are two advantages for normalizing the equation. First, a better understanding of the parametric effects on the process can be gained. Second, by expressing all variables in the same scale 0-1, the compounded truncation error caused in the numerical computation is minimized [90].

### 2.3 NUMERICAL METHODS

For the model equations, the partial differential equations are reduced to ordinary differential equations by the method of orthogonal collocation. The total mass balance equation reduces to a set of simultaneous algebraic linear equations. Simultaneous ordinary differential equations are solved using the fourth order Rung-Kutta method. Gaussian elimination method is used to solve simultaneous algebraic equations. Twenty internal collocation points are used. The solution-flow diagram for a step in the PSA unit is as shown in Figure 2.21.

Orthogonal Collocation method is used to integrate model differential equations. Orthogonal Collocation methods are based on orthogonal polynomials. The advantage of using orthogonal polynomials over other classes of polynomials is that the number of the tuning parameters is reduced to two: alpha and beta [43]. Lefevre presents a method to obtain optimum values for alpha and beta for a specific number of collocation points. His method is based on finding the optimum values of alpha and beta that reduce an M matrix. The M matrix is defined as:

$$M = -uL_1 + D_mL_2 \quad (2.93a)$$

Or in dimensionless form

$$M = t_{ref}(-UL_1 + D_mL_2) \quad (2.93b)$$

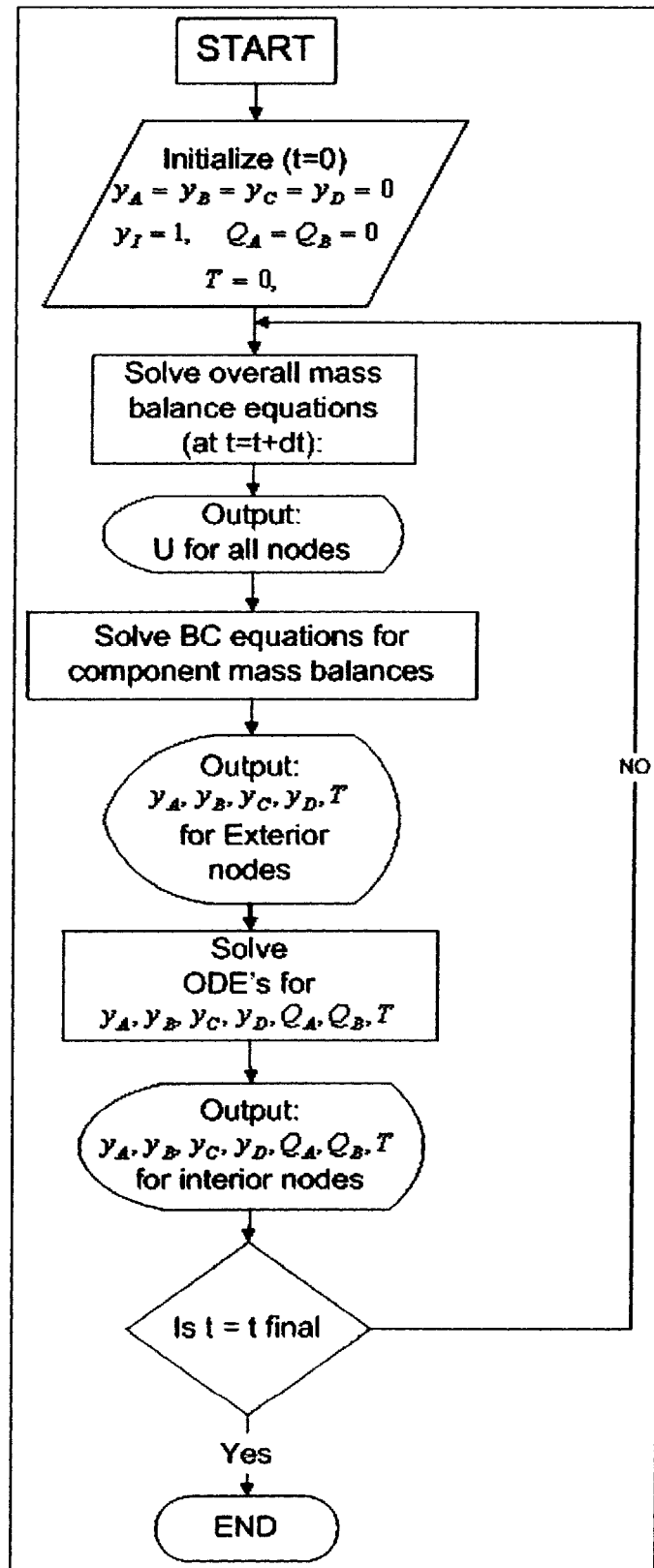


Figure 2.2: Solution Flow Diagram for a single PSA step.

Where:       $u$       : model velocity (cm/s)  
                   $D_m$     : axial mass dispersion coefficient (cm<sup>2</sup>/s)  
                   $L_1$     : first Spatial derivative matrix  
                   $L_2$     : second special derivative matrix  
                   $U$       : dimensionless model velocity (-)  
                   $Pe$     : dimensionless Peclet number

Lefevre et al's concept is based on finding an  $M$  matrix such that the maximum eigenvalue in that matrix is less than all maximum values produced by changing alpha and beta on a specified domain for both alpha and beta. Although Lefevre et al's  $M$  function is based on constant velocity models, it can be well applied to variable velocity models.  $U$ , in variable velocity models becomes the maximum attainable velocity in the model at hand.

According to Lefevre et al., optimum values of alpha and beta are calculated for a number of nodes ranging from 10 to 20. Table 2.1 illustrates Residual (Re) values for zero values of both alpha and beta parameters. Also, it illustrates the Re value at optimum values of alpha and beta. A three-dimensional plot of Re vs alpha and beta is shown in Figure 2.3.

Table 2.2 illustrates the CPU time required to complete the first cycle for a PSA unit. Also, the table illustrates the resulting reduction in time when using optimum values of alpha and beta compared to a value of zero for both variables. Results are obtained from a 1.8 GHz machine. Analysis of PSA data in Table 2.2 clearly indicates the benefit of using optimum values of alpha and beta.

An optimum number of nodes need to be selected for a specified model. This number should be large enough to fully represent the solution domain. Yet, it should not be too large to slowdown the solution time of the simulation model. The family of Figures 2.4 illustrates the integration of the pressurization step for a PSA model for a number of nodes ranging from 10 to 20. To help finding a suitable number of nodes for each model, the reciprocal of the integration time and the smoothness of curves can both be plotted against the number of nodes. The optimum number of nodes is the

number corresponding to the intersection of the two curves. Unfortunately, this method is very subjective. The user has to assume that a certain pre-selected number of nodes would result an exact solution. Alternatively, in this work, we make use of a different technique. First, a number of equidistance points are selected. Then, the output of the first cycle, for each number of collocation points, is used to interpolate a curve for the selected number of equidistance points. Next, the resultants curves are compared to a reference selection of orthogonal points. The best selection is the one that produces a relatively acceptable error while keeping an acceptable CPU integration time.

Results of applying this procedure are illustrated in Figures 2.5a and 2.5b. In those figures, 50 interpolation points are selected. Twenty collocation points are assumed to give exact solution. The error introduced by interpolating 10 collocation points is illustrated in Figure 2.5a. The error introduced by interpolating 19 collocation points is illustrated in Figure 2.5b. The error is reduced by more than four times when selecting 19 points.

Table 2.1:  $Re$  Values at  $\alpha=\beta=0$  and at optimum  $\alpha$  and  $\beta$

No. of Nodes	Optimum		$10^{-4} * Re$ @ Alpha=Beta=0 (1/sec)	$10^{-4} * Re_{min}$ (1/sec)	$100 * (Re_{min}/Re)$
	Alpha	Beta			
10	0.6	0.7	0.590	0.348	59.0
11	0.6	0.7	0.854	0.486	56.9
12	0.7	0.7	1.188	0.666	56.1
13	0.7	0.7	1.610	0.890	55.3
14	0.7	0.7	2.138	1.166	54.5
15	0.7	0.7	2.785	1.503	54.0
16	0.7	0.7	3.570	1.907	53.4
17	0.7	0.7	4.511	2.389	53.0
18	0.7	0.7	5.626	2.956	52.5
19	0.7	0.7	6.937	3.688	53.2
20	0.7	0.7	8.466	4.375	51.7



Table 2.2: First cycle time for  $\alpha=\beta=0$  and for optimum values of  $\alpha$  and  $\beta$ .

No. of Nodes	1 <sup>st</sup> cycle time @ $\alpha=\beta=0$ (min)	1 <sup>st</sup> Cycle Time @ optimum $\alpha$ & $\beta$ (min)	% Reduction in Cycle time
10	2.686	2.215	17.5
11	2.814	2.584	8.2
12	3.089	2.673	13.5
13	3.988	3.464	13.1
14	3.602	4.324	-20.0
15	4.358	3.83	12.1
16	5.197	4.313	17.0
17	4.749	4.715	0.7
18	5.849	5.732	2.0
19	5.635	5.049	10.4
20	6.042	4.699	22.2

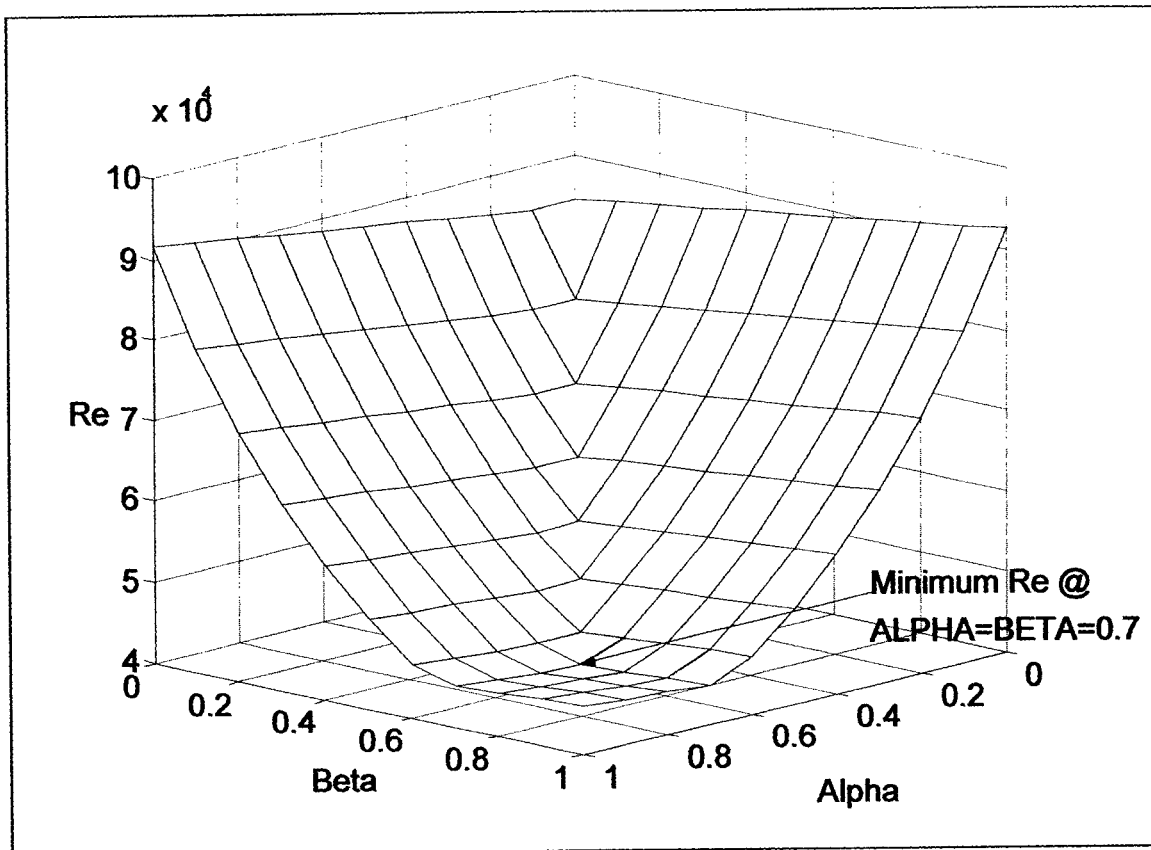


Figure 2.3: Optimum values of alpha and beta corresponding to minimum Re for N=20.

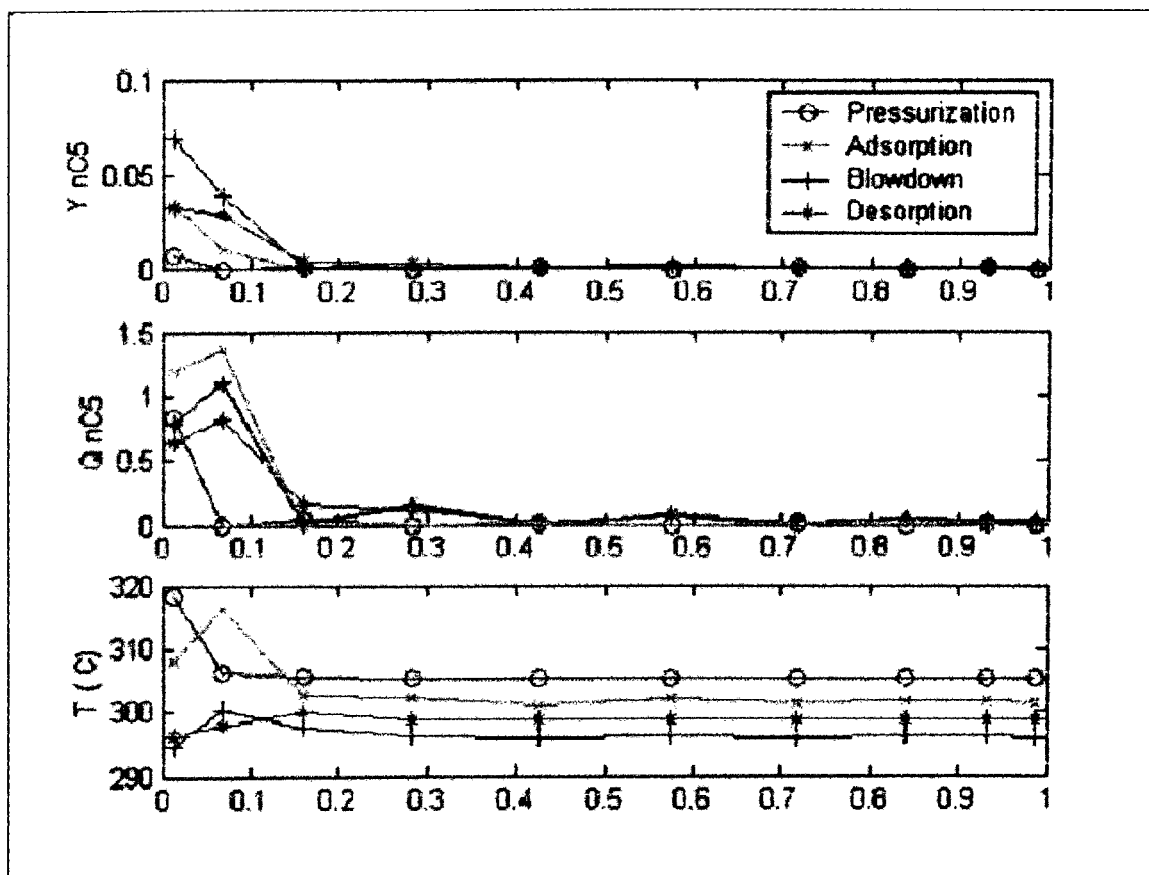


Figure 2.4a: Selected profiles for the first cycle for  $N = 10$ .

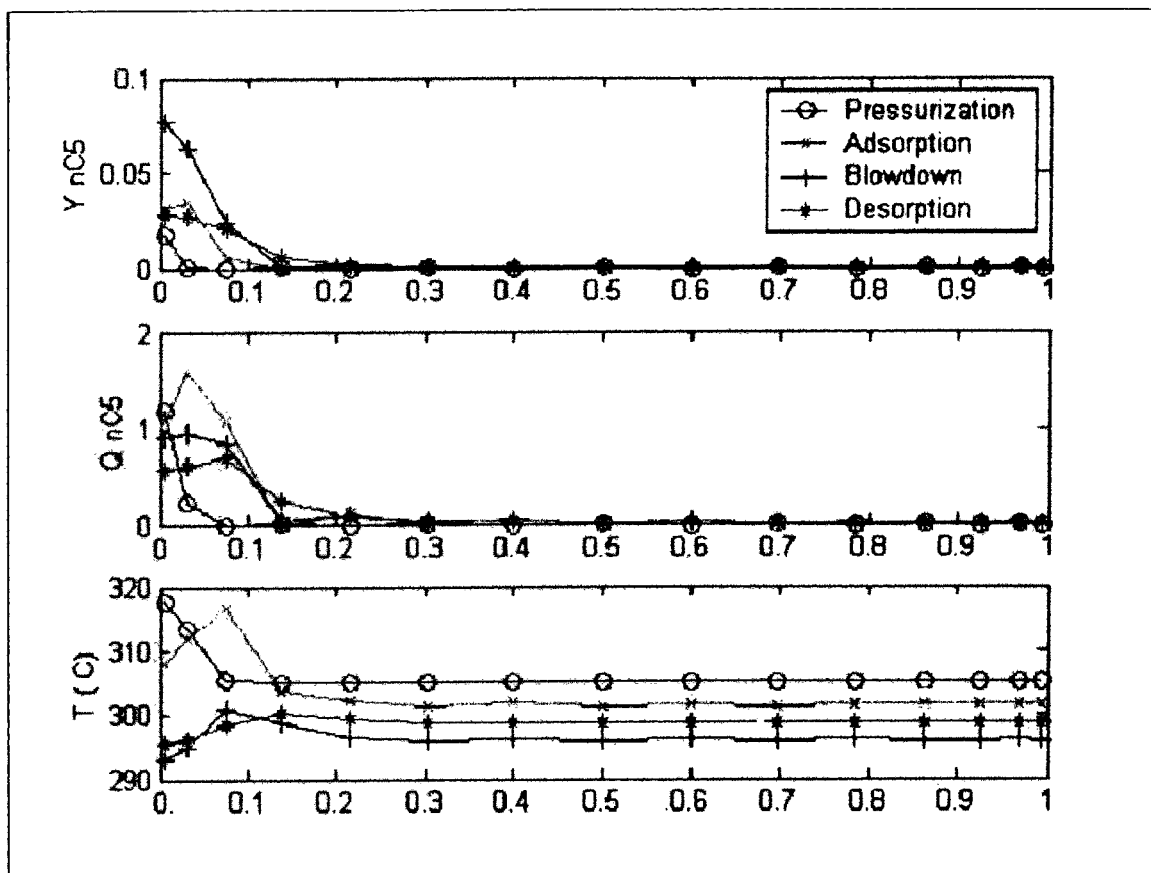


Figure 2.4b: Selected profiles for the first cycle for  $N = 15$ .

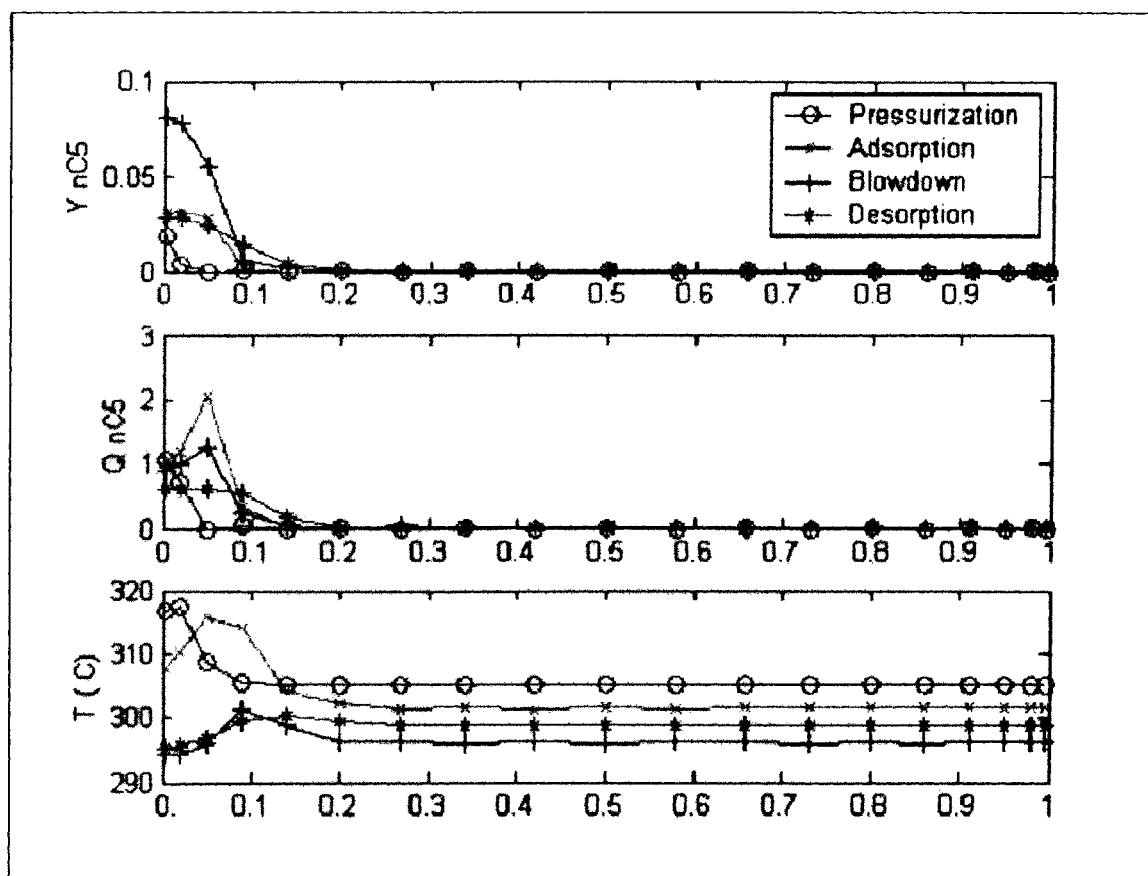


Figure 2.4c: Selected profiles for the first cycle for  $N = 19$ .

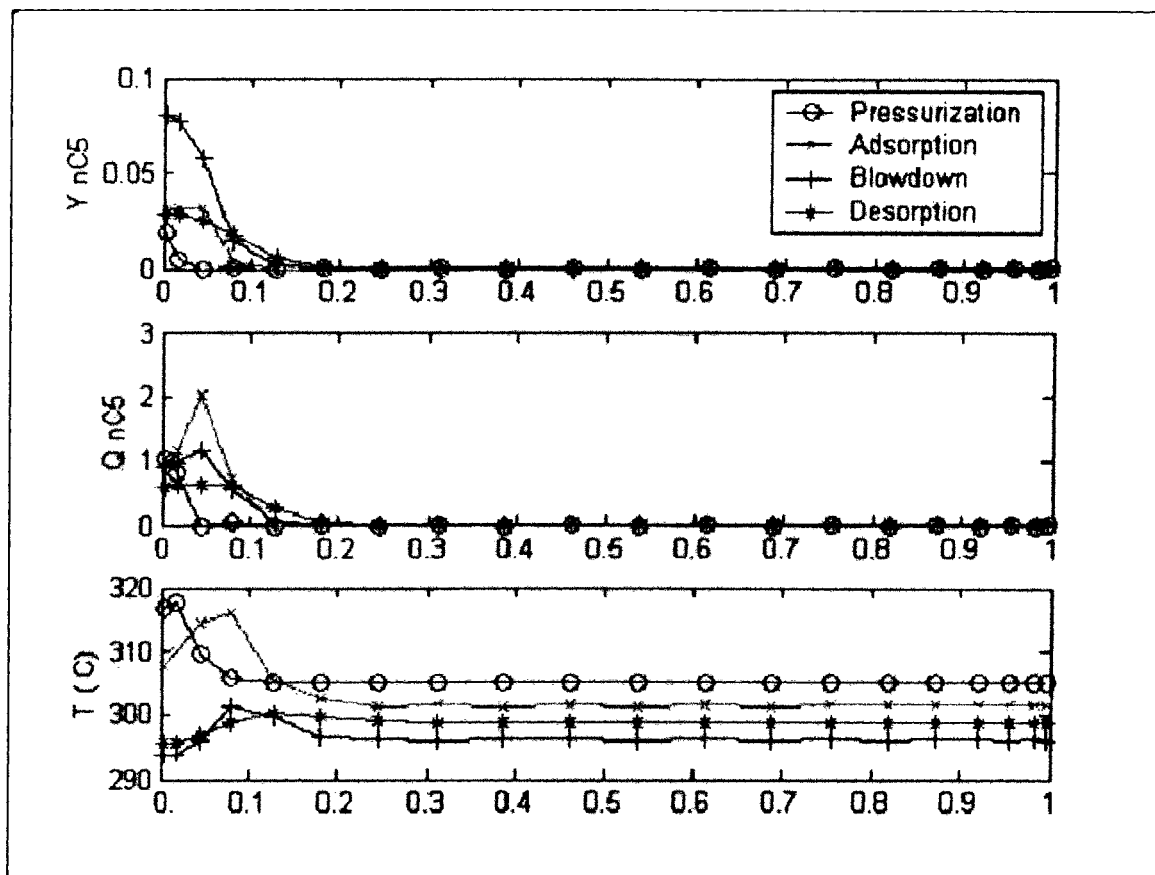


Figure 2.4d: Selected profiles for the first cycle for  $N = 20$ .

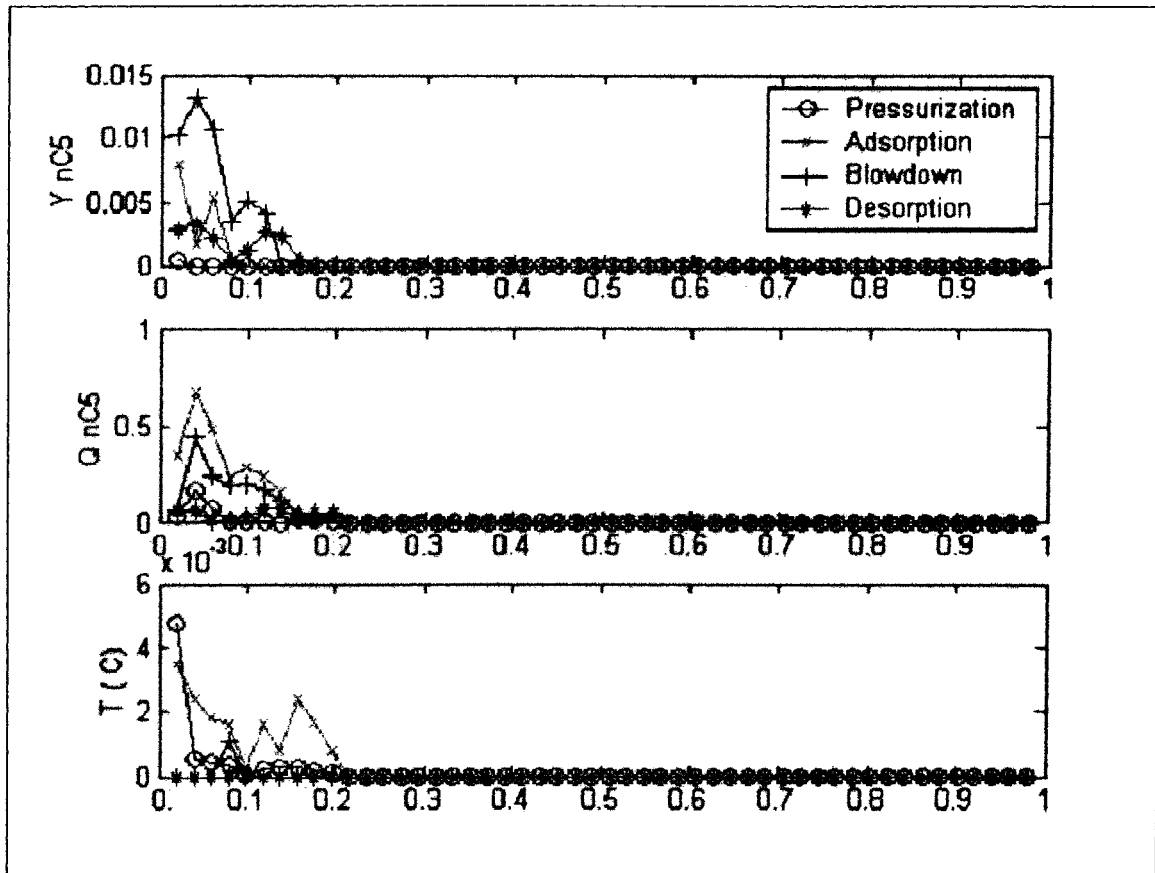


Figure 2.5a: Absolute interpolation error introduced with  $N=10$ , assuming  $N=20$  is the exact solution.

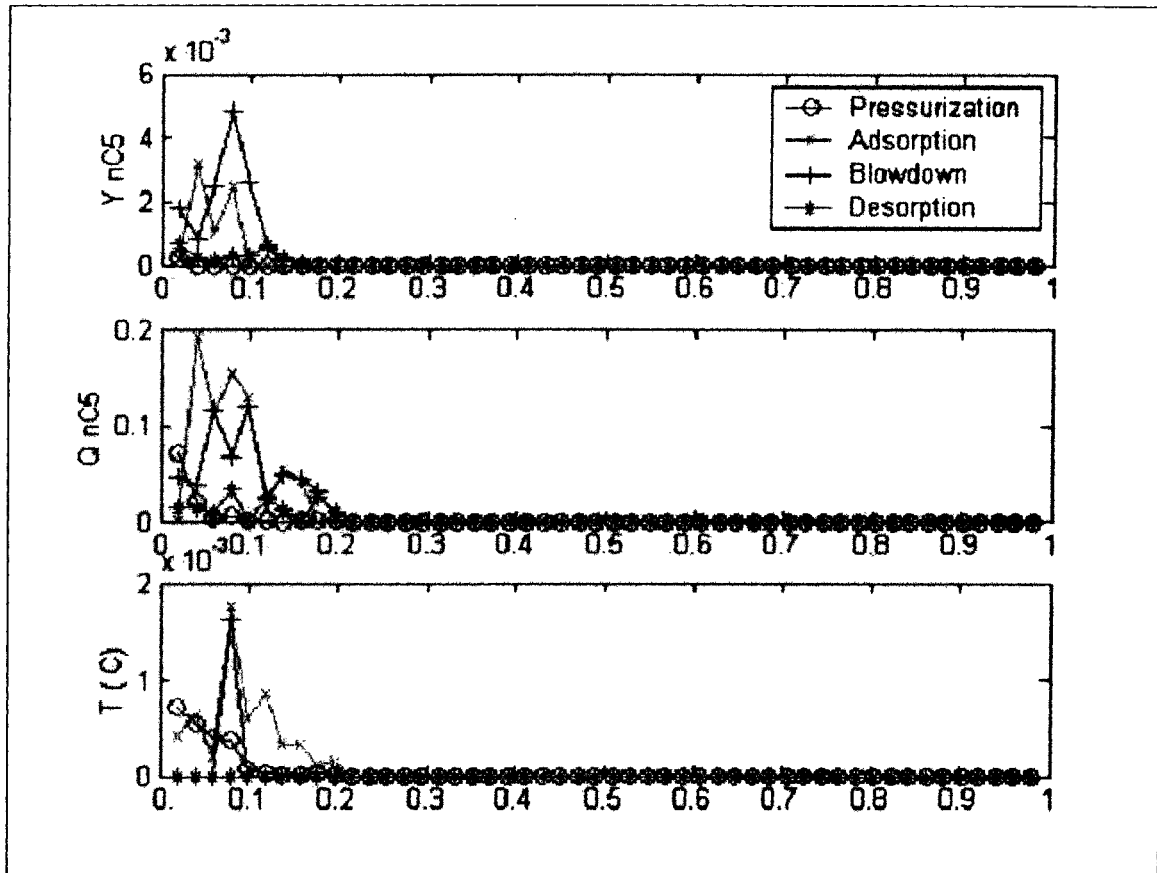


Figure 2.5b: Absolute interpolation error introduced with  $N=19$ , assuming  $N=20$  is the exact solution.



## 2.4 PARAMETERS ESTIMATIONS

Model parameters were estimated from independent experiments and correlations available in the literature. Table 2.3 summarizes the column characteristics, adsorbent properties, adsorption equilibrium isotherm and reaction parameters. The data for the adsorption section are experimental data published by Silva and Rudrigus [75,77]. The axial dispersion coefficient ( $D_L$ ) is approximated by:

$$D_L = 0.7D_m + 0.5ud_p \quad (2.94)$$

At low Renolds number, the second term in the above equation may be neglected [70,71]. This approximation is validated in the next section.

According to a lumped model proposed by Glueckauf [27], the overall mass transfer coefficient ( $k_{gl}$ ) can be calculated by

$$\frac{1}{K_{gk}} = \frac{1}{k_e} + \frac{1}{\varepsilon_p k_i} \quad (2.95)$$

where the intraparticle mass transfer coefficient ( $k_i$ ) can be calculated by:

$$k_i = \frac{5D_p}{R_p} \quad (2.96)$$

The external mass transfer coefficients ( $k_e$ ) were estimated from the correlation obtained by Wakao and Kaguei [87].

$$Sh = 2.0 + 1.1(Re)^{0.6}(Sc)^{0.33} \quad (2.97)$$

The parameter values and operating conditions used in the simulations are listed in Table 2.3.

Table 2.3: Data for the base case system

Adsorption Column Characteristics:	
• $L$	$= 400 \text{ cm}$
• $d_c$	$= 12.7 \text{ cm}$
Adsorbent Properties	
• $\rho_b$	$= 0.77 \text{ g/cm}^3$
• $\rho_s$	$= 1.13 \text{ g/cm}^3$
• $\varepsilon$	$= 0.32$
• $\varepsilon_p$	$= 0.35$
• $d_p$	$= 1.6 \text{ mm}$
• $a_p$	$= 25 \text{ cm}^{-1}$
Adsorption Equilibrium Isotherm Parameters	
• $-\Delta H_{ads, nC_5}$	$= 13.2 \text{ kcal/mol}$
• $-\Delta H_{ads, nC_6}$	$= 14.2 \text{ kcal/mol}$
• $n_{nC_5}$	$= 5$
• $n_{nC_6}$	$= 6$
• $q_{max, nC_5}$	$= 13.0 \text{ g/100g}$
• $q_{max, nC_6}$	$= 13.0 \text{ g/100g}$
• $K_{o, nC_5}$	$= 2.013 * 10^{-5} \text{ bar}^{-1}$
• $K_{o, nC_6}$	$= 4.9187 * 10^{-5} \text{ bar}^{-1}$

## 2.5 RESULTS AND DISCUSSION

Figures 2.6 to 2.9 illustrate bed profiles of concentrations for n-C<sub>5</sub>, n-C<sub>6</sub> and the temperature in the gas phase for the four cyclic steps: pressurization, adsorption, blowdown and desorption, respectively. The figures also, illustrate the results of the previous work conducted by Silva and Rudrigues. The simulation is performed at a temperature of 573 K. Other parameters used in the simulation are summarized in Table 2.4.

As shown in Figure 2.6, during pressurization, the initial gas concentration in the bed is pushed toward the closed product end, where it forms a plateau that is totally enriched in i-C<sub>5</sub>, i-C<sub>6</sub> and H<sub>2</sub>. The region before the plateau shows the penetration of the feed gas. In the high-pressure adsorption step, the concentration profile moves down the column, and a raffinate product, totally enriched in i-C<sub>5</sub>, i-C<sub>6</sub> and H<sub>2</sub> is withdrawn at the product end. In the blowdown and purge steps, the concentration profile is pushed back and a relatively clean initial bed condition is reestablished for the next cycle at the end of the purge step.

As shown in Figure 2.8, in the blowdown step, increasing concentration of n-C<sub>5</sub> and n-C<sub>6</sub> in the bed arises due to desorption, where it increases about four times relative to feed conditions. At the end of desorption step, the mole fractions of n-C<sub>5</sub> and n-C<sub>6</sub> are below feed conditions.

The difference between the results of this work and those obtained by Silva and Rudrigues is because Silva and Rudrigues used a parabolic wall temperature profile. However, they made no notion of the profile distribution mechanism in their paper.

Figure 2.10 illustrates the approach to cyclic steady state, which is about 15 cycles in this work.

Table 2.4: Parametric Values used for simulation of the base case of the n-C<sub>5</sub>/n-C<sub>6</sub>/N<sub>2</sub> system.

Parameter	Value
$y_{nC5f}$ (mol/mol)	0.139
$y_{nC6f}$ (mol/mol)	0.046
$F_f$ (mol/m <sup>2</sup> /s)	7.55
$P_H$ (bar)	15
$P_L$ (bar)	2
$T$ (K)	573
$U_f$ (cm/s)	16.4
$U_p$ (cm/s)	50
$\zeta_{nC5,m}$	2.8082
$\zeta_{nC6,m}$	2.9827
$\theta_{nC5,ref}$	0.2203
$\theta_{nC6,ref}$	0.2340

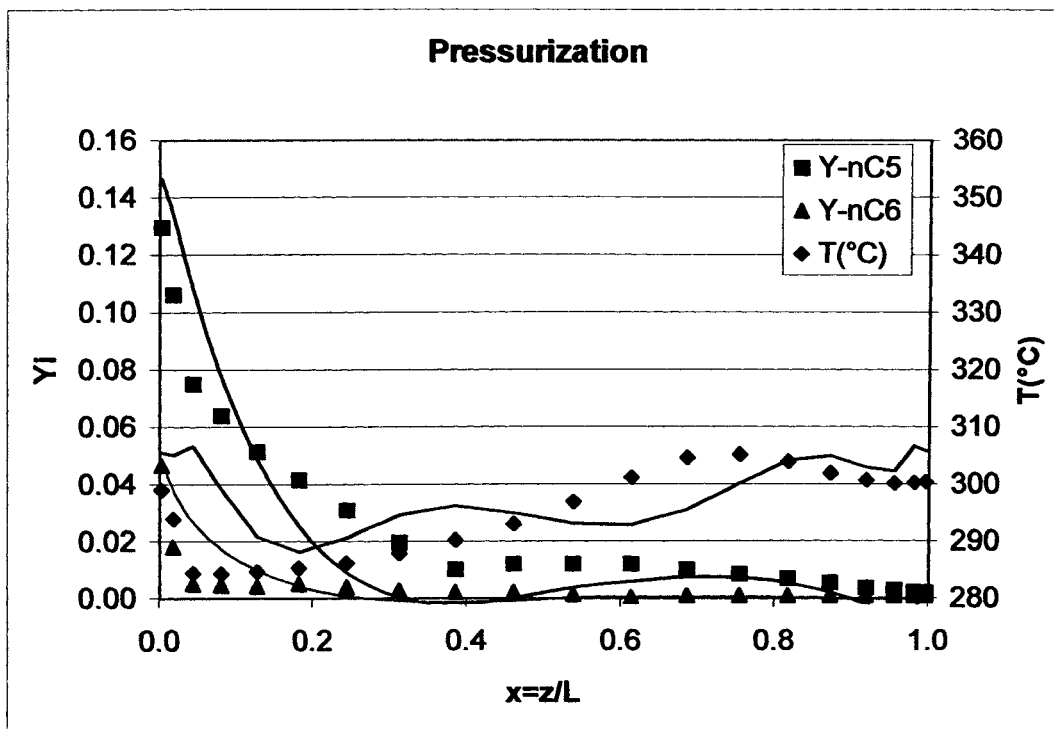


Figure 2.6: Gas Phase concentration profiles of n-C<sub>5</sub>, n-C<sub>6</sub> and Temperature profile at the end of the cyclic steady state (Pressurization Step). Points represent data provided by Silva & Rudrigues. Continuous Lines represent this work. The temperature is plotted in the secondary Y-axis to the right of the figure. Parametric Values are in Table 2.2.

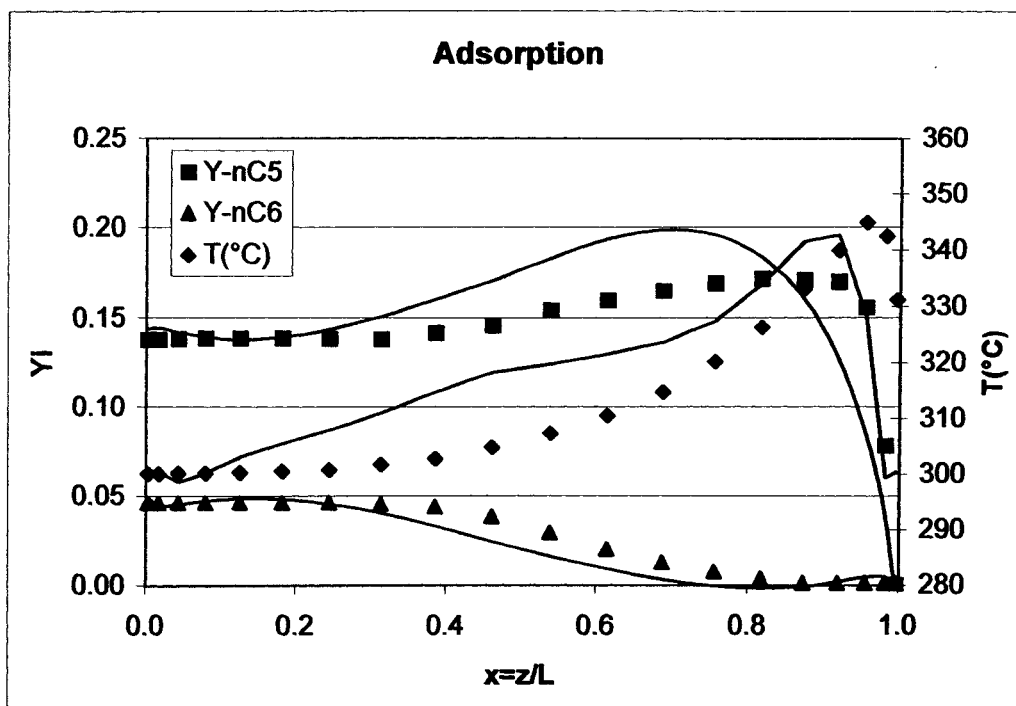


Figure 2.7: Gas Phase concentration profiles of n-C<sub>5</sub>, n-C<sub>6</sub> and Temperature profile at the end of the cyclic steady state (Adsorption Step). Points represent data provided by Silva & Rudrigues. Continuous Lines represent this work. The temperature is plotted in the secondary Y-axis to the right of the figure. Parametric Values are in Table 2.2.

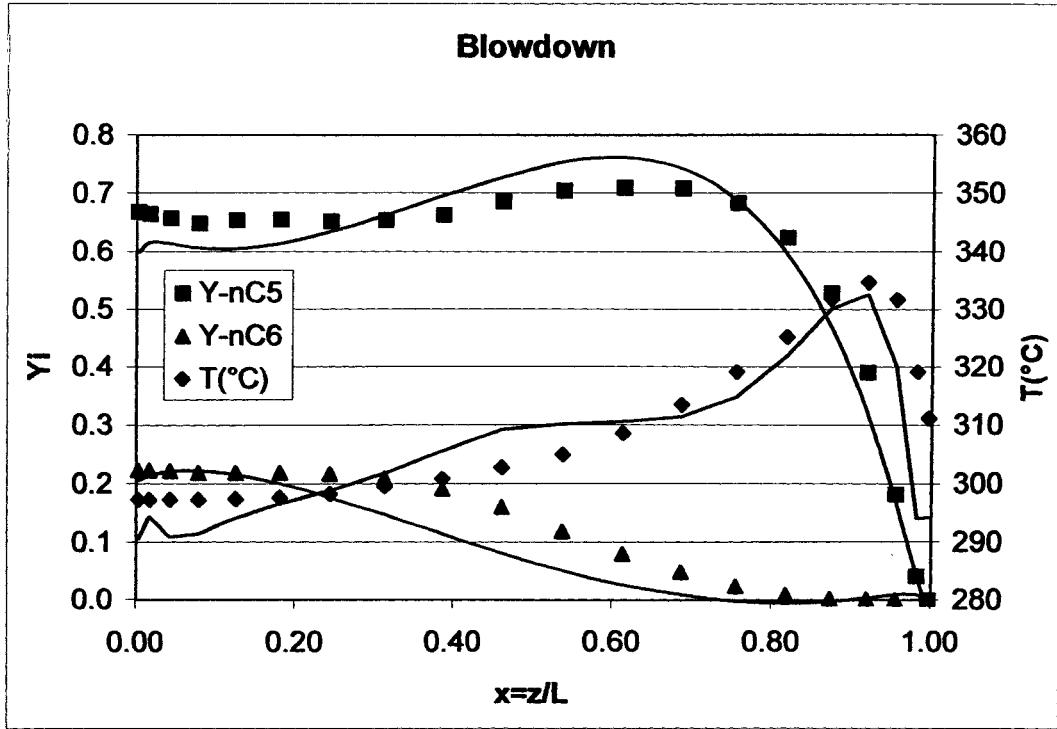


Figure 2.8: Gas Phase concentration profiles of n-C<sub>5</sub>, n-C<sub>6</sub> and Temperature profile at the end of the cyclic steady state (Blow down Step). Points represent data provided by Silva & Rodrigues. Continuous Lines represent this work. The temperature is plotted in the secondary Y-axis to the right of the figure. Parametric Values are in Table 2.2.

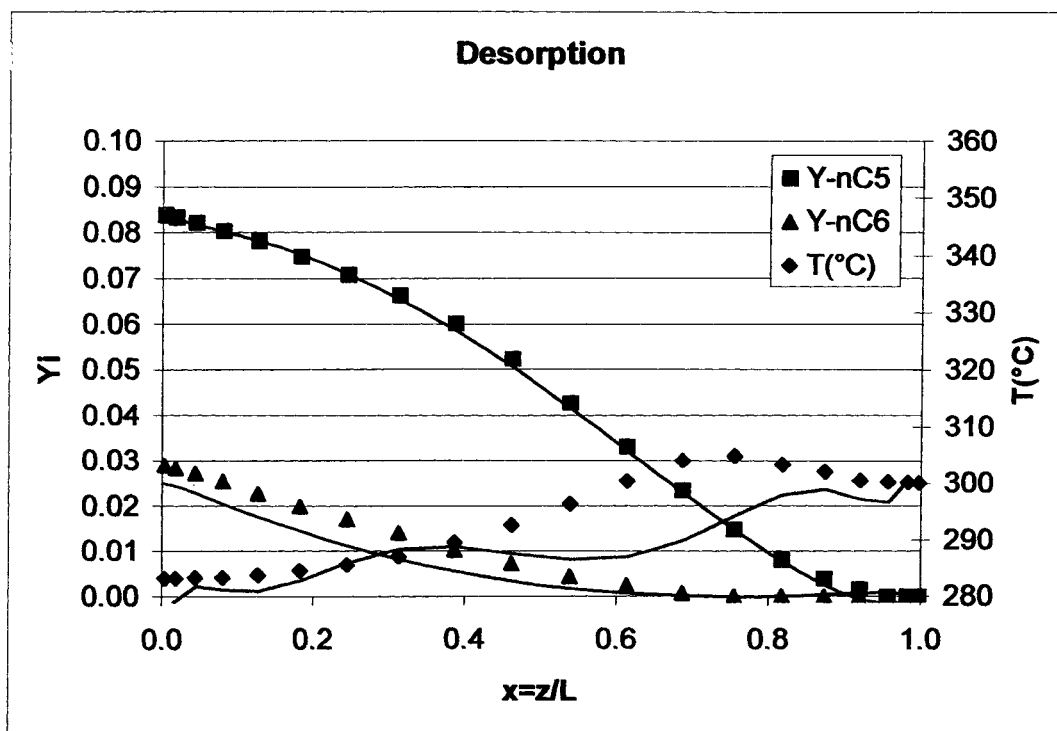


Figure 2.9: Gas Phase concentration profiles of n-C<sub>5</sub>, n-C<sub>6</sub> and Temperature profile at the end of the cyclic steady state (Desorption Step). Points represent data provided by Silva & Rodrigues. Continuous Lines represent this work. The temperature is plotted in the secondary Y-axis to the right of the figure. Parametric Values are in Table 2.2.



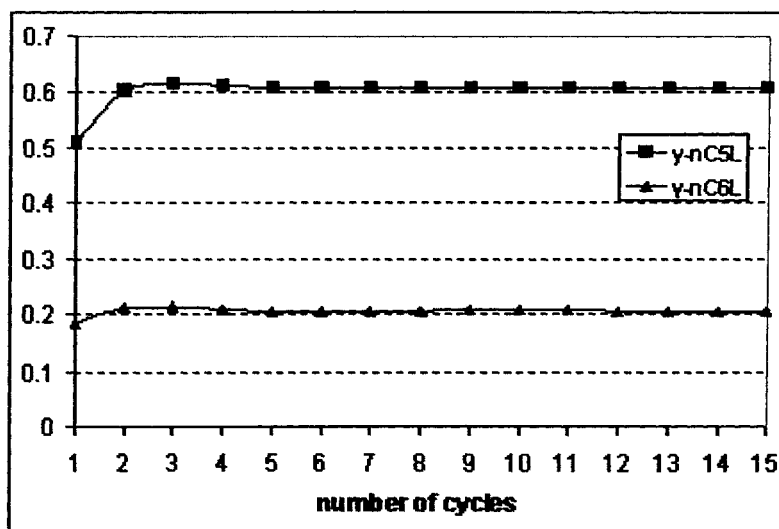


Figure 2.10: Approach to cyclic steady state, illustrating exit concentration of n-C<sub>5</sub>, n-C<sub>6</sub> at end of blowdown step. Parametric values are in Table 2.2.

## Nomenclature

$B$	dimensionless adiabatic temperature rise [-] = $(-\Delta H_{ads})q_{A,ref}/(C_{ps}T_f)$
$c_T$	total gas concentration in the column [mol/cm <sup>3</sup> ]
$c_{Tf}$	total feed gas concentration [mol/cm <sup>3</sup> ]
$C_T$	dimensionless total gas concentration in the column
$C_{pg}$	heat capacity of the gas phase [J/(mol·K)]
$C_{ps}$	heat capacity of the adsorbent [J/(g·K)]
$D_A$	pore diffusivity of component A [cm <sup>2</sup> /s]
$D_L$	axial mass dispersion coefficient [cm <sup>2</sup> /s]
$d_C$	column diameter [cm]
$h$	overall heat transfer coefficient [W/cm <sup>2</sup> ·K]
$(-\Delta H_{ads})$	isosteric heat of adsorption [J/mol]
$k_{gl}$	global mass-transfer coefficient [cm/s]
$K_{ads}$	adsorption equilibrium constant [bar <sup>-1</sup> ] = $K_o \cdot \exp(-\Delta H/R/T)$
$K_O$	limiting adsorption equilibrium constant [bar <sup>-1</sup> ]
$K_L$	axial bed thermal conductivity [W/(cm·K)]
$L$	length of the PSA column [cm]
$n$	coefficient of Nitta et al. isotherm [-]
$N_f$	number of film mass-transfer units [-]
$N_w$	number of wall heat-transfer units [-] = $4hL/(d_c u_f C_{pg} c_{Tf} \varepsilon)$
$P$	total pressure in the column [bar]
$Pe$	mass Peclet number [-]
$Pe_H$	thermal Peclet number [-] = $u_f L C_{pg} c_{Tf} / K_L$
$P_H$	constant high pressure during adsorption step [bar]
$P_L$	constant low pressure during desorption step [bar]
$\langle q_A \rangle$	average adsorbed-phase concentration [mol/kg]
$q_{A,ref}$	adsorbed-phase concentration at equilibrium with $y_{Af}$ at $P_H$ and $T_f$ [mol/kg]
$q_{max}$	maximum adsorbed-phase concentration [mol/kg]
$Q_A$	dimensionless adsorbed-phase concentration [-] = $\langle q_A \rangle / q_{max}$
$R$	ideal gas constant [bar·cm <sup>3</sup> /mol/K]
$t$	time [s]

$T$	column gas temperature [K]
$T_f$	feed gas temperature [K]
$\bar{T}$	dimensionless column gas temperature [-] = $(T - T_f)/T_f$
$u$	interstitial velocity [cm/s]
$u_f$	interstitial feed velocity [cm/s]
$u_p$	purge gas velocity [cm/s]
$U$	dimensionless interstitial velocity [-]
$x$	dimensionless axial coordinate in the column [-] = $z/L$
$y_A$	mole fraction of component A in the bulk phase in the column [-]
$y_{Af}$	mole fraction of component A in the feed [-]
$y_{Aj}$	mole fraction of component A in the bulk phase in bed i [-]
$y_{Bf}$	mole fraction of component B in the feed [-]
$y_{Bj}$	mole fraction of component B in the bulk phase in bed i [-]
$y_{AL}$	mole fraction of component A at the exit of the column [-]
$\langle y_{A2} \rangle$	average mole fraction of the sorbate in the pores of the adsorbent pellet in bed 2 [-]
$z$	axial coordinate in the column [cm]

#### Greek Letters

$\varepsilon_1$	bed void fraction [-]
$\varepsilon_2$	adsorbent void fraction [-]
$\zeta_H$	thermal capacity factor [-] = $(1 - \varepsilon_1 - \varepsilon_2)\rho_s C_{ps} / (\varepsilon_{Tf} C_{pg})$
$\zeta_m$	mass capacity factor [-]
$\theta_{A,,ref}$	coverage of adsorbent at $y_{Af}$ and $P_H$ [-]
$\rho_s$	apparent density of the adsorbent [g/cm <sup>3</sup> ]
$\tau$	dimensionless time [-] = $u_f t / L$
$\gamma_f$	dimensionless heat of adsorption [-] = $(-\Delta H_{ads}) / (RT_f)$

#### Subscripts

A	n-pentane
B	n-hexane
C	i-hexane
D	n-hexane
I	inert (Hydrogen)
T	total
f	feed

## CHAPTER 3

### PSAR MODELING FOR n-C<sub>5</sub>, i-C<sub>5</sub>, n-C<sub>6</sub>, i-C<sub>6</sub> SYSTEM

#### 3.1 MODEL ASSUMPTIONS

For the catalyst and adsorbent zones, mass and energy balances are conducted to reveal the profiles of conversion against time and reaction zone distance. The dispersed PFR model is applied to describe the dynamic behavior of the unit in both reaction and PSA sections. Methods suggested by Spivey and Bryant. [81] and by Runstraat et al. [62] are followed for building reaction rate expressions.

#### 3.2 PSAR PROCESS DESCRIPTION

Figure 3.1 is the proposed process flow diagram for the isomerization of n-alkanes to isoalkanes in the PSAR unit. The unit consists of two columns. Each column consists of a catalyst-packed region followed by adsorbent packed region. The system is modeled as a non-isothermal process containing five components (n-C<sub>5</sub>/i-C<sub>5</sub>/n-C<sub>6</sub>/i-C<sub>6</sub>/H<sub>2</sub>). The cyclic steps shown in Figure 3.2 are as follow:

**Step 1: Pressurization/Reaction:** The unit is pressurized by feeding the feedstock (at high pressure), into the catalyst bed. In the catalyst bed, partial conversion of n-C<sub>5</sub> and n-C<sub>6</sub> to i-C<sub>5</sub> and i-C<sub>6</sub>, respectively, takes place. There is no effluent from the unit at this step.

**Step 2: Reaction/Adsorption:** The feedstock, at high pressure, is fed to the catalyst bed where partial conversion of n-C<sub>5</sub>/n-C<sub>6</sub> to i-C<sub>5</sub>/i-C<sub>6</sub>, respectively, takes place. Then it enters the adsorbent region where unreacted n-C<sub>5</sub> and n-C<sub>6</sub> are adsorbed. The effluent from the unit, composed of i-C<sub>5</sub>, i-C<sub>6</sub> and hydrogen is fed to H<sub>2</sub> PSA unit where i-C<sub>5</sub> and i-C<sub>6</sub> are separated and taken off as process product. H<sub>2</sub> is

recycled to the process. This step continues until the adsorbent bed reaches a specified saturation limit. Then, feed is shut off, and step 3 is introduced.

**Step 3: Blowdown/Reaction:** The unit is depressurized to a lower pressure level in a similar direction to that of the reaction/adsorption step. Desorption of reactive components takes place in both sections. A gas stream containing all components of the system exits the unit. Usually, this stream is considered as waste stream and discharged off in most conventional PSA processes. In the present case, however, the blowdown stream is reutilized since it contains considerable portion of  $i\text{-C}_5$  and  $i\text{-C}_6$ . The reutilization of this gas stream is studied in this thesis.

**Step 4: Desorption/Reaction:** Hydrogen gas, which is considered as inert, is introduced to the adsorbent bed at low pressure. Alternatively, a portion of step 2 product can be introduced to the adsorbent bed. This step desorbs the remaining  $n\text{-C}_5$  and  $n\text{-C}_6$  from the adsorbent and catalyst beds. The purge stream is introduced from both ends of the vessel. The waste stream is collected from the interface region. In the study by Al-Juhani [1], the resulting stream was considered a waste. In this study, this stream is combined with the fresh feed of step 1 to maximize conversion of  $n\text{-C}_5/n\text{C}_6$  to  $i\text{-C}_5/i\text{C}_6$  and recovery of product.

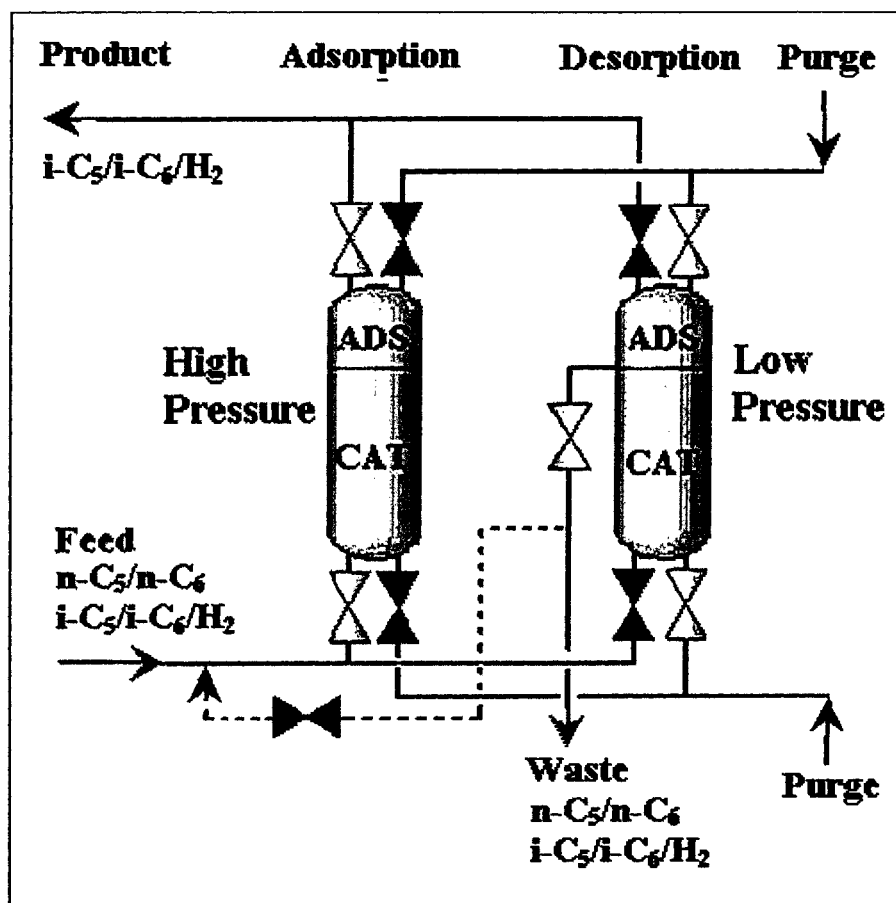


Figure 3.1: Flow diagram for the Combined Isomerization Reactor/Adsorber Process.

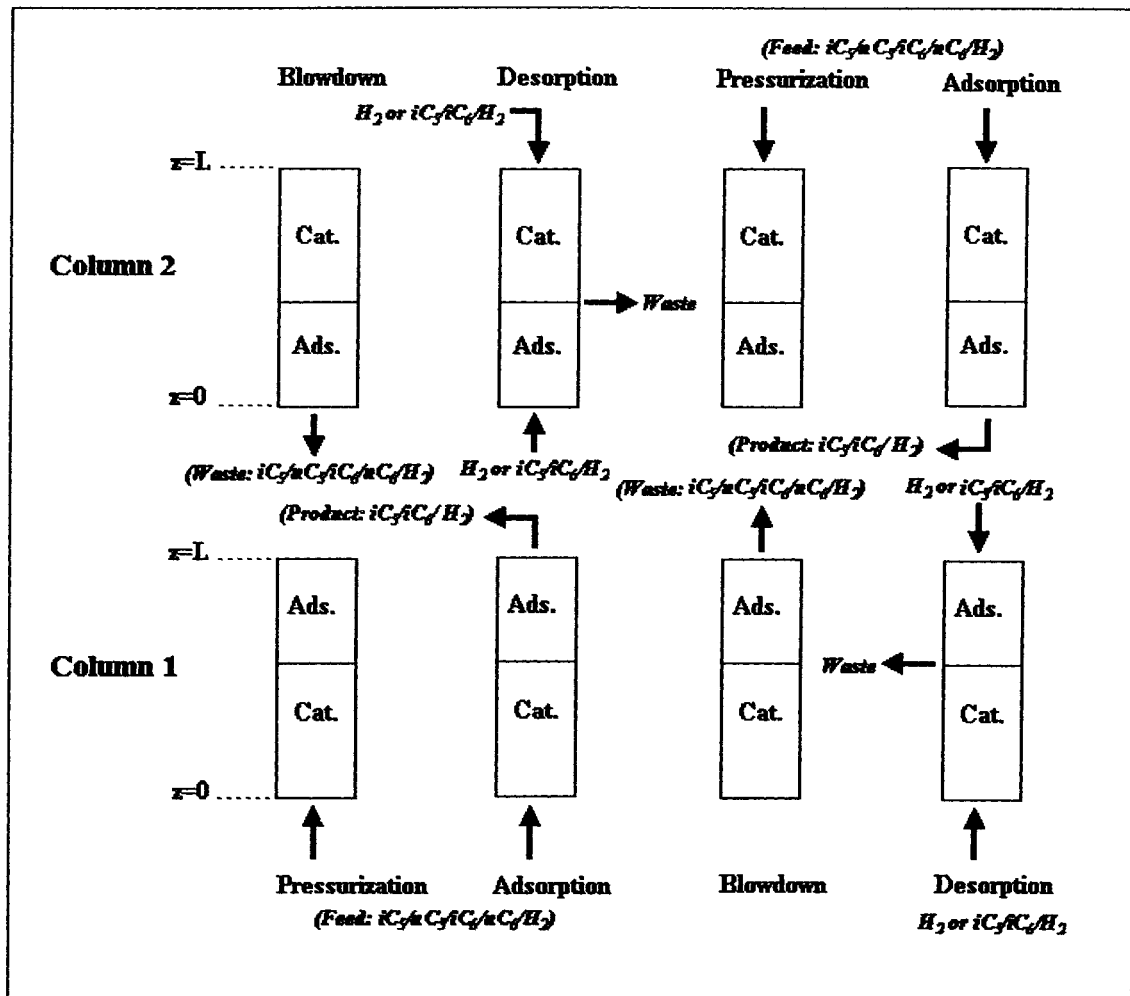


Figure 3.2: Proposed Cyclic Steps for PSAR Unit.

### 3.3 MODEL EQUATIONS

A mathematical representation of the problem is as shown in Figure 3.3. The normalized equations developed in Chapter 2 (equations 2.60-2.97) are rewritten in terms of two space variables illustrated in Figure 3.3 and defined as follow:

$$v_1 = \frac{x}{\omega} \quad ; 0 < x < \omega \quad (3.1a)$$

$$v_2 = \frac{x - \omega}{1 - \omega} \quad ; \omega < x < 1 \quad (3.1b)$$

The model assumptions in Chapter 2 are also valid in this Chapter. In addition, the continuity of concentration, mass flux, and velocity are applicable at the junction of the two sub domains. Thus, the final form of the model equations becomes:

Step 1 (Reaction/Pressurization)

$$\frac{\partial y_{A1}}{\partial \tau} = \frac{1}{\omega^2} \frac{1}{Pe} \frac{\partial^2 y_{A1}}{\partial v_1^2} - \frac{1}{\omega} \frac{\partial(U_1 y_{A1})}{\partial v_1} - \frac{y_{A1}}{C_T} \frac{\partial C_T}{\partial \tau} - \frac{Da_{i1}}{\omega} \left[ y_{A1} - \frac{y_{C1}}{K_{C1}} \right] - \zeta_{mA1} \frac{\partial Q_{A1}}{\partial \tau} \quad (3.2)$$

$$\frac{\partial y_{B1}}{\partial \tau} = \frac{1}{\omega^2} \frac{1}{Pe} \frac{\partial^2 y_{B1}}{\partial v_1^2} - \frac{1}{\omega} \frac{\partial(U_1 y_{B1})}{\partial v_1} - \frac{y_{B1}}{C_T} \frac{\partial C_T}{\partial \tau} - \frac{Da_{i2}}{\omega} \left[ y_{B1} - \frac{y_{D1}}{K_{C2}} \right] - \zeta_{mB1} \frac{\partial Q_{B1}}{\partial \tau} \quad (3.3)$$

$$\frac{\partial y_{C1}}{\partial \tau} = \frac{1}{\omega^2} \frac{1}{Pe} \frac{\partial^2 y_{C1}}{\partial v_1^2} - \frac{1}{\omega} \frac{\partial(U_1 y_{C1})}{\partial v_1} - \frac{y_{C1}}{C_T} \frac{\partial C_T}{\partial \tau} + \frac{Da_{i1}}{\omega} \left[ y_{A1} - \frac{y_{C1}}{K_{C1}} \right] - \zeta_{mC1} \frac{\partial Q_{C1}}{\partial \tau} \quad (3.4)$$

$$\frac{\partial y_{D1}}{\partial \tau} = \frac{1}{\omega^2} \frac{1}{Pe} \frac{\partial^2 y_{D1}}{\partial v_1^2} - \frac{1}{\omega} \frac{\partial(U_1 y_{D1})}{\partial v_1} - \frac{y_{D1}}{C_T} \frac{\partial C_T}{\partial \tau} + \frac{Da_{i2}}{\omega} \left[ y_{B1} - \frac{y_{D1}}{K_{C2}} \right] - \zeta_{mD1} \frac{\partial Q_{D1}}{\partial \tau} \quad (3.5)$$

$$\frac{\partial y_{H_21}}{\partial \tau} = \frac{1}{\omega^2} \frac{1}{Pe} \frac{\partial^2 y_{H_21}}{\partial v_1^2} - \frac{1}{\omega} \frac{\partial(U_1 y_{H_21})}{\partial v_1} - \frac{y_{H_21}}{C_T} \frac{\partial C_T}{\partial \tau} \quad (3.6)$$

$$\frac{\partial U_1}{\partial v_1} = - \frac{\omega}{C_T} \frac{\partial C_T}{\partial \tau} \quad (3.7)$$

$$(C_T + \zeta_{H,1}) \frac{\partial \bar{T}_1}{\partial \tau} = \frac{1}{\omega^2} \frac{1}{Pe_H} \frac{\partial^2 \bar{T}_1}{\partial v_1^2} - \frac{C_T}{\omega} \frac{\partial}{\partial v_1} [U(\bar{T}_1 + 1)] + \sum F_{i,1} \zeta_H \frac{\partial Q_i}{\partial \tau} + \sum E_i (-r_{Ai}) - N_w (\bar{T}_1 - \bar{T}_{w1}) \quad (3.8)$$



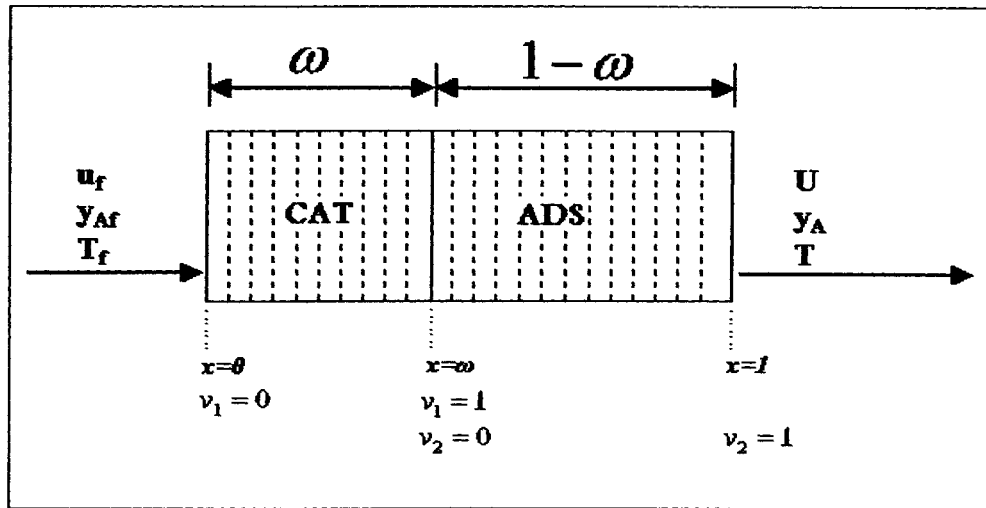


Figure 3.3a: Mathematical Representation for the PSAR Unit (Steps 1, 2 and 3).

Note: for step 1, the product end is closed. For step 3, the feed end is closed.

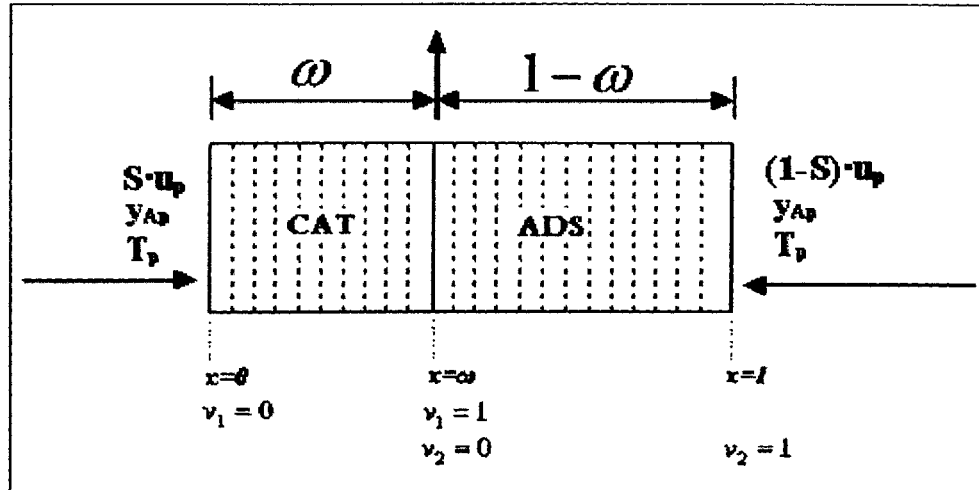


Figure 3.3b: Mathematical Representation for the PSAR Unit (Step 4).

$$\frac{\partial y_{A2}}{\partial \tau} = \frac{1}{(1-\omega)^2} \frac{1}{Pe} \frac{\partial^2 y_{A2}}{\partial v_2^2} - \frac{1}{(1-\omega)} \frac{\partial(U_2 y_{A2})}{\partial v_2} - \frac{y_{A2}}{C_T} \frac{\partial C_T}{\partial \tau} - \zeta_{mA2} \frac{\partial Q_{A2}}{\partial \tau} \quad (3.9)$$

$$\frac{\partial y_{B2}}{\partial \tau} = \frac{1}{(1-\omega)^2} \frac{1}{Pe} \frac{\partial^2 y_{B2}}{\partial v_2^2} - \frac{1}{(1-\omega)} \frac{\partial(U_2 y_{B2})}{\partial v_2} - \frac{y_{B2}}{C_T} \frac{\partial C_T}{\partial \tau} - \zeta_{mB2} \frac{\partial Q_{B2}}{\partial \tau} \quad (3.10)$$

$$\frac{\partial y_{C2}}{\partial \tau} = \frac{1}{(1-\omega)^2} \frac{1}{Pe} \frac{\partial^2 y_{C2}}{\partial v_2^2} - \frac{1}{(1-\omega)} \frac{\partial(U_2 y_{C2})}{\partial v_2} - \frac{y_{C2}}{C_T} \frac{\partial C_T}{\partial \tau} \quad (3.11)$$

$$\frac{\partial y_{D2}}{\partial \tau} = \frac{1}{(1-\omega)^2} \frac{1}{Pe} \frac{\partial^2 y_{D2}}{\partial v_2^2} - \frac{1}{(1-\omega)} \frac{\partial(U_2 y_{D2})}{\partial v_2} - \frac{y_{D2}}{C_T} \frac{\partial C_T}{\partial \tau} \quad (3.12)$$

$$\frac{\partial y_{H_2,2}}{\partial \tau} = \frac{1}{(1-\omega)^2} \frac{1}{Pe} \frac{\partial^2 y_{H_2,2}}{\partial v_2^2} - \frac{1}{(1-\omega)} \frac{\partial(U_2 y_{H_2,2})}{\partial v_2} - \frac{y_{H_2,2}}{C_T} \frac{\partial C_T}{\partial \tau} \quad (3.13)$$

$$\frac{\partial U_2}{\partial v_2} = -\frac{(1-\omega)}{C_T} \left( \frac{\partial C_T}{\partial \tau} - \sum \zeta_{mi} \frac{\partial Q_i}{\partial \tau} \right) \quad (3.14)$$

$$(C_T + \zeta_{H,2}) \frac{\partial \bar{T}_2}{\partial \tau} = \frac{1}{\omega^2} \frac{1}{Pe_H} \frac{\partial^2 \bar{T}_2}{\partial v_2^2} - \frac{1}{\omega} C_T \frac{\partial}{\partial v_2} [U(\bar{T}_2 + 1)] + \sum F_{i,2} \zeta_H \frac{\partial Q_i}{\partial \tau} - N_w (\bar{T}_2 - \bar{T}_{w2}) \quad (3.15)$$

The boundary conditions are

$$v_1 = 0, \tau > 0 \quad -\frac{1}{Pe} \frac{\partial y_{A1}}{\partial v_1} = U_1|_{v_1=0} \omega (y_{Af} - y_{A1}) \quad (3.16a)$$

$$v_1 = 0, \tau > 0 \quad -\frac{1}{Pe} \frac{\partial y_{B1}}{\partial v_1} = U_1|_{v_1=0} \omega (y_{Bf} - y_{B1}) \quad (3.16b)$$

$$v_1 = 0, \tau > 0 \quad -\frac{1}{Pe} \frac{\partial y_{C1}}{\partial v_1} = U_1|_{v_1=0} \omega (y_{Cf} - y_{C1}) \quad (3.16c)$$

$$v_1 = 0, \tau > 0 \quad -\frac{1}{Pe} \frac{\partial y_{D1}}{\partial v_1} = U_1|_{v_1=0} \omega (y_{Df} - y_{D1}) \quad (3.16d)$$

$$v_1 = 0, \tau > 0 \quad -\frac{1}{Pe} \frac{\partial y_{H_2,1}}{\partial v_1} = U_1|_{v_1=0} \omega (y_{H_2,f} - y_{H_2,1}) \quad (3.16e)$$

$$v_1 = 0, \tau > 0 \quad -\frac{1}{Pe_H} \frac{\partial \bar{T}_1}{\partial v_1} = U_1|_{v_1=0} \omega C_T \bar{T}_1 \quad (3.16f)$$

$$v_1 = 1, (v_2 = 0), \tau > 0 \quad y_{A1} = y_{A2} \quad (3.16g)$$

$$v_1 = 1, (v_2 = 0), \tau > 0 \quad y_{B1} = y_{B2} \quad (3.16h)$$

$$v_1 = 1, (v_2 = 0), \tau > 0 \quad y_{C1} = y_{C2} \quad (3.16i)$$

$$v_1 = 1, (v_2 = 0), \tau > 0 \quad y_{D1} = y_{D2} \quad (3.16j)$$

$$v_1 = 1, (v_2 = 0), \tau > 0 \quad y_{H_2,1} = y_{H_2,2} \quad (3.16k)$$

$$v_1 = 1, (v_2 = 0), \tau > 0 \quad -(1-\omega) \frac{\partial y_{A1}}{\partial v_1} = -\omega \frac{\partial y_{A2}}{\partial v_2} \quad (3.16l)$$

$$v_1 = 1, (v_2 = 0), \tau > 0 \quad -(1-\omega) \frac{\partial y_{B1}}{\partial v_1} = -\omega \frac{\partial y_{B2}}{\partial v_2} \quad (3.16m)$$

$$v_1 = 1, (v_2 = 0), \tau > 0 \quad -(1-\omega) \frac{\partial y_{C1}}{\partial v_1} = -\omega \frac{\partial y_{C2}}{\partial v_2} \quad (3.16n)$$

$$v_1 = 1, (v_2 = 0), \tau > 0 \quad -(1-\omega) \frac{\partial y_{D1}}{\partial v_1} = -\omega \frac{\partial y_{D2}}{\partial v_2} \quad (3.16o)$$

$$v_1 = 1, (v_2 = 0), \tau > 0 \quad -(1-\omega) \frac{\partial y_{H_21}}{\partial v_1} = -\omega \frac{\partial y_{H_22}}{\partial v_2} \quad (3.16p)$$

$$v_1 = 1, (v_2 = 0), \tau > 0 \quad U_1 = U_2 \quad (3.16q)$$

$$v_1 = 1, (v_2 = 0), \tau > 0 \quad -(1-\omega) \frac{\partial \bar{T}_1}{\partial v_1} = -\omega \frac{\partial \bar{T}_2}{\partial v_2} \quad (3.16r)$$

$$v_1 = 1, (v_2 = 0), \tau > 0 \quad \bar{T}_1 = \bar{T}_2 \quad (3.16s)$$

$$v_2 = 1, \tau > 0 \quad \frac{\partial y_{A2}}{\partial v_2} = 0 \quad (3.16t)$$

$$v_2 = 1, \tau > 0 \quad \frac{\partial y_{B2}}{\partial v_2} = 0 \quad (3.16u)$$

$$v_2 = 1, \tau > 0 \quad \frac{\partial y_{C2}}{\partial v_2} = 0 \quad (3.16v)$$

$$v_2 = 1, \tau > 0 \quad \frac{\partial y_{D2}}{\partial v_2} = 0 \quad (3.16w)$$

$$v_2 = 1, \tau > 0 \quad \frac{\partial y_{H_22}}{\partial v_2} = 0 \quad (3.16x)$$

$$v_2 = 1, \tau > 0 \quad U_2 = 0 \quad (3.16y)$$

$$v_2 = 1, \tau > 0 \quad \frac{\partial \bar{T}}{\partial v_2} = 0 \quad (3.16z)$$

## Step 2 (Reaction/Adsorption)

$$\frac{\partial y_{A1}}{\partial \tau} = \frac{1}{\omega^2} \frac{1}{Pe} \frac{\partial^2 y_{A1}}{\partial v_1^2} - \frac{1}{\omega} \frac{\partial(U_1 y_{A1})}{\partial v_1} - \frac{y_{A1}}{C_T} \frac{\partial C_T}{\partial \tau} - \frac{Da_{11}}{\omega} \left[ y_{A1} - \frac{y_{C1}}{K_{C1}} \right] - \zeta_{mA1} \frac{\partial Q_{A1}}{\partial \tau} \quad (3.17)$$

$$\frac{\partial y_{B1}}{\partial \tau} = \frac{1}{\omega^2} \frac{1}{Pe} \frac{\partial^2 y_{B1}}{\partial v_1^2} - \frac{1}{\omega} \frac{\partial(U_1 y_{B1})}{\partial v_1} - \frac{y_{B1}}{C_T} \frac{\partial C_T}{\partial \tau} - \frac{Da_{12}}{\omega} \left[ y_{B1} - \frac{y_{D1}}{K_{C2}} \right] - \zeta_{mB1} \frac{\partial Q_{B1}}{\partial \tau} \quad (3.18)$$

$$\frac{\partial y_{C1}}{\partial \tau} = \frac{1}{\omega^2} \frac{1}{Pe} \frac{\partial^2 y_{C1}}{\partial v_1^2} - \frac{1}{\omega} \frac{\partial(U_1 y_{C1})}{\partial v_1} - \frac{y_{C1}}{C_T} \frac{\partial C_T}{\partial \tau} + \frac{Da_{11}}{\omega} \left[ y_{A1} - \frac{y_{C1}}{K_{C1}} \right] - \zeta_{mC1} \frac{\partial Q_{C1}}{\partial \tau} \quad (3.19)$$

$$\frac{\partial y_{D1}}{\partial \tau} = \frac{1}{\omega^2} \frac{1}{Pe} \frac{\partial^2 y_{D1}}{\partial v_1^2} - \frac{1}{\omega} \frac{\partial(U_1 y_{D1})}{\partial v_1} - \frac{y_{D1}}{C_T} \frac{\partial C_T}{\partial \tau} + \frac{Da_{t2}}{\omega} \left[ y_{B1} - \frac{y_{D1}}{K_{C2}} \right] - \zeta_{mD1} \frac{\partial Q_{D1}}{\partial \tau} \quad (3.20)$$

$$\frac{\partial y_{H21}}{\partial \tau} = \frac{1}{\omega^2} \frac{1}{Pe} \frac{\partial^2 y_{H21}}{\partial v_1^2} - \frac{1}{\omega} \frac{\partial(U_1 y_{H21})}{\partial v_1} - \frac{y_{H21}}{C_T} \frac{\partial C_T}{\partial \tau} \quad (3.21)$$

$$\frac{\partial U_1}{\partial v_1} = - \frac{\omega}{C_T} \frac{\partial C_T}{\partial \tau} \quad (3.22)$$

$$(C_T + \zeta_{H,1}) \frac{\partial \bar{T}_1}{\partial \tau} = \frac{1}{\omega^2} \frac{1}{Pe_H} \frac{\partial^2 \bar{T}_1}{\partial v_1^2} - \frac{C_T}{\omega} \frac{\partial}{\partial v_1} [U(\bar{T}_1 + 1)] + \sum F_{i,1} \zeta_H \frac{\partial Q_i}{\partial \tau} + \sum E_i(-r_{Ai}) - N_w(\bar{T}_1 - \bar{T}_{w1}) \quad (3.23)$$

$$\frac{\partial y_{A2}}{\partial \tau} = \frac{1}{(1-\omega)^2} \frac{1}{Pe} \frac{\partial^2 y_{A2}}{\partial v_2^2} - \frac{1}{(1-\omega)} \frac{\partial(U_2 y_{A2})}{\partial v_2} - \frac{y_{A2}}{C_T} \frac{\partial C_T}{\partial \tau} - \zeta_{mA2} \frac{\partial Q_{A2}}{\partial \tau} \quad (3.24)$$

$$\frac{\partial y_{B2}}{\partial \tau} = \frac{1}{(1-\omega)^2} \frac{1}{Pe} \frac{\partial^2 y_{B2}}{\partial v_2^2} - \frac{1}{(1-\omega)} \frac{\partial(U_2 y_{B2})}{\partial v_2} - \frac{y_{B2}}{C_T} \frac{\partial C_T}{\partial \tau} - \zeta_{mB2} \frac{\partial Q_{B2}}{\partial \tau} \quad (3.25)$$

$$\frac{\partial y_{C2}}{\partial \tau} = \frac{1}{(1-\omega)^2} \frac{1}{Pe} \frac{\partial^2 y_{C2}}{\partial v_2^2} - \frac{1}{(1-\omega)} \frac{\partial(U_2 y_{C2})}{\partial v_2} - \frac{y_{C2}}{C_T} \frac{\partial C_T}{\partial \tau} \quad (3.26)$$

$$\frac{\partial y_{D2}}{\partial \tau} = \frac{1}{(1-\omega)^2} \frac{1}{Pe} \frac{\partial^2 y_{D2}}{\partial v_2^2} - \frac{1}{(1-\omega)} \frac{\partial(U_2 y_{D2})}{\partial v_2} - \frac{y_{D2}}{C_T} \frac{\partial C_T}{\partial \tau} \quad (3.27)$$

$$\frac{\partial y_{H22}}{\partial \tau} = \frac{1}{(1-\omega)^2} \frac{1}{Pe} \frac{\partial^2 y_{H22}}{\partial v_2^2} - \frac{1}{(1-\omega)} \frac{\partial(U_2 y_{H22})}{\partial v_2} - \frac{y_{H22}}{C_T} \frac{\partial C_T}{\partial \tau} \quad (3.28)$$

$$\frac{\partial U_2}{\partial v_2} = - \frac{(1-\omega)}{C_T} \left( \frac{\partial C_T}{\partial \tau} - \sum \zeta_{mi} \frac{\partial Q_i}{\partial \tau} \right) \quad (3.29)$$

$$(C_T + \zeta_{H,2}) \frac{\partial \bar{T}_2}{\partial \tau} = \frac{1}{\omega^2} \frac{1}{Pe_H} \frac{\partial^2 \bar{T}_2}{\partial v_2^2} - \frac{1}{\omega} C_T \frac{\partial}{\partial v_2} [U(\bar{T}_2 + 1)] + \sum F_{i,2} \zeta_H \frac{\partial Q_i}{\partial \tau} - N_w(\bar{T}_2 - \bar{T}_{w2}) \quad (3.30)$$

The boundary conditions are

$$v_1 = 0, \tau > 0 \quad - \frac{1}{Pe} \frac{\partial y_{A1}}{\partial v_1} = U_1 \Big|_{v_1=0} \omega (y_{Af} - y_{A1}) \quad (3.31a)$$

$$v_1 = 0, \tau > 0 \quad - \frac{1}{Pe} \frac{\partial y_{B1}}{\partial v_1} = U_1 \Big|_{v_1=0} \omega (y_{Bf} - y_{B1}) \quad (3.31b)$$

$$v_1 = 0, \tau > 0 \quad - \frac{1}{Pe} \frac{\partial y_{C1}}{\partial v_1} = U_1 \Big|_{v_1=0} \omega (y_{Cf} - y_{C1}) \quad (3.31c)$$

$$v_1 = 0, \tau > 0 \quad - \frac{1}{Pe} \frac{\partial y_{D1}}{\partial v_1} = U_1 \Big|_{v_1=0} \omega (y_{Df} - y_{D1}) \quad (3.31d)$$

$$v_1 = 0, \tau > 0 \quad - \frac{1}{Pe} \frac{\partial y_{H21}}{\partial v_1} = U_1 \Big|_{v_1=0} \omega (y_{H2f} - y_{H21}) \quad (3.31e)$$

$$\begin{aligned}
v_1 = 0, \tau > 0 & \quad -\frac{1}{Pe_H} \frac{\partial \bar{T}_1}{\partial v_1} = U_1 \Big|_{v_1=0} \omega C_T \bar{T}_1 & (3.31f) \\
v_2 = 1, \tau > 0 & \quad U_1 = 1 & (3.31g) \\
v_1 = 1, (v_2 = 0), \tau > 0 & \quad y_{A1} = y_{A2} & (3.31h) \\
v_1 = 1, (v_2 = 0), \tau > 0 & \quad y_{B1} = y_{B2} & (3.31i) \\
v_1 = 1, (v_2 = 0), \tau > 0 & \quad y_{C1} = y_{C2} & (3.31j) \\
v_1 = 1, (v_2 = 0), \tau > 0 & \quad y_{D1} = y_{D2} & (3.31k) \\
v_1 = 1, (v_2 = 0), \tau > 0 & \quad y_{H_2 1} = y_{H_2 2} & (3.31l) \\
v_1 = 1, (v_2 = 0), \tau > 0 & \quad -(1-\omega) \frac{\partial y_{A1}}{\partial v_1} = -\omega \frac{\partial y_{A2}}{\partial v_2} & (3.31m) \\
v_1 = 1, (v_2 = 0), \tau > 0 & \quad -(1-\omega) \frac{\partial y_{B1}}{\partial v_1} = -\omega \frac{\partial y_{B2}}{\partial v_2} & (3.31n) \\
v_1 = 1, (v_2 = 0), \tau > 0 & \quad -(1-\omega) \frac{\partial y_{C1}}{\partial v_1} = -\omega \frac{\partial y_{C2}}{\partial v_2} & (3.31o) \\
v_1 = 1, (v_2 = 0), \tau > 0 & \quad -(1-\omega) \frac{\partial y_{D1}}{\partial v_1} = -\omega \frac{\partial y_{D2}}{\partial v_2} & (3.31p) \\
v_1 = 1, (v_2 = 0), \tau > 0 & \quad -(1-\omega) \frac{\partial y_{H_2 1}}{\partial v_1} = -\omega \frac{\partial y_{H_2 2}}{\partial v_2} & (3.31q) \\
v_1 = 1, (v_2 = 0), \tau > 0 & \quad U_1 = U_2 & (3.31r) \\
v_1 = 1, (v_2 = 0), \tau > 0 & \quad -(1-\omega) \frac{\partial \bar{T}_1}{\partial v_1} = -\omega \frac{\partial \bar{T}_2}{\partial v_2} & (3.31s) \\
v_1 = 1, (v_2 = 0), \tau > 0 & \quad \bar{T}_1 = \bar{T}_2 & (3.31t) \\
v_2 = 1, \tau > 0 & \quad \frac{\partial y_{A2}}{\partial v_2} = 0 & (3.31u) \\
v_2 = 1, \tau > 0 & \quad \frac{\partial y_{B2}}{\partial v_2} = 0 & (3.31v) \\
v_2 = 1, \tau > 0 & \quad \frac{\partial y_{C2}}{\partial v_2} = 0 & (3.31w) \\
v_2 = 1, \tau > 0 & \quad \frac{\partial y_{D2}}{\partial v_2} = 0 & (3.31x) \\
v_2 = 1, \tau > 0 & \quad \frac{\partial y_{H_2 2}}{\partial v_2} = 0 & (3.31y) \\
v_2 = 1, \tau > 0 & \quad \frac{\partial \bar{T}_2}{\partial v_2} = 0 & (3.31z)
\end{aligned}$$

### Step 3 (Blowdown/ Reaction)

$$\frac{\partial y_{A1}}{\partial \tau} = \frac{1}{\omega^2} \frac{1}{Pe} \frac{\partial^2 y_{A1}}{\partial v_1^2} - \frac{1}{\omega} \frac{\partial(U_1 y_{A1})}{\partial v_1} - \frac{y_{A1}}{C_T} \frac{\partial C_T}{\partial \tau} - \frac{Da_{t1}}{\omega} \left[ y_{A1} - \frac{y_{C1}}{K_{C1}} \right] - \zeta_{mA1} \frac{\partial Q_{A1}}{\partial \tau} \quad (3.32)$$

$$\frac{\partial y_{B1}}{\partial \tau} = \frac{1}{\omega^2} \frac{1}{Pe} \frac{\partial^2 y_{B1}}{\partial v_1^2} - \frac{1}{\omega} \frac{\partial(U_1 y_{B1})}{\partial v_1} - \frac{y_{B1}}{C_T} \frac{\partial C_T}{\partial \tau} - \frac{Da_{t2}}{\omega} \left[ y_{B1} - \frac{y_{D1}}{K_{C2}} \right] - \zeta_{mB1} \frac{\partial Q_{B1}}{\partial \tau} \quad (3.33)$$

$$\frac{\partial y_{C1}}{\partial \tau} = \frac{1}{\omega^2} \frac{1}{Pe} \frac{\partial^2 y_{C1}}{\partial v_1^2} - \frac{1}{\omega} \frac{\partial(U_1 y_{C1})}{\partial v_1} - \frac{y_{C1}}{C_T} \frac{\partial C_T}{\partial \tau} + \frac{Da_{t1}}{\omega} \left[ y_{A1} - \frac{y_{C1}}{K_{C1}} \right] - \zeta_{mC1} \frac{\partial Q_{C1}}{\partial \tau} \quad (3.34)$$

$$\frac{\partial y_{D1}}{\partial \tau} = \frac{1}{\omega^2} \frac{1}{Pe} \frac{\partial^2 y_{D1}}{\partial v_1^2} - \frac{1}{\omega} \frac{\partial(U_1 y_{D1})}{\partial v_1} - \frac{y_{D1}}{C_T} \frac{\partial C_T}{\partial \tau} + \frac{Da_{t2}}{\omega} \left[ y_{B1} - \frac{y_{D1}}{K_{C2}} \right] - \zeta_{mD1} \frac{\partial Q_{D1}}{\partial \tau} \quad (3.35)$$

$$\frac{\partial y_{H_21}}{\partial \tau} = \frac{1}{\omega^2} \frac{1}{Pe} \frac{\partial^2 y_{H_21}}{\partial v_1^2} - \frac{1}{\omega} \frac{\partial(U_1 y_{H_21})}{\partial v_1} - \frac{y_{H_21}}{C_T} \frac{\partial C_T}{\partial \tau} \quad (3.36)$$

$$\frac{\partial U_1}{\partial v_1} = -\frac{\omega}{C_T} \frac{\partial C_T}{\partial \tau} \quad (3.37)$$

$$(C_T + \zeta_{H,1}) \frac{\partial \bar{T}_1}{\partial \tau} = \frac{1}{\omega^2} \frac{1}{Pe_H} \frac{\partial^2 \bar{T}_1}{\partial v_1^2} - \frac{C_T}{\omega} \frac{\partial}{\partial v_1} [U(\bar{T}_1 + 1)] + \sum F_{i,1} \zeta_H \frac{\partial Q_i}{\partial \tau} + \sum E_i (-r_{Ai}) - N_W (\bar{T}_1 - \bar{T}_{w1}) \quad (3.38)$$

$$\frac{\partial y_{A2}}{\partial \tau} = \frac{1}{(1-\omega)^2} \frac{1}{Pe} \frac{\partial^2 y_{A2}}{\partial v_2^2} - \frac{1}{(1-\omega)} \frac{\partial(U_2 y_{A2})}{\partial v_2} - \frac{y_{A2}}{C_T} \frac{\partial C_T}{\partial \tau} - \zeta_{mA2} \frac{\partial Q_{A2}}{\partial \tau} \quad (3.39)$$

$$\frac{\partial y_{B2}}{\partial \tau} = \frac{1}{(1-\omega)^2} \frac{1}{Pe} \frac{\partial^2 y_{B2}}{\partial v_2^2} - \frac{1}{(1-\omega)} \frac{\partial(U_2 y_{B2})}{\partial v_2} - \frac{y_{B2}}{C_T} \frac{\partial C_T}{\partial \tau} - \zeta_{mB2} \frac{\partial Q_{B2}}{\partial \tau} \quad (3.40)$$

$$\frac{\partial y_{C2}}{\partial \tau} = \frac{1}{(1-\omega)^2} \frac{1}{Pe} \frac{\partial^2 y_{C2}}{\partial v_2^2} - \frac{1}{(1-\omega)} \frac{\partial(U_2 y_{C2})}{\partial v_2} - \frac{y_{C2}}{C_T} \frac{\partial C_T}{\partial \tau} \quad (3.41)$$

$$\frac{\partial y_{D2}}{\partial \tau} = \frac{1}{(1-\omega)^2} \frac{1}{Pe} \frac{\partial^2 y_{D2}}{\partial v_2^2} - \frac{1}{(1-\omega)} \frac{\partial(U_2 y_{D2})}{\partial v_2} - \frac{y_{D2}}{C_T} \frac{\partial C_T}{\partial \tau} \quad (3.42)$$

$$\frac{\partial y_{H_22}}{\partial \tau} = \frac{1}{(1-\omega)^2} \frac{1}{Pe} \frac{\partial^2 y_{H_22}}{\partial v_2^2} - \frac{1}{(1-\omega)} \frac{\partial(U_2 y_{H_22})}{\partial v_2} - \frac{y_{H_22}}{C_T} \frac{\partial C_T}{\partial \tau} \quad (3.43)$$

$$\frac{\partial U_2}{\partial v_2} = -\frac{(1-\omega)}{C_T} \left( \frac{\partial C_T}{\partial \tau} - \sum \zeta_{mi} \frac{\partial Q_i}{\partial \tau} \right) \quad (3.44)$$

$$(C_T + \zeta_{H,2}) \frac{\partial \bar{T}_2}{\partial \tau} = \frac{1}{\omega^2} \frac{1}{Pe_H} \frac{\partial^2 \bar{T}_2}{\partial v_2^2} - \frac{1}{\omega} C_T \frac{\partial}{\partial v_2} [U(\bar{T}_2 + 1)] + \sum F_{i,2} \zeta_H \frac{\partial Q_i}{\partial \tau} - N_W (\bar{T}_2 - \bar{T}_{w2}) \quad (3.45)$$

The boundary conditions are

$$v_1 = 0, \tau > 0 \quad \frac{\partial y_{A1}}{\partial v_1} = 0 \quad (3.46a)$$

$$v_1 = 0, \tau > 0 \quad \frac{\partial y_{B1}}{\partial v_1} = 0 \quad (3.46b)$$

$$v_1 = 0, \tau > 0 \quad \frac{\partial y_{C1}}{\partial v_1} = 0 \quad (3.46c)$$

$$v_1 = 0, \tau > 0 \quad \frac{\partial y_{D1}}{\partial v_1} = 0 \quad (3.46d)$$

$$v_1 = 0, \tau > 0 \quad \frac{\partial y_{H_21}}{\partial v_1} = 0 \quad (3.46e)$$

$$v_1 = 0, \tau > 0 \quad \frac{\partial \bar{T}_1}{\partial v_1} = 0 \quad (3.46f)$$

$$v_1 = 0, \tau > 0 \quad U_1 = 0 \quad (3.46g)$$

$$v_1 = 1, (v_2 = 0), \tau > 0 \quad y_{A1} = y_{A2} \quad (3.46h)$$

$$v_1 = 1, (v_2 = 0), \tau > 0 \quad y_{B1} = y_{B2} \quad (3.46i)$$

$$v_1 = 1, (v_2 = 0), \tau > 0 \quad y_{C1} = y_{C2} \quad (3.46j)$$

$$v_1 = 1, (v_2 = 0), \tau > 0 \quad y_{D1} = y_{D2} \quad (3.46k)$$

$$v_1 = 1, (v_2 = 0), \tau > 0 \quad y_{H_21} = y_{H_22} \quad (3.46l)$$

$$v_1 = 1, (v_2 = 0), \tau > 0 \quad -(1-\omega) \frac{\partial y_{A1}}{\partial v_1} = -\omega \frac{\partial y_{A2}}{\partial v_2} \quad (3.46m)$$

$$v_1 = 1, (v_2 = 0), \tau > 0 \quad -(1-\omega) \frac{\partial y_{B1}}{\partial v_1} = -\omega \frac{\partial y_{B2}}{\partial v_2} \quad (3.46n)$$

$$v_1 = 1, (v_2 = 0), \tau > 0 \quad -(1-\omega) \frac{\partial y_{C1}}{\partial v_1} = -\omega \frac{\partial y_{C2}}{\partial v_2} \quad (3.46o)$$

$$v_1 = 1, (v_2 = 0), \tau > 0 \quad -(1-\omega) \frac{\partial y_{D1}}{\partial v_1} = -\omega \frac{\partial y_{D2}}{\partial v_2} \quad (3.46p)$$

$$v_1 = 1, (v_2 = 0), \tau > 0 \quad -(1-\omega) \frac{\partial y_{H_21}}{\partial v_1} = -\omega \frac{\partial y_{H_22}}{\partial v_2} \quad (3.46q)$$

$$v_1 = 1, (v_2 = 0), \tau > 0 \quad U_1 = U_2 \quad (3.46r)$$

$$v_1 = 1, (v_2 = 0), \tau > 0 \quad -(1-\omega) \frac{\partial \bar{T}_1}{\partial v_1} = -\omega \frac{\partial \bar{T}_2}{\partial v_2} \quad (3.46s)$$

$$v_1 = 1, (v_2 = 0), \tau > 0 \quad \bar{T}_1 = \bar{T}_2 \quad (3.46t)$$

$$v_2 = 1, \tau > 0 \quad \frac{\partial y_{A2}}{\partial v_2} = 0 \quad (3.46u)$$

$$v_2 = 1, \tau > 0 \quad \frac{\partial y_{B2}}{\partial v_2} = 0 \quad (3.46v)$$

$$v_2 = 1, \tau > 0 \quad \frac{\partial y_{C2}}{\partial v_2} = 0 \quad (3.46w)$$

$$v_2 = 1, \tau > 0 \quad \frac{\partial y_{D2}}{\partial v_2} = 0 \quad (3.46x)$$

$$v_2 = 1, \tau > 0 \quad \frac{\partial y_{H22}}{\partial v_2} = 0 \quad (3.46y)$$

$$v_2 = 1, \tau > 0 \quad \frac{\partial \bar{T}}{\partial v_2} = 0 \quad (3.46z)$$

Step 4 (Desorption/ Reaction)

$$\frac{\partial y_{A1}}{\partial \tau} = \frac{1}{\omega^2} \frac{1}{Pe} \frac{\partial^2 y_{A1}}{\partial v_1^2} - \frac{1}{\omega} \frac{\partial(U_1 y_{A1})}{\partial v_1} - \frac{y_{A1}}{C_T} \frac{\partial C_T}{\partial \tau} - \frac{Da_{t1}}{\omega} \left[ y_{A1} - \frac{y_{C1}}{K_{C1}} \right] - \zeta_{mA1} \frac{\partial Q_{A1}}{\partial \tau} \quad (3.47)$$

$$\frac{\partial y_{B1}}{\partial \tau} = \frac{1}{\omega^2} \frac{1}{Pe} \frac{\partial^2 y_{B1}}{\partial v_1^2} - \frac{1}{\omega} \frac{\partial(U_1 y_{B1})}{\partial v_1} - \frac{y_{B1}}{C_T} \frac{\partial C_T}{\partial \tau} - \frac{Da_{t2}}{\omega} \left[ y_{B1} - \frac{y_{D1}}{K_{C2}} \right] - \zeta_{mB1} \frac{\partial Q_{B1}}{\partial \tau} \quad (3.48)$$

$$\frac{\partial y_{C1}}{\partial \tau} = \frac{1}{\omega^2} \frac{1}{Pe} \frac{\partial^2 y_{C1}}{\partial v_1^2} - \frac{1}{\omega} \frac{\partial(U_1 y_{C1})}{\partial v_1} - \frac{y_{C1}}{C_T} \frac{\partial C_T}{\partial \tau} + \frac{Da_{t1}}{\omega} \left[ y_{A1} - \frac{y_{C1}}{K_{C1}} \right] - \zeta_{mC1} \frac{\partial Q_{C1}}{\partial \tau} \quad (3.49)$$

$$\frac{\partial y_{D1}}{\partial \tau} = \frac{1}{\omega^2} \frac{1}{Pe} \frac{\partial^2 y_{D1}}{\partial v_1^2} - \frac{1}{\omega} \frac{\partial(U_1 y_{D1})}{\partial v_1} - \frac{y_{D1}}{C_T} \frac{\partial C_T}{\partial \tau} + \frac{Da_{t2}}{\omega} \left[ y_{B1} - \frac{y_{D1}}{K_{C2}} \right] - \zeta_{mD1} \frac{\partial Q_{D1}}{\partial \tau} \quad (3.50)$$

$$\frac{\partial y_{H21}}{\partial \tau} = \frac{1}{\omega^2} \frac{1}{Pe} \frac{\partial^2 y_{H21}}{\partial v_1^2} - \frac{1}{\omega} \frac{\partial(U_1 y_{H21})}{\partial v_1} - \frac{y_{H21}}{C_T} \frac{\partial C_T}{\partial \tau} \quad (3.51)$$

$$\frac{\partial U_1}{\partial v_1} = -\frac{\omega}{C_T} \frac{\partial C_T}{\partial \tau} \quad (3.52)$$

$$(C_T + \zeta_{H,1}) \frac{\partial \bar{T}_1}{\partial \tau} = \frac{1}{\omega^2} \frac{1}{Pe_H} \frac{\partial^2 \bar{T}_1}{\partial v_1^2} - \frac{C_T}{\omega} \frac{\partial}{\partial v_1} [U(\bar{T}_1 + 1)] + \sum F_{i,1} \zeta_H \frac{\partial Q_i}{\partial \tau} + \sum E_i (-r_{Ai}) - N_w (\bar{T}_1 - \bar{T}_{w1}) \quad (3.53)$$

$$\frac{\partial y_{A2}}{\partial \tau} = \frac{1}{(1-\omega)^2} \frac{1}{Pe} \frac{\partial^2 y_{A2}}{\partial v_2^2} - \frac{1}{(1-\omega)} \frac{\partial(U_2 y_{A2})}{\partial v_2} - \frac{y_{A2}}{C_T} \frac{\partial C_T}{\partial \tau} - \zeta_{mA2} \frac{\partial Q_{A2}}{\partial \tau} \quad (3.54)$$

$$\frac{\partial y_{B2}}{\partial \tau} = \frac{1}{(1-\omega)^2} \frac{1}{Pe} \frac{\partial^2 y_{B2}}{\partial v_2^2} - \frac{1}{(1-\omega)} \frac{\partial(U_2 y_{B2})}{\partial v_2} - \frac{y_{B2}}{C_T} \frac{\partial C_T}{\partial \tau} - \zeta_{mB2} \frac{\partial Q_{B2}}{\partial \tau} \quad (3.55)$$

$$\frac{\partial y_{C2}}{\partial \tau} = \frac{1}{(1-\omega)^2} \frac{1}{Pe} \frac{\partial^2 y_{C2}}{\partial v_2^2} - \frac{1}{(1-\omega)} \frac{\partial(U_2 y_{C2})}{\partial v_2} - \frac{y_{C2}}{C_T} \frac{\partial C_T}{\partial \tau} \quad (3.56)$$



$$\frac{\partial y_{D2}}{\partial \tau} = \frac{1}{(1-\omega)^2} \frac{1}{Pe} \frac{\partial^2 y_{D2}}{\partial v_2^2} - \frac{1}{(1-\omega)} \frac{\partial(U_2 y_{D2})}{\partial v_2} - \frac{y_{D2}}{C_T} \frac{\partial C_T}{\partial \tau} \quad (3.57)$$

$$\frac{\partial y_{H22}}{\partial \tau} = \frac{1}{(1-\omega)^2} \frac{1}{Pe} \frac{\partial^2 y_{H22}}{\partial v_2^2} - \frac{1}{(1-\omega)} \frac{\partial(U_2 y_{H22})}{\partial v_2} - \frac{y_{H22}}{C_T} \frac{\partial C_T}{\partial \tau} \quad (3.58)$$

$$\frac{\partial U_2}{\partial v_2} = -\frac{(1-\omega)}{C_T} \left( \frac{\partial C_T}{\partial \tau} - \sum \zeta_{mi} \frac{\partial Q_i}{\partial \tau} \right) \quad (3.59)$$

$$(C_T + \zeta_{H,2}) \frac{\partial \bar{T}_2}{\partial \tau} = \frac{1}{\omega^2} \frac{1}{Pe_H} \frac{\partial^2 \bar{T}_2}{\partial v_2^2} - \frac{1}{\omega} C_T \frac{\partial}{\partial v_2} [U(\bar{T}_2 + 1)] + \sum F_{i,2} \zeta_H \frac{\partial Q_i}{\partial \tau} - N_w (\bar{T}_2 - \bar{T}_{w2}) \quad (3.60)$$

The boundary conditions are

$$v_1 = 0, \tau > 0 \quad -\frac{1}{Pe} \frac{\partial y_{A1}}{\partial v_1} = U_1|_{v_1=0} \omega (y_{Af} - y_{A1}) \quad (3.31a)$$

$$v_1 = 0, \tau > 0 \quad -\frac{1}{Pe} \frac{\partial y_{B1}}{\partial v_1} = U_1|_{v_1=0} \omega (y_{Bf} - y_{B1}) \quad (3.31b)$$

$$v_1 = 0, \tau > 0 \quad -\frac{1}{Pe} \frac{\partial y_{C1}}{\partial v_1} = U_1|_{v_1=0} \omega (y_{Cf} - y_{C1}) \quad (3.31c)$$

$$v_1 = 0, \tau > 0 \quad -\frac{1}{Pe} \frac{\partial y_{D1}}{\partial v_1} = U_1|_{v_1=0} \omega (y_{Df} - y_{D1}) \quad (3.31d)$$

$$v_1 = 0, \tau > 0 \quad -\frac{1}{Pe} \frac{\partial y_{H21}}{\partial v_1} = U_1|_{v_1=0} \omega (y_{H2f} - y_{H21}) \quad (3.31e)$$

$$v_1 = 0, \tau > 0 \quad -\frac{1}{Pe_H} \frac{\partial \bar{T}_1}{\partial v_1} = U_1|_{v_1=0} \omega C_T \bar{T}_1 \quad (3.31f)$$

$$v_1 = 0, \tau > 0 \quad U_1 = S \frac{u_p}{u_f} \quad (3.31g)$$

$$v_1 = 0, \tau > 0 \quad \frac{\partial y_{A1}}{\partial v_1} = 0 \quad (3.61a)$$

$$v_1 = 0, \tau > 0 \quad \frac{\partial y_{B1}}{\partial v_1} = 0 \quad (3.61b)$$

$$v_1 = 0, \tau > 0 \quad \frac{\partial y_{C1}}{\partial v_1} = 0 \quad (3.61c)$$

$$v_1 = 0, \tau > 0 \quad \frac{\partial y_{D1}}{\partial v_1} = 0 \quad (3.61d)$$

$$v_1 = 0, \tau > 0 \quad \frac{\partial y_{H21}}{\partial v_1} = 0 \quad (3.61e)$$

$$v_1 = 0, \tau > 0 \quad \frac{\partial \bar{T}_1}{\partial v_1} = 0 \quad (3.61f)$$

$$v_1 = 1, (v_2 = 0), \tau > 0 \quad y_{A1} = y_{A2} \quad (3.61g)$$

$$v_1 = 1, (v_2 = 0), \tau > 0 \quad y_{B1} = y_{B2} \quad (3.61h)$$

$$v_1 = 1, (v_2 = 0), \tau > 0 \quad y_{C1} = y_{C2} \quad (3.61i)$$

$$v_1 = 1, (v_2 = 0), \tau > 0 \quad y_{D1} = y_{D2} \quad (3.61j)$$

$$v_1 = 1, (v_2 = 0), \tau > 0 \quad y_{H_2 1} = y_{H_2 2} \quad (3.61k)$$

$$v_1 = 1, (v_2 = 0), \tau > 0 \quad -(1-\omega) \frac{\partial y_{A1}}{\partial v_1} = -\omega \frac{\partial y_{A2}}{\partial v_2} \quad (3.61l)$$

$$v_1 = 1, (v_2 = 0), \tau > 0 \quad -(1-\omega) \frac{\partial y_{B1}}{\partial v_1} = -\omega \frac{\partial y_{B2}}{\partial v_2} \quad (3.61m)$$

$$v_1 = 1, (v_2 = 0), \tau > 0 \quad -(1-\omega) \frac{\partial y_{C1}}{\partial v_1} = -\omega \frac{\partial y_{C2}}{\partial v_2} \quad (3.61n)$$

$$v_1 = 1, (v_2 = 0), \tau > 0 \quad -(1-\omega) \frac{\partial y_{D1}}{\partial v_1} = -\omega \frac{\partial y_{D2}}{\partial v_2} \quad (3.61o)$$

$$v_1 = 1, (v_2 = 0), \tau > 0 \quad -(1-\omega) \frac{\partial y_{H_2 1}}{\partial v_1} = -\omega \frac{\partial y_{H_2 2}}{\partial v_2} \quad (3.61p)$$

$$v_1 = 1, (v_2 = 0), \tau > 0 \quad -(1-\omega) D_A \frac{\partial y_{H_2 1}}{\partial v_1} = -\omega D_A \frac{\partial y_{H_2 2}}{\partial v_2} \quad (3.61q)$$

$$v_1 = 1, (v_2 = 0), \tau > 0 \quad U_1 = U_2 \quad (3.61r)$$

$$v_1 = 1, (v_2 = 0), \tau > 0 \quad -(1-\omega) \frac{\partial \bar{T}_1}{\partial v_1} = -\omega \frac{\partial \bar{T}_2}{\partial v_2} \quad (3.61s)$$

$$v_1 = 1, (v_2 = 0), \tau > 0 \quad \bar{T}_1 = \bar{T}_2 \quad (3.61t)$$

$$v_2 = 1, \tau > 0 \quad -\frac{1}{Pe} \frac{\partial y_{A2}}{\partial v_2} = U_2 \Big|_{v_2=1} \omega (y_{Ap} - y_{A2}) \quad (3.61u)$$

$$v_2 = 1, \tau > 0 \quad -\frac{1}{Pe} \frac{\partial y_{B2}}{\partial v_2} = U_2 \Big|_{v_2=1} \omega (y_{Bp} - y_{B2}) \quad (3.61v)$$

$$v_2 = 1, \tau > 0 \quad -\frac{1}{Pe} \frac{\partial y_{C2}}{\partial v_2} = U_2 \Big|_{v_2=1} \omega (y_{Cp} - y_{C2}) \quad (3.61w)$$

$$v_2 = 1, \tau > 0 \quad -\frac{1}{Pe} \frac{\partial y_{D2}}{\partial v_2} = U_2 \Big|_{v_2=1} \omega (y_{Dp} - y_{D2}) \quad (3.61x)$$

$$v_2 = 1, \tau > 0 \quad -\frac{1}{Pe} \frac{\partial y_{H_2 2}}{\partial v_2} = U_2 \Big|_{v_2=1} \omega (y_{H_2 p} - y_{H_2 2}) \quad (3.61y)$$

$$v_2 = 1, \tau > 0 \quad -\frac{1}{Pe_H} \frac{\partial \bar{T}_2}{\partial v_2} = U_2|_{v_2=1} \omega C_T (\bar{T}_2 - \bar{T}_p) \quad (3.61z)$$

$$v_2 = 1, \tau > 0 \quad U_2 = -(1-S) \frac{u_p}{u_f} \quad (3.61aa)$$

In all the four steps, the mass transfer rate and the adsorption equilibrium isotherm for reactor and adsorbent region are

$$\zeta_{mA1} \frac{\partial Q_{A1}}{\partial \tau} = N_{f1} C_T (y_{A1} - \langle y_{A1} \rangle) \quad (3.62)$$

$$\zeta_{mB1} \frac{\partial Q_{B1}}{\partial \tau} = N_{f1} C_T (y_{B1} - \langle y_{B1} \rangle) \quad (3.63)$$

$$\zeta_{mC1} \frac{\partial Q_{C1}}{\partial \tau} = N_{f1} C_T (y_{C1} - \langle y_{C1} \rangle) \quad (3.64)$$

$$\zeta_{mD1} \frac{\partial Q_{D1}}{\partial \tau} = N_{f1} C_T (y_{D1} - \langle y_{D1} \rangle) \quad (3.65)$$

$$\zeta_{mA2} \frac{\partial Q_{A2}}{\partial \tau} = N_{f2} C_T (y_{A2} - \langle y_{A2} \rangle) \quad (3.66)$$

$$\zeta_{mB2} \frac{\partial Q_{B2}}{\partial \tau} = N_{f2} C_T (y_{B2} - \langle y_{B2} \rangle) \quad (3.67)$$

$$\langle y_{A1} \rangle = \frac{1}{P \cdot K_{ads}} \frac{\theta_{Aref1} Q_{A1}}{(1 - \theta_{Aref1} Q_{A1} - \theta_{Bref1} Q_{B1} - \theta_{Cref1} Q_{C1} - \theta_{Dref1} Q_{D1})} \quad (3.68)$$

$$\langle y_{B1} \rangle = \frac{1}{P \cdot K_{ads}} \frac{\theta_{Bref,1} Q_{B1}}{(1 - \theta_{Aref1} Q_{A1} - \theta_{Bref1} Q_{B1} - \theta_{Cref1} Q_{C1} - \theta_{Dref1} Q_{D1})} \quad (3.69)$$

$$\langle y_{C1} \rangle = \frac{1}{P \cdot K_{ads}} \frac{\theta_{Cref1} Q_{C1}}{(1 - \theta_{Aref1} Q_{A1} - \theta_{Bref1} Q_{B1} - \theta_{Cref1} Q_{C1} - \theta_{Dref1} Q_{D1})} \quad (3.70)$$

$$\langle y_{D1} \rangle = \frac{1}{P \cdot K_{ads}} \frac{\theta_{Dref,1} Q_{D,1}}{(1 - \theta_{Aref1} Q_{A1} - \theta_{Bref1} Q_{B1} - \theta_{Cref1} Q_{C1} - \theta_{Dref1} Q_{D1})} \quad (3.71)$$

$$\langle y_{A2} \rangle = \frac{1}{P \cdot K_{ads}} \frac{\theta_{Aref2} Q_{A2}}{(1 - \theta_{Aref2} Q_{A2} - \theta_{Bref2} Q_{B2})^{n_A}} \quad (3.72)$$

$$\langle y_{B2} \rangle = \frac{1}{P \cdot K_{ads}} \frac{\theta_{ref2} Q_{B2}}{(1 - \theta_{ref2} Q_{A2} - \theta_{ref2} Q_{B2})^{n_B}} \quad (3.73)$$

$$N_{f1} = \frac{(1 - \varepsilon_1) a_{p1} k_{gl} L}{\varepsilon_1 u_f} \quad (3.74)$$

$$N_{f2} = \frac{(1 - \varepsilon_2) a_{p2} k_{gl} L}{\varepsilon_2 u_f} \quad (3.75)$$

$$\zeta_{mA1} = \frac{(1 - \varepsilon_1) \rho_{s1} q_{Aref1}}{\varepsilon_1 C_T} \quad (3.76)$$

$$\zeta_{mB1} = \frac{(1-\varepsilon_1)}{\varepsilon_1} \frac{\rho_{s1} q_{Bref1}}{C_T} \quad (3.77)$$

$$\zeta_{mC1} = \frac{(1-\varepsilon_1)}{\varepsilon_1} \frac{\rho_{s1} q_{Cref1}}{C_T} \quad (3.78)$$

$$\zeta_{mD1} = \frac{(1-\varepsilon_1)}{\varepsilon_1} \frac{\rho_{s1} q_{Dref1}}{C_T} \quad (3.79)$$

$$\zeta_{mA2} = \frac{(1-\varepsilon_2)}{\varepsilon_2} \frac{\rho_{s2} q_{Aref2}}{C_T} \quad (3.80)$$

$$\zeta_{mB2} = \frac{(1-\varepsilon_2)}{\varepsilon_2} \frac{\rho_{s2} q_{Bref2}}{C_T} \quad (3.81)$$

The initial conditions are

$$y_{A1}(v_1, \tau = 0) = 0 \quad (3.82a)$$

$$y_{B1}(v_1, \tau = 0) = 0 \quad (3.82b)$$

$$y_{C1}(v_1, \tau = 0) = 0 \quad (3.82c)$$

$$y_{D1}(v_1, \tau = 0) = 0 \quad (3.82d)$$

$$y_{H_{2,1}}(v_1, \tau = 0) = 1 \quad (3.82e)$$

$$y_{A2}(v_2, \tau = 0) = 0 \quad (3.82f)$$

$$y_{B2}(v_2, \tau = 0) = 0 \quad (3.82g)$$

$$y_{C2}(v_2, \tau = 0) = 0 \quad (3.82h)$$

$$y_{D2}(v_2, \tau = 0) = 0 \quad (3.82i)$$

$$y_{H_{2,2}}(v_2, \tau = 0) = 1 \quad (3.82j)$$

$$Q_{A,1}(v_1, \tau = 0) = 0 \quad (3.82k)$$

$$Q_{B,1}(v_1, \tau = 0) = 0 \quad (3.82l)$$

$$Q_{C,1}(v_1, \tau = 0) = 0 \quad (3.82m)$$

$$Q_{D,1}(v_1, \tau = 0) = 0 \quad (3.82n)$$

$$Q_{A,2}(v_2, \tau = 0) = 0 \quad (3.82o)$$

$$Q_{B,2}(v_2, \tau = 0) = 0 \quad (3.82p)$$

### 3.4 HANDLING RECYCLE STREAM

All recycled streams are recycled to adjacent units during the reaction/adsorption step. Exit streams from blowdown/reaction and desorption/reaction steps are blended with fresh feed before entering the adjacent unit undergoing reaction/adsorption step.

If the recycle stream is recycled during reaction/pressurization step, the adsorption region to be pressurized will pressurize in less time than that required to depressurize the adjacent unit undergoing blowdown/reaction step. This situation will cause a back flow when the vessel undergoing blowdown/reaction step not fully depressurized is opened for purge (desorption/reaction) step. This backflow phenomena is difficult to model. Thus, no recycle is made during reaction/pressurization step.

To avoid this situation, a third vessel is introduced to the system as a holding vessel. The third vessel contains neither catalyst nor adsorbent. The purpose of this vessel is to act as a container holding the effluent stream of the blowdown/reaction step and then re-injecting it back with the effluent of the subsequent desorption/reaction step to either the feed of the adjacent vessel undergoing reaction/adsorption step.

The process flow diagram for recycling the waste to feed is illustrated in Figure 3.4. In Figure 3.4a, the first vessel (V1) is pressurized with fresh feed only. The second vessel (V2) will blow its content to a third vessel (V3). The third vessel is an empty reservoir that serves as an intermediate holder of blowdown step effluent. This vessel contains neither catalyst nor adsorbent pellets.

In Figure 3.4b, V1 has started its adsorption step. During this step, feed to V1 is received from three sources: Fresh Feed from upstream units, desorption step effluent from V2 and the content reserved in V3 during previous step. Since V3 pressure is at the high side, a control valve is needed to bring down the pressure to the desorption-vessel pressure. A turbine to generate electricity may replace this control valve. The effluent of the control valve and V2 are then combined before entering the compressor C1. The compressor then compresses its feed to the high pressure. The

compressor in the Figure represents a multistage compressor with inter-stage cooling. Inter-stage cooling is used to assure bringing the compressor effluent to the fresh feed temperature. Interstage cooling may also be used to preheat the feed to the desired temperature. A recycle temperature that is higher than the feed temperature will result in loss of catalyst activity. Compressor effluent is then mixed with the feed prior to entering V1. The duration of the adsorption and desorption steps is greater than that of the pressurization and blowdown steps. Thus the content of V3 will be emptied at a fraction the adsorption step time. V3 is then closed for the rest of the adsorption step. A second control valve is added downstream of the compressor to control recycle flow. A hydrogen makeup stream is introduced with the recycle stream to ensure minimum feed hydrogen to hydrocarbon ratio of 7.5.

Figures 3.4c and 3.4d are similar to Figures 3.4a and 3.4b, respectively. The only difference in the latter figures is the swap in roles of V1 and V2.

The internal model equations for handling recycle to feed are identical to those introduced in the conventional PSAR unit. Recycle stream is blended with the feed prior to entering the vessel in adsorption step. Thus, no change is required to the internal model equations. It should be noted that for the first time interval, of the reaction/adsorption step, that is equivalent to reaction/pressurization step time, the blended feed is introduced at a higher rate than that of a conventional PSAR unit.

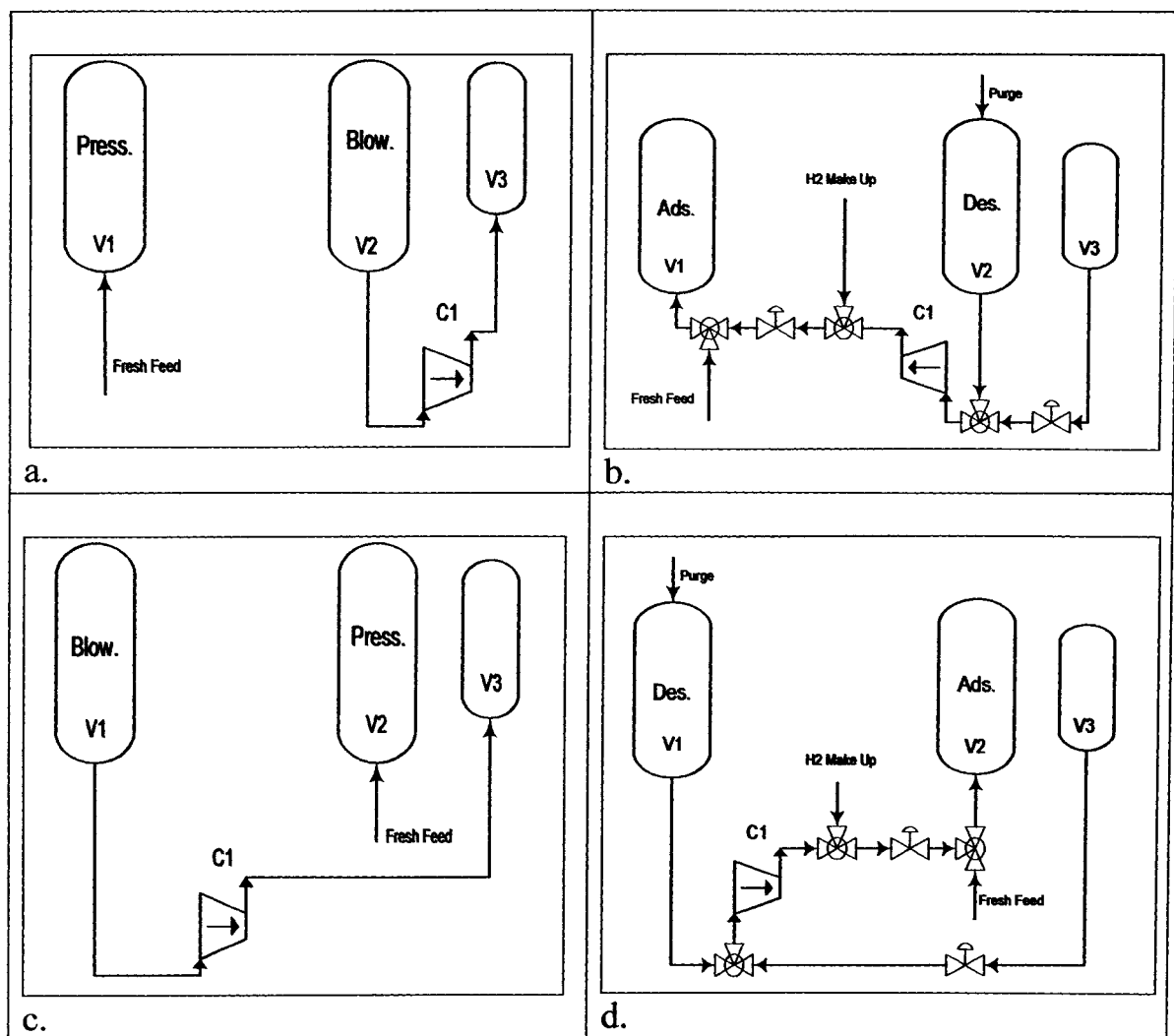


Figure 3.4: Connectivity diagram for handling recycle to feed in all four cyclic steps:

- a.) V1 in reaction/pressurization, V2 in blowdown/reaction.
- b.) V1 in reaction/adsorption, V2 in desorption/reaction.
- c.) V1 in blowdown/reaction, V2 in reaction/pressurization.
- d.) V1 in desorption/reaction, V2 in reaction/adsorption.

### 3.4 PARAMETERS ESTIMATIONS

Estimation methods for parameters used in Chapter II are also applicable in this chapter. In addition, the reaction equilibrium constants for n-butane and n-hexane isomerization were calculated from adsorption equilibrium curves provided by Barrer and Sutherland [8]. Also, adsorption parameters for n-C5, i-C5, n-C6 and i-C6 were obtained from the same source [8]. Reaction and adsorption parameters for the reactor section are listed in Table 3.1:

To obtain an optimum reactor length, the plug flow reactor equation (eq. 3.85) is integrated along the reactor length. A plot of conversion versus reactor length is established as illustrated in Figures 3.6a and 3.6b. In Figure 3.6a, the n-pentane conversion is plotted against reactor length. In Figure 3.6b, the n-hexane conversion is plotted against reactor length. Equilibrium conversion is calculated by taking the limit of  $X_A$  at  $L \rightarrow \infty$  (eq. 3.72). Equilibrium conversion for n-pentane ( $y_{eq.} = 0.0139$ ) is reached after 3 cm. For n-hexane, conversion reached 99.86 of its equilibrium value ( $y_{eq.} = 0.0155$ ) after 64 cm. This length is taken to be the optimum reactor length. Results obtained later verified that this length is adequate for n-hexane to reach equilibrium conversion; especially when bed temperature rise is taken into consideration.

$$\tau = \frac{L}{u_f} = C_{Ao} \int_0^{X_A} \frac{dX_A}{-r_A} = C_{Ao} \frac{K_C}{k_1} \int_0^{X_A} \frac{dX_A}{B - CX_A} \quad (3.85)$$

or

$$X_A = \frac{B}{C} \left[ 1 - e^{\left( -\frac{L}{A} \right)} \right]$$

$$\begin{aligned} \text{where: } A &= \frac{u_f}{k_1} \frac{K_C}{(1 + K_C)} \\ B &= K_C C_{Ao} - C_{Bo} \\ C &= C_{Ao} (1 + K_C) \end{aligned}$$

$$X_{A,eq.} = \lim_{L \rightarrow \infty} \frac{B}{C} \left[ 1 - e^{\left( -\frac{L}{A} \right)} \right] = \frac{B}{C} = \frac{K_C C_{Ao} - C_{Bo}}{C_{Ao} (1 + K_C)} \quad (3.86)$$



where:  $A$ ,  $B$  and  $C$  are described in equation 3.85.

For the adsorber, the longer the adsorption section, the more cycles it takes the adsorber before saturation of molecular sieves. A 16-cm length is chosen for the adsorption section.

### 3.5 NUMERICAL METHODS

The numerical technique used to solve the PSAR model is basically the same as that used for solving the PSA model discussed in chapter 2. Twenty collocation points are used for each sub domain. Since there are three boundaries (two at the inlet and the outlet, and one at the junction point), and the entire column length is divided into 44 distance intervals. The simulation program calculates the concentration in the gas and solid phases and the velocity and temperature at all distance intervals throughout integration time. The solution flow diagram for a step in the PSAR unit is as the same as that shown in Figure 2.2 for a PSA unit.

Lefevre et al's [43] concept, applied to find optimum values of alpha and beta in chapter two, is also applied to the PSAR model. Table 3.2 illustrates the reduction in time introduced by selecting optimum values of alpha and beta. Apparently, results are not promising. This is probably due to the fact of integrating a different set of differential equations for each section of vessel. A more accurate approach to this problem is to treat each section separately. This will result in two separate optimum values for alpha and beta for each section of the vessel. Rice and Do [60] discussed splitting the integration domain into two separate sections, each having its own set of space discretization

Table 3.1: Reaction & Adsorption Parameters for Reactor Section

**Reaction Parameters**

- n-Pentane

$$k_o = 9.4657 * 10^7 \text{ s}^{-1}$$

$$\Delta H_{\text{Reaction}} = -22.0 * 10^3 \text{ (cal/gmol)}$$

$$K_C = 3.310$$

- n-Hexane

$$k_o = 3.472 * 10^9 \text{ s}^{-1}$$

$$\Delta H_{\text{Reaction}} = -31.6 * 10^3 \text{ (cal/gmol)}$$

$$K_C = 2.865$$

**Adsorption Parameters**

- n- Pentane

$$n = 3$$

$$K_o = 6.46 * 10^{-10} \text{ bar}^{-1}$$

$$-\Delta H_{\text{Adsorption}} = 17.0 * 10^3 \text{ (cal/gmol)}$$

$$q_{\text{max}} = 13.92 \text{ g/100g}$$

- n-Hexane

$$n = 4$$

$$K_o = 2.44 * 10^{-12} \text{ bar}^{-1}$$

$$-\Delta H_{\text{Adsorption}} = 20.5 * 10^3 \text{ (cal/gmol)}$$

$$q_{\text{max}} = 14.48 \text{ g/100g}$$

- i- Pentane

$$n = 3$$

$$K_o = 6.46 * 10^{-10} \text{ bar}^{-1}$$

$$-\Delta H_{\text{Adsorption}} = 17.0 * 10^3 \text{ (cal/gmol)}$$

$$q_{\text{max}} = 13.65 \text{ g/100g}$$

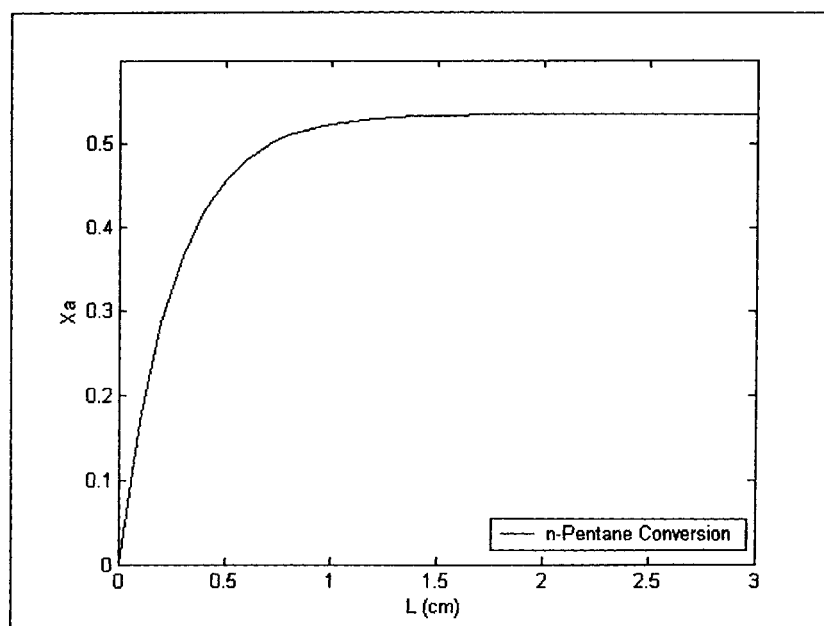
- i-Hexane

$$n = 4$$

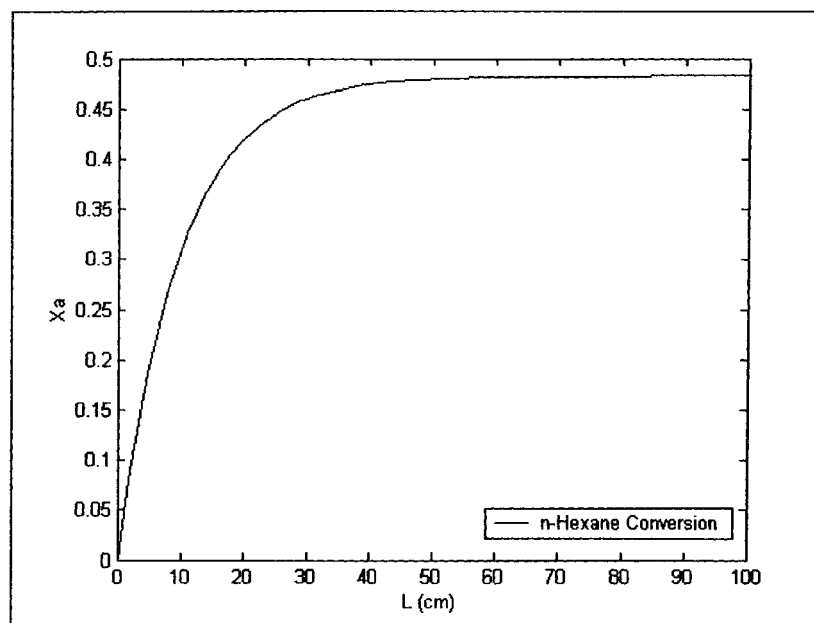
$$K_o = 2.44 * 10^{-12} \text{ bar}^{-1}$$

$$-\Delta H_{\text{Adsorption}} = 20.5 * 10^3 \text{ (cal/gmol)}$$

$$q_{\text{max}} = 14.48 \text{ g/100g}$$



a.



b.

Figure 3.5: Conversion versus reactor length at 300°C: a: n-Pentane, b: n-Hexane.

Table 3.2: First cycle time for  $\alpha=\beta=0$  and for optimum values of  $\alpha$  and  $\beta$ .

No. of Nodes	1 <sup>st</sup> cycle time @ $\alpha=\beta=0$ (min)	1 <sup>st</sup> Cycle Time @ optimum $\alpha$ & $\beta$ (min)	% Reduction in cycle time
10	24.53	30.41	-24.0
11	34.42	32.43	5.8
12	45.22	35.70	21.1
13	45.33	46.84	-3.3
14	50.61	47.87	5.4
15	57.18	53.55	6.4
16	65.08	65.83	-1.2
17	74.14	71.71	3.3
18	98.57	83.06	15.7
19	88.32	96.86	-9.7
20	94.51	90.27	4.5

Table 3.3: Parametric Values used for simulation of PSARM systems

Parameter	Value
$y_{Af}=y_{Bf}=y_{Cf}=y_{Df}$	0.03
H <sub>2</sub> /HC ratio (mol/mol)	7.33
$F_f$ (mol/m <sup>2</sup> /s)	0.134
$P_H$ (bar)	15
$P_L$ (bar)	2
$T_f$ (K)	573
$L$ (cm)	110
$U_f$ (cm/s)	0.5
$U_R$ (cm/s)	1.75
Purge/Feed volumetric ratio	3.5
S Reactor Section Purge Velocity Ratio	0.1
$D_L$ @ high pressure (cm <sup>2</sup> /s)	0.088
$D_L$ @ low pressure (cm <sup>2</sup> /s)	0.66
$K_{gl}$ @ high pressure (cm/s)	0.62
$K_{gl}$ @ low pressure (cm/s)	2.23
$Pe$ @ high pressure	59.1
$Pe$ @ low pressure	7.87
Pressurization & Blowdown time (min)	3.67
Adsorption & Desorption time (min)	165
$\omega$	0.58
$\theta_{Aref,1}$ @ 573K	0.0541
$\theta_{Bref,1}$ @ 573K	0.1187
$\theta_{C,ref,1}$ @ 573K	0.0541
$\theta_{D,ref,1}$ @ 573K	0.1187
$\theta_{Aref,2}$ @ 573K	0.0844
$\theta_{Bref,2}$ @ 573K	0.3036

## 3.6 RESULTS AND DISCUSSION

### 3.6.1 Conventional PSAR Cyclic Process

In this section, we will discuss the results obtained from conventional PSAR units. We define a conventional PSAR unit as a unit producing a product stream in the (reaction/adsorption) step and producing waste streams in the (blowdown/reaction) and (desorption/reaction) steps. In this type of process, no use is made to the waste stream produced by the (blowdown/reaction) and (desorption/reaction) steps. Moreover, the purge stream is either pure hydrogen stream (hydrogen purge) or a portion of the adsorption step product (self regeneration). First, we will discuss the hydrogen purge case.

The cycle starts initially with clean adsorbent and a gas phase free of n-C<sub>5</sub>, n-C<sub>6</sub>, i-C<sub>5</sub> and i-C<sub>6</sub>. The total length of the column is 100 cm. Parametric values used for simulations of conventional PSAR cycle are summarized in Table 3.3.

#### 3.6.1.1 Conventional PSAR Cyclic Process with hydrogen purge

Figure 3.6a illustrates the concentrations of reactive components at the end of the steady state reaction/pressurization step. It should be noted that only internal collocation points are plotted in all figures. The boundary points are not included in all figures. The only exception to this rule is the velocity profiles. The purpose of the reaction/pressurization step is to elevate the vessel pressure from 2 to 15 bars as a preparation for the next step. During this step the other end of the vessel is closed. Fresh feed is introduced to the bed with an equivalent molar ratio of 0.03 for each of the reactive components. The molar ratios of reactive components are chosen to allow overall minimum hydrogen to hydrocarbon ratio of 7.33. Maintaining the minimum ratio is very crucial to prevent any hydrocracking reactions from taking place. All reactive components are adsorbed in the catalyst bed before reacting. All isomerization reactions are equilibrium based reactions. Thus, reactants react to form products until equilibrium is reached. A very minimal reaction takes place at this step. During this step, components are mainly adsorbed into the solid phase. The isohexane peak appearing towards the end

of the adsorber bed is due to the shift of the amounts of isohexane that were present in the interface region at the end of the previous desorption/reaction step. Figures A.1a to A.4a in Appendix A illustrate the change in transient and Spatial concentration for n-C<sub>5</sub>, n-C<sub>6</sub>, i-C<sub>5</sub> and i-C<sub>6</sub> as a function of both time and distance for reaction/pressurization step, respectively.

Figure 3.6b illustrates the concentrations of reactive components at the end of the steady state reaction/adsorption step. In this step, the back end of the vessel is open for product collection. Isomerization of n-C<sub>5</sub> takes place at the first three centimeters of the bed. It takes the entire reactor section length to bring n-C<sub>6</sub> isomerization to its equilibrium state. In the adsorber section, any unreacted n-C<sub>5</sub> and n-C<sub>6</sub> is adsorbed by the 5A zeolite pellets. It takes 16 minutes for i-C<sub>5</sub> to breakthrough the reactor section. It takes 43 minutes for i-C<sub>6</sub> to breakthrough the reactor section. Noticeable amounts of n-C<sub>5</sub> and n-C<sub>6</sub> start appearing at the inlet of the adsorber section. This is due to the pellets at this section reaching their equilibrium occupation. Because of the higher adsorption equilibrium constant for n-C<sub>6</sub> over n-C<sub>5</sub>, the amounts of n-C<sub>6</sub> adsorbed are higher than those of n-C<sub>5</sub>. The equilibrium K values favor the adsorption of n-C<sub>6</sub> over n-C<sub>5</sub> replacing additional amounts of n-C<sub>5</sub> initially adsorbed by the pellets. The additional amounts of n-C<sub>5</sub> released to the gas phase cause a small peak in n-C<sub>5</sub> gas phase concentration. These amounts are pushed towards the next available unsaturated pellets. This is illustrated, in the adsorption section of the figure, with the n-C<sub>5</sub> concentration building up in the gas phase for a longer length than n-C<sub>6</sub>. This step is set to run at a time interval that is 50 times higher than the reaction/pressurization time. The choice of the time interval for this step is arbitrary, provided the time is not large enough to allow the adsorption pellets to reach their equilibrium occupation causing n-C<sub>5</sub> or n-C<sub>6</sub> to escape with the product. Also, the selected time should be enough to allow for i-C<sub>5</sub> and i-C<sub>6</sub> to breakthrough the adsorber section. A.1b to A.4b in Appendix A illustrate the change in transient and Spatial concentration for n-C<sub>5</sub>, n-C<sub>6</sub>, i-C<sub>5</sub> and i-C<sub>6</sub> as a function of both time and distance for reaction/adsorption step, respectively.

Figure 3.6c illustrates the concentrations of reactive components at the end of the steady state blowdown/reaction step. The vessel setup in this step is similar to the setup of the reaction/pressurization step. However, in this step, the front end of the vessel is closed and vessel contents are blown out of the vessel from the back end. Blowing vessel contents from the same open end of the previous reaction/adsorption step is contrary to conventional practice.

The reason for reversing the conventional practice setup is to avoid high reactants concentrations leaving the adsorber section and entering the reactor section. These high concentrations will violate the minimum hydrogen to hydrocarbon ratio and will result in a very high temperature profile in the interface region. The high interface temperature will promote cracking over isomeration, a phenomena that is avoided by reversing the conventional practice. This setup allows for a pressure reduction from 15 bars to 2 bars. This step prepares the vessel for introduction of purge stream in the next step. The shift in equilibrium, due to pressure decrease, causes the amounts of reactive components present in the solid phase of both sections to escape to the gas phase. The escape of these compounds to the gas phase causes their gas phase concentrations to increase. The time interval for this step is exactly the same as that of the reaction/pressurization step. Figures A.1c to A.5c in Appendix A illustrate the transient and Spatial change in concentration for n-C<sub>5</sub>, n-C<sub>6</sub>, i-C<sub>5</sub>, i-C<sub>6</sub> and H<sub>2</sub> as a function of both time and distance for blowdown/reaction step, respectively. Figures A.1c to A.4c in Appendix A illustrate the change in transient and Spatial concentration for n-C<sub>5</sub>, n-C<sub>6</sub>, i-C<sub>5</sub> and i-C<sub>6</sub> as a function of both time and distance for reaction/adsorption step, respectively.

Figure 3.6d illustrates the concentrations of reactive components at the end of the steady state desorption/reaction step. In the present model, pure H<sub>2</sub> is used as a purge stream. The desorption of n-C<sub>5</sub> and n-C<sub>6</sub> amounts present in the solid phase of the adsorber section causes an increase in their gas phase concentrations. To avoid temperature spike, the purge stream is introduced at both ends of the vessel and the waste stream is collected from the interface zone. Very little reaction takes place at this step because components in the reaction zone are close to their equilibrium conversions. It should be noted that the y-scale of this figure is much smaller than those figures of other steps. Figures A.1d to A.4d in Appendix A illustrate the change in transient and Spatial concentration for n-C<sub>5</sub>, n-C<sub>6</sub>, i-C<sub>5</sub> and i-C<sub>6</sub> as a function of both time and distance for reaction/adsorption step, respectively.

Figure 3.7 illustrates the concentration profiles for hydrogen at the end of the four cyclic steps. The increase in hydrogen concentration towards the end of the adsorber bed in reaction/pressurization step is due to the presence of hydrogen from the previous desorption/reaction step. The hydrogen present from the desorption/reaction step of the previous cycle is removed in the reaction/adsorption step. The increase in hydrogen concentration, at the



entrance of the adsorber section, at the end of the reaction/adsorption step is due to the adsorption of  $n\text{-C}_5$  and  $n\text{-C}_6$  in the solid pellets. During blowdown step, the pressure starts reducing from 15 bars to 2 bars. Because of this reduction, a shift in equilibrium occurs for the components present in the solid phase of both sections. The equilibrium shift causes the amounts initially present in the solid phase to escape to the gas phase causing a decrease in the gas phase hydrogen concentration. This decrease is illustrated in the figure by a large drop in hydrogen concentration. During desorption/reaction step, pure hydrogen is used as a purge stream. The time for this step is the same as the one for the reaction/adsorption step. This long time allows for the removal of most of the amounts present in the solid phase from the previous reaction/pressurization and reaction/adsorption steps. Figure A.5 in Appendix A illustrates the change in transient and Spatial concentration for  $\text{H}_2$  as a function of both time and distance for reaction/adsorption step, respectively.

The noticeable increase of the temperature at the start of the reactor bed (Figure 3.8), during reaction/pressurization step, is due to the combined effects of adsorption and chemical reactions. Temperature decline through the rest of the bed is due to the disappearance of both of these terms. The disappearance of both terms is due to the absence of reactive components at the remaining portion of the reactor section. Figure A.6a in Appendix A illustrates the transient and Spatial change in temperature as a function of both time and distance for reaction/pressurization step.

The temperature profile of the reaction section, at reaction/adsorption step, is initially lower than that of the reaction/pressurization step. This is due to the equilibrium reached in the solid phase. The temperature peak, formed towards the end of the adsorber section, is due to releasing the heat of adsorption while adsorbing  $n\text{-C}_5$  and  $n\text{-C}_6$  into the solid phase. Figure A.6b in Appendix A illustrates the transient and Spatial change in temperature as a function of both time and distance for reaction/adsorption step.

A temperature drop to an average of  $289^\circ\text{C}$  is noticed in the reactor section during blowdown/reaction step. This drop in temperature is due to heat adsorbed by reactive components to release them from the solid phase to the gas phase. The same concept holds for the temperature drop in the adsorber section. The temperature rise at the end of the adsorption section is due to the adsorption of  $n\text{-C}_5$  into the bed. The higher temperature reduction in reactor section, compared to the adsorber section, is due to the desorption of

higher amounts from the reactor section solid phase than their counterparts of the adsorber section. Figure A.6c in Appendix A illustrates the transient and Spatial change in temperature as a function of both time and distance for blowdown/reaction step.

Due to negligible reaction rates in desorption/reaction step, the final vessel temperature settles at a value close to the purge stream temperature (300°C) A three dimensional profile illustrating temperature profile against space and time for the desorption/reaction step is illustrated in Figure A.6d of Appendix A.

The velocity profiles at the end of each of the four steps are illustrated in Figure 3.9. Initially, at reaction/pressurization step, the velocity at the vessel inlet is 7.5 times higher than its original value due to pressurization effect. At the end of reaction/pressurization step, the inlet velocity reaches its normal value since all the bed at this time is pressurized. The velocity at the end of the bed is always zero since the bed is closed at the adsorber-section end during this step. The bed velocity during reaction/adsorption step is the same as the inlet velocity. Because of the pressure reduction, the final velocity of the blowdown/reaction step is expected to be at least 7.5 times higher than feed velocity. The increase in velocity, above the expected 7.5, is due to the desorption of components that were adsorbed in the solid phase during the previous steps. The reported velocity at the end of this step reaches 88 times the feed velocity at some locations. The velocity of desorption/reaction step is chosen to be 3.5 times greater than the feed velocity. As mentioned earlier, 90% of the purge stream is directed into the adsorber section and the rest is directed into the reactor section. The waste stream is collected at the interface zone. Again, the increase of the velocity in this step is due to the desorption of components that were adsorbed in the previous step reaction/pressurization and reaction/adsorption steps. Figure A.7 in Appendix A illustrates the transient and Spatial change in velocity as a function of both time and distance for reaction/pressurization, reaction/adsorption, blowdown/reaction and desorption/reaction steps, respectively.

As illustrated in Figure 3.10, capacitance terms for reactive species are rising in reaction/pressurization and reaction/adsorption steps. During blowdown/reaction step, a shift in  $n\text{-C}_5$  and  $n\text{-C}_6$  profiles is noticed in the adsorber bed. This shift is due to blowing down the vessel from the back

end. Capacitance terms drop to their minimal values, in both sections, during desorption/reaction step.

The equilibrium solid phase capacitance for all components is calculated and normalized at feed conditions. Thus, during the absence or reduction of concentration of one component over the others, the capacitance term may exceed 100% of the feed value. Upon converting the normalized capacitances to their real values, this phenomenon will disappear.

Integration of capacitances' profiles yields the occupation of adsorbates in the solid phase for both of reactor and adsorber sections. Summing up the capacities of adsorbed species provides the total coverage of the solid phase. Results are shown in Table 3.4. For example,  $n\text{-C}_5$  occupies 2.05% of the total adsorption capacity for the reactor section during the pressurization step. The total solid phase coverages of the reactor section for reaction/pressurization, reaction/adsorption, blowdown/reaction and desorption/reaction are 23.33%, 91.93%, 60.63% and 5.63%, respectively. Similar analysis to the adsorber section gives values of 2.5%, 47.74%, 52.33% and 2.46% for reaction/adsorption, blowdown/reaction and desorption/reaction, respectively.

The total occupation of all reactive components, in the reactor section, at the end of the reaction pressurization step is 23.33% compared to 5.63% at the end of the desorption step. This is an indication of a high adsorption in the reactor section of the vessel. For the adsorber section, no breakthrough of normals from the reactor section to the adsorber section occurs yet. Thus little change is noticed in the total capacitance. The small increase in total capacitance is due to the adsorption of some of  $n\text{-C}_5$  and  $n\text{-C}_6$  amounts that are present from previous step.

Comparing total occupation figures for the reaction/adsorption step to those of reaction/pressurization step in the adsorber section indicates an increase from 2.5% to 47.74%. This increase is due to the breakthrough of normal alkanes into the adsorber section.

For the reactor section, total occupation figures at the end of the blowdown/reaction step illustrate a large decrease compared to those from the previous reaction/adsorption step. This is an indication of fast desorption of components in this section. Comparing the figures of the adsorber section for the same steps illustrates an increase in occupation. This is due to the

introduction of additional amounts of n-C<sub>5</sub> and n-C<sub>6</sub> from the reactor section into the adsorber section.

Comparing reactor section occupation figures for reactive components, at the end of the reaction/pressurization step, illustrates that the lowest occupation is for n-C<sub>5</sub> followed by n-C<sub>6</sub>, i-C<sub>5</sub> and i-C<sub>6</sub>, respectively. The difference between n-C<sub>5</sub> and n-C<sub>6</sub> occupations is due to the difference in their equilibrium K values. At a temperature of 573K, the adsorption equilibrium constant for n-C<sub>5</sub> is 0.4 bar<sup>-1</sup>. The adsorption equilibrium constant for n-C<sub>6</sub>, at the same temperature, is 1.45 bar<sup>-1</sup>. The same analogy holds for i-C<sub>5</sub> and i-C<sub>6</sub> occupations. The higher occupation of i-C<sub>5</sub> compared to n-C<sub>6</sub> is due to its higher gas phase concentration relative to n-C<sub>6</sub>. For the adsorber section, n-C<sub>6</sub> illustrates higher occupation due to its larger equilibrium adsorption constant compared to that of n-C<sub>5</sub>.

At the end of the reaction/adsorption step, the increase in n-C<sub>5</sub> occupation over n-C<sub>6</sub> occupation in the adsorber section is attributed to the large amounts of n-C<sub>5</sub> breaking through compared to the amounts of n-C<sub>6</sub>.

The exit concentrations of reactive components at the end of the blowdown/reaction step are plotted in Figure 3.11. It takes 5 cycles for this system to reach cyclic steady state.

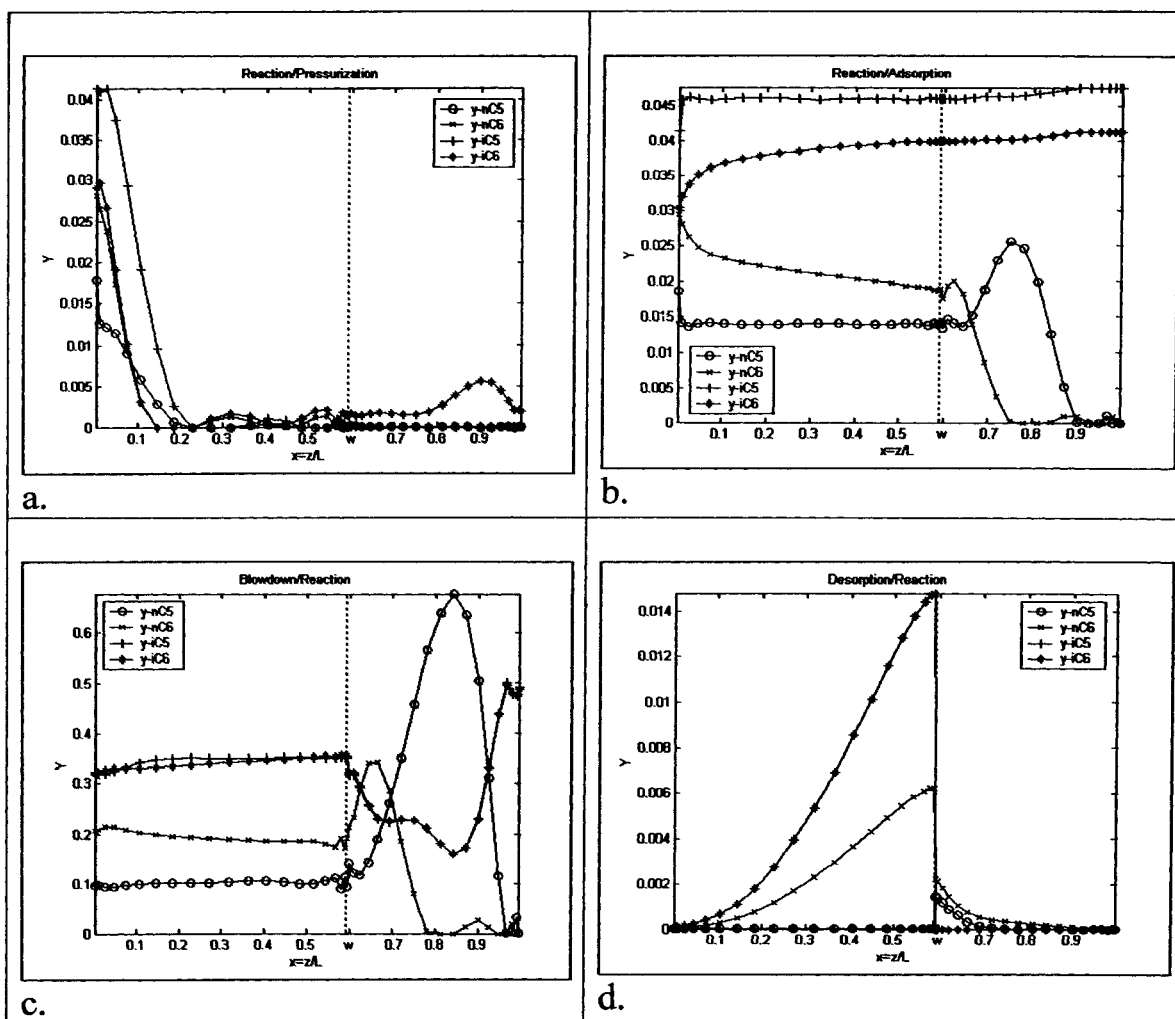


Figure 3.6: Gas phase concentration profiles for reactive components in the PSAR bed at the end of cyclic steady state:

- a.) reaction/pressurization,
- b.) reaction/adsorption,
- c.) blowdown/reaction,
- d.) desorption/reaction.

Parametric values are in Table 3.3. (Conventional PSAR unit/ $H_2$  purge).

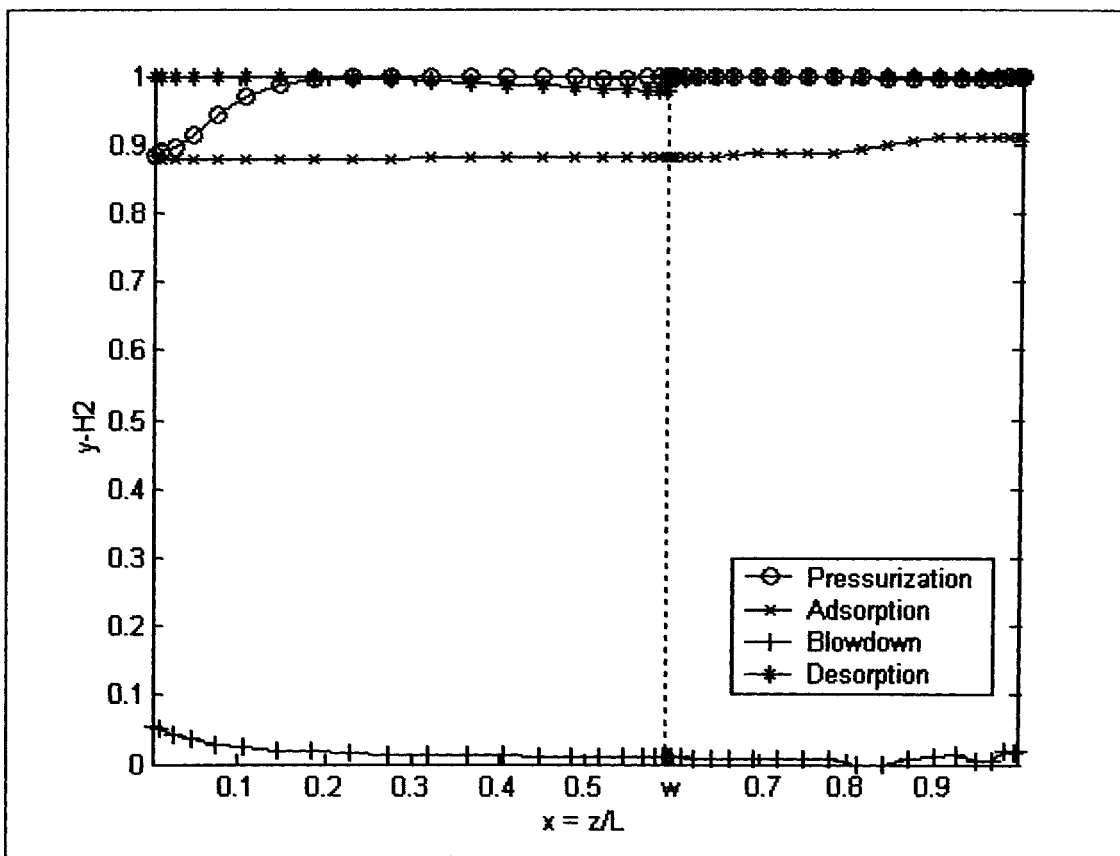


Figure 3.7: Gas phase concentration profiles for  $H_2$  in the PSAR bed at the end of cyclic steady state. Parametric values are in Table 3.3. (Conventional PSAR unit/ $H_2$  purge).

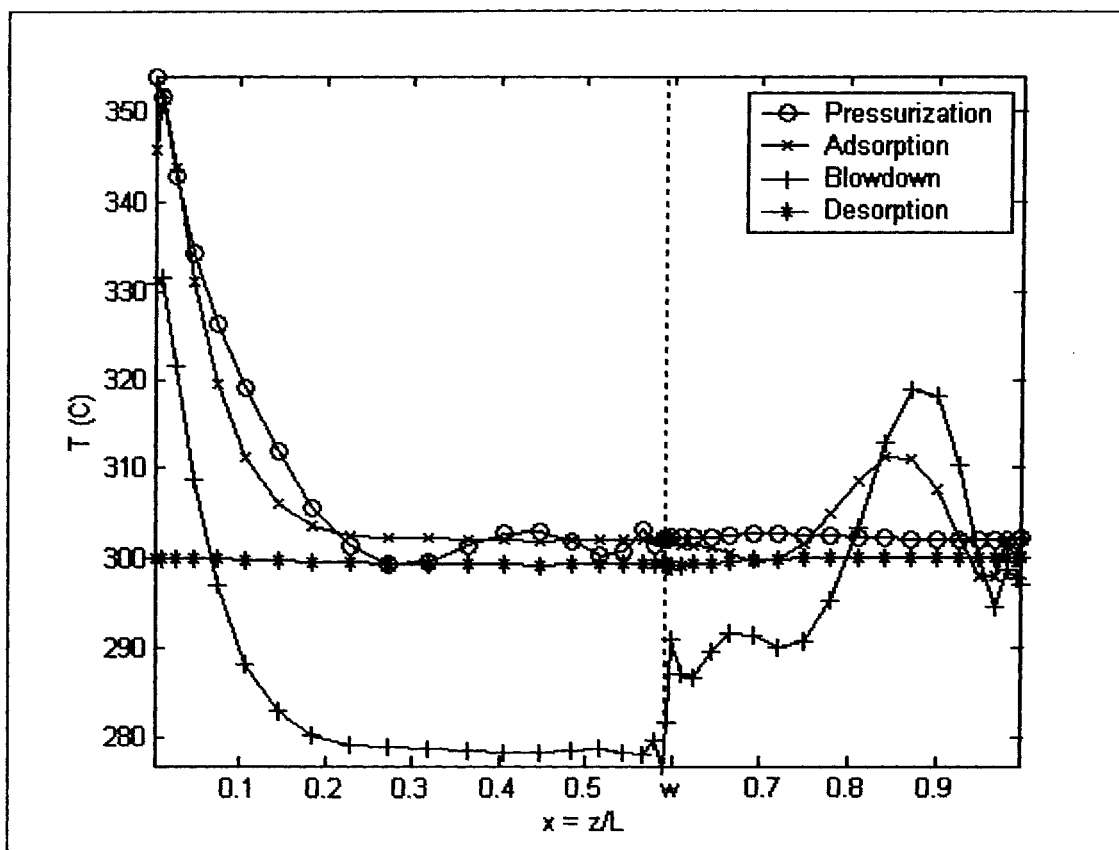


Figure 3.8: Temperature Profiles in the bed at the end of cyclic steady state. Parametric values are in Table 3.3. (Conventional PSAR unit/ $H_2$  purge).

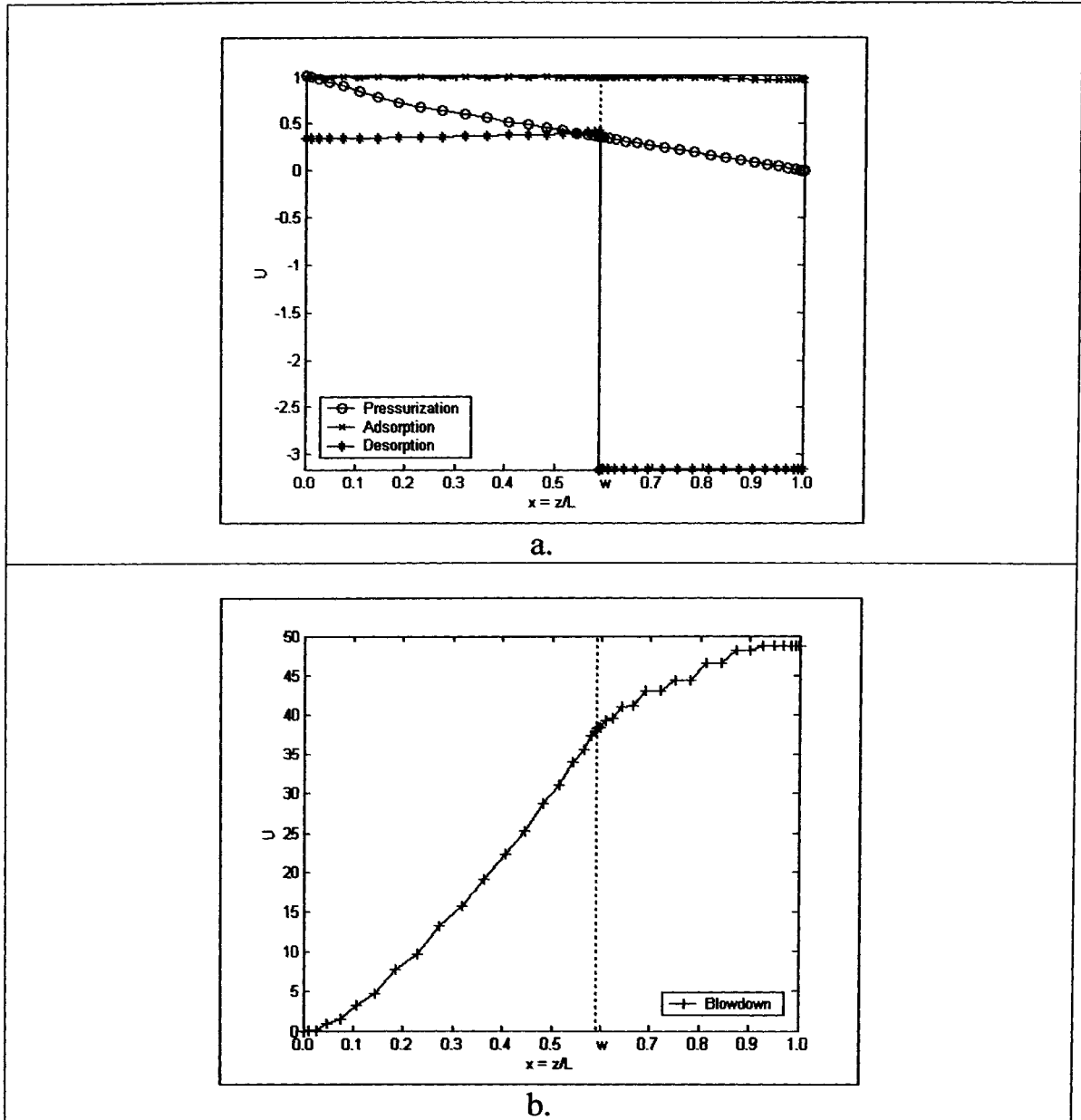


Figure 3.9: Velocity Profiles in the bed at the end of cyclic steady state:

a. Pressurization, Adsorption and Desorption steps Profiles.

b. Blowdown step profile.

Parametric values are in Table 3.3. (Conventional PSAR unit/ $H_2$  purge).



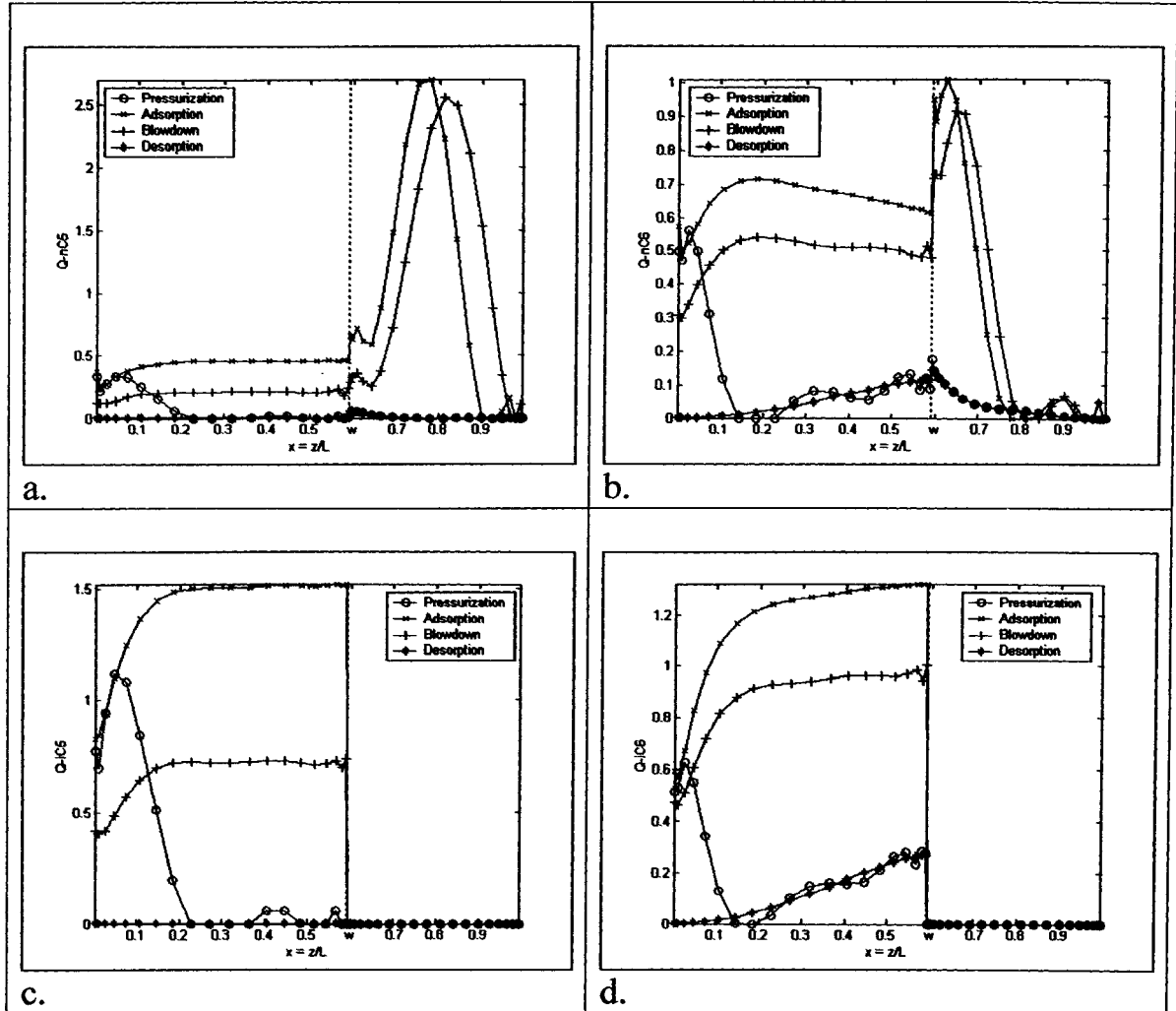


Figure 3.10: Solid phase capacitance profiles for reactive components in the PSAR bed at the end of cyclic steady state:

a.)  $n-C_5$ ,

b.)  $n-C_6$ ,

c.)  $i-C_5$ ,

d.)  $i-C_6$

Parametric values are in Table 3.3. (Conventional PSAR unit/ $H_2$  purge).

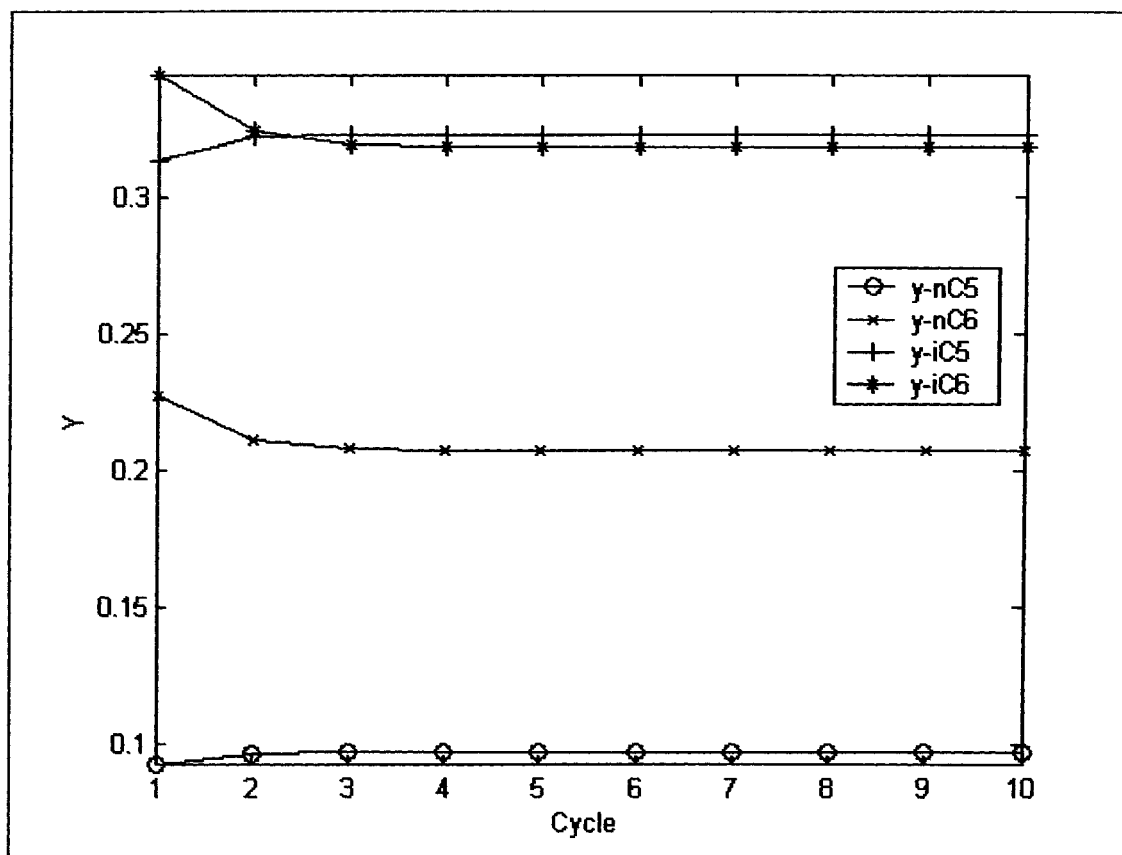


Figure 3.11: Approach to cyclic steady state, showing exit concentrations of reactants and products at end of Blowdown/Reaction step. Parametric values are in Table 3.3. (Conventional PSAR unit/H<sub>2</sub> purge).

Table 3.4: Percentage Relative Occupation for reactive components of the solid phase for both catalyst and adsorber sections (Conventional PSAR unit/H<sub>2</sub> purge).

Component	Pressurization		Adsorption		Blowdown		Desorption	
	Catalyst	Adsorber	Catalyst	Adsorber	Catalyst	Adsorber	Catalyst	Adsorber
n-C <sub>5</sub>	1.23	0.17	6.71	24.57	3.12	27.97	0.00	0.17
n-C <sub>6</sub>	4.13	2.61	22.53	20.07	16.92	24.36	1.68	2.58
i-C <sub>5</sub>	4.04	0.00	22.16	0.00	10.58	0.00	0.00	0.00
i-C <sub>6</sub>	6.50	0.00	40.51	0.00	30.14	0.00	3.95	0.00
Total	15.90	2.78	91.91	44.64	60.75	52.33	5.63	2.75

### 3.6.1.2 Conventional PSAR Cyclic Process with Self Regeneration

Most of the discussion, pertaining to the shape of the uptake curves obtained, is performed in the previous section. In this section, and later sections, we will focus on differences between uptake obtained using pure Hydrogen purge and those obtained by purging with a portion of the product stream.

Figure 3.12a illustrates the concentrations of reactive components at the end of the steady state reaction/pressurization step. A noticeable increase in i-C<sub>5</sub> and i-C<sub>6</sub> concentrations is observed, over the H<sub>2</sub> purge case, in the adsorption section. This increase is expected since we are purging with stream containing i-C<sub>5</sub> and i-C<sub>6</sub>.

Concentration profiles for the reaction/adsorption and blowdown/reaction steps are very similar to those obtained previously using H<sub>2</sub> as a purge stream. The reason is that neither of these steps involves use of a purge stream. The profiles are plotted in Figures 3.12b and 3.12c for reaction/adsorption and blowdown/reaction, respectively.

Concentration profiles for reactive components at the end of the desorption/reaction step are illustrated in Figure 3.12d. Concentrations of i-C<sub>5</sub> and i-C<sub>6</sub> in the desorption/reaction step are higher than their counterparts of the hydrogen purge case. This is due to purging with a portion of the product stream. The drop in i-C<sub>5</sub> and i-C<sub>6</sub> concentrations in the reactor section is due to their adsorption into the catalyst bed.

Figure 3.13 illustrates hydrogen profiles at the end of each of the steps. At the end of the reaction/pressurization step, the drop in hydrogen concentration at the end of the adsorber section is attributed to the presence of amounts of i-C<sub>5</sub> and i-C<sub>6</sub>. The i-C<sub>5</sub> and i-C<sub>6</sub> amounts that were previously distributed over both sections of the vessel are pushed to the end of the vessel in reaction/pressurization step causing a drop in hydrogen concentration. Hydrogen profiles for reaction/adsorption and blowdown/reaction steps are similar to those introduced in the hydrogen purge case. Due to purging with part of the product stream that contains amounts of i-C<sub>5</sub> and i-C<sub>6</sub>, a lower hydrogen concentration is noticed in the current desorption/reaction step over that reported by the hydrogen purge case.

Temperature profiles for the four steps are illustrated in Figure 3.14. At the end of the reaction/pressurization step, a lower temperature profile is noticed at the front end of catalyst bed compared the hydrogen purge case. This decrease is due to the presence of amounts of i-C<sub>5</sub> and i-C<sub>6</sub> in the bed gas and solid phases from the previous step.

Temperature profiles for the reaction/adsorption and blowdown/reaction steps are similar to those produced in the hydrogen purge case.

The lower catalyst bed front temperature profiles at the end of desorption/reaction step, compared to hydrogen purge case, is due to the reverse chemical reaction taking effect at the entrance. The reverse chemical reaction is a direct result of the higher inlet concentrations of isoalkanes compared to normal alkanes. This is an expected result since we are purging with a portion of the product stream.

Figure 3.15 illustrates the velocity profiles at the end of each of the four steps. Velocity profiles are similar to those reported by the hydrogen purge case.

Solid phase capacitance profiles are illustrated in Figure 3.16. The total solid phase coverages of both reactor and adsorber sections are illustrated in Table 3.5. At the end of the reaction/pressurization step, the noticeable overall increase in the reactor section solid occupation for i-C<sub>5</sub> and i-C<sub>6</sub> is due to purging with a stream that contains amounts of these two components. Also, the noticeable increase in n-C<sub>5</sub> concentration in the reactor section at the end of the desorption/reaction step is attributed to the reverse chemical reaction taking place at this step. Due to the slow reaction kinetics for n-C<sub>6</sub>/i-C<sub>6</sub> pair, no noticeable increase is reported in n-C<sub>6</sub> solid phase occupation. The reverse chemical reaction is a direct result of purging with a stream containing only isoalkanes and hydrogen. Solid phase coverages for reaction/adsorption and blowdown/reaction steps are close to their counterparts of the hydrogen purge case.

Three dimensional drawings demonstrating the transient and Spatial change in concentration and temperature profiles are illustrated in Appendix B.

The approach to cyclic steady state is illustrated in Figure 3.17. It takes approximately 10 cycles for this system to reach steady state.

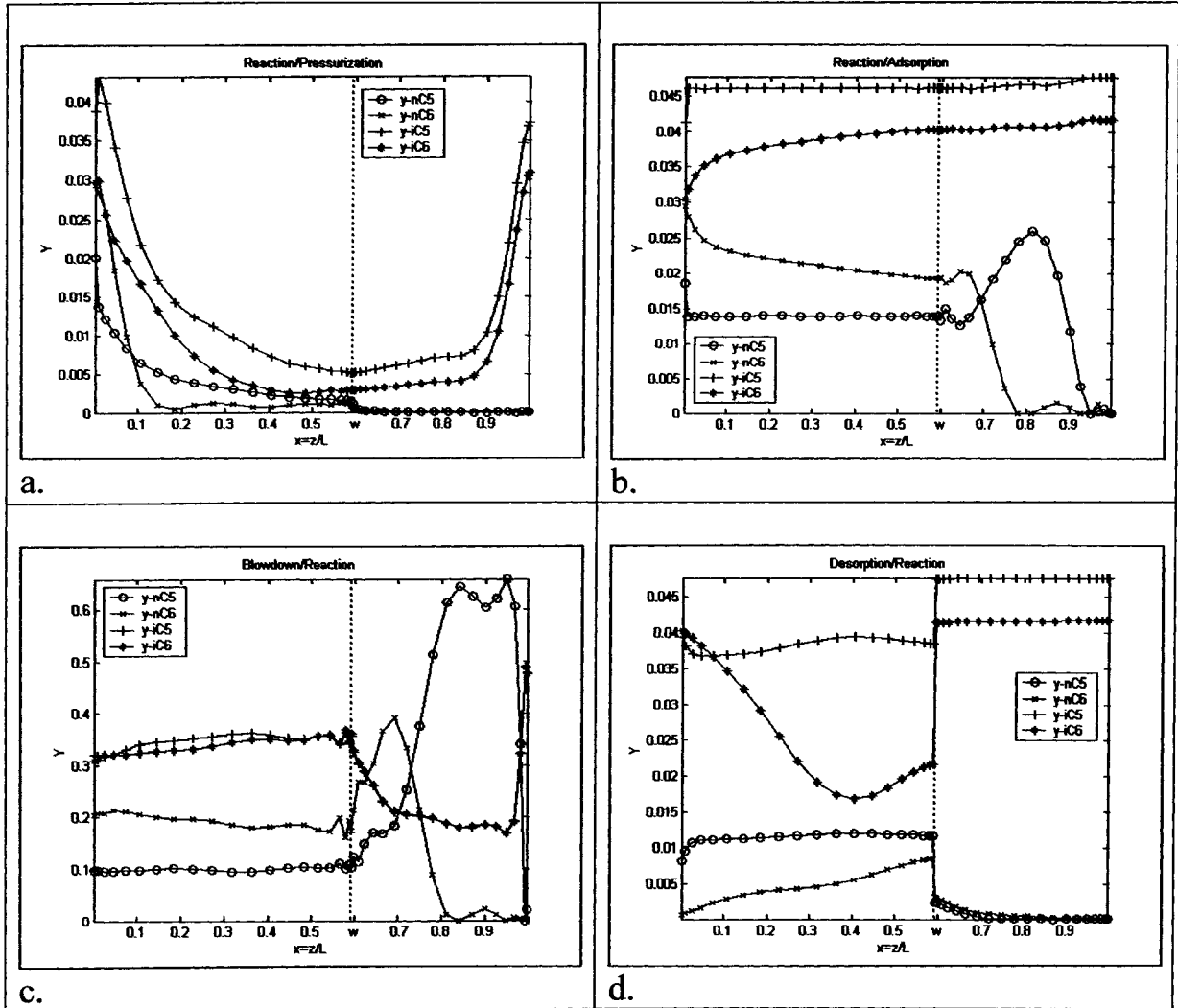


Figure 3.12: Gas phase concentration profiles for reactive components in the PSAR bed at the end of cyclic steady state:

- a.) reaction/pressurization ,
- b.) reaction/adsorption,
- c.) blowdown/reaction,
- d.) desorption/reaction.

Parametric values are in Table 3.3. (Conventional PSAR unit/Self Regeneration).

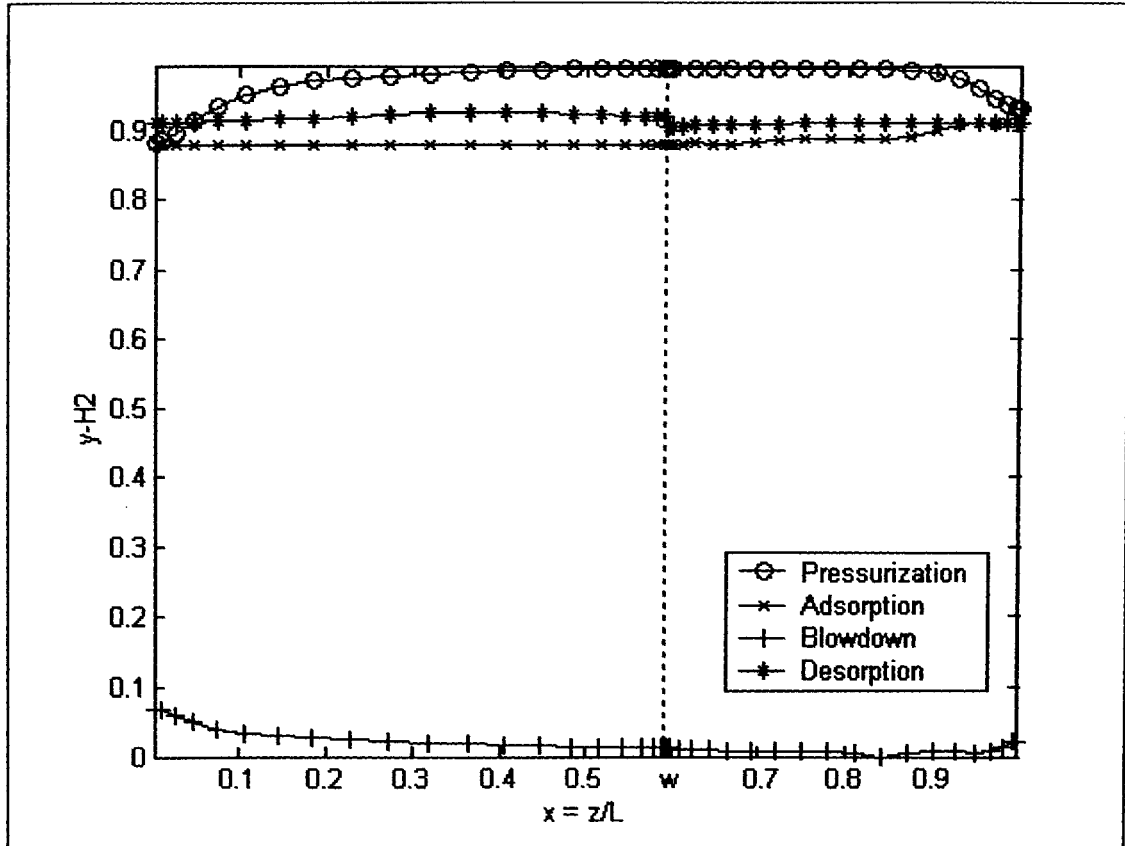


Figure 3.13: Gas phase concentration profiles for  $H_2$  in the PSAR bed at the end of cyclic steady state. Parametric values are in Table 3.3. (Conventional PSAR unit/Self Regeneration).

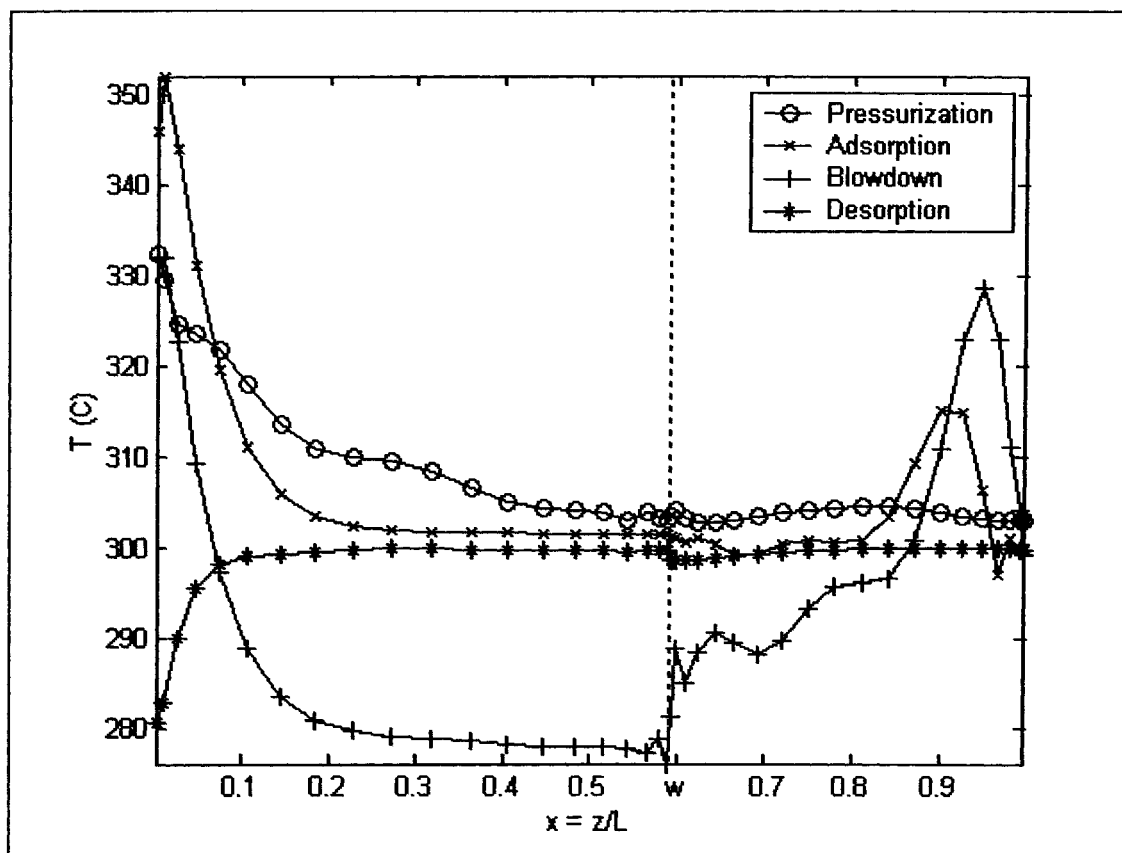


Figure 3.14: Temperature Profiles in the bed at the end of cyclic steady state. Parametric values are in Table 3.3. (Conventional PSAR unit/Self Regeneration).



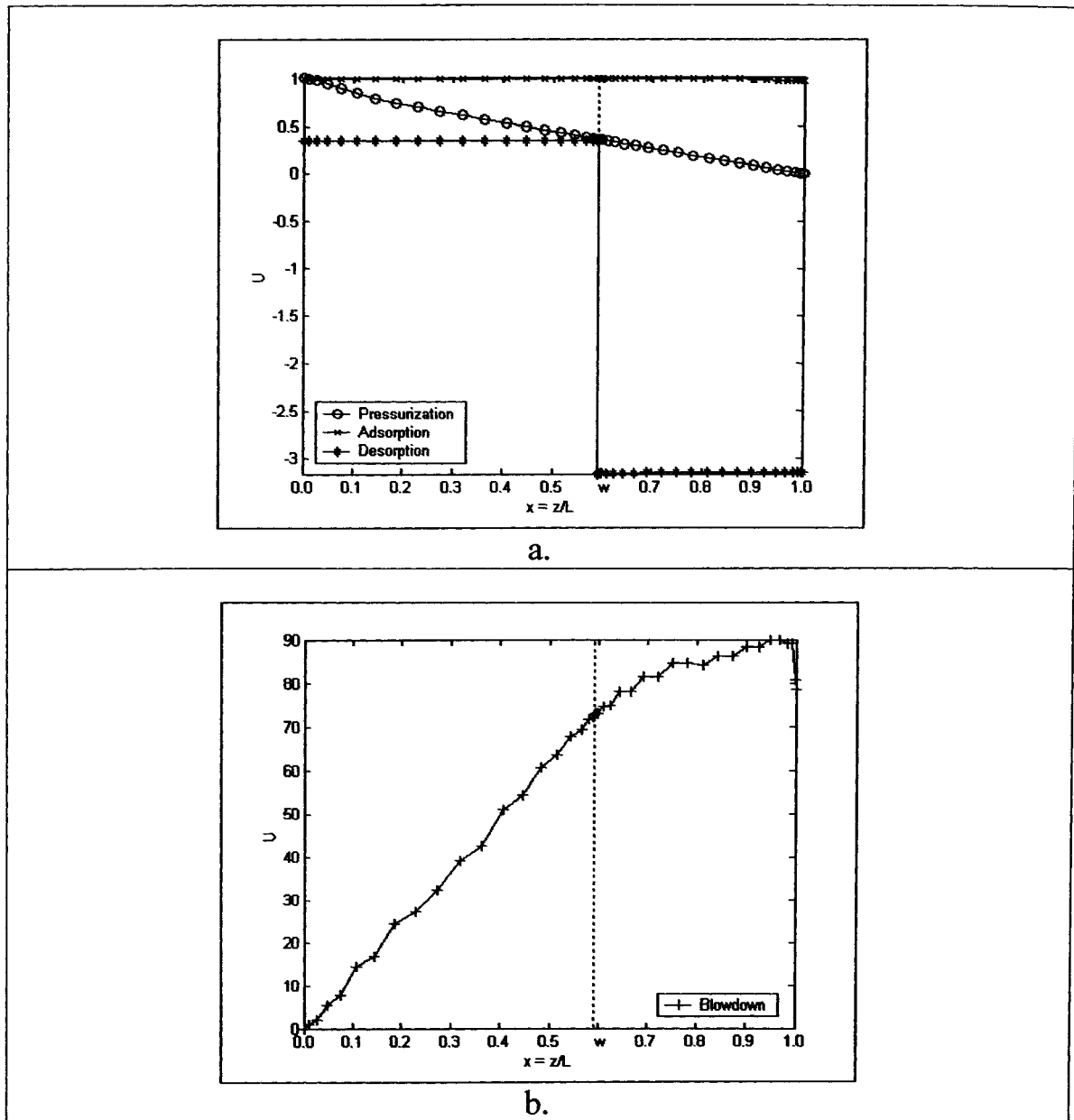


Figure 3.15: Velocity Profiles in the bed at the end of cyclic steady state:

- a. Pressurization, Adsorption and Desorption steps Profiles.
- b. Blowdown step profile.

Parametric values are in Table 3.3. (Conventional PSAR unit/Self Regeneration).

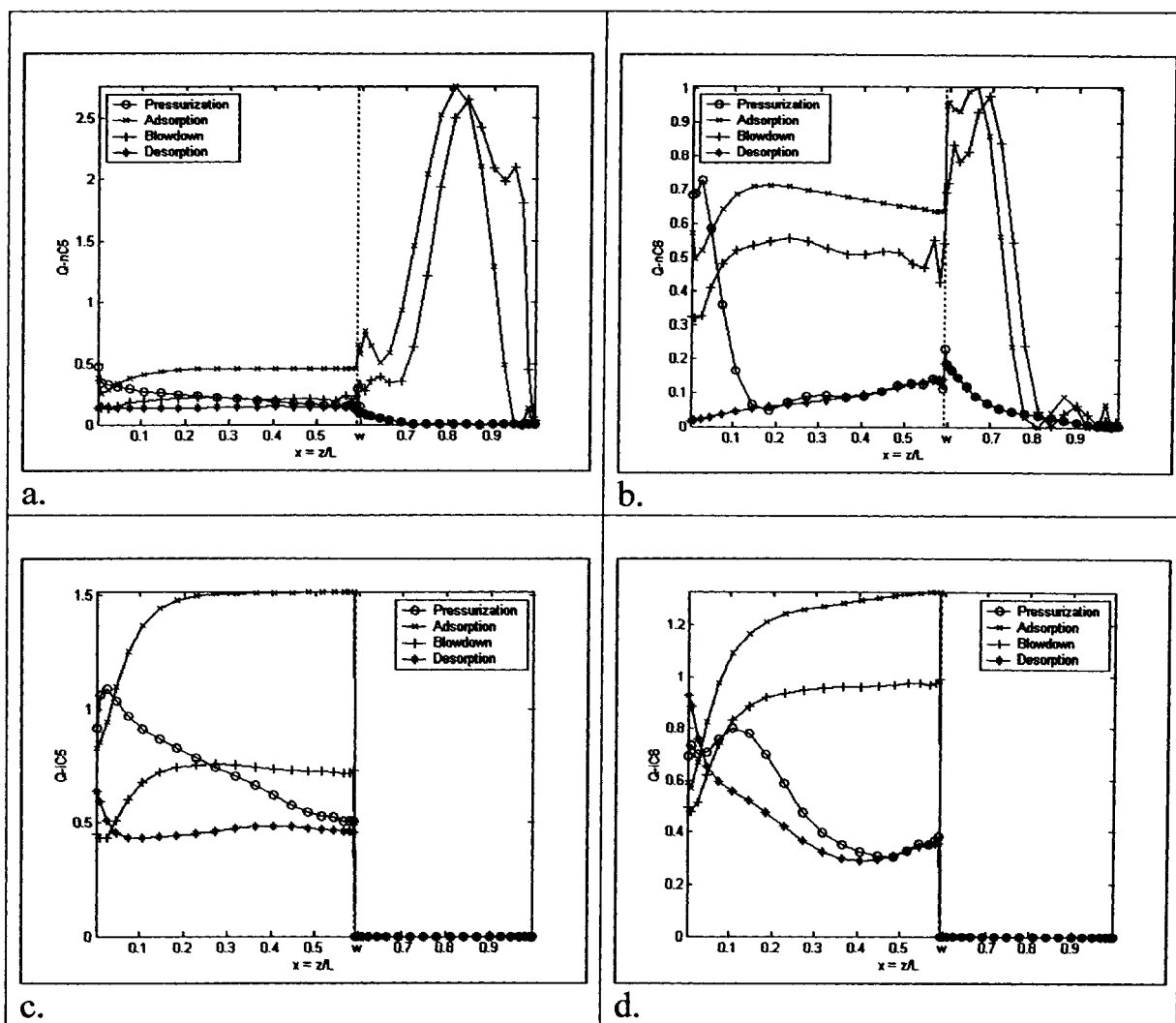


Figure 3.16: Solid phase capacitance profiles for reactive components in the PSAR bed at the end of cyclic steady state: a.) n-C<sub>5</sub>, b.) n-C<sub>6</sub>, c.) i-C<sub>5</sub>, d.) i-C<sub>6</sub>. Parametric values are in Table 3.3. (Conventional PSAR unit/Self Regeneration).

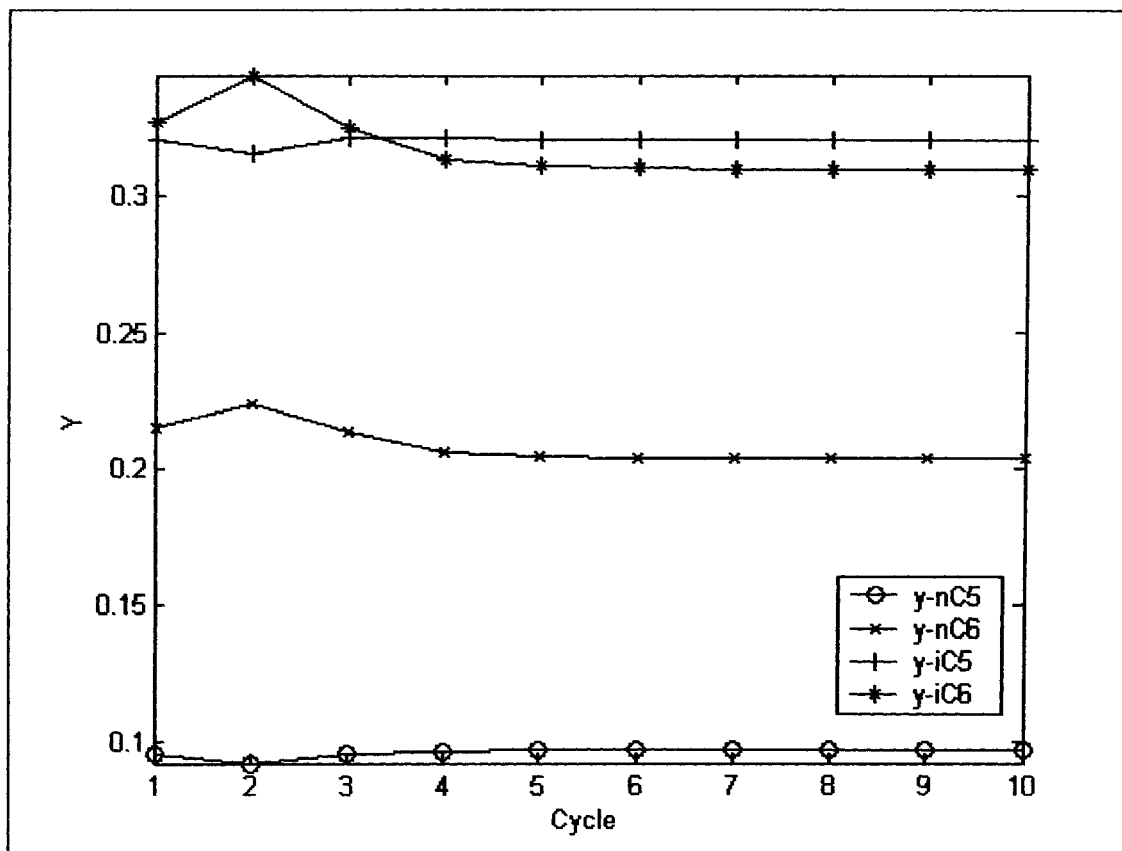


Figure 3.17: Approach to cyclic steady state, showing exit concentrations of reactants and products at end of Blowdown/Reaction step. Parametric values are in Table 3.3. (Conventional PSAR unit/Self Regeneration).

Table 3.5: Percentage Relative Occupation for reactive components of the solid phase for both catalyst and adsorber sections (Conventional PSAR unit/Self Regeneration).

Component	Pressurization		Adsorption		Blowdown		Desorption	
	Catalyst	Adsorber	Catalyst	Adsorber	Catalyst	Adsorber	Catalyst	Adsorber
n-C <sub>5</sub>	3.49	0.38	6.71	28.44	3.13	30.22	2.16	0.30
n-C <sub>6</sub>	5.77	3.92	22.66	26.14	17.22	29.02	2.68	3.88
i-C <sub>5</sub>	11.44	0.00	22.17	0.00	10.85	0.00	7.22	0.00
i-C <sub>6</sub>	17.44	0.00	40.59	0.00	30.45	0.00	14.51	0.00
Total	38.13	4.30	92.14	54.58	61.65	59.24	26.57	4.18

### 3.6.2 PSAR Cyclic Process with Waste Stream Recycled to Feed

In this section, the effluent of the blowdown/reaction and desorption/reaction steps is combined with the fresh feed before entering the reaction section during the reaction/adsorption step.

#### 3.6.2.1 PSAR Cyclic Process with Waste Stream Recycled to Feed (Hydrogen Purge)

In this section, pure hydrogen is used as purge stream during desorption/reaction step. Most of the discussion pertaining to the uptake of the curves obtained is performed in sections 3.6.1.1 and 3.6.1.2. In this section, we focus on differences between uptakes obtained with conventional PSAR unit and those obtained with recycling waste stream to feed.

Figure 3.18a illustrates the concentrations of reactive components at the end of the steady state reaction/pressurization step. The observed large peak in i-C<sub>6</sub> concentration, at the end of the adsorber section, is due to the higher i-C<sub>6</sub> concentration in this section at the end of the previous desorption/reaction step.

Figure 3.18b illustrates the concentrations of reactive components at the end of the steady state reaction/adsorption step. The decline in n-C<sub>5</sub> and n-C<sub>6</sub> conversions is due to the higher velocity at the start of this step and due to the recycle stream concentrations. The higher velocity at dimensionless time interval of (0-0.989) is due to recycling of third vessel contents. The observed i-C<sub>6</sub> peak at the end of the reactor section is a direct result of the change in recycle stream i-C<sub>6</sub> concentration from the adjacent column undergoing desorption/reaction step.

Figures 3.18c and 3.18d illustrates the concentrations of reactive components at the end of the steady state blowdown/reaction and desorption/reaction steps. Profiles in these steps are similar to the profiles generated by the conventional PSAR model. However, higher concentrations are observed in this model due to the higher solid phase loadings from the previous step.

Figure 3.19 illustrates the hydrogen profiles at the end of each of the steps for the last cycle. Hydrogen profiles produced with this model are very close to those produced with a conventional PSAR model.

Figure 3.20 illustrates the temperature profiles for all steps at the end of the steady state cycle. Temperature profiles for all steps are similar to their counterparts of the Conventional PSAR unit.

Three dimensional drawings demonstrating the transient and Spatial change in concentration and temperature profiles are illustrated in Appendix C.

Capacitance profiles for each of the reactive components are illustrated in Figure 3.22. Also, the percentage relative solid phase occupation for each of the components is illustrated in table 3.6. An overall lower solid phase occupation is noticed in this model over the conventional PSAR model. The recycle of low reactive components' streams to the unit is the reason behind this low occupation.

The approach to cyclic steady state is illustrated in Figure 3.23. It takes ten cycles for this system to reach steady state.

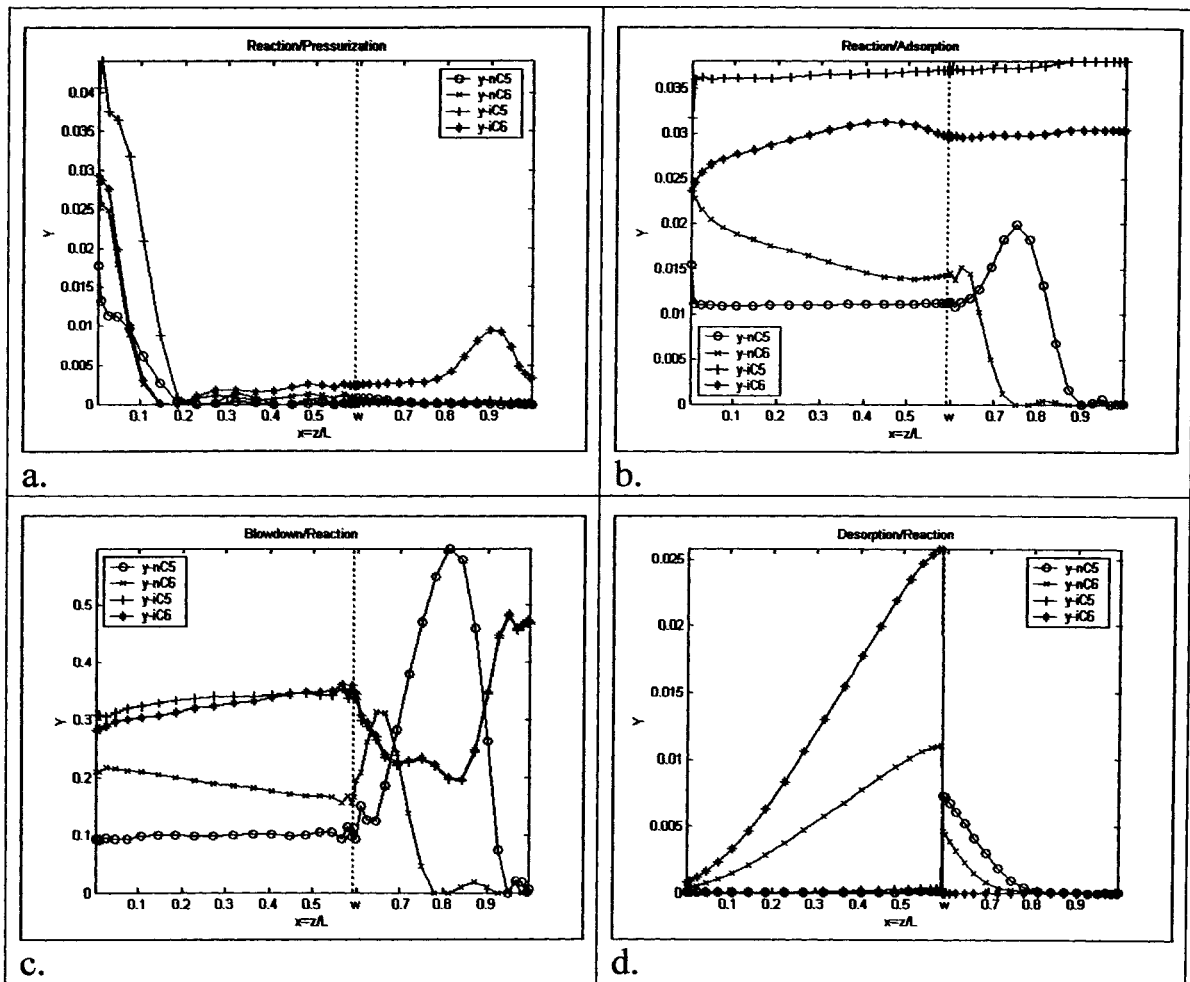


Figure 3.18: Gas phase concentration profiles for reactive components in the PSAR bed at the end of cyclic steady state:

- a.) reaction/pressurization ,
- b.) reaction/adsorption,
- c.) blowdown/reaction ,
- d.) desorption/reaction.

Parametric values are in Table 3.3. (PSAR with waste recycled to feed/ $H_2$  Purge).

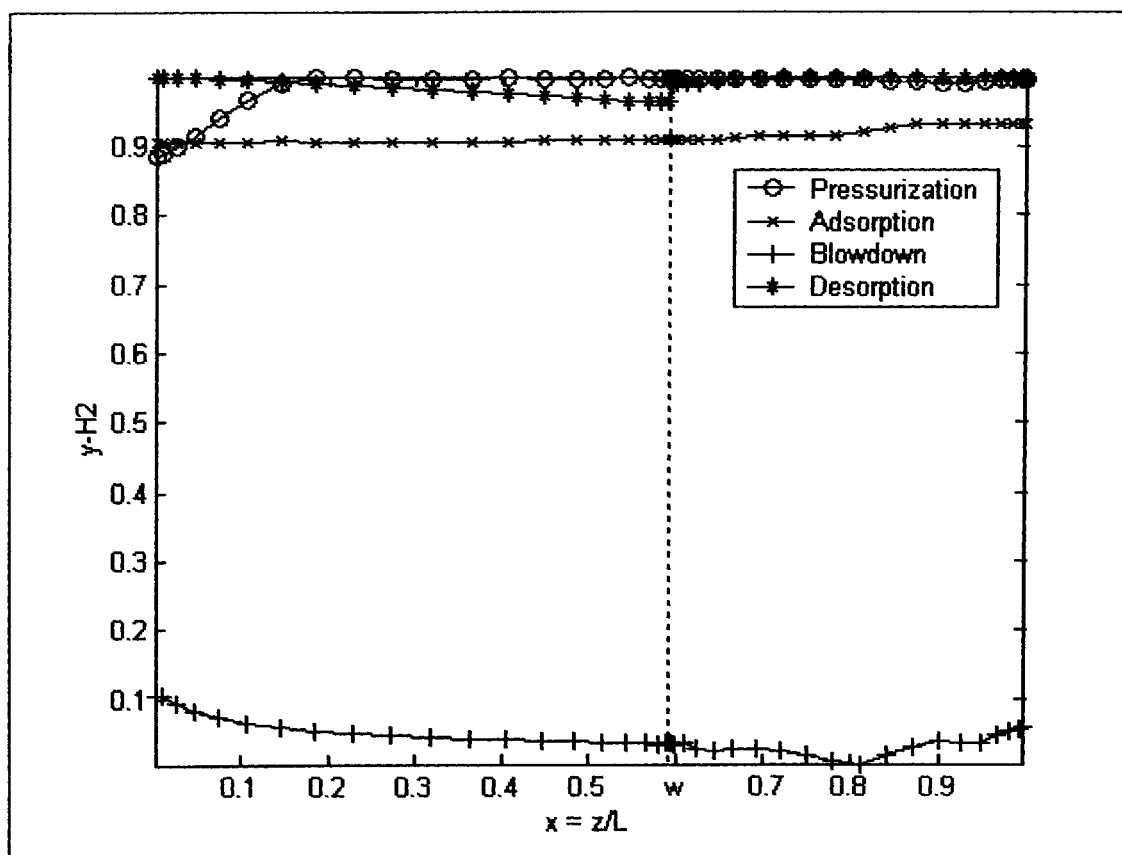


Figure 3.19: Gas phase concentration profiles for  $H_2$  in the PSAR bed at the end of cyclic steady state. Parametric values are in Table 3.3. (PSAR with waste recycled to feed/ $H_2$  Purge).



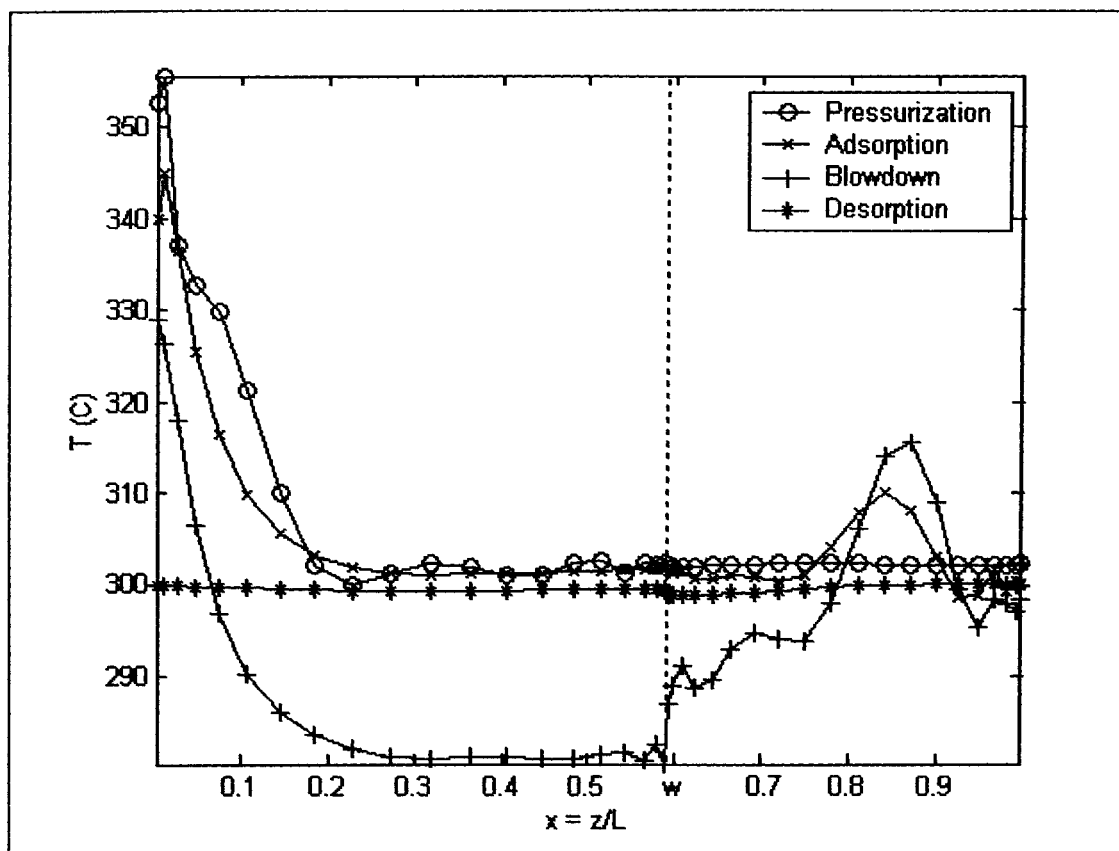


Figure 3.20: Temperature Profiles in the bed at the end of cyclic steady state. Parametric values are in Table 3.3. (PSAR with waste recycled to feed/ $H_2$  Purge).

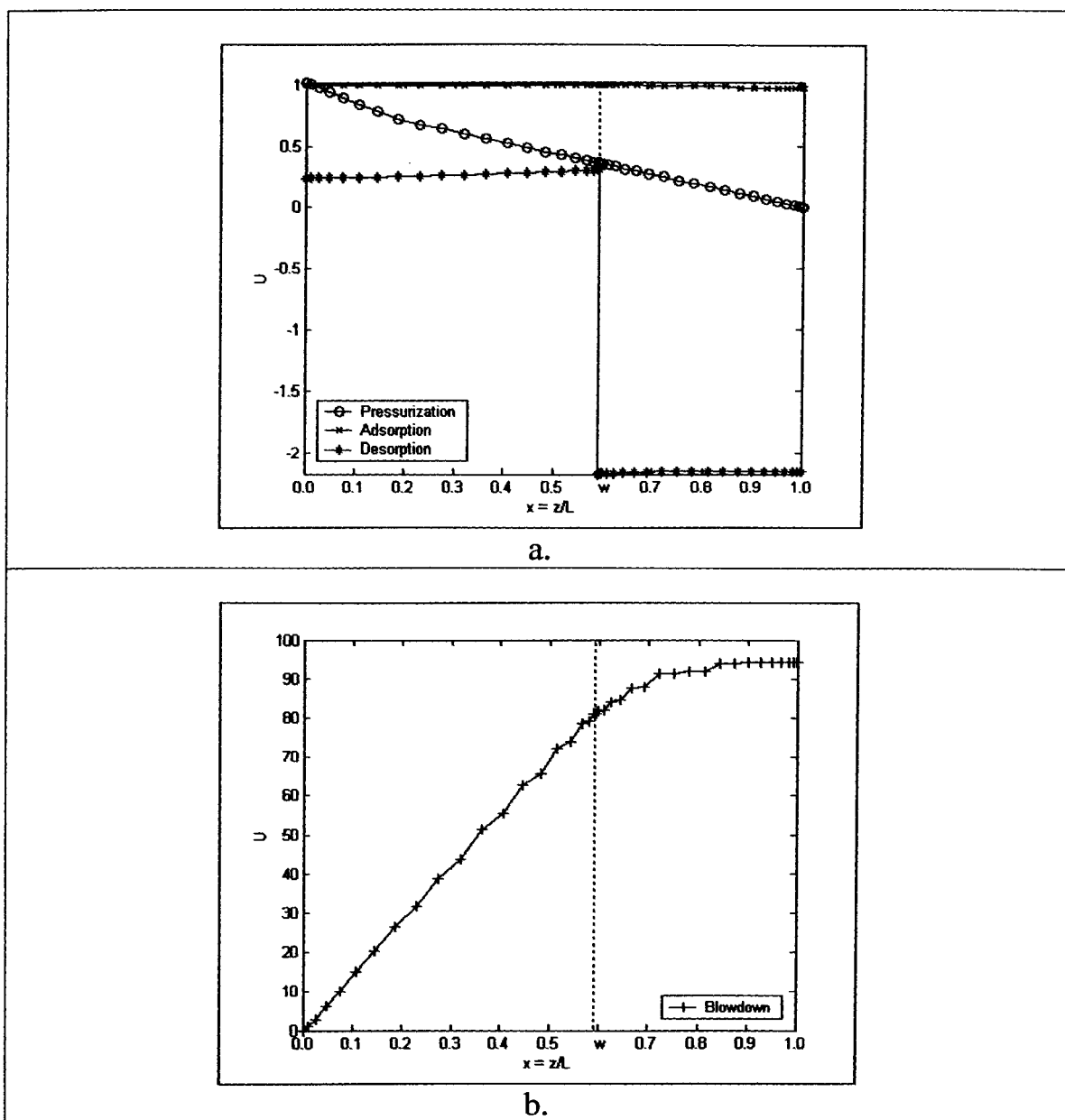


Figure 3.21: Velocity Profiles in the bed at the end of cyclic steady state:

- a. Pressurization, Adsorption and Desorption steps Profiles.
- b. Blowdown step profile.

Parametric values are in Table 3.3. (PSAR with waste recycled to feed/ $H_2$  Purge).

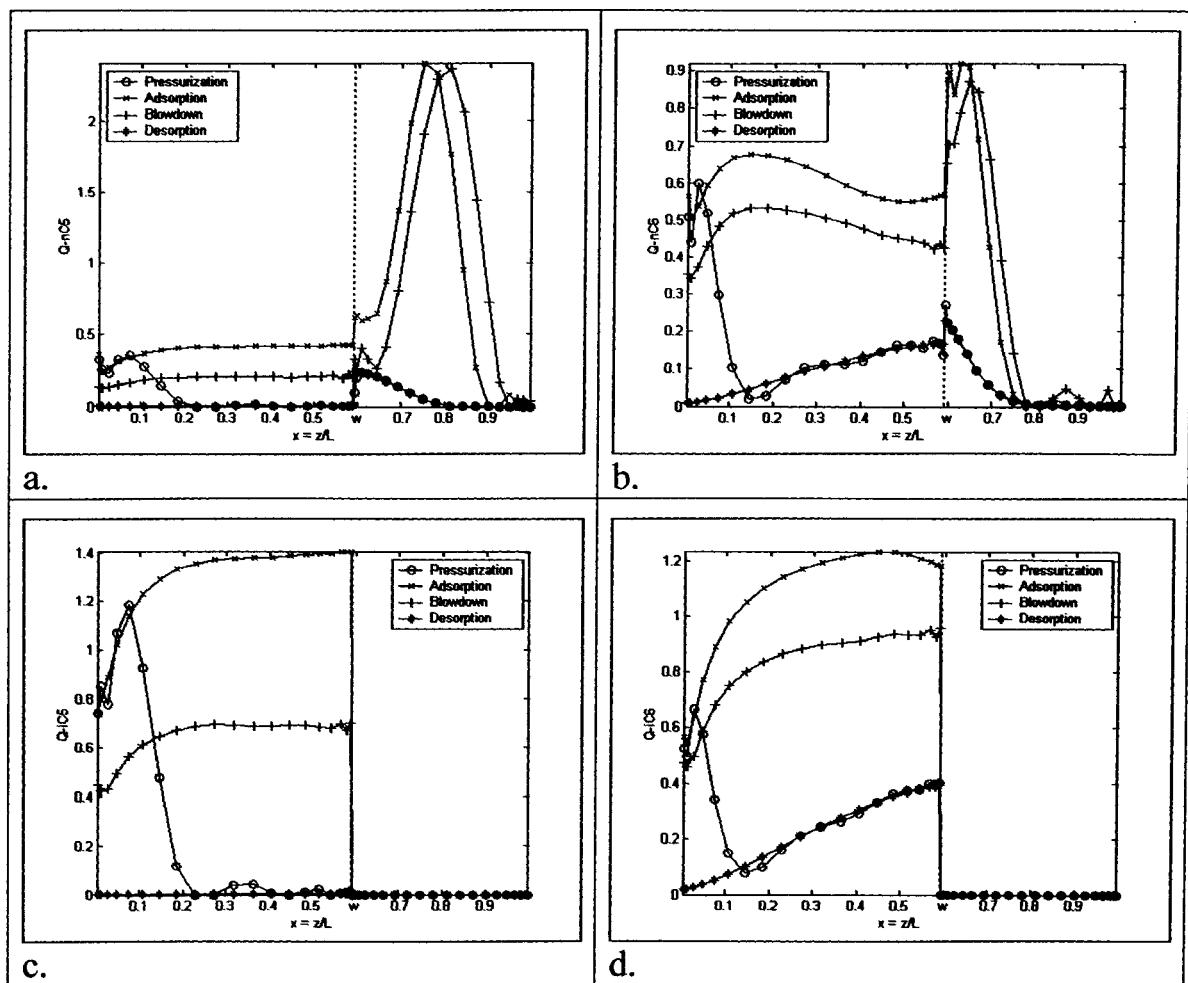


Figure 3.22: Solid phase capacitance profiles for reactive components in the PSAR bed at the end of cyclic steady state:

a.)  $n-C_5$ ,

b.)  $n-C_6$ ,

c.)  $i-C_5$ ,

d.)  $i-C_6$ .

Parametric values are in Table 3.3. (PSAR with waste recycled to feed/ $H_2$  Purge).

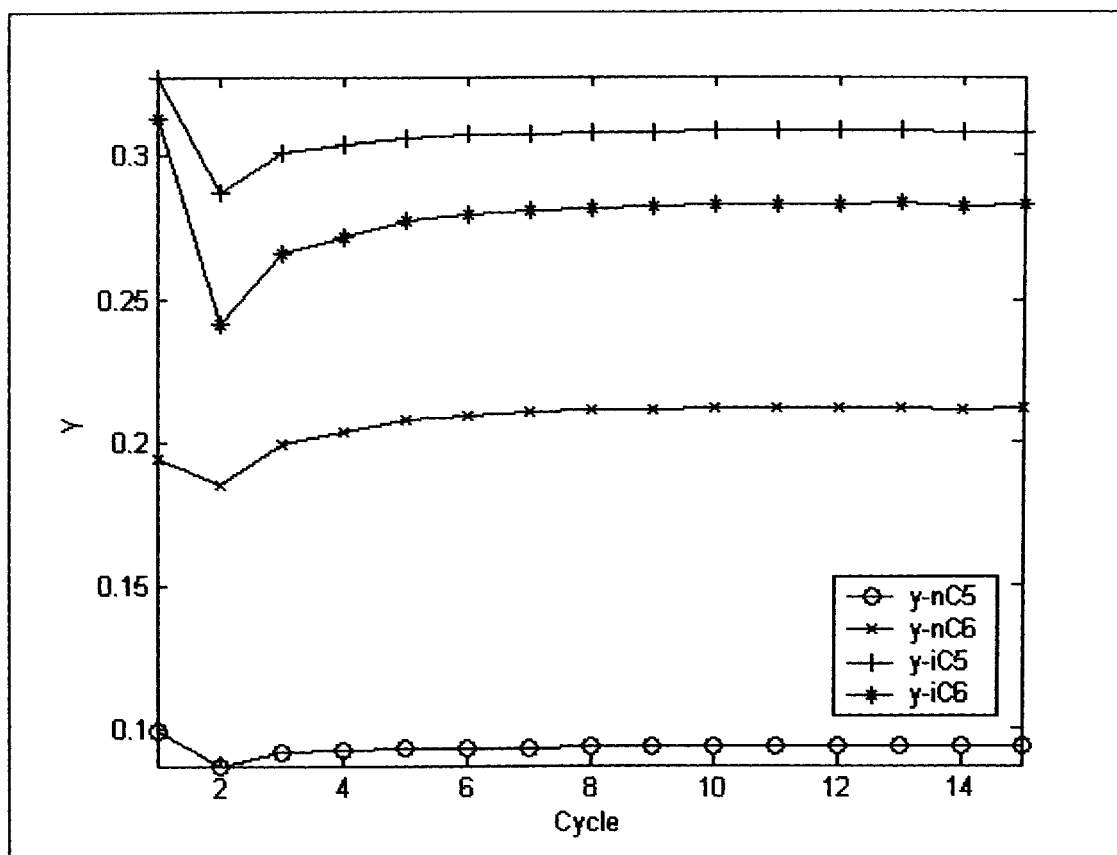


Figure 3.23: Approach to cyclic steady state, showing exit concentrations of reactants and products at end of Blowdown/Reaction step. Parametric values are in Table 3.3. (PSAR with waste recycled to feed/ $\text{H}_2$  Purge).

Table 3.6: Percentage Relative Occupation for reactive components of the solid phase for both catalyst and adsorber sections (PSAR with waste recycled to feed/H<sub>2</sub> Purge).

Component	Pressurization		Adsorption		Blowdown		Desorption	
	Catalyst	Adsorber	Catalyst	Adsorber	Catalyst	Adsorber	Catalyst	Adsorber
n-C <sub>5</sub>	1.16	1.40	6.13	20.82	3.04	22.35	0.01	1.41
n-C <sub>6</sub>	5.48	3.27	20.73	17.42	16.36	19.42	3.22	3.21
i-C <sub>5</sub>	3.72	0.00	20.24	0.00	10.12	0.00	0.02	0.00
i-C <sub>6</sub>	9.76	0.00	37.56	0.00	28.54	0.00	7.37	0.00
Total	20.11	4.67	84.67	38.24	58.06	41.78	10.62	4.62

### 3.6.2.2 PSAR Cyclic Process with Waste Stream Recycled to feed (Self Regeneration)

In this section, a portion of the product stream is recycled as a purge stream during desorption/reaction step. Moreover, the effluents of blowdown/reaction and desorption/reaction steps are recycled back and combined with the feed before entering the vessel. As mentioned previously, most of the discussion pertaining to the shape of the uptake curves obtained is performed in sections 3.6.1.1 and 3.6.1.2. In this section, we will focus on differences between uptakes obtained with conventional PSAR unit with self-regeneration and those obtained with recycling waste stream to feed.

Figure 3.24a illustrates the concentrations of reactive components at the end of the steady state reaction/pressurization step. Profiles for this step are no different than those produced with a conventional PSAR unit (Figure 3.12a).

Figure 3.24b illustrates the concentrations of reactive components at the end of the steady state reaction/adsorption step. The effect of the recycle stream is demonstrated by the difference in inlet concentrations of this model and those of the conventional PSAR unit model.

Figure 3.24c illustrates the concentrations of reactive components at the end of the steady state blowdown/reaction step. The breakthrough in n-C5 concentration of this model is due to the additional (third vessel) recycle stream introduced at the previous step.

Figure 3.24d illustrates the concentrations of reactive components at the end of the steady state desorption/reaction step. The effect of the reaction/adsorption recycle stream is also evident in this step. The difference in concentration profiles of this step and the conventional PSAR unit are due to the difference in capacitance profiles of their respective reaction/adsorption steps.

Figure 3.25 illustrates the hydrogen concentration profiles at the end of each step. Profiles for this model are close to their counterparts from the conventional PSAR unit.

Figure 3.26 illustrates the temperature profiles for all steps at the end of the steady state cycle. The temperature profiles for the reaction/pressurization, blowdown/reaction and desorption reaction steps are similar to the profiles

of the conventional PSAR unit. Due to the dilution of the feed concentrations with the recycle stream concentrations, the inlet temperature at the end of the reaction/adsorption step is lower than that of the conventional PSAR unit.

Results of total coverage of the solid phase are illustrated in Table 3.7. The overall higher relative solid phase occupation, relative to conventional PSAR unit, is a direct result of recycling a higher reactive components concentration streams with the fresh feed. Capacitance profiles for each of the reactive components are illustrated in Figure 3.28.

Three dimensional drawings demonstrating the transient and Spatial change in concentration and temperature profiles are illustrated in Appendix D.

The approach to cyclic state for this model is illustrated in Figure 3.29. It takes twenty cycles for this model to reach steady state.

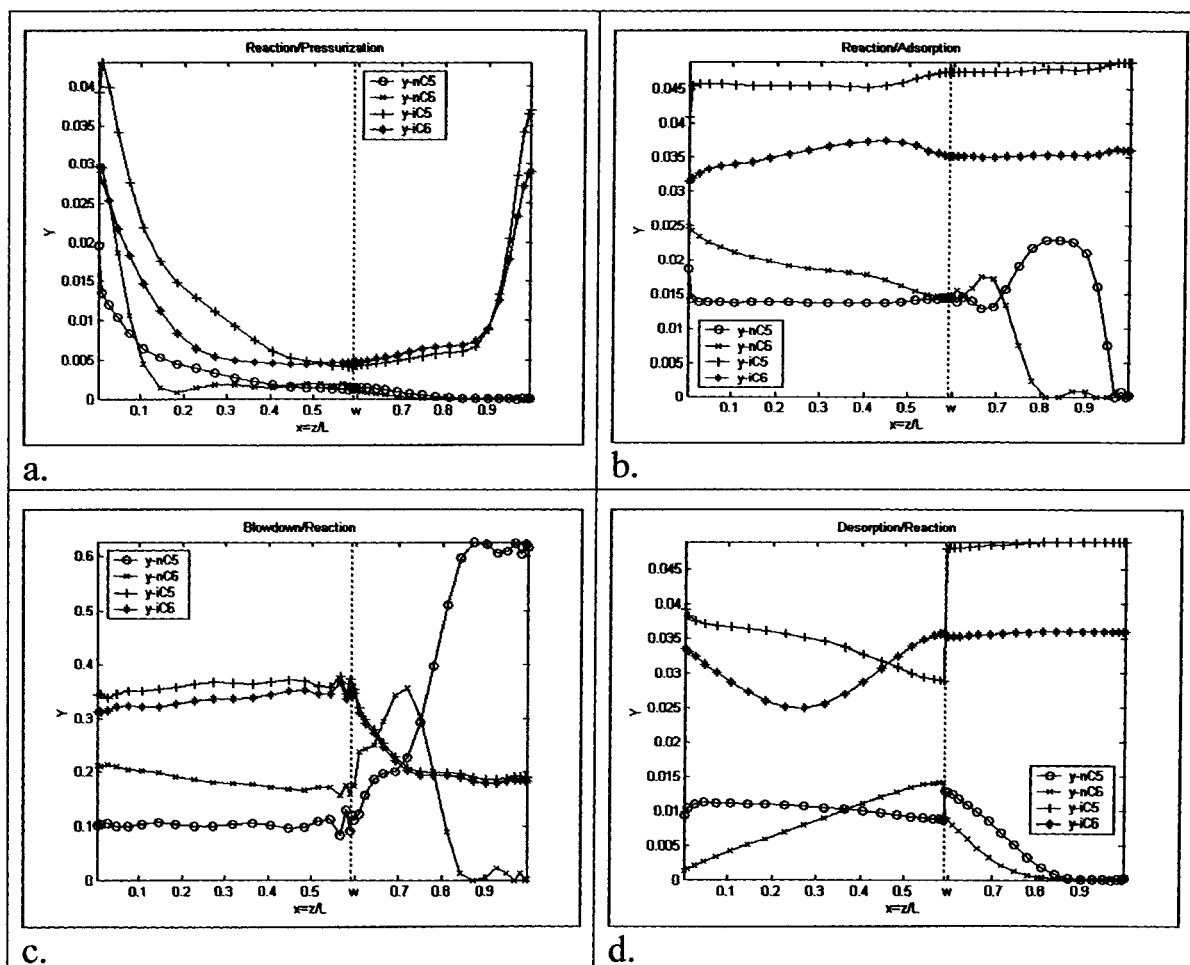


Figure 3.24: Gas phase concentration profiles for reactive components in the PSAR bed at the end of cyclic steady state:

- a.) reaction/pressurization,
- b.) reaction/adsorption,
- c.) blowdown/reaction ,
- d.) desorption/reaction.

Parametric values are in Table 3.3. (PSAR with waste recycled to feed/self regeneration).



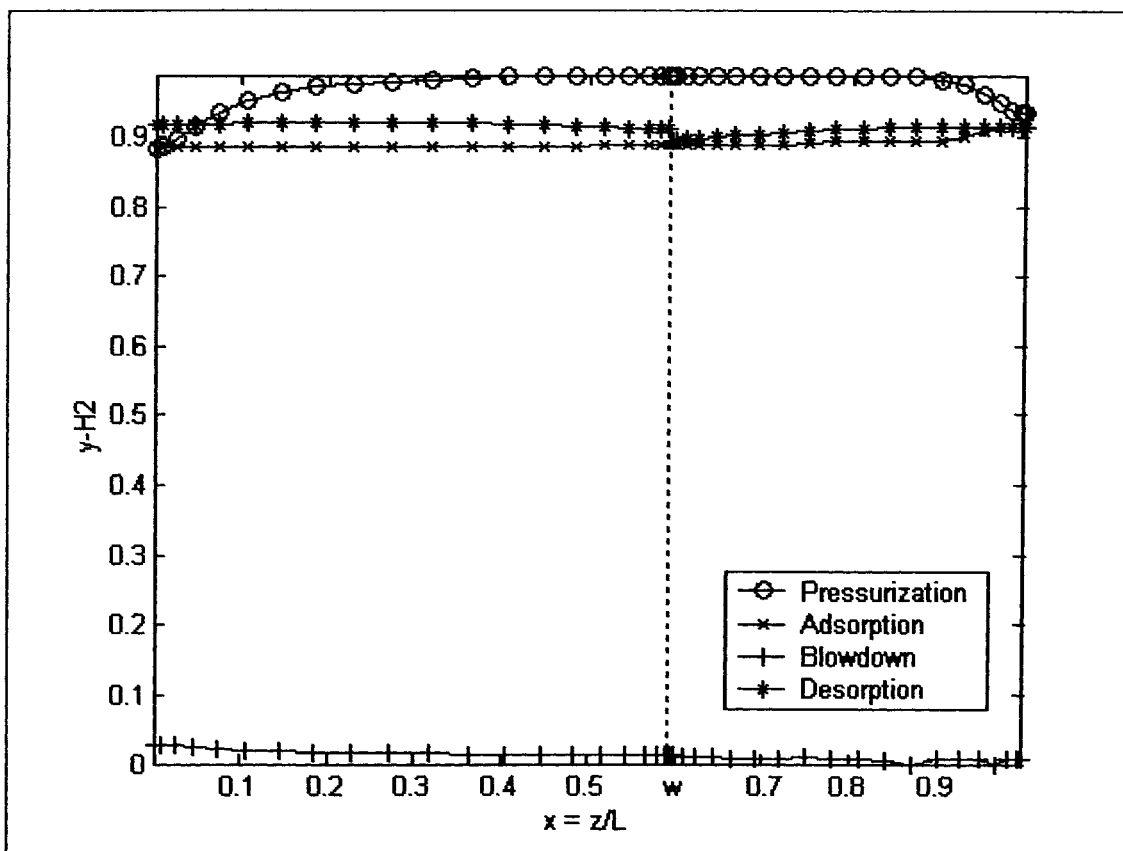


Figure 3.25: Gas phase concentration profiles for  $H_2$  in the PSAR bed at the end of cyclic steady state. Parametric values are in Table 3.3. (PSAR with waste recycled to feed/self regeneration).

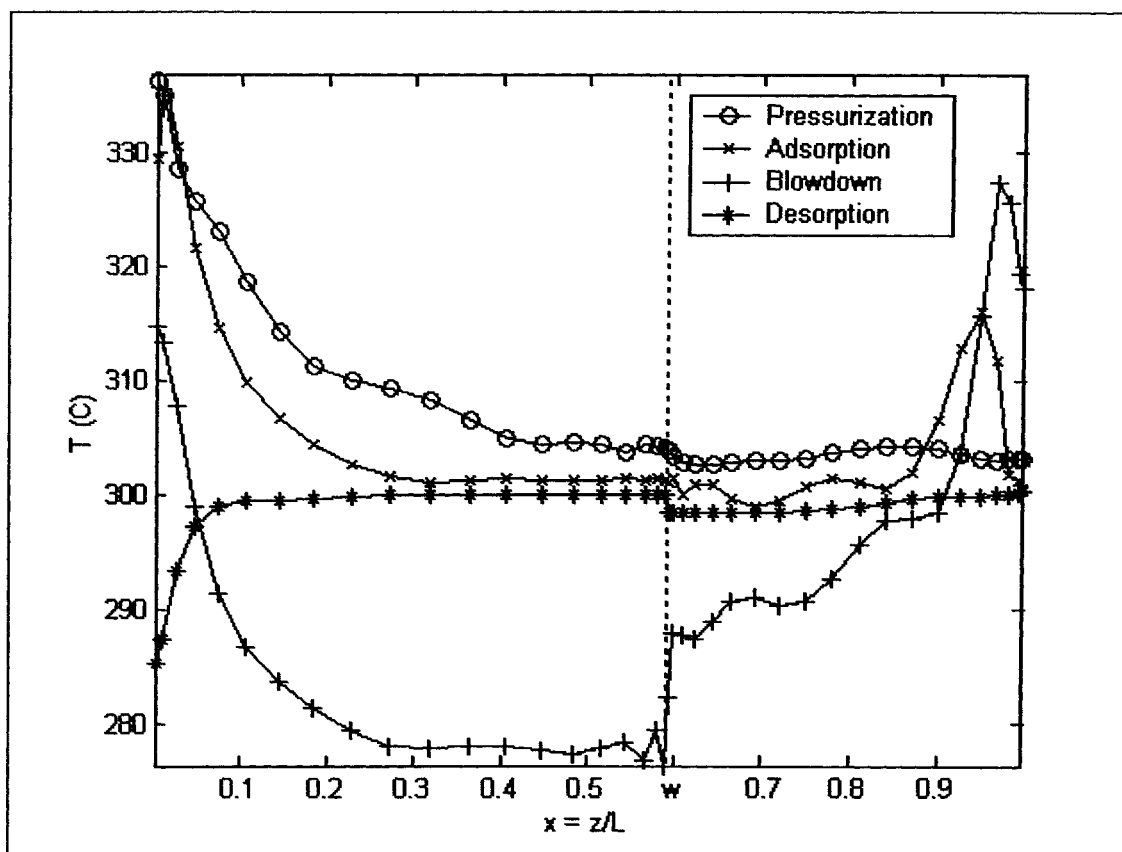


Figure 3.26: Temperature Profiles in the bed at the end of cyclic steady state. Parametric values are in Table 3.3. (PSAR with waste recycled to feed/self regeneration).

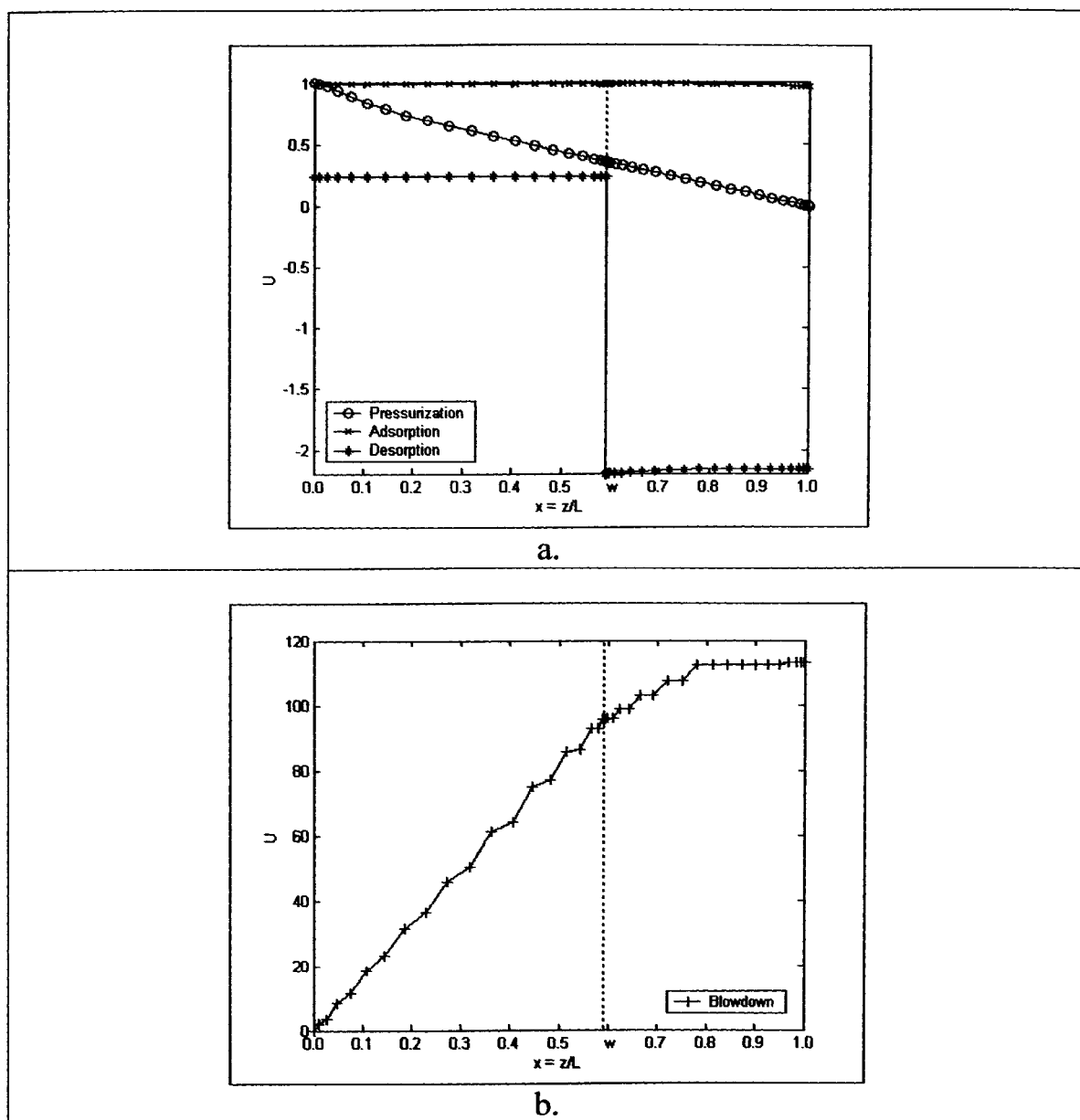


Figure 3.27: Velocity Profiles in the bed at the end of cyclic steady state:

- c. Pressurization, Adsorption and Desorption steps Profiles.
- d. Blowdown step profile.

Parametric values are in Table 3.3. (PSAR with waste recycled to feed/self regeneration).

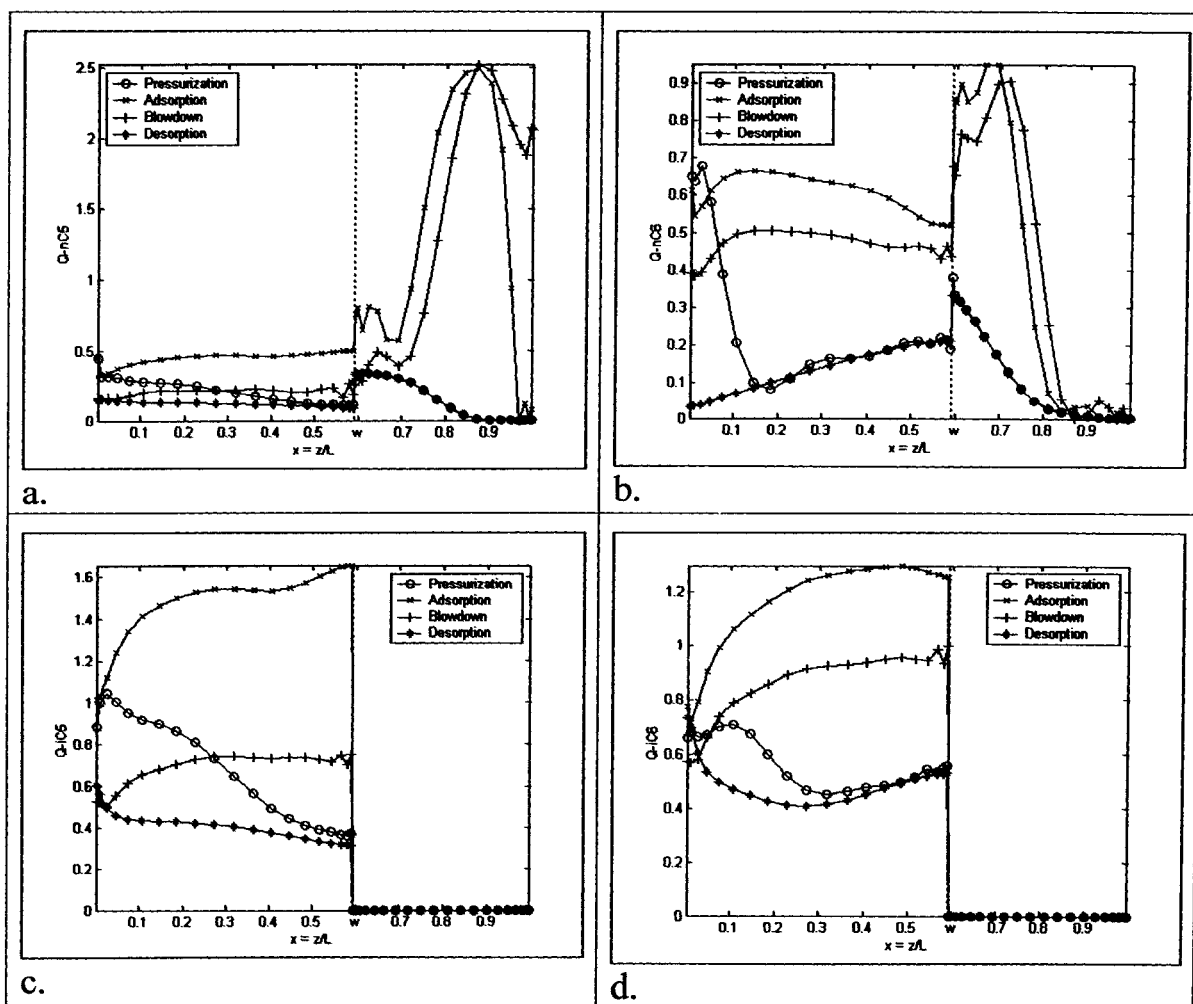


Figure 3.28: Solid phase capacitance profiles for reactive components in the PSAR bed at the end of cyclic steady state:

- a.) n-C<sub>5</sub>,
- b.) n-C<sub>6</sub>,
- c.) i-C<sub>5</sub>,
- d.) i-C<sub>6</sub>.

Parametric values are in Table 3.3. (PSAR with waste recycled to feed/self regeneration).

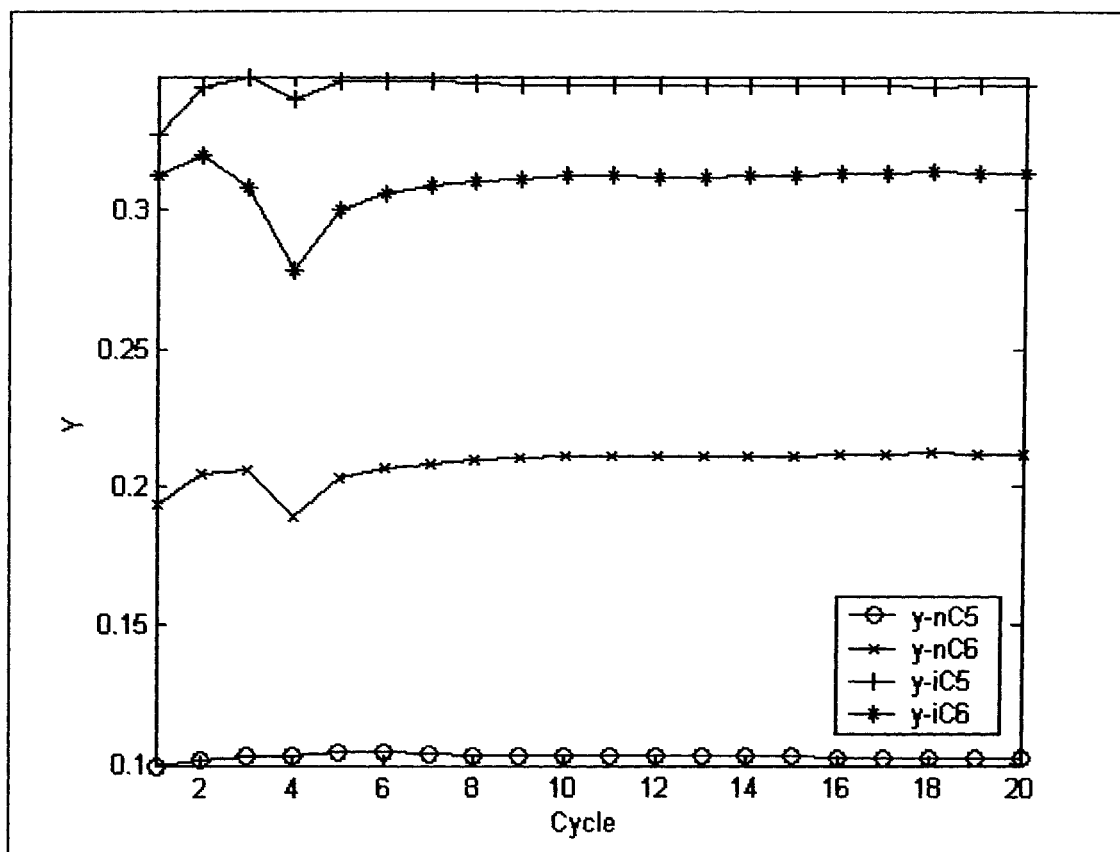


Figure 3.29: Approach to cyclic steady state, showing exit concentrations of reactants and products at end of Blowdown/Reaction step. Parametric values are in Table 3.3. (PSAR with waste recycled to feed/Self Regeneration).

Table 3.7: Percentage Relative Occupation for reactive components of the solid phase for both catalyst and adsorber sections (PSAR with waste recycled to feed/Self Regeneration).

Component	Pressurization		Adsorption		Blowdown		Desorption	
	Catalyst	Adsorber	Catalyst	Adsorber	Catalyst	Adsorber	Catalyst	Adsorber
n-C <sub>5</sub>	3.22	3.22	7.02	29.94	3.19	30.24	1.87	3.17
n-C <sub>6</sub>	7.50	7.29	20.90	29.38	16.21	31.62	4.51	7.22
i-C <sub>5</sub>	10.58	0.00	23.16	0.00	10.85	0.00	6.23	0.00
i-C <sub>6</sub>	18.91	0.00	40.15	0.00	29.71	0.00	16.11	0.00
Total	40.20	10.51	91.23	59.32	59.96	61.86	28.72	10.38

### 3.6.3 Overall Comparison of PSAR Systems

In this section, we compare models against each other to determine the best practical model. Since all models perform the separation task adequately, we need different criteria to judge the effectiveness of models. The objective of this research is to produce isomers. Thus, we chose the exit concentration of isomers during the reaction/adsorption step and process yield to be the main judging criteria. The full reaction/adsorption profile, at the end of cyclic steady state, for iso-pentane is plotted in Figure 3.30a. A similar plot for iso-hexane is plotted in Figure 3.30b. Values for exit concentrations of iso-pentane and iso-hexane, at the end of reaction/adsorption cyclic steady state are reported in Table 3.8.

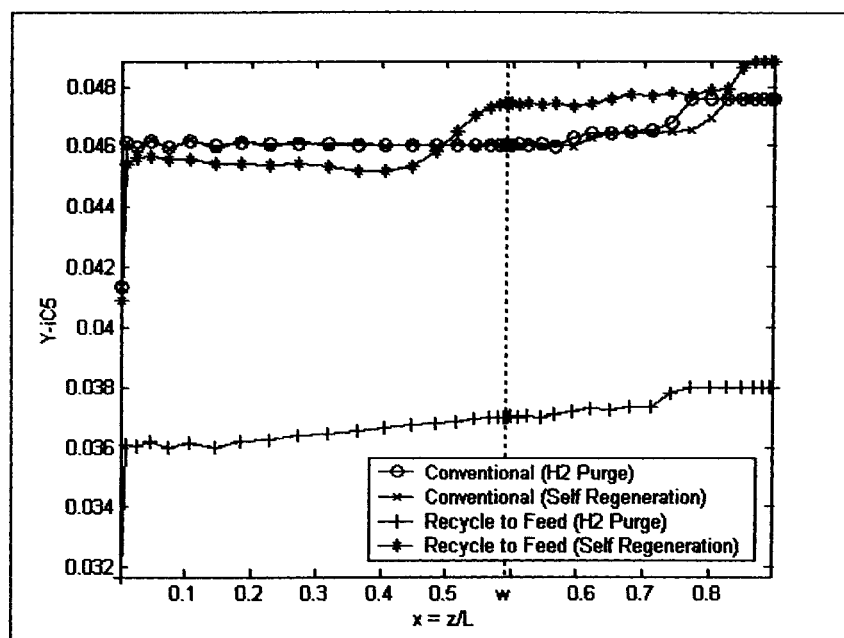
As illustrated in Figure 3.30a, the system that produces the highest concentration of iso-pentane is the one that recycles waste stream to feed and uses part of the product stream as purge stream. The system is fully described in section 3.6.2.2 of this chapter. Also, it can be concluded from the figures that the system producing the least concentration of desired product is the system that recycles the waste to the feed and uses  $H_2$  as the purge stream. This system is fully described in section 3.6.2.1. The rest of the systems produce product concentrations that fall between the two pre-mentioned systems.

Figure 3.30b illustrates concentration profiles for all models at the reaction/adsorption step. The system that produces the highest concentrations of iso-pentane is the conventional PSAR model that uses part of the product stream as a purge stream. The system is fully described in section 3.6.1.2 of this chapter. Also, it can be concluded from the figures that the system producing the least concentration of desired product is the system that recycles the waste to the feed and uses  $H_2$  as the purge stream. This system is fully described in section 3.6.2.1. The rest of the systems produce product concentrations that fall between the two pre-mentioned systems.

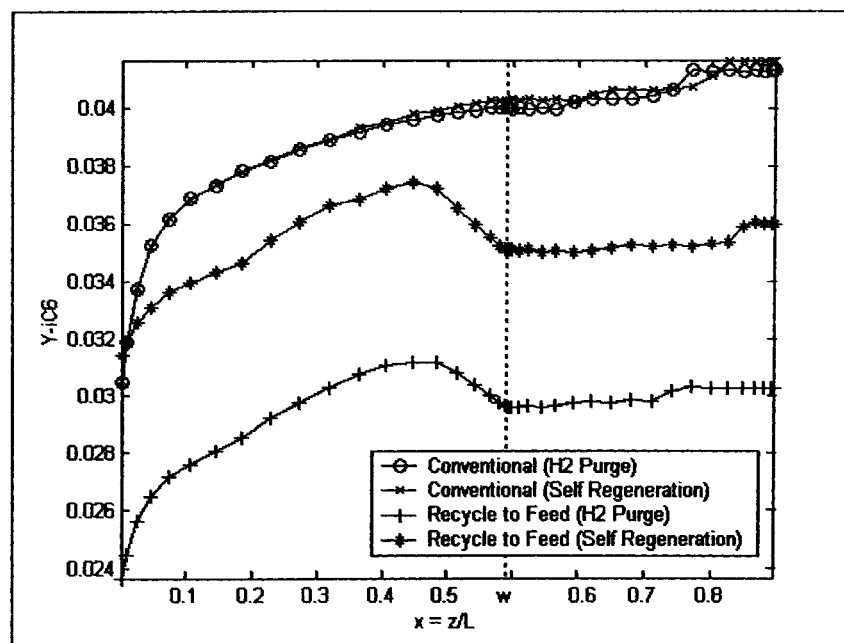
The yield of conventional PSAR units is 66.2 %. The yield of recycle models is 100%.

To conclude and summarize our findings in this section, the best suitable model for PSAR systems is the one that recycles the waste to the feed stream and uses portion of the product stream as a purge stream.





a.



b.

Figure 3.30: Products' profiles for all models at the end of cyclic steady state reaction/adsorption step:

- a. iso-pentane
- b. iso-hexane

Table 3.8: Exit concentrations of iso-pentane and iso-hexane and process yields for each of the models at the end of steady state cyclic reaction/adsorption step.

<b>Model</b>	<b>Iso-Pentane Exit Molar Fraction</b>	<b>Iso-Hexane Exit Molar Fraction</b>	<b>% Yield</b>
Conventional PSAR (H <sub>2</sub> Purge)	0.0475	0.0412	66.2
Conventional PSAR (Self Regeneration)	0.0476	0.0416	66.2
PSAR with waste recycled to feed (H <sub>2</sub> Purge)	0.0380	0.0303	100.0
PSAR with waste recycled to feed (Self Regeneration)	0.0489	0.0360	100.0

## Nomenclature

$A_H$	heat of adsorption [cal/mol]
$B$	dimensionless adiabatic temperature rise [-] $= (-\Delta H_{ads}) / (C_{ps} T_f)$
$c_T$	total gas concentration in the column [mol/cm <sup>3</sup> ]
$c_{Tf}$	total feed gas concentration [mol/cm <sup>3</sup> ]
$C_o$	total gas concentration in the column [mol/cm <sup>3</sup> ]
$C_T$	dimensionless total gas concentration in the column [-]
$C_{pg}$	heat capacity of the gas phase [J/(mol.K)]
$C_{ps}$	heat capacity of the adsorbent [J/(g.K)]
$Da_t$	true Damkohler number [-] = $\omega \frac{k_1 L}{u_f}$
$D_A$	pore diffusivity of component A [cm <sup>2</sup> /s]
$D_L$	axial mass dispersion coefficient [cm <sup>2</sup> /s]
$d_C$	column diameter [cm]
$h$	overall heat transfer coefficient [WAm <sup>2</sup> /K]
$(-\Delta H_{ads})$	isosteric heat of adsorption [J/mol]
$k_{gl}$	global mass-transfer coefficient [cm/s]
$K_{ads}$	adsorption equilibrium constant [bar <sup>-1</sup> ] = $K_o \exp(-A_H/R/T)$
$K_{C1}$	equilibrium reaction rate constant for nC <sub>5</sub> [-]
$K_{C2}$	equilibrium reaction rate constant for nC <sub>6</sub> [-]
$K_O$	limiting adsorption equilibrium constant [bar <sup>-1</sup> ]
$k_{1,1}$	forward reaction rate constant for nC <sub>5</sub> [cm <sup>3</sup> /g of cat/s]
$k_{1,2}$	forward reaction rate constant for nC <sub>6</sub> [cm <sup>3</sup> /g of cat/s]
$K_L$	axial bed thermal conductivity [W/(m.K)]
$L$	length of the PSA column [cm]
$n$	coefficient of Nitta et al. isotherm [-]
$N_f$	number of film mass-transfer units [-]
$N_w$	number of wall heat-transfer units [-] = $4hL / (d_c u_f C_{pg} c_{Tf} \varepsilon)$
$P$	total pressure in the column [bar]
$Pe$	mass Peclet number [-]
$Pe_H$	thermal Peclet number [-] = $u_f L C_{pg} c_{Tf} / K_L$
$P_H$	constant high pressure during adsorption step [bar]

$P_L$	constant low pressure during desorption step [bar]
$\langle q_A \rangle$	average adsorbed-phase concentration [mol/kg]
$q_{A,ref}$	adsorbed-phase concentration at equilibrium with $y_{Af}$ at $P_H$ and $T_f$ [mol/kg]
$q_{max}$	maximum adsorbed-phase concentration [mol/kg]
$Q_A$	dimensionless adsorbed-phase concentration [-] = $\langle q_A \rangle / q_{max}$
$R$	ideal gas constant [bar.cm <sup>3</sup> /mol/K]
$S$	Reactor Section Purge Velocity Ratio [-]
$t$	time [s]
$T$	column gas temperature [K]
$T_f$	feed gas temperature [K]
$\bar{T}$	dimensionless column gas temperature [-] = $(T - T_f) / T_f$
$u$	interstitial velocity [cm/s]
$u_f$	interstitial feed velocity [cm/s]
$u_p$	purge gas velocity [cm/s]
$U$	dimensionless interstitial velocity [-] = $u / u_f$
$V_1$	First PSAR Vessel
$V_2$	Second PSAR Vessel
$V_3$	A container used to hold effluent of blowdown/reaction step.
$x$	dimensionless axial coordinate in the column [-] = $z / L$
$y_A$	mole fraction of component A in the bulk phase in the column [-]
$y_{Af}$	mole fraction of component A in the feed [-]
$y_{Aj}$	mole fraction of component A in the bulk phase in bed i [-]
$y_{Bf}$	mole fraction of component B in the feed [-]
$y_{Bj}$	mole fraction of component B in the bulk phase in bed i [-]
$y_{AL}$	mole fraction of component A at the exit of the column [-]
$\langle y_{A2} \rangle$	average mole fraction of the sorbate in the pores of the adsorbent pellet in bed 2 [-]
$y_{A,eq}$	equilibrium mole fraction of component A for isomerization reaction [-]
$z$	axial coordinate in the column [cm]

## Greek Letters

$v_1$	dimensionless axial coordinate in the catalyst-bed region [-]
$v_2$	dimensionless axial coordinate in the adsorbent-bed region [-]
$\varepsilon_1$	bed void fraction [-]

$\varepsilon_2$	adsorbent void fraction [-]
$\zeta_H$	thermal capacity factor [-] = $(1 - \varepsilon_1 - \varepsilon_2)\rho_s C_{ps} / (\alpha_{Tf} C_{pg})$
$\zeta_m$	mass capacity factor [-]
$\theta_{A,,ref}$	coverage of adsorbent at $y_{Af}$ and $P_H$ [-]
$\rho_s$	apparent density of the adsorbent [g/cm <sup>3</sup> ]
$\tau$	dimensionless time [-] = $u_f t / L$
$\gamma_f$	dimensionless heat of adsorption [-] = $(-\Delta H_{ads}) / (RT_f)$

### Subscripts

A	n-pentane
B	n-hexane
C	i-hexane
D	n-hexane
f	feed
I	inert (Nitrogen / Hydrogen)
P	Purge
R	Recycle
T	total
1	Reactor Section
2	Adsorber Section

## CHAPTER 4

### PSARM MODELING FOR n-C<sub>5</sub>, i-C<sub>5</sub>, n-C<sub>6</sub>, i-C<sub>6</sub> SYSTEM with H<sub>2</sub> SEPARATION MEMBRANE

#### 4.1 MODEL ASSUMPTIONS

All assumptions outlined in previous chapters are also applicable to the model developed in this chapter. In addition, linear driving force is assumed for hydrogen migration through the membrane section. The data, used to build the hydrogen membrane, are taken from the paper by Morreale et al. [51].

#### 4.2 PSARM PROCESS DESCRIPTION

Figure 4.1 is the proposed process flow diagram for the isomerization of n-alkanes to isoalkanes in the PSARM unit. The unit consists of two columns. Each column consists of a catalyst-packed region followed by adsorbent packed region. The system is modeled as non-isothermal process containing five components (n-C<sub>5</sub>/i-C<sub>5</sub>/n-C<sub>6</sub>/i-C<sub>6</sub>/H<sub>2</sub>). The hydrogen membrane is modeled as a group of adjacent tubes stacked together along the outside surface of the adsorption section. Figure 4.2 illustrates cross sectional and isometric views of the vessel topology.

The cyclic steps shown in Figure 4.3 are as follow:

**Step 1: Pressurization/Reaction:** The unit is pressurized by feeding it a portion of the feedstock (at high pressure), injected into the catalyst bed. In the catalyst bed, partial conversion of n-C<sub>5</sub> and n-C<sub>6</sub> to i-C<sub>5</sub> and i-C<sub>6</sub>, respectively, takes place. The unit is not open for hydrogen permeation in this step to allow for less pressurization time. There is no effluent from the unit at this step. Thus, any hydrogen permeation will call for a more time that is lost to pressurize the unit.

**Step 2: Reaction/Adsorption:** The feedstock, at high pressure, is fed to the catalyst bed where conversion of n-C<sub>5</sub>/n-C<sub>6</sub> to i-C<sub>5</sub>/i-C<sub>6</sub>, respectively, takes place. Then it enters the adsorbent region where

unreacted n-C<sub>5</sub> and n-C<sub>6</sub> are adsorbed and part of H<sub>2</sub> is filtered through the hydrogen membrane. The effluent from the unit, composed of i-C<sub>5</sub>, i-C<sub>6</sub> and hydrogen, is fed to H<sub>2</sub> PSA unit where i-C<sub>5</sub> and i-C<sub>6</sub> are separated and taken off as process product. H<sub>2</sub> is recycled to the process. This step continues until the adsorbent bed reaches a specified saturation limit. Then, feed is shut off, and step 3 is introduced. Although not covered in this study, the pure hydrogen produced from the membrane side can be utilized to boost hydrogen to hydrocarbon ratio of recycle streams. This is very crucial in recycling waste streams to the feed because it prevents cracking.

**Step 3: Blowdown/Reaction:** The unit is depressurized to a lower pressure level in the same direction to that of the feed flow. Desorption of n-C<sub>5</sub> takes place in the adsorbent region, followed by partial isomerization in the catalyst region. A gas stream containing all components of the system exits the unit. Usually, this stream is considered as waste stream and discharged off in most conventional PSA processes. In the present case, however, the blowdown stream should be utilized since it contains considerable portion of i-C<sub>5</sub> and i-C<sub>6</sub>. The utilization of this gas stream is also studied in this section of the thesis. Hydrogen permeation in this step is considered a waste, especially when recycling the effluent of this step with the fresh feed to the second unit running in reaction/adsorption step. In such a case, the hydrogen removed through permeation should be compensated in the recycle stream to maintain constant hydrogen to hydrocarbon ratio. Thus, Hydrogen permeation does not take place during this step.

**Step 4: Desorption/Reaction:** Hydrogen gas, which is considered as inert, is introduced simultaneously to reactor and adsorber beds at low pressure and different velocities. Alternatively, a portion of step 2 products can be introduced into the unit in the same manner explained. This step desorbs the remaining n-C<sub>5</sub> and n-C<sub>6</sub> from the adsorbent and catalyst beds. The purge stream is introduced from both ends of the vessel. The waste stream is collected from the interface region. Hydrogen permeation does not take place during this step. Similarly to the previous step, hydrogen permeation in this step is considered a waste, especially when recycling the effluent of this step with the fresh feed to the second unit running in reaction/adosorption step. In such a case, the hydrogen removed through permeation should be compensated in the recycle stream to maintain constant hydrogen to hydrocarbon ratio. Thus,

hydrogen permeation does not take place during this step. In the study by Al-Juhani [1], the resulting stream was considered a waste. In this study, this stream is combined with the fresh feed of step 1 to maximize conversion of  $n\text{-C}_5/n\text{C}_6$  to  $i\text{-C}_5/i\text{C}_6$  and recovery of product.



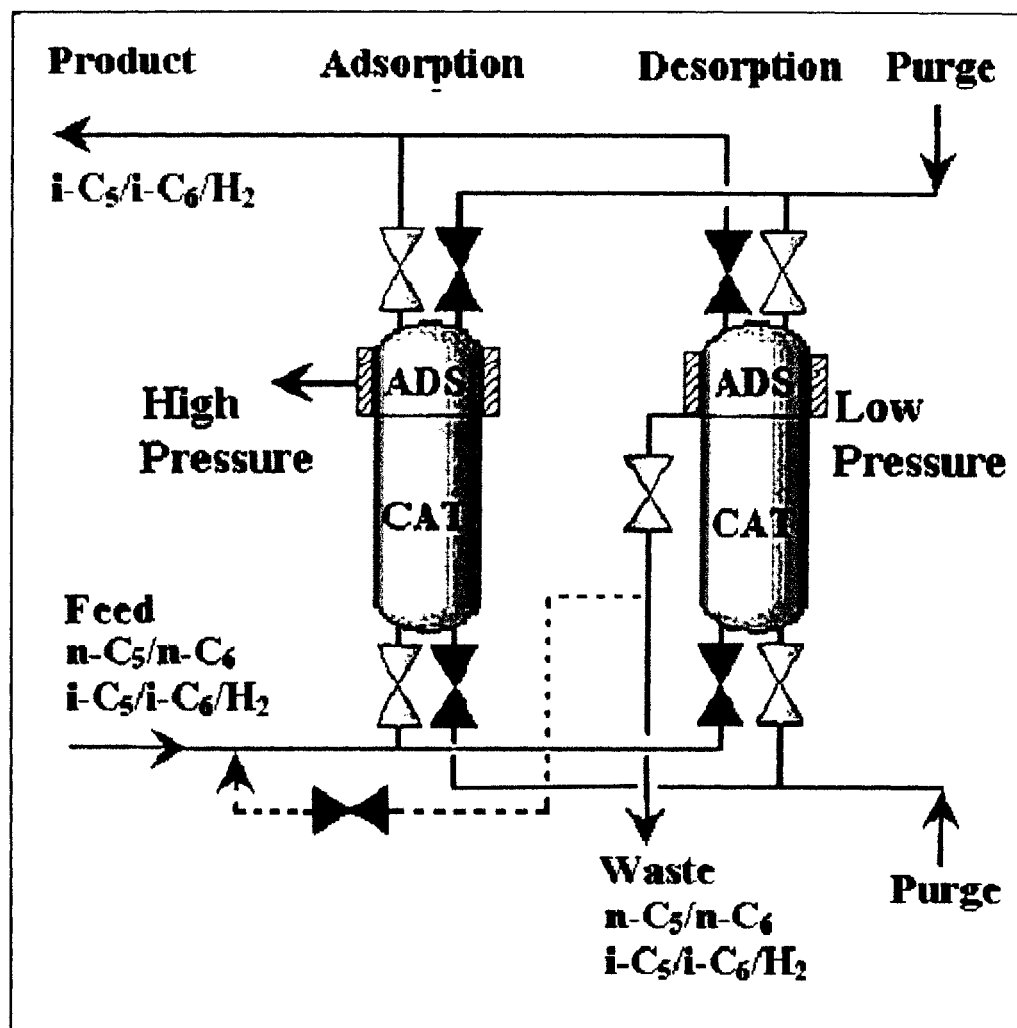


Figure 4.1: Flow diagram for the Combined Isomerization Reactor/Adsorber /Membrane Process.

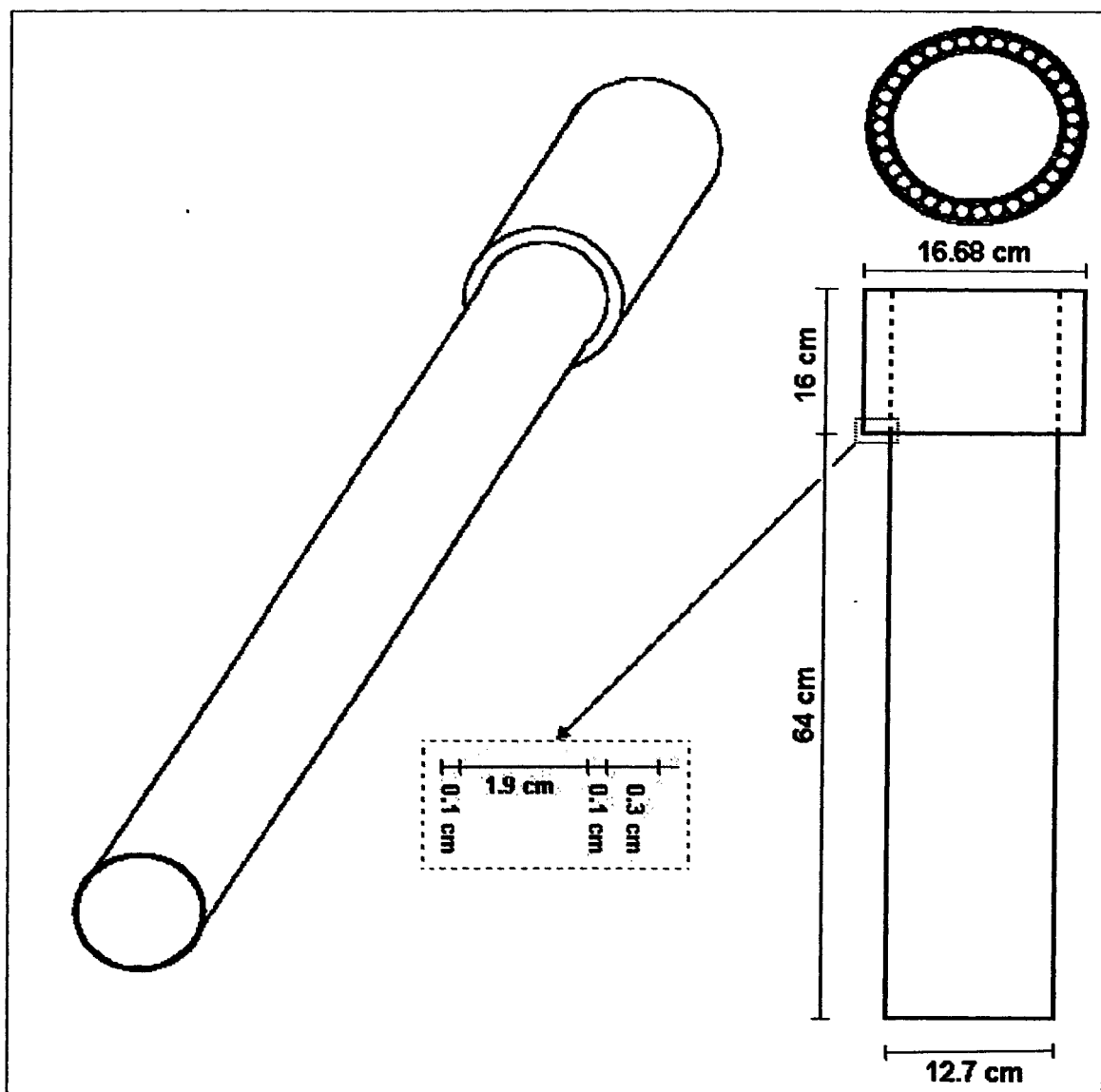


Figure 4.2: Cross sectional and isometric views of the PSARM vessel topology.

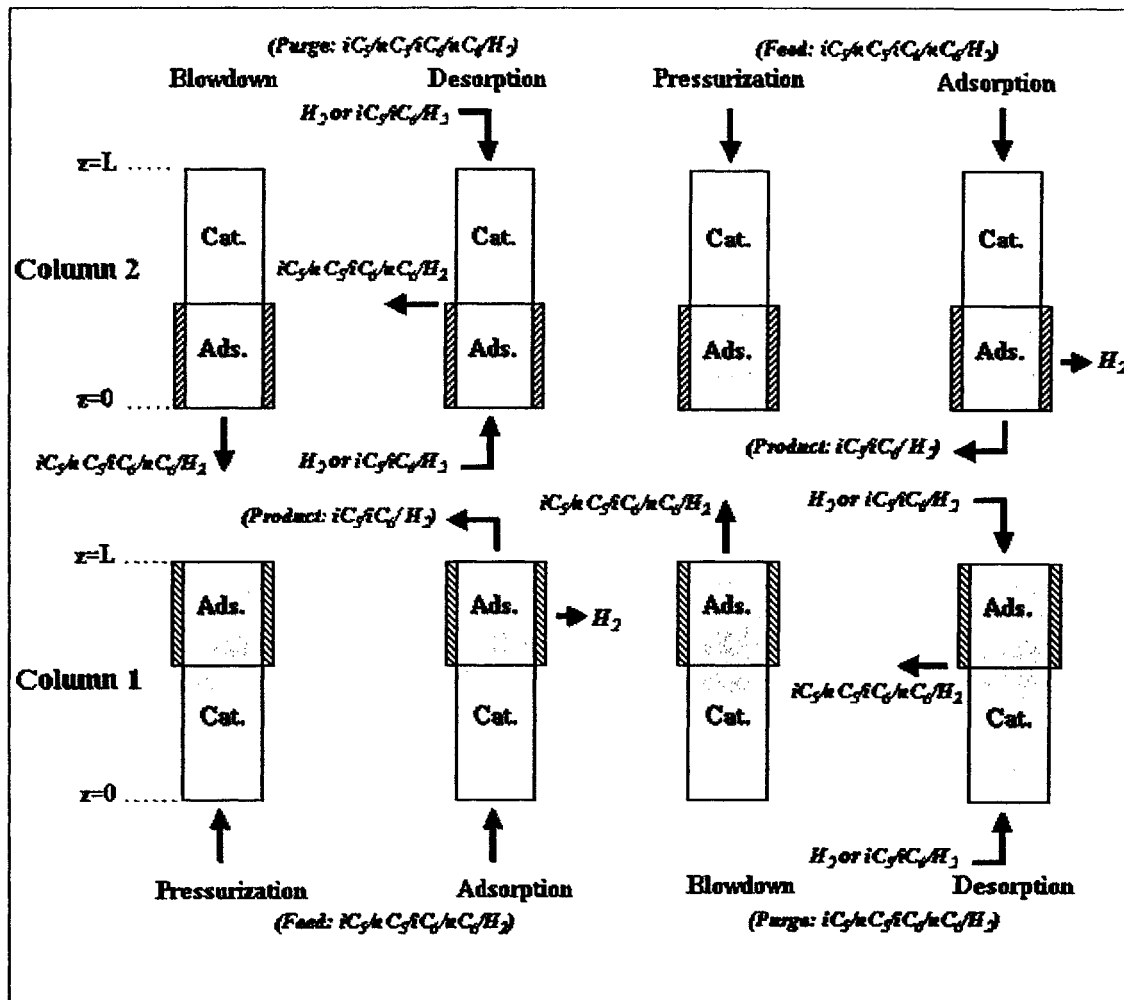


Figure 4.3: Proposed Cyclic Steps for PSARM Unit.

### 4.3 MODEL EQUATIONS

The normalized equations developed in chapter III are also applicable to this chapter with minor modifications to account for permeation effects.

The model assumptions in chapters II and III are also valid in this chapter. In addition, linear driving force is assumed in migrating hydrogen through the membrane. Thus, the final form of the model equations becomes:

Step 1 (Reaction/Pressurization)

$$\frac{\partial y_{A1}}{\partial \tau} = \frac{1}{\omega^2} \frac{1}{Pe} \frac{\partial^2 y_{A1}}{\partial v_1^2} - \frac{1}{\omega} \frac{\partial(U_1 y_{A1})}{\partial v_1} - \frac{y_{A1}}{C_T} \frac{\partial C_T}{\partial \tau} - \frac{Da_{t1}}{\omega} \left[ y_{A1} - \frac{y_{C1}}{K_{C1}} \right] - \zeta_{mA1} \frac{\partial Q_{A1}}{\partial \tau} \quad (4.2)$$

$$\frac{\partial y_{B1}}{\partial \tau} = \frac{1}{\omega^2} \frac{1}{Pe} \frac{\partial^2 y_{B1}}{\partial v_1^2} - \frac{1}{\omega} \frac{\partial(U_1 y_{B1})}{\partial v_1} - \frac{y_{B1}}{C_T} \frac{\partial C_T}{\partial \tau} - \frac{Da_{t2}}{\omega} \left[ y_{B1} - \frac{y_{D1}}{K_{C2}} \right] - \zeta_{mB1} \frac{\partial Q_{B1}}{\partial \tau} \quad (4.3)$$

$$\frac{\partial y_{C1}}{\partial \tau} = \frac{1}{\omega^2} \frac{1}{Pe} \frac{\partial^2 y_{C1}}{\partial v_1^2} - \frac{1}{\omega} \frac{\partial(U_1 y_{C1})}{\partial v_1} - \frac{y_{C1}}{C_T} \frac{\partial C_T}{\partial \tau} + \frac{Da_{t1}}{\omega} \left[ y_{A1} - \frac{y_{C1}}{K_{C1}} \right] - \zeta_{mC1} \frac{\partial Q_{C1}}{\partial \tau} \quad (4.4)$$

$$\frac{\partial y_{D1}}{\partial \tau} = \frac{1}{\omega^2} \frac{1}{Pe} \frac{\partial^2 y_{D1}}{\partial v_1^2} - \frac{1}{\omega} \frac{\partial(U_1 y_{D1})}{\partial v_1} - \frac{y_{D1}}{C_T} \frac{\partial C_T}{\partial \tau} + \frac{Da_{t2}}{\omega} \left[ y_{B1} - \frac{y_{D1}}{K_{C2}} \right] - \zeta_{mD1} \frac{\partial Q_{D1}}{\partial \tau} \quad (4.5)$$

$$\frac{\partial y_{H_2,1}}{\partial \tau} = \frac{1}{\omega^2} \frac{1}{Pe} \frac{\partial^2 y_{H_2,1}}{\partial v_1^2} - \frac{1}{\omega} \frac{\partial(U_1 y_{H_2,1})}{\partial v_1} - \frac{y_{H_2,1}}{C_T} \frac{\partial C_T}{\partial \tau} \quad (4.6)$$

$$\frac{\partial U_1}{\partial v_1} = - \frac{\omega}{C_T} \frac{\partial C_T}{\partial \tau} \quad (4.7)$$

$$(C_T + \zeta_{H,1}) \frac{\partial \bar{T}_1}{\partial \tau} = \frac{1}{\omega^2} \frac{1}{Pe_H} \frac{\partial^2 \bar{T}_1}{\partial v_1^2} - \frac{C_T}{\omega} \frac{\partial}{\partial v_1} [U(\bar{T}_1 + 1)] + \sum F_{i,1} \zeta_H \frac{\partial Q_i}{\partial \tau} + \sum E_i (-r_{A1}) - N_w (\bar{T}_1 - \bar{T}_{w1}) \quad (4.8)$$

$$\frac{\partial y_{A2}}{\partial \tau} = \frac{1}{(1-\omega)^2} \frac{1}{Pe} \frac{\partial^2 y_{A2}}{\partial v_2^2} - \frac{1}{(1-\omega)} \frac{\partial(U_2 y_{A2})}{\partial v_2} - \frac{y_{A2}}{C_T} \frac{\partial C_T}{\partial \tau} - \zeta_{mA2} \frac{\partial Q_{A2}}{\partial \tau} \quad (4.9)$$

$$\frac{\partial y_{B2}}{\partial \tau} = \frac{1}{(1-\omega)^2} \frac{1}{Pe} \frac{\partial^2 y_{B2}}{\partial v_2^2} - \frac{1}{(1-\omega)} \frac{\partial(U_2 y_{B2})}{\partial v_2} - \frac{y_{B2}}{C_T} \frac{\partial C_T}{\partial \tau} - \zeta_{mB2} \frac{\partial Q_{B2}}{\partial \tau} \quad (4.10)$$

$$\frac{\partial y_{C2}}{\partial \tau} = \frac{1}{(1-\omega)^2} \frac{1}{Pe} \frac{\partial^2 y_{C2}}{\partial v_2^2} - \frac{1}{(1-\omega)} \frac{\partial(U_2 y_{C2})}{\partial v_2} - \frac{y_{C2}}{C_T} \frac{\partial C_T}{\partial \tau} \quad (4.11)$$

$$\frac{\partial y_{D2}}{\partial \tau} = \frac{1}{(1-\omega)^2} \frac{1}{Pe} \frac{\partial^2 y_{D2}}{\partial v_2^2} - \frac{1}{(1-\omega)} \frac{\partial(U_2 y_{D2})}{\partial v_2} - \frac{y_{D2}}{C_T} \frac{\partial C_T}{\partial \tau} \quad (4.12)$$

$$\frac{\partial y_{H22}}{\partial \tau} = \frac{1}{(1-\omega)^2} \frac{1}{Pe} \frac{\partial^2 y_{H22}}{\partial v_2^2} - \frac{1}{(1-\omega)} \frac{\partial(U_2 y_{H22})}{\partial v_2} - \frac{y_{H22}}{C_T} \frac{\partial C_T}{\partial \tau} \quad (4.13)$$

$$\frac{\partial U_2}{\partial v_2} = -\frac{(1-\omega)}{C_T} \left( \frac{\partial C_T}{\partial \tau} - \frac{\partial M_{H2,2}}{\partial \tau} - \sum \zeta_{mi} \frac{\partial Q_i}{\partial \tau} \right) \quad (4.14)$$

$$(C_T + \zeta_{H,2}) \frac{\partial \bar{T}_2}{\partial \tau} = \frac{1}{\omega^2} \frac{1}{Pe_H} \frac{\partial^2 \bar{T}_2}{\partial v_2^2} - \frac{1}{\omega} C_T \frac{\partial}{\partial v_2} [U(\bar{T}_2 + 1)] + \sum F_{i,2} \zeta_{H,2} \frac{\partial Q_i}{\partial \tau} - N_w (\bar{T}_2 - \bar{T}_{w2}) \quad (4.15)$$

The boundary conditions are

$$v_1 = 0, \tau > 0 \quad -\frac{1}{Pe} \frac{\partial y_{A1}}{\partial v_1} = U_1 \Big|_{v_1=0} \omega (y_{Af} - y_{A1}) \quad (4.16a)$$

$$v_1 = 0, \tau > 0 \quad -\frac{1}{Pe} \frac{\partial y_{B1}}{\partial v_1} = U_1 \Big|_{v_1=0} \omega (y_{Bf} - y_{B1}) \quad (4.16b)$$

$$v_1 = 0, \tau > 0 \quad -\frac{1}{Pe} \frac{\partial y_{C1}}{\partial v_1} = U_1 \Big|_{v_1=0} \omega (y_{Cf} - y_{C1}) \quad (4.16c)$$

$$v_1 = 0, \tau > 0 \quad -\frac{1}{Pe} \frac{\partial y_{D1}}{\partial v_1} = U_1 \Big|_{v_1=0} \omega (y_{Df} - y_{D1}) \quad (4.16d)$$

$$v_1 = 0, \tau > 0 \quad -\frac{1}{Pe} \frac{\partial y_{H21}}{\partial v_1} = U_1 \Big|_{v_1=0} \omega (y_{H2f} - y_{H21}) \quad (4.16e)$$

$$v_1 = 0, \tau > 0 \quad -\frac{1}{Pe_H} \frac{\partial \bar{T}_1}{\partial v_1} = U_1 \Big|_{v_1=0} \omega C_T \bar{T}_1 \quad (4.16f)$$

$$v_1 = 1, (v_2 = 0), \tau > 0 \quad y_{A1} = y_{A2} \quad (4.16g)$$

$$v_1 = 1, (v_2 = 0), \tau > 0 \quad y_{B1} = y_{B2} \quad (4.16h)$$

$$v_1 = 1, (v_2 = 0), \tau > 0 \quad y_{C1} = y_{C2} \quad (4.16i)$$

$$v_1 = 1, (v_2 = 0), \tau > 0 \quad y_{D1} = y_{D2} \quad (4.16j)$$

$$v_1 = 1, (v_2 = 0), \tau > 0 \quad y_{H21} = y_{H22} \quad (4.16k)$$

$$v_1 = 1, (v_2 = 0), \tau > 0 \quad -(1-\omega) D_A \frac{\partial y_{A1}}{\partial v_1} = -\omega D_A \frac{\partial y_{A2}}{\partial v_2} \quad (4.16l)$$

$$v_1 = 1, (v_2 = 0), \tau > 0 \quad -(1-\omega) D_A \frac{\partial y_{B1}}{\partial v_1} = -\omega D_A \frac{\partial y_{B2}}{\partial v_2} \quad (4.16m)$$

$$v_1 = 1, (v_2 = 0), \tau > 0 \quad -(1-\omega) D_A \frac{\partial y_{C1}}{\partial v_1} = -\omega D_A \frac{\partial y_{C2}}{\partial v_2} \quad (4.16n)$$

$$v_1 = 1, (v_2 = 0), \tau > 0 \quad -(1-\omega) D_A \frac{\partial y_{D1}}{\partial v_1} = -\omega D_A \frac{\partial y_{D2}}{\partial v_2} \quad (4.16o)$$

$$v_1 = 1, (v_2 = 0), \tau > 0 \quad -(1-\omega)D_A \frac{\partial y_{H_2 1}}{\partial v_1} = -\omega D_A \frac{\partial y_{H_2 2}}{\partial v_2} \quad (4.16p)$$

$$v_1 = 1, (v_2 = 0), \tau > 0 \quad U_1 = U_2 \quad (4.16q)$$

$$v_1 = 1, (v_2 = 0), \tau > 0 \quad -(1-\omega) \frac{\partial \bar{T}_1}{\partial v_1} = -\omega \frac{\partial \bar{T}_2}{\partial v_2} \quad (4.16r)$$

$$v_1 = 1, (v_2 = 0), \tau > 0 \quad \bar{T}_1 = \bar{T}_2 \quad (4.16s)$$

$$v_2 = 1, \tau > 0 \quad \frac{\partial y_{A2}}{\partial v_2} = 0 \quad (4.16t)$$

$$v_2 = 1, \tau > 0 \quad \frac{\partial y_{B2}}{\partial v_2} = 0 \quad (4.16u)$$

$$v_2 = 1, \tau > 0 \quad \frac{\partial y_{C2}}{\partial v_2} = 0 \quad (4.16v)$$

$$v_2 = 1, \tau > 0 \quad \frac{\partial y_{D2}}{\partial v_2} = 0 \quad (4.16w)$$

$$v_2 = 1, \tau > 0 \quad \frac{\partial y_{H_2 2}}{\partial v_2} = 0 \quad (4.16x)$$

$$v_2 = 1, \tau > 0 \quad U_2 = 0 \quad (4.16y)$$

$$v_2 = 1, \tau > 0 \quad \frac{\partial \bar{T}}{\partial v_2} = 0 \quad (4.16z)$$

## Step 2 (Reaction/Adsorption)

$$\frac{\partial y_{A1}}{\partial \tau} = \frac{1}{\omega^2} \frac{1}{Pe} \frac{\partial^2 y_{A1}}{\partial v_1^2} - \frac{1}{\omega} \frac{\partial(U_1 y_{A1})}{\partial v_1} - \frac{y_{A1}}{C_T} \frac{\partial C_T}{\partial \tau} - \frac{Da_{t1}}{\omega} \left[ y_{A1} - \frac{y_{C1}}{K_{C1}} \right] - \zeta_{mA1} \frac{\partial Q_{A1}}{\partial \tau} \quad (4.17)$$

$$\frac{\partial y_{B1}}{\partial \tau} = \frac{1}{\omega^2} \frac{1}{Pe} \frac{\partial^2 y_{B1}}{\partial v_1^2} - \frac{1}{\omega} \frac{\partial(U_1 y_{B1})}{\partial v_1} - \frac{y_{B1}}{C_T} \frac{\partial C_T}{\partial \tau} - \frac{Da_{t2}}{\omega} \left[ y_{B1} - \frac{y_{D1}}{K_{C2}} \right] - \zeta_{mB1} \frac{\partial Q_{B1}}{\partial \tau} \quad (4.18)$$

$$\frac{\partial y_{C1}}{\partial \tau} = \frac{1}{\omega^2} \frac{1}{Pe} \frac{\partial^2 y_{C1}}{\partial v_1^2} - \frac{1}{\omega} \frac{\partial(U_1 y_{C1})}{\partial v_1} - \frac{y_{C1}}{C_T} \frac{\partial C_T}{\partial \tau} + \frac{Da_{t1}}{\omega} \left[ y_{A1} - \frac{y_{C1}}{K_{C1}} \right] - \zeta_{mC1} \frac{\partial Q_{C1}}{\partial \tau} \quad (4.19)$$

$$\frac{\partial y_{D1}}{\partial \tau} = \frac{1}{\omega^2} \frac{1}{Pe} \frac{\partial^2 y_{D1}}{\partial v_1^2} - \frac{1}{\omega} \frac{\partial(U_1 y_{D1})}{\partial v_1} - \frac{y_{D1}}{C_T} \frac{\partial C_T}{\partial \tau} + \frac{Da_{t2}}{\omega} \left[ y_{B1} - \frac{y_{D1}}{K_{C2}} \right] - \zeta_{mD1} \frac{\partial Q_{D1}}{\partial \tau} \quad (4.20)$$

$$\frac{\partial y_{H_2 1}}{\partial \tau} = \frac{1}{\omega^2} \frac{1}{Pe} \frac{\partial^2 y_{H_2 1}}{\partial v_1^2} - \frac{1}{\omega} \frac{\partial(U_1 y_{H_2 1})}{\partial v_1} - \frac{y_{H_2 1}}{C_T} \frac{\partial C_T}{\partial \tau} \quad (4.21)$$

$$\frac{\partial U_1}{\partial v_1} = -\frac{\omega}{C_T} \frac{\partial C_T}{\partial \tau} \quad (4.22)$$

$$(C_T + \zeta_{H,1}) \frac{\partial \bar{T}_1}{\partial \tau} = \frac{1}{\omega^2} \frac{1}{Pe_H} \frac{\partial^2 \bar{T}_1}{\partial v_1^2} - \frac{C_T}{\omega} \frac{\partial}{\partial v_1} [U(\bar{T}_1 + 1)] + \sum F_{i,1} \zeta_H \frac{\partial Q_i}{\partial \tau} + \sum E_i (-r_{A,i}) - N_w (\bar{T}_1 - \bar{T}_{w1}) \quad (4.23)$$

$$\frac{\partial y_{A2}}{\partial \tau} = \frac{1}{(1-\omega)^2} \frac{1}{Pe} \frac{\partial^2 y_{A2}}{\partial v_2^2} - \frac{1}{(1-\omega)} \frac{\partial (U_2 y_{A2})}{\partial v_2} - \frac{y_{A2}}{C_T} \frac{\partial C_T}{\partial \tau} - \zeta_{mA2} \frac{\partial Q_{A2}}{\partial \tau} \quad (4.24)$$

$$\frac{\partial y_{B2}}{\partial \tau} = \frac{1}{(1-\omega)^2} \frac{1}{Pe} \frac{\partial^2 y_{B2}}{\partial v_2^2} - \frac{1}{(1-\omega)} \frac{\partial (U_2 y_{B2})}{\partial v_2} - \frac{y_{B2}}{C_T} \frac{\partial C_T}{\partial \tau} - \zeta_{mB2} \frac{\partial Q_{B2}}{\partial \tau} \quad (4.25)$$

$$\frac{\partial y_{C2}}{\partial \tau} = \frac{1}{(1-\omega)^2} \frac{1}{Pe} \frac{\partial^2 y_{C2}}{\partial v_2^2} - \frac{1}{(1-\omega)} \frac{\partial (U_2 y_{C2})}{\partial v_2} - \frac{y_{C2}}{C_T} \frac{\partial C_T}{\partial \tau} \quad (4.26)$$

$$\frac{\partial y_{D2}}{\partial \tau} = \frac{1}{(1-\omega)^2} \frac{1}{Pe} \frac{\partial^2 y_{D2}}{\partial v_2^2} - \frac{1}{(1-\omega)} \frac{\partial (U_2 y_{D2})}{\partial v_2} - \frac{y_{D2}}{C_T} \frac{\partial C_T}{\partial \tau} \quad (4.27)$$

$$\frac{\partial y_{H_2,2}}{\partial \tau} = \frac{1}{(1-\omega)^2} \frac{1}{Pe} \frac{\partial^2 y_{H_2,2}}{\partial v_2^2} - \frac{1}{(1-\omega)} \frac{\partial (U_2 y_{H_2,2})}{\partial v_2} - \frac{y_{H_2,2}}{C_T} \frac{\partial C_T}{\partial \tau} - \frac{\partial M_{H_2,2}}{\partial \tau} \quad (4.28)$$

$$\frac{\partial U_2}{\partial v_2} = -\frac{(1-\omega)}{C_T} \left( \frac{\partial C_T}{\partial \tau} - \frac{\partial M_{H_2,2}}{\partial \tau} - \sum \zeta_{mi} \frac{\partial Q_i}{\partial \tau} \right) \quad (4.29)$$

$$(C_T + \zeta_{H,2}) \frac{\partial \bar{T}_2}{\partial \tau} = \frac{1}{\omega^2} \frac{1}{Pe_H} \frac{\partial^2 \bar{T}_2}{\partial v_2^2} - \frac{1}{\omega} C_T \frac{\partial}{\partial v_2} [U(\bar{T}_2 + 1)] + \sum F_{i,2} \zeta_{H,2} \frac{\partial Q_i}{\partial \tau} - N_w (\bar{T}_2 - \bar{T}_{w2}) + \mu_H \frac{\partial M_{H_2,2}}{\partial \tau} \quad (4.30)$$

The boundary conditions are

$$v_1 = 0, \tau > 0 \quad -\frac{1}{Pe} \frac{\partial y_{A1}}{\partial v_1} = U_1 \Big|_{v_1=0} \omega (y_{Af} - y_{A1}) \quad (4.31a)$$

$$v_1 = 0, \tau > 0 \quad -\frac{1}{Pe} \frac{\partial y_{B1}}{\partial v_1} = U_1 \Big|_{v_1=0} \omega (y_{Bf} - y_{B1}) \quad (4.31b)$$

$$v_1 = 0, \tau > 0 \quad -\frac{1}{Pe} \frac{\partial y_{C1}}{\partial v_1} = U_1 \Big|_{v_1=0} \omega (y_{Cf} - y_{C1}) \quad (4.31c)$$

$$v_1 = 0, \tau > 0 \quad -\frac{1}{Pe} \frac{\partial y_{D1}}{\partial v_1} = U_1 \Big|_{v_1=0} \omega (y_{Df} - y_{D1}) \quad (4.31d)$$

$$v_1 = 0, \tau > 0 \quad -\frac{1}{Pe} \frac{\partial y_{H_2,1}}{\partial v_1} = U_1 \Big|_{v_1=0} \omega (y_{H_2f} - y_{H_2,1}) \quad (4.31e)$$

$$v_1 = 0, \tau > 0 \quad -\frac{1}{Pe_H} \frac{\partial \bar{T}_1}{\partial v_1} = U_1 \Big|_{v_1=0} \omega C_T \bar{T}_1 \quad (4.31f)$$

$$v_1 = 0, \tau > 0 \quad U_1 = 1 \quad (4.31g)$$

$$v_1 = 1, (v_2 = 0), \tau > 0 \quad y_{A1} = y_{A2} \quad (4.31h)$$

$$v_1 = 1, (v_2 = 0), \tau > 0 \quad y_{B1} = y_{B2} \quad (4.31i)$$

$$v_1 = 1, (v_2 = 0), \tau > 0 \quad y_{C1} = y_{C2} \quad (4.31j)$$

$$v_1 = 1, (v_2 = 0), \tau > 0 \quad y_{D1} = y_{D2} \quad (4.31k)$$

$$v_1 = 1, (v_2 = 0), \tau > 0 \quad y_{H_2 1} = y_{H_2 2} \quad (4.31l)$$

$$v_1 = 1, (v_2 = 0), \tau > 0 \quad -(1-\omega)D_A \frac{\partial y_{A1}}{\partial v_1} = -\omega D_A \frac{\partial y_{A2}}{\partial v_2} \quad (4.31m)$$

$$v_1 = 1, (v_2 = 0), \tau > 0 \quad -(1-\omega)D_A \frac{\partial y_{B1}}{\partial v_1} = -\omega D_A \frac{\partial y_{B2}}{\partial v_2} \quad (4.31n)$$

$$v_1 = 1, (v_2 = 0), \tau > 0 \quad -(1-\omega)D_A \frac{\partial y_{C1}}{\partial v_1} = -\omega D_A \frac{\partial y_{C2}}{\partial v_2} \quad (4.31o)$$

$$v_1 = 1, (v_2 = 0), \tau > 0 \quad -(1-\omega)D_A \frac{\partial y_{D1}}{\partial v_1} = -\omega D_A \frac{\partial y_{D2}}{\partial v_2} \quad (4.31p)$$

$$v_1 = 1, (v_2 = 0), \tau > 0 \quad -(1-\omega)D_A \frac{\partial y_{H_2 1}}{\partial v_1} = -\omega D_A \frac{\partial y_{H_2 2}}{\partial v_2} \quad (4.31q)$$

$$v_1 = 1, (v_2 = 0), \tau > 0 \quad U_1 = U_2 \quad (4.31r)$$

$$v_1 = 1, (v_2 = 0), \tau > 0 \quad -(1-\omega) \frac{\partial \bar{T}_1}{\partial v_1} = -\omega \frac{\partial \bar{T}_2}{\partial v_2} \quad (4.31s)$$

$$v_1 = 1, (v_2 = 0), \tau > 0 \quad \bar{T}_1 = \bar{T}_2 \quad (4.31t)$$

$$v_2 = 1, \tau > 0 \quad \frac{\partial y_{A2}}{\partial v_2} = 0 \quad (4.31u)$$

$$v_2 = 1, \tau > 0 \quad \frac{\partial y_{B2}}{\partial v_2} = 0 \quad (4.31v)$$

$$v_2 = 1, \tau > 0 \quad \frac{\partial y_{C2}}{\partial v_2} = 0 \quad (4.31w)$$

$$v_2 = 1, \tau > 0 \quad \frac{\partial y_{D2}}{\partial v_2} = 0 \quad (4.31x)$$

$$v_2 = 1, \tau > 0 \quad \frac{\partial y_{H_2 2}}{\partial v_2} = 0 \quad (4.31y)$$

$$v_2 = 1, \tau > 0 \quad \frac{\partial \bar{T}_2}{\partial v_2} = 0 \quad (4.31z)$$

Step 3 (Blowdown/Reaction/)

$$\frac{\partial y_{A1}}{\partial \tau} = \frac{1}{\omega^2} \frac{1}{Pe} \frac{\partial^2 y_{A1}}{\partial v_1^2} - \frac{1}{\omega} \frac{\partial(U_1 y_{A1})}{\partial v_1} - \frac{y_{A1}}{C_T} \frac{\partial C_T}{\partial \tau} - \frac{Da_n}{\omega} \left[ y_{A1} - \frac{y_{C1}}{K_{C1}} \right] - \zeta_{mA1} \frac{\partial Q_{A1}}{\partial \tau} \quad (4.32)$$



$$\frac{\partial y_{B1}}{\partial \tau} = \frac{1}{\omega^2} \frac{1}{Pe} \frac{\partial^2 y_{B1}}{\partial v_1^2} - \frac{1}{\omega} \frac{\partial(U_1 y_{B1})}{\partial v_1} - \frac{y_{B1}}{C_T} \frac{\partial C_T}{\partial \tau} - \frac{Da_{t2}}{\omega} \left[ y_{B1} - \frac{y_{D1}}{K_{C2}} \right] - \zeta_{mB1} \frac{\partial Q_{B1}}{\partial \tau} \quad (4.33)$$

$$\frac{\partial y_{C1}}{\partial \tau} = \frac{1}{\omega^2} \frac{1}{Pe} \frac{\partial^2 y_{C1}}{\partial v_1^2} - \frac{1}{\omega} \frac{\partial(U_1 y_{C1})}{\partial v_1} - \frac{y_{C1}}{C_T} \frac{\partial C_T}{\partial \tau} + \frac{Da_{t1}}{\omega} \left[ y_{A1} - \frac{y_{C1}}{K_{C1}} \right] - \zeta_{mC1} \frac{\partial Q_{C1}}{\partial \tau} \quad (4.34)$$

$$\frac{\partial y_{D1}}{\partial \tau} = \frac{1}{\omega^2} \frac{1}{Pe} \frac{\partial^2 y_{D1}}{\partial v_1^2} - \frac{1}{\omega} \frac{\partial(U_1 y_{D1})}{\partial v_1} - \frac{y_{D1}}{C_T} \frac{\partial C_T}{\partial \tau} + \frac{Da_{t2}}{\omega} \left[ y_{B1} - \frac{y_{D1}}{K_{C2}} \right] - \zeta_{mD1} \frac{\partial Q_{D1}}{\partial \tau} \quad (4.35)$$

$$\frac{\partial y_{H_21}}{\partial \tau} = \frac{1}{\omega^2} \frac{1}{Pe} \frac{\partial^2 y_{H_21}}{\partial v_1^2} - \frac{1}{\omega} \frac{\partial(U_1 y_{H_21})}{\partial v_1} - \frac{y_{H_21}}{C_T} \frac{\partial C_T}{\partial \tau} \quad (4.36)$$

$$\frac{\partial U_1}{\partial v_1} = - \frac{\omega}{C_T} \frac{\partial C_T}{\partial \tau} \quad (4.37)$$

$$(C_T + \zeta_{H,1}) \frac{\partial \bar{T}_1}{\partial \tau} = \frac{1}{\omega^2} \frac{1}{Pe_H} \frac{\partial^2 \bar{T}_1}{\partial v_1^2} - \frac{C_T}{\omega} \frac{\partial}{\partial v_1} [U(\bar{T}_1 + 1)] + \sum F_{i,1} \zeta_H \frac{\partial Q_i}{\partial \tau} + \sum E_i (-r_{Ai}) - N_W (\bar{T}_1 - \bar{T}_{w1}) \quad (4.38)$$

$$\frac{\partial y_{A2}}{\partial \tau} = \frac{1}{(1-\omega)^2} \frac{1}{Pe} \frac{\partial^2 y_{A2}}{\partial v_2^2} - \frac{1}{(1-\omega)} \frac{\partial(U_2 y_{A2})}{\partial v_2} - \frac{y_{A2}}{C_T} \frac{\partial C_T}{\partial \tau} - \zeta_{mA2} \frac{\partial Q_{A2}}{\partial \tau} \quad (4.39)$$

$$\frac{\partial y_{B2}}{\partial \tau} = \frac{1}{(1-\omega)^2} \frac{1}{Pe} \frac{\partial^2 y_{B2}}{\partial v_2^2} - \frac{1}{(1-\omega)} \frac{\partial(U_2 y_{B2})}{\partial v_2} - \frac{y_{B2}}{C_T} \frac{\partial C_T}{\partial \tau} - \zeta_{mB2} \frac{\partial Q_{B2}}{\partial \tau} \quad (4.40)$$

$$\frac{\partial y_{C2}}{\partial \tau} = \frac{1}{(1-\omega)^2} \frac{1}{Pe} \frac{\partial^2 y_{C2}}{\partial v_2^2} - \frac{1}{(1-\omega)} \frac{\partial(U_2 y_{C2})}{\partial v_2} - \frac{y_{C2}}{C_T} \frac{\partial C_T}{\partial \tau} \quad (4.41)$$

$$\frac{\partial y_{D2}}{\partial \tau} = \frac{1}{(1-\omega)^2} \frac{1}{Pe} \frac{\partial^2 y_{D2}}{\partial v_2^2} - \frac{1}{(1-\omega)} \frac{\partial(U_2 y_{D2})}{\partial v_2} - \frac{y_{D2}}{C_T} \frac{\partial C_T}{\partial \tau} \quad (4.42)$$

$$\frac{\partial y_{H_22}}{\partial \tau} = \frac{1}{(1-\omega)^2} \frac{1}{Pe} \frac{\partial^2 y_{H_22}}{\partial v_2^2} - \frac{1}{(1-\omega)} \frac{\partial(U_2 y_{H_22})}{\partial v_2} - \frac{y_{H_22}}{C_T} \frac{\partial C_T}{\partial \tau} \quad (4.43)$$

$$\frac{\partial U_2}{\partial v_2} = - \frac{(1-\omega)}{C_T} \left( \frac{\partial C_T}{\partial \tau} - \sum \zeta_{mi} \frac{\partial Q_i}{\partial \tau} \right) \quad (4.44)$$

$$(C_T + \zeta_{H,2}) \frac{\partial \bar{T}_2}{\partial \tau} = \frac{1}{\omega^2} \frac{1}{Pe_H} \frac{\partial^2 \bar{T}_2}{\partial v_2^2} - \frac{1}{\omega} C_T \frac{\partial}{\partial v_2} [U(\bar{T}_2 + 1)] + \sum F_{i,2} \zeta_H \frac{\partial Q_i}{\partial \tau} - N_W (\bar{T}_2 - \bar{T}_{w2}) \quad (4.45)$$

The boundary conditions are

$$v_1 = 0, \tau > 0 \quad \frac{\partial y_{A1}}{\partial v_1} = 0 \quad (4.46a)$$

$$v_1 = 0, \tau > 0 \quad \frac{\partial y_{B1}}{\partial v_1} = 0 \quad (4.46b)$$

$$v_1 = 0, \tau > 0 \quad \frac{\partial y_{C1}}{\partial v_1} = 0 \quad (4.46c)$$

$$v_1 = 0, \tau > 0 \quad \frac{\partial y_{D1}}{\partial v_1} = 0 \quad (4.46d)$$

$$v_1 = 0, \tau > 0 \quad \frac{\partial y_{H_2 1}}{\partial v_1} = 0 \quad (4.46e)$$

$$v_1 = 0, \tau > 0 \quad \frac{\partial \bar{T}_1}{\partial v_1} = 0 \quad (4.46f)$$

$$v_1 = 0, \tau > 0 \quad U_1 = 0 \quad (4.46g)$$

$$v_1 = 1, (v_2 = 0), \tau > 0 \quad y_{A1} = y_{A2} \quad (4.46h)$$

$$v_1 = 1, (v_2 = 0), \tau > 0 \quad y_{B1} = y_{B2} \quad (4.46i)$$

$$v_1 = 1, (v_2 = 0), \tau > 0 \quad y_{C1} = y_{C2} \quad (4.46j)$$

$$v_1 = 1, (v_2 = 0), \tau > 0 \quad y_{D1} = y_{D2} \quad (4.46k)$$

$$v_1 = 1, (v_2 = 0), \tau > 0 \quad y_{H_2 1} = y_{H_2 2} \quad (4.46l)$$

$$v_1 = 1, (v_2 = 0), \tau > 0 \quad -(1 - \omega) D_A \frac{\partial y_{A1}}{\partial v_1} = -\omega D_A \frac{\partial y_{A2}}{\partial v_2} \quad (4.46m)$$

$$v_1 = 1, (v_2 = 0), \tau > 0 \quad -(1 - \omega) D_A \frac{\partial y_{B1}}{\partial v_1} = -\omega D_A \frac{\partial y_{B2}}{\partial v_2} \quad (4.46n)$$

$$v_1 = 1, (v_2 = 0), \tau > 0 \quad -(1 - \omega) D_A \frac{\partial y_{C1}}{\partial v_1} = -\omega D_A \frac{\partial y_{C2}}{\partial v_2} \quad (4.46o)$$

$$v_1 = 1, (v_2 = 0), \tau > 0 \quad -(1 - \omega) D_A \frac{\partial y_{D1}}{\partial v_1} = -\omega D_A \frac{\partial y_{D2}}{\partial v_2} \quad (4.46p)$$

$$v_1 = 1, (v_2 = 0), \tau > 0 \quad -(1 - \omega) D_A \frac{\partial y_{H_2 1}}{\partial v_1} = -\omega D_A \frac{\partial y_{H_2 2}}{\partial v_2} \quad (4.46q)$$

$$v_1 = 1, (v_2 = 0), \tau > 0 \quad U_1 = U_2 \quad (4.46r)$$

$$v_1 = 1, (v_2 = 0), \tau > 0 \quad -(1 - \omega) \frac{\partial \bar{T}_1}{\partial v_1} = -\omega \frac{\partial \bar{T}_2}{\partial v_2} \quad (4.46s)$$

$$v_1 = 1, (v_2 = 0), \tau > 0 \quad \bar{T}_1 = \bar{T}_2 \quad (4.46t)$$

$$v_2 = 1, \tau > 0 \quad \frac{\partial y_{A2}}{\partial v_2} = 0 \quad (4.46u)$$

$$v_2 = 1, \tau > 0 \quad \frac{\partial y_{B2}}{\partial v_2} = 0 \quad (4.46v)$$

$$v_2 = 1, \tau > 0 \quad \frac{\partial y_{C2}}{\partial v_2} = 0 \quad (4.46w)$$

$$v_2 = 1, \tau > 0 \quad \frac{\partial y_{D2}}{\partial v_2} = 0 \quad (4.46x)$$

$$v_2 = 1, \tau > 0 \quad \frac{\partial y_{H_2,2}}{\partial v_2} = 0 \quad (4.46y)$$

$$v_2 = 1, \tau > 0 \quad \frac{\partial \bar{T}}{\partial v_2} = 0 \quad (4.46z)$$

Step 4 (Desorption/ Reaction)

$$\frac{\partial y_{A1}}{\partial \tau} = \frac{1}{\omega^2} \frac{1}{Pe} \frac{\partial^2 y_{A1}}{\partial v_1^2} - \frac{1}{\omega} \frac{\partial(U_1 y_{A1})}{\partial v_1} - \frac{y_{A1}}{C_T} \frac{\partial C_T}{\partial \tau} - \frac{Da_{t1}}{\omega} \left[ y_{A1} - \frac{y_{C1}}{K_{C1}} \right] - \zeta_{mA1} \frac{\partial Q_{A1}}{\partial \tau} \quad (4.47)$$

$$\frac{\partial y_{B1}}{\partial \tau} = \frac{1}{\omega^2} \frac{1}{Pe} \frac{\partial^2 y_{B1}}{\partial v_1^2} - \frac{1}{\omega} \frac{\partial(U_1 y_{B1})}{\partial v_1} - \frac{y_{B1}}{C_T} \frac{\partial C_T}{\partial \tau} - \frac{Da_{t2}}{\omega} \left[ y_{B1} - \frac{y_{D1}}{K_{C2}} \right] - \zeta_{mB1} \frac{\partial Q_{B1}}{\partial \tau} \quad (4.48)$$

$$\frac{\partial y_{C1}}{\partial \tau} = \frac{1}{\omega^2} \frac{1}{Pe} \frac{\partial^2 y_{C1}}{\partial v_1^2} - \frac{1}{\omega} \frac{\partial(U_1 y_{C1})}{\partial v_1} - \frac{y_{C1}}{C_T} \frac{\partial C_T}{\partial \tau} + \frac{Da_{t1}}{\omega} \left[ y_{A1} - \frac{y_{C1}}{K_{C1}} \right] - \zeta_{mC1} \frac{\partial Q_{C1}}{\partial \tau} \quad (4.49)$$

$$\frac{\partial y_{D1}}{\partial \tau} = \frac{1}{\omega^2} \frac{1}{Pe} \frac{\partial^2 y_{D1}}{\partial v_1^2} - \frac{1}{\omega} \frac{\partial(U_1 y_{D1})}{\partial v_1} - \frac{y_{D1}}{C_T} \frac{\partial C_T}{\partial \tau} + \frac{Da_{t2}}{\omega} \left[ y_{B1} - \frac{y_{D1}}{K_{C2}} \right] - \zeta_{mD1} \frac{\partial Q_{D1}}{\partial \tau} \quad (4.50)$$

$$\frac{\partial y_{H_2,1}}{\partial \tau} = \frac{1}{\omega^2} \frac{1}{Pe} \frac{\partial^2 y_{H_2,1}}{\partial v_1^2} - \frac{1}{\omega} \frac{\partial(U_1 y_{H_2,1})}{\partial v_1} - \frac{y_{H_2,1}}{C_T} \frac{\partial C_T}{\partial \tau} \quad (4.51)$$

$$\frac{\partial U_1}{\partial v_1} = - \frac{\omega}{C_T} \frac{\partial C_T}{\partial \tau} \quad (4.52)$$

$$(C_T + \zeta_{H,1}) \frac{\partial \bar{T}_1}{\partial \tau} = \frac{1}{\omega^2} \frac{1}{Pe_H} \frac{\partial^2 \bar{T}_1}{\partial v_1^2} - \frac{C_T}{\omega} \frac{\partial}{\partial v_1} [U(\bar{T}_1 + 1)] + \sum F_{i,1} \zeta_H \frac{\partial Q_i}{\partial \tau} + \sum E_i (-r_{Ai}) - N_w (\bar{T}_1 - \bar{T}_{w1}) \quad (4.53)$$

$$\frac{\partial y_{A2}}{\partial \tau} = \frac{1}{(1-\omega)^2} \frac{1}{Pe} \frac{\partial^2 y_{A2}}{\partial v_2^2} - \frac{1}{(1-\omega)} \frac{\partial(U_2 y_{A2})}{\partial v_2} - \frac{y_{A2}}{C_T} \frac{\partial C_T}{\partial \tau} - \zeta_{mA2} \frac{\partial Q_{A2}}{\partial \tau} \quad (4.54)$$

$$\frac{\partial y_{B2}}{\partial \tau} = \frac{1}{(1-\omega)^2} \frac{1}{Pe} \frac{\partial^2 y_{B2}}{\partial v_2^2} - \frac{1}{(1-\omega)} \frac{\partial(U_2 y_{B2})}{\partial v_2} - \frac{y_{B2}}{C_T} \frac{\partial C_T}{\partial \tau} - \zeta_{mB2} \frac{\partial Q_{B2}}{\partial \tau} \quad (4.55)$$

$$\frac{\partial y_{C2}}{\partial \tau} = \frac{1}{(1-\omega)^2} \frac{1}{Pe} \frac{\partial^2 y_{C2}}{\partial v_2^2} - \frac{1}{(1-\omega)} \frac{\partial(U_2 y_{C2})}{\partial v_2} - \frac{y_{C2}}{C_T} \frac{\partial C_T}{\partial \tau} \quad (4.56)$$

$$\frac{\partial y_{D2}}{\partial \tau} = \frac{1}{(1-\omega)^2} \frac{1}{Pe} \frac{\partial^2 y_{D2}}{\partial v_2^2} - \frac{1}{(1-\omega)} \frac{\partial(U_2 y_{D2})}{\partial v_2} - \frac{y_{D2}}{C_T} \frac{\partial C_T}{\partial \tau} \quad (4.57)$$

$$\frac{\partial y_{H_2,2}}{\partial \tau} = \frac{1}{(1-\omega)^2} \frac{1}{Pe} \frac{\partial^2 y_{H_2,2}}{\partial v_2^2} - \frac{1}{(1-\omega)} \frac{\partial(U_2 y_{H_2,2})}{\partial v_2} - \frac{y_{H_2,2}}{C_T} \frac{\partial C_T}{\partial \tau} \quad (4.58)$$

$$\frac{\partial U_2}{\partial v_2} = -\frac{(1-\omega)}{C_T} \left( \frac{\partial C_T}{\partial \tau} - \sum \zeta_{mi} \frac{\partial Q_i}{\partial \tau} \right) \quad (4.59)$$

$$(C_T + \zeta_{H,2}) \frac{\partial \bar{T}_2}{\partial \tau} = \frac{1}{\omega^2} \frac{1}{Pe_H} \frac{\partial^2 \bar{T}_2}{\partial v_2^2} - \frac{1}{\omega} C_T \frac{\partial}{\partial v_2} [U(\bar{T}_2 + 1)] + \sum F_{i,2} \zeta_H \frac{\partial Q_i}{\partial \tau} - N_w (\bar{T}_2 - \bar{T}_{w2}) \quad (4.60)$$

The boundary conditions are

$$v_1 = 0, \tau > 0 \quad -\frac{1}{Pe} \frac{\partial y_{A1}}{\partial v_1} = U_1 \Big|_{v_1=0} \omega (y_{Af} - y_{A1}) \quad (4.61a)$$

$$v_1 = 0, \tau > 0 \quad -\frac{1}{Pe} \frac{\partial y_{B1}}{\partial v_1} = U_1 \Big|_{v_1=0} \omega (y_{Bf} - y_{B1}) \quad (4.61b)$$

$$v_1 = 0, \tau > 0 \quad -\frac{1}{Pe} \frac{\partial y_{C1}}{\partial v_1} = U_1 \Big|_{v_1=0} \omega (y_{Cf} - y_{C1}) \quad (4.61c)$$

$$v_1 = 0, \tau > 0 \quad -\frac{1}{Pe} \frac{\partial y_{D1}}{\partial v_1} = U_1 \Big|_{v_1=0} \omega (y_{Df} - y_{D1}) \quad (4.61d)$$

$$v_1 = 0, \tau > 0 \quad -\frac{1}{Pe} \frac{\partial y_{H_2,1}}{\partial v_1} = U_1 \Big|_{v_1=0} \omega (y_{H_2,f} - y_{H_2,1}) \quad (4.61e)$$

$$v_1 = 0, \tau > 0 \quad -\frac{1}{Pe_H} \frac{\partial \bar{T}_1}{\partial v_1} = U_1 \Big|_{v_1=0} \omega C_T \bar{T}_1 \quad (4.61f)$$

$$v_1 = 0, \tau > 0 \quad U_1 = S \frac{u_p}{u_f} \quad (4.61g)$$

$$v_1 = 1, (v_2 = 0), \tau > 0 \quad \frac{\partial y_{A1}}{\partial v_1} = 0 \quad (4.61h)$$

$$v_1 = 1, (v_2 = 0), \tau > 0 \quad \frac{\partial y_{B1}}{\partial v_1} = 0 \quad (4.61i)$$

$$v_1 = 1, (v_2 = 0), \tau > 0 \quad \frac{\partial y_{C1}}{\partial v_1} = 0 \quad (4.61j)$$

$$v_1 = 1, (v_2 = 0), \tau > 0 \quad \frac{\partial y_{D1}}{\partial v_1} = 0 \quad (4.61k)$$

$$v_1 = 1, (v_2 = 0), \tau > 0 \quad \frac{\partial y_{H_2,1}}{\partial v_1} = 0 \quad (4.61l)$$

$$v_1 = 1, (v_2 = 0), \tau > 0 \quad \frac{\partial \bar{T}_1}{\partial v_1} = 0 \quad (4.61m)$$

$$v_1 = 1, (v_2 = 0), \tau > 0 \quad \frac{\partial y_{A2}}{\partial v_2} = 0 \quad (4.61n)$$

$$v_1 = 1, (v_2 = 0), \tau > 0 \quad \frac{\partial y_{B2}}{\partial v_2} = 0 \quad (4.61o)$$

$$v_1 = 1, (v_2 = 0), \tau > 0 \quad \frac{\partial y_{C2}}{\partial v_2} = 0 \quad (4.61p)$$

$$v_1 = 1, (v_2 = 0), \tau > 0 \quad \frac{\partial y_{D2}}{\partial v_2} = 0 \quad (4.61q)$$

$$v_1 = 1, (v_2 = 0), \tau > 0 \quad \frac{\partial y_{H_2,2}}{\partial v_2} = 0 \quad (4.61r)$$

$$v_1 = 1, (v_2 = 0), \tau > 0 \quad \frac{\partial \bar{T}_2}{\partial v_2} = 0 \quad (4.61s)$$

$$v_2 = 1, \tau > 0 \quad -\frac{1}{Pe} \frac{\partial y_{A2}}{\partial v_2} = U_2 \big|_{v_2=1} \omega(y_{Ap} - y_{A2}) \quad (4.61t)$$

$$v_2 = 1, \tau > 0 \quad -\frac{1}{Pe} \frac{\partial y_{B2}}{\partial v_2} = U_2 \big|_{v_2=1} \omega(y_{Bp} - y_{B2}) \quad (4.61u)$$

$$v_2 = 1, \tau > 0 \quad -\frac{1}{Pe} \frac{\partial y_{C2}}{\partial v_2} = U_2 \big|_{v_2=1} \omega(y_{Cp} - y_{C2}) \quad (4.61v)$$

$$v_2 = 1, \tau > 0 \quad -\frac{1}{Pe} \frac{\partial y_{D2}}{\partial v_2} = U_2 \big|_{v_2=1} \omega(y_{Dp} - y_{D2}) \quad (4.61x)$$

$$v_2 = 1, \tau > 0 \quad -\frac{1}{Pe} \frac{\partial y_{H_2,2}}{\partial v_2} = U_2 \big|_{v_2=1} \omega(y_{H_2p} - y_{H_2,2}) \quad (4.61y)$$

$$v_2 = 1, \tau > 0 \quad -\frac{1}{Pe_H} \frac{\partial \bar{T}_2}{\partial v_2} = U_2 \big|_{v_2=1} \omega C_T (\bar{T}_2 - \bar{T}_p) \quad (4.61z)$$

$$v_2 = 1, \tau > 0 \quad U_2 = -(1-S) \frac{u_p}{u_f} \quad (4.61aa)$$

In all the four steps, the mass transfer rate and the adsorption equilibrium isotherm for reactor and adsorbent region are

$$\zeta_{mA1} \frac{\partial Q_{A1}}{\partial \tau} = N_{f1} C_T (y_{A1} - \langle y_{A1} \rangle) \quad (4.62)$$

$$\zeta_{mB1} \frac{\partial Q_{B1}}{\partial \tau} = N_{f1} C_T (y_{B1} - \langle y_{B1} \rangle) \quad (4.63)$$

$$\zeta_{mC1} \frac{\partial Q_{C1}}{\partial \tau} = N_{f1} C_T (y_{C1} - \langle y_{C1} \rangle) \quad (4.64)$$

$$\zeta_{mD1} \frac{\partial Q_{D,1}}{\partial \tau} = N_{f1} C_T (y_{D1} - \langle y_{D1} \rangle) \quad (4.65)$$

$$\zeta_{mA2} \frac{\partial Q_{A2}}{\partial \tau} = N_{f2} C_T (y_{A2} - \langle y_{A2} \rangle) \quad (4.66)$$

$$\zeta_{mB2} \frac{\partial Q_{B2}}{\partial \tau} = N_{f2} C_T (y_{B2} - \langle y_{B2} \rangle) \quad (4.67)$$

$$\langle y_{A1} \rangle = \frac{1}{P \cdot K_{ads}} \frac{\theta_{Aref1} Q_{A1}}{(1 - \theta_{Aref1} Q_{A1} - \theta_{Bref1} Q_{B1} - \theta_{Cref1} Q_{C1} - \theta_{Dref2} Q_{D1})} \quad (4.68)$$

$$\langle y_{B1} \rangle = \frac{1}{P \cdot K_{ads}} \frac{\theta_{Bref1} Q_{B1}}{(1 - \theta_{Aref1} Q_{A1} - \theta_{Bref1} Q_{B1} - \theta_{Cref1} Q_{C1} - \theta_{Dref1} Q_{D1})} \quad (4.69)$$

$$\langle y_{C1} \rangle = \frac{1}{P \cdot K_{ads}} \frac{\theta_{Cref,1} Q_{C1}}{(1 - \theta_{Aref,2} Q_{A1} - \theta_{Bref,2} Q_{B1} - \theta_{Cref,2} Q_{C1} - \theta_{Dref,2} Q_{D1})} \quad (4.70)$$

$$\langle y_{D1} \rangle = \frac{1}{P \cdot K_{ads}} \frac{\theta_{Dref1} Q_{D1}}{(1 - \theta_{Aref1} Q_{A1} - \theta_{Bref1} Q_{B1} - \theta_{Cref1} Q_{C1} - \theta_{Dref1} Q_{D1})} \quad (4.71)$$

$$\langle y_{A2} \rangle = \frac{1}{P \cdot K_{ads}} \frac{\theta_{Aref2} Q_{A2}}{(1 - \theta_{Aref2} Q_{A2} - \theta_{Bref2} Q_{B2})}^{r_A} \quad (4.72)$$

$$\langle y_{B2} \rangle = \frac{1}{P \cdot K_{ads}} \frac{\theta_{ref} Q_{B2}}{(1 - \theta_{ref} Q_{A2} - \theta_{ref} Q_{B2})}^{r_B} \quad (4.73)$$

$$N_{f1} = \frac{(1 - \varepsilon_1) a_{p1} k_{gl} L}{\varepsilon_1 u_f} \quad (4.74)$$

$$N_{f2} = \frac{(1 - \varepsilon_2) a_{p2} k_{gl} L}{\varepsilon_2 u_f} \quad (4.75)$$

$$\zeta_{mA1} = \frac{(1 - \varepsilon_1) \rho_{s1} q_{Aref1}}{\varepsilon_1 C_T} \quad (4.76)$$

$$\zeta_{mB1} = \frac{(1 - \varepsilon_1) \rho_{s1} q_{Bref1}}{\varepsilon_1 C_T} \quad (4.77)$$

$$\zeta_{mC1} = \frac{(1 - \varepsilon_1) \rho_{s1} q_{Cref1}}{\varepsilon_1 C_T} \quad (4.78)$$

$$\zeta_{mD1} = \frac{(1 - \varepsilon_1) \rho_{s1} q_{Dref1}}{\varepsilon_1 C_T} \quad (4.79)$$

$$\zeta_{mA2} = \frac{f_s \rho_{s2} q_{Aref2}}{\varepsilon_2 C_T} \quad (4.80)$$

$$\zeta_{mB2} = \frac{f_s \rho_{s2} q_{Bref2}}{\varepsilon_2 C_T} \quad (4.81)$$

$$\frac{\partial M_{H_2}}{\partial \tau} = \mu_2 \left( y_{H_2} \frac{P}{P_H} \right)^{0.59} \quad (4.82)$$

$$\mu_2 = \frac{A_M L k P_H^{0.59}}{u_f C_o V_2 X_M} \quad (4.83)$$

$$k = k_o e^{\left( -\frac{E_P}{RT} \right)}$$

The initial conditions are

$$y_{A1}(v_1, \tau = 0) = 0 \quad (4.84a)$$

$$y_{B1}(v_1, \tau = 0) = 0 \quad (4.84b)$$

$$y_{C1}(v_1, \tau = 0) = 0 \quad (4.84c)$$

$$y_{D1}(v_1, \tau = 0) = 0 \quad (4.84d)$$

$$y_{H_2,1}(v_1, \tau = 0) = 1 \quad (4.84e)$$

$$y_{A2}(v_2, \tau = 0) = 0 \quad (4.84f)$$

$$y_{B2}(v_2, \tau = 0) = 0 \quad (4.84g)$$

$$y_{C2}(v_2, \tau = 0) = 0 \quad (4.84h)$$

$$y_{D2}(v_2, \tau = 0) = 0 \quad (4.84i)$$

$$y_{H_2,2}(v_2, \tau = 0) = 1 \quad (4.84j)$$

$$Q_{A,1}(v_1, \tau = 0) = 0 \quad (4.84k)$$

$$Q_{B,1}(v_1, \tau = 0) = 0 \quad (4.84l)$$

$$Q_{C,1}(v_1, \tau = 0) = 0 \quad (4.84m)$$

$$Q_{D,1}(v_1, \tau = 0) = 0 \quad (4.84n)$$

$$Q_{A,2}(v_2, \tau = 0) = 0 \quad (4.84o)$$

$$Q_{B,2}(v_2, \tau = 0) = 0 \quad (4.84p)$$

#### 4.4 HANDLING RECYCLE STREAM

All recycled streams are recycled to adjacent units during the reaction/adsorption step. Exit streams from blowdown/reaction and desorption/reaction steps are blended with fresh feed before entering the adjacent unit undergoing reaction/adsorption step.

If the recycle stream is recycled during reaction/pressurization step, the adsorption region to be pressurized will pressurize in less time than that required to depressurize the adjacent unit undergoing blowdown/reaction step. This situation will cause a back flow when the vessel undergoing blowdown/reaction step not fully depressurized is opened for purge (desorption/reaction) step. This backflow phenomena is difficult to model. Thus, no recycle is made during reaction/pressurization step.

To avoid this situation, a third vessel is introduced to the system as a holding vessel. The third vessel contains neither catalyst nor adsorbent. The purpose of this vessel is to act as a container holding the effluent stream of the blowdown/reaction step and then re-injecting it back with the effluent of the subsequent desorption/reaction step to either the feed of the adjacent vessel undergoing reaction/adsorption step.

The process flow diagram for recycling the waste effluent to feed is illustrated in Figure 4.4. In Figure 4.4a, the first vessel (V1) is pressurized with fresh feed only. The second vessel (V2) will blow its content to a third vessel (V3). The third vessel is an empty container that serves as an intermediate holder of blowdown step effluent. This vessel contains neither catalyst nor adsorbent pellets.

In Figure 4.4b, V1 has started its adsorption step. During this step, feed to V1 is received from three sources: Fresh Feed from upstream units, desorption step effluent from V2 and the content reserved in V3 during previous step. Since V3 pressure is at the high side, a control valve is needed to bring down the pressure to the desorption-vessel pressure. A turbine to generate electricity may replace this control valve. The effluent of ~~the~~ control valve and V2 are then combined before entering the compressor C1. The compressor then compresses its feed to the high pressure. The



compressor in the Figure represents a multistage compressor with inter-stage cooling. Inter-stage cooling is used to assure bringing the compressor effluent to the fresh feed temperature. A recycle temperature that is higher than the feed temperature will result in loss of catalyst activity. Compressor effluent is then mixed with the feed prior to entering V1. The duration of the adsorption and desorption steps is much greater than that of the pressurization and blowdown steps. Thus the content of V3 will be emptied at a fraction the adsorption step time. V3 is then closed for the rest of the adsorption step. A second control valve is added downstream of the compressor to control recycle flow. A hydrogen makeup stream is introduced with the recycle stream to ensure minimum feed hydrogen to hydrocarbon ratio of 7.5.

Figures 4.4c and 4.4d are similar to Figures 4.4a and 4.4b, respectively. The only difference in the latter figures is the swap in roles of V1 and V2.

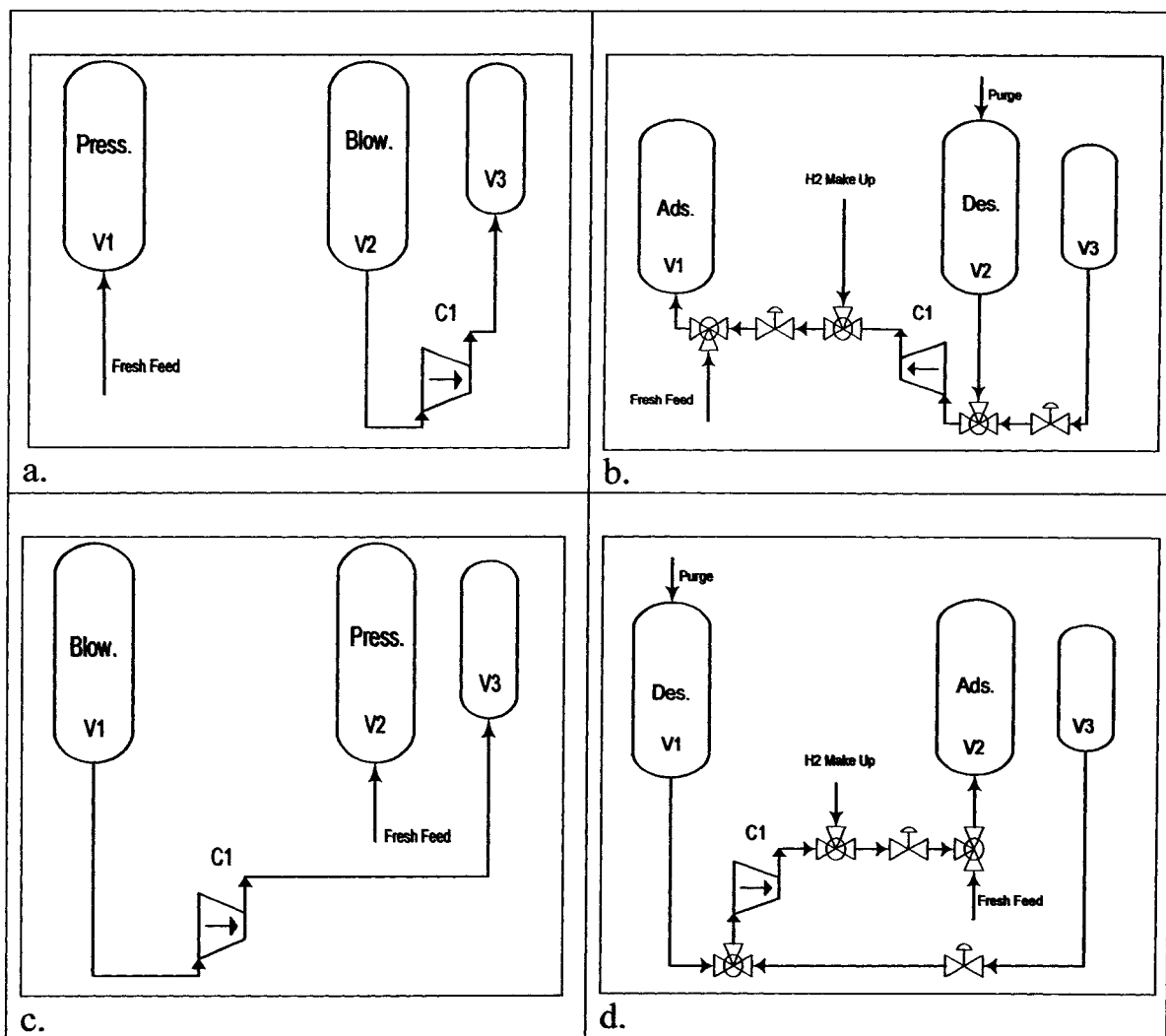


Figure 4.4: Connectivity diagram for handling recycle to feed in all four cyclic steps:

- a.) V1 in reaction/pressurization, V2 in blowdown/reaction.
- b.) V1 in reaction/adsorption, V2 in desorption/reaction.
- c.) V1 in blowdown/reaction, V2 in reaction/pressurization.
- d.) V1 in desorption/reaction, V2 in reaction/adsorption.

## 4.5 PARAMETERS ESTIMATIONS

Estimation methods for parameters used in Chapters II and III are also applicable in this chapter. In addition, hydrogen permeation parameters are obtained from Morreal et al [51]. All parameters are listed in Table 4.1.

Palladium tubes are used for hydrogen separation. Tubes have inside diameters of 1.588 centimeters and a thickness of 0.1 cm. The tubes are structured in rows surrounding the adsorptions section shell. To obtain a minimum acceptable hydrogen separation, a minimum membrane volume fraction of 0.1527 is required. For a column diameter of 12.7 cm, permeation tube inside diameter of 1.588 cm, column thickness of 0.3 cm and pipe thickness of 0.1 cm; the number of tubes needed to surround the shell column shell side is 67 tubes. The number is rounded off to the lower integer to allow for a space between adjacent tubes. This space will assure maximum utilization of membrane area.

Due to the introduction of the hydrogen membrane to separate hydrogen, higher temperatures are encountered in the adsorber section than those reported in PSAR systems. Higher temperatures result in low adsorption capacities. Thus a longer adsorber length is required to compensate the loss in adsorption capacity.

Table 4.1: Parametric Values used for simulation of conventional PSAR system

Parameter	Value
$Y_{Af} = Y_{Bf} = Y_{Cf} = Y_{Df}$	0.03
H <sub>2</sub> /HC ratio (mol/mol)	7.33
F <sub>f</sub> (mol/m <sup>2</sup> /s)	0.5037
P <sub>H</sub> (bar)	15
P <sub>L</sub> (bar)	2
T <sub>f</sub> (K)	573
L (cm)	140
U <sub>f</sub> (cm/s)	0.5
U <sub>R</sub> (cm/s)	1.75
Purge/Feed volumetric ratio	3.5
S Reactor Section Purge Velocity Ratio	0.1
D <sub>L</sub> @ high pressure (cm <sup>2</sup> /s)	0.088
D <sub>L</sub> @ low pressure (cm <sup>2</sup> /s)	0.66
K <sub>gl</sub> @ high pressure (cm/s)	0.62
K <sub>gl</sub> @ low pressure (cm/s)	2.23
Pe @ high pressure	59.1
Pe @ low pressure	7.87
Pressurization & Blowdown time (min)	4.6
Adsorption & Desorption time [Conventional PSARM] (min)	115
Adsorption & Desorption time [PSARM with waste recycled to feed] (min)	170
$\omega$	0.4643
$f_m$ (Membrane volume fraction)	0.1527
$f_s$ (Adsorbent volume fraction)	0.3675
$\theta_{Aref,1}$ @ 573K	0.0541
$\theta_{Bref,1}$ @ 573K	0.1187
$\theta_{C,ref,1}$ @ 573K	0.0541
$\theta_{D,ref,1}$ @ 573K	0.1187
$\theta_{Aref,2}$ @ 573K	0.0844
$\theta_{Bref,2}$ @ 573K	0.3036

## 4.6 NUMERICAL METHODS

The numerical technique used to solve the PSARM model is basically the same as that used for solving the PSAR model discussed in chapter 3.

## 4.7 RESULTS AND DISCUSSION

Hydrogen separation during the adsorption step is a very strong function of feed velocity. The more the feed velocity is, the less hydrogen is filtered through the membrane, and vice versa. Also, a satisfactory effluent velocity needs to be sustained to assure continuity of product supply. Minimum velocity and maximum hydrogen separation are two conflicting objectives that need to be met (optimized). A feed velocity of 0.5 cm/s is used throughout this chapter.

### 4.7.1 Conventional PSARM Cyclic Process

In this section, we will discuss the results obtained from conventional PSARM units. We define a conventional PSARM unit as a unit producing a product stream in the (reaction/adsorption) step and producing waste streams in the (blowdown/reaction) and (desorption/reaction) steps. In this type of process, no use is made to the waste stream produced by the (blowdown/reaction) and (desorption/reaction) steps. Moreover, the purge stream is either pure hydrogen stream (hydrogen purge) or a portion of the adsorption step product (self regeneration). Moreover, part of the hydrogen in the product stream is removed through hydrogen permeation. First, we will discuss the hydrogen purge case.

The cycle starts initially with clean adsorbent and a gas phase free of n-C<sub>5</sub> and n-C<sub>6</sub>. The total length of the column is 120 cm. Parametric values used for simulations of conventional PSARM cycle are summarized in Table 4.1.

#### 4.7.1.1 Conventional PSARM Cyclic Process with Hydrogen Purge

Figure 4.5a illustrates the concentrations of reactive components at the end of the steady state reaction/pressurization step. The purpose of this step is to bring the vessel pressure from 2 to 15 bars as a preparation for the next step. During this step the other end of the vessel is closed. Fresh feed is introduced to the bed through the reactor section with equivalent molar ratios of 0.03 for all reactive components. The molar ratios of reactive components are chosen to allow overall minimum hydrogen to hydrocarbon ratio of 7.33. Maintaining the minimum ratio is very crucial to preventing any hydrocracking reactions from taking place. All reactive components are adsorbed in the catalyst bed before reacting. All isomerization reactions are equilibrium based reactions. Thus, reactants react to form products until equilibrium is reached. The  $i\text{-C}_6$  peak appearing towards the end of the adsorber bed is due to the shift of the amounts of  $i\text{-C}_6$  that were present in the interface region at the end of the previous desorption/reaction step.

Figure 4.5b illustrates the concentrations of reactive components at the end of the steady state reaction/adsorption step. In this step, the other end of the vessel is open for product collection. In the adsorber section, any unreacted  $n\text{-C}_5$  and  $n\text{-C}_6$  is adsorbed by adsorber section pellets. Isomerization of  $n\text{-C}_5$  takes place at the first two centimeters of the bed. It takes the entire reactor section length to bring  $n\text{-C}_6$  isomerization to its equilibrium state. The increase in  $i\text{-C}_5$  and  $i\text{-C}_6$  concentrations in the adsorption section is due to the migration of  $\text{H}_2$  through the membrane. Noticeable amounts of  $n\text{-C}_5$  and  $n\text{-C}_6$  start appearing at the inlet of the adsorber section. This is due to the saturation of the solid pellets at this section with  $n\text{-C}_5$  and  $n\text{-C}_6$ . Because of its higher equilibrium constant, higher amounts of  $n\text{-C}_6$  are adsorbed than those of  $n\text{-C}_5$ . This causes the pellets to saturate with more  $n\text{-C}_6$  than  $n\text{-C}_5$ . The remaining  $n\text{-C}_5$  is pushed towards the next available unsaturated pellets. This is illustrated, in the adsorption section of the figure, with the  $n\text{-C}_5$  concentration holding in the gas phase for a longer length than  $n\text{-C}_6$ . This step is set to run at a time interval that is 25 times more than the reaction/pressurization step time. The choice of the time interval for this step is arbitrary, as long as the time is large enough to allow escape of  $i\text{-C}_5$  and  $i\text{-C}_6$  from the other end of the vessel. In addition, the time should not be large enough to allow breakthrough of normal alkanes. Figure 4.6 illustrates the drop in  $\text{H}_2$  concentration during this step. Due to the effect of  $\text{H}_2$  diffusion,  $\text{H}_2$  concentration drops from 88.0% at the inlet of the vessel to 79.8% at the exit of the vessel.

Figure 4.5c illustrates the concentrations of reactive components at the end of the steady state blowdown/reaction step. The vessel setup in this step is similar to the setup of the reaction/pressurization step. However, in this step, the front end of the vessel is closed. Vessel contents are blown out of the vessel from the back end. This setup allows for a pressure reduction from 15 bars to 2 bars. This step prepares the vessel for introduction of purge stream in the next step. The shift in equilibrium, due to pressure decrease, causes the amounts of reactive components present in the solid phase of both sections to escape to the gas phase. The escape of these compounds to the gas phase causes their gas phase concentrations to increase. The time interval for this step is exactly the same as that of the reaction/pressurization step. Figures E.1c to E.5c in Appendix E illustrate the transient and spatial change in concentration for n-C<sub>5</sub>, n-C<sub>6</sub>, i-C<sub>5</sub>, i-C<sub>6</sub> and H<sub>2</sub> as a function of both time and distance for blowdown/reaction step, respectively.

Figure 4.5d illustrates the concentrations of reactive components at the end of the steady state desorption/reaction step. In the present model, pure H<sub>2</sub> is used as a purge stream. The desorption of the n-C<sub>5</sub> and n-C<sub>6</sub> amounts present in the solid phase of the adsorber section causes an increase in their gas phase concentrations. To avoid temperature spike, the purge stream is introduced at both ends of the vessel and the waste stream is collected from the interface zone. Very little reaction takes place at this step because components in the reaction zone are close to their equilibrium conversions. It should be noted that the y-scale of this figure is much smaller than those figures of other steps. Figures E.1d to E.4d in Appendix E illustrate the change in transient and spatial concentration for n-C<sub>5</sub>, n-C<sub>6</sub>, i-C<sub>5</sub> and i-C<sub>6</sub> as a function of both time and distance for reaction/adsorption step, respectively.

Figure 4.6 illustrates the concentration profiles for hydrogen at the end of the four cyclic steps. The increase in hydrogen concentration towards the end of the adsorber bed in reaction/pressurization step is due to the presence of hydrogen from the previous desorption/reaction step. The hydrogen present from the desorption/reaction step of the previous cycle is removed in the reaction/adsorption step. During blowdown step, the pressure starts reducing from 15 bars to 2 bars. Because of this reduction, a shift in equilibrium occurs for the components present in the solid phase of both sections. The equilibrium shift causes the amounts initially present in the solid phase to escape to the gas phase causing a decrease in the gas phase hydrogen

concentration. This decrease is illustrated in the figure by a large drop in hydrogen concentration. During desorption/reaction step, pure hydrogen is used as a purge stream. The time for this step is the same as the one for the reaction/adsorption step. This long time allows for the removal of most of the amounts present in the solid phase from the previous reaction/pressurization and reaction/adsorption steps. Figure E.5 in Appendix E illustrates the change in transient and spatial concentration for  $H_2$  as a function of both time and distance for reaction/adsorption step, respectively.

The noticeable increase of the temperature at the start of the reactor bed (Figure 4.7), during reaction/pressurization step, is due to the combined effects of adsorption and chemical reactions. Temperature decline through the rest of the bed is due to the lowering of both of these terms. The lowering of both terms is due to the less reactive components at the remaining portion of the reactor section. The small temperature peak that is noticed towards the end of the reactor section is formed because of the adsorption of  $n-C_5$  and  $n-C_6$  amounts present in the gas phase from the previous step. Figure E.6a in Appendix E illustrates the transient and spatial change in temperature as a function of both time and distance for reaction/pressurization step.

The temperature profile at the front end of the reaction section, in reaction/adsorption step, is lower than that of the reaction/pressurization step. This is due to the equilibrium reached in the solid phase. The higher temperature observed in the rest of the reactor bed, compared to the reaction/pressurization step, is due to continuous adsorption of reactive components. The temperature peak, formed towards the middle of the adsorber section, is due to adsorption of  $n-C_5$  and  $n-C_6$  into the solid phase. A higher temperature rise is noticed in this model when compared to the conventional PSAR model. The reason behind this higher temperature rise is the reduction in hydrogen concentration. The reduction in hydrogen concentration reduces gas flow inside the adsorber section. Due to the reduction in gas flow, the energy released through the adsorption of alkanes will heat the gas to a higher temperature than that observed in PSAR systems. A lower adsorption capacity is the direct result of the increased gas phase temperature. This is the main reason behind increasing the adsorber section length. The extra length is added to compensate for the loss in adsorption capacity due to the increase in adsorber section temperature. Figure E.6b in Appendix E illustrates the transient and spatial change in



temperature as a function of both time and distance for reaction/adsorption step.

A temperature drop is noticed in the reactor section during blowdown/reaction step. This drop in temperature is due to heat adsorbed by reactive components to release them from the solid phase to the gas phase. The same concept holds for the initial temperature drop in the adsorber section. The temperature rise at the end of the adsorption section is due to the adsorption of displaced  $n\text{-C}_5$  into the bed. The faster temperature reduction in reactor section, compared to the adsorber section, is due to desorption of higher amounts from the reactor section than those of the adsorber section. Figure E.6c in Appendix E illustrates the transient and spatial change in temperature as a function of both time and distance for blowdown/reaction step.

Due to negligible reaction rates in desorption/reaction step, the final vessel temperature settles at a value closer to the purge stream temperature. A three dimensional profile illustrating temperature profile against space and time for the desorption/reaction step is illustrated in Figure E.6d of Appendix E.

The velocity profile at the end of the reaction/pressurization step is shown in Figure 4.9. Initially, the velocity at the vessel inlet is 7.5 times higher than its original value due to pressurization effect. At the end of reaction/pressurization step, the inlet velocity reaches its normal value since all the bed at this time is pressurized. The velocity at the end of the bed is always zero since the bed is closed at the back end of the adsorber section during this step.

The bed velocity during reaction/adsorption step, for the reactor section, is the same as the feed velocity. The velocity drop in the adsorption section is due to hydrogen permeation.

Because of the pressure decrease, the final velocity at the end of the blowdown/reaction step is 62 times higher than feed velocity. The additional increase of velocity, from the expected 7.5 times of the feed velocity, is due to desorption of previously adsorbed components from the solid to the gas phase.

The velocity of desorption/reaction step is chosen to be 3.5 times greater than the feed velocity. 10% of the purge stream is injected into the reactor

section. The rest of the purge stream is injected into the adsorber section. Again, the increase of the velocity in this step is due to the desorption of components that were adsorbed in the previous step reaction/pressurization and reaction/adsorption steps. Figure E.7 in Appendix A illustrates the transient and spatial change in velocity as a function of both time and distance for reaction/pressurization, reaction/adsorption, blowdown/reaction and desorption/reaction steps, respectively.

The increase in n-C<sub>5</sub> and n-C<sub>6</sub> capacitances (Figure 4.9) in the adsorption section, during reaction/adsorption step, is a direct result of H<sub>2</sub> diffusion through the membrane. H<sub>2</sub> diffusion through the membrane causes the velocity to drop. The drop in velocity allows a larger residence time for n-C<sub>5</sub> and n-C<sub>6</sub> to adsorb in the same region.

The equilibrium solid phase capacitance for all components is calculated at feed conditions. Thus, during the absence or reduction of concentration of one component over others, the capacitance term shoots above 100%. This is a normalization issue. It does not affect the results produced by the simulation. Upon converting the normalized capacitances to their true values, this phenomenon disappears. Figure 4.9 illustrates the amount of saturation (capacitance) of the solid phase for reactive components in all steps.

Integration of capacitances profiles yields the concentration of adsorbents in the solid phase for either of reactor and adsorber sections. Summing up the capacities of adsorbed species provides the total coverage of the solid phase. Results are illustrated in Table 4.2.

The total occupation of all reactive components, in the reactor section, at the end of the reaction pressurization step is 22.87% compared to 11.06% at the end of the desorption step. This is an indication of a high adsorption in the reactor section of the vessel. For the adsorber section, no breakthrough of normals from the reactor section to the adsorber section occurs yet. Thus little change is noticed in the total capacitance. The small increase in total capacitance is due to the adsorption of some of n-C<sub>5</sub> and n-C<sub>6</sub> amounts that are present from previous step.

Comparing total occupation figures for the reaction/adsorption step to those of reaction/pressurization step in the adsorber section indicates an increase

from 1.46% to 30.28%. This increase is due to the breakthrough of normal alkanes into the adsorber section.

For the reactor section, total occupation figures at the end of the blowdown/reaction step illustrate a large decrease compared to those from the previous reaction/adsorption step. This is an indication of fast desorption of components in this section. Comparing the figures of the adsorber section for the same steps illustrates an increase in occupation. This is due to the introduction of additional amounts of n-C<sub>5</sub> and n-C<sub>6</sub> from the reactor section into the adsorber section.

Comparing reactor section occupation figures for reactive components, at the end of the reaction/pressurization step, illustrates that the lowest occupation is for n-C<sub>5</sub> followed by n-C<sub>6</sub>, i-C<sub>5</sub> and i-C<sub>6</sub>, respectively. The difference between n-C<sub>5</sub> and n-C<sub>6</sub> occupations is due to the difference in their equilibrium K values. At a temperature of 573K, the adsorption equilibrium constant for n-C<sub>5</sub> is 0.4 bar<sup>-1</sup>. The adsorption equilibrium constant for n-C<sub>6</sub>, at the same temperature, is 1.45 bar<sup>-1</sup>. The same analogy holds for i-C<sub>5</sub> and i-C<sub>6</sub> occupations. The higher occupation of i-C<sub>5</sub> compared to n-C<sub>6</sub> is due to its higher gas phase concentration relative to n-C<sub>6</sub>. For the adsorber section, n-C<sub>6</sub> illustrates higher occupation due to its larger equilibrium adsorption constant compared to that of n-C<sub>5</sub>.

At the end of the reaction/adsorption step, the increase in n-C<sub>5</sub> occupation over n-C<sub>6</sub> occupation in the adsorber section is attributed to the large amounts of n-C<sub>5</sub> breaking through compared to the amounts of n-C<sub>6</sub>.

The exit concentrations of reactive components at the end of the blowdown/reaction step are plotted in Figure 4.10. It takes 5 cycles for this system to reach cyclic steady state.

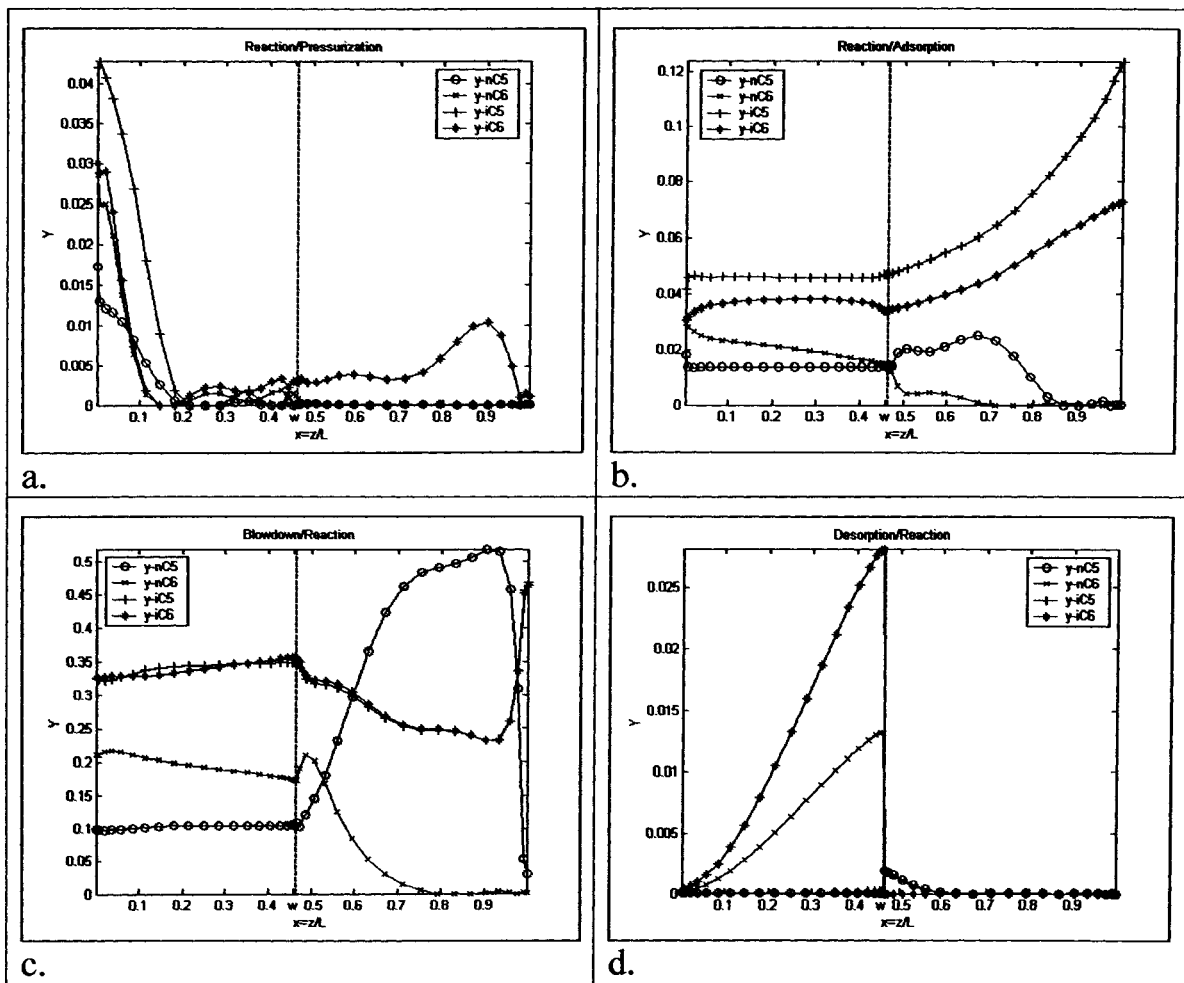


Figure 4.5: Gas phase concentration profiles for reactive components in the PSARM bed at the end of cyclic steady state:  
a.) reaction/pressurization,  
b.) reaction/adsorption,  
c.) blowdown/reaction,  
d.) desorption/reaction.  
Parametric values are in Table 4.1. (Conventional PSARM unit/ $H_2$  purge).

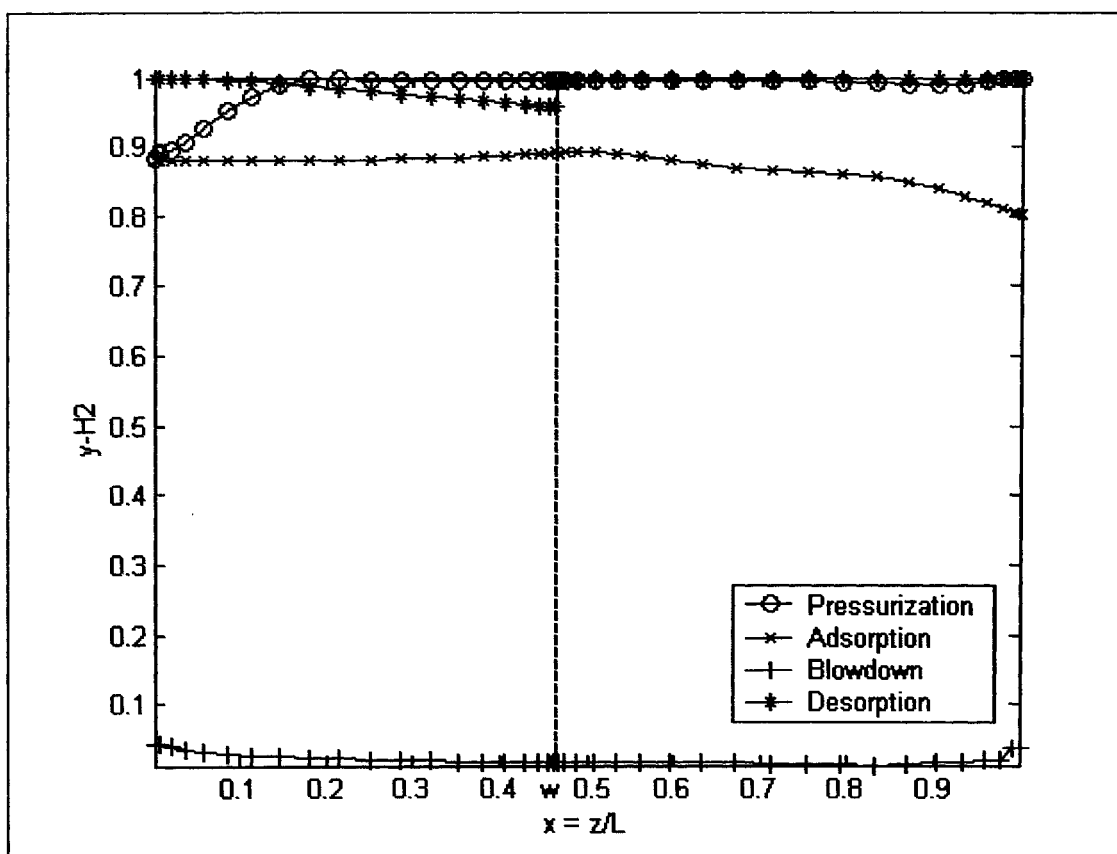


Figure 4.6: Gas phase concentration profiles for  $H_2$  in the PSARM bed at the end of cyclic steady state. Parametric values are in Table 4.1. (Conventional PSARM unit/ $H_2$  purge).

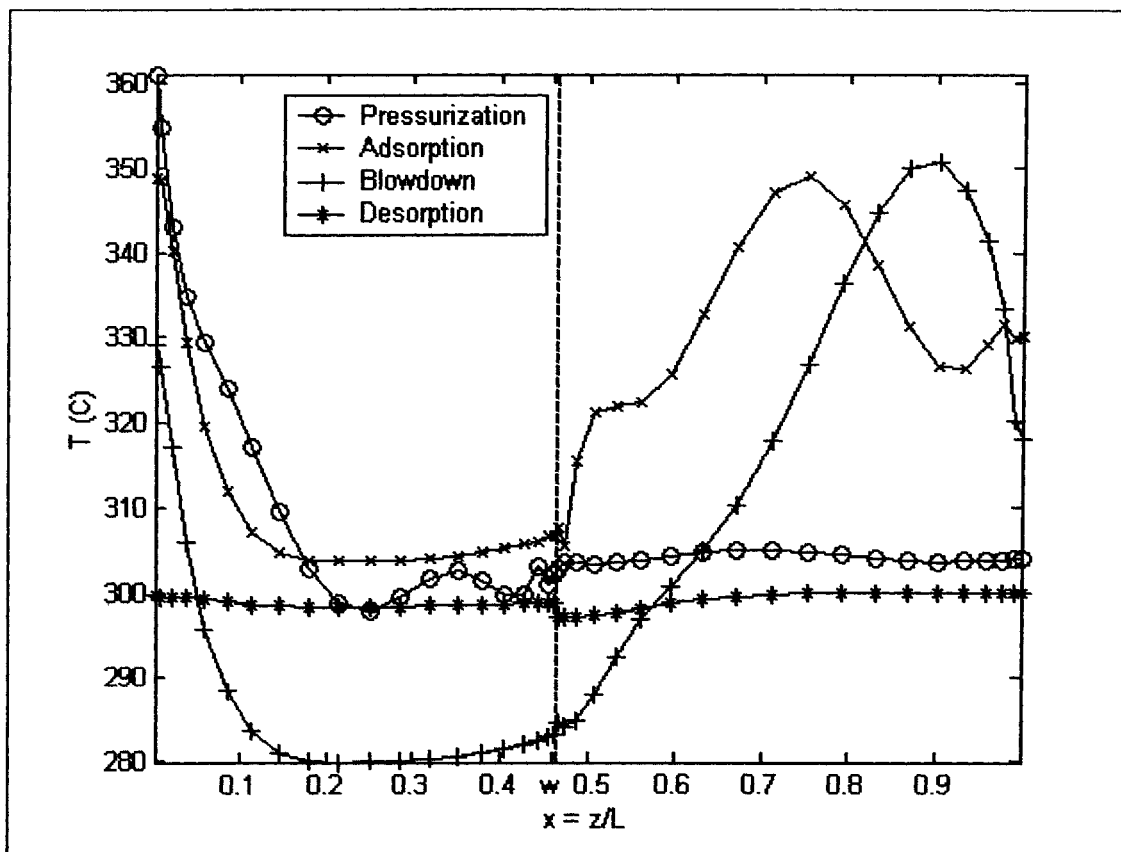


Figure 4.7: Temperature Profiles in the bed at the end of cyclic steady state. Parametric values are in Table 4.1. (Conventional PSARM unit/H<sub>2</sub> purge).

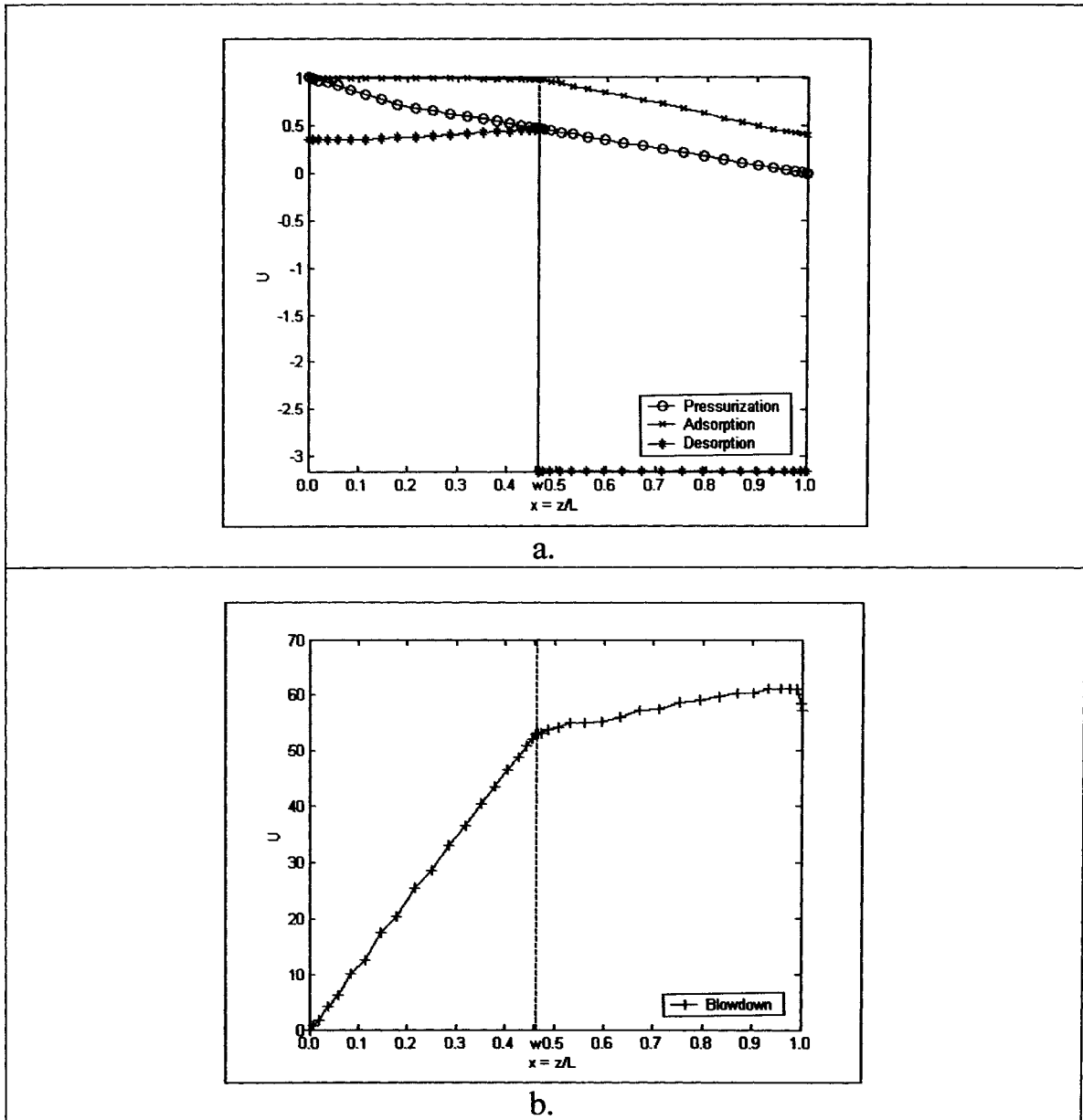


Figure 4.8: Velocity Profiles in the bed at the end of cyclic steady state:

c. Pressurization, Adsorption and Desorption steps Profiles.

d. Blowdown step profile.

Parametric values are in Table 4.1. (Conventional PSARM unit/Hydrogen Purge).

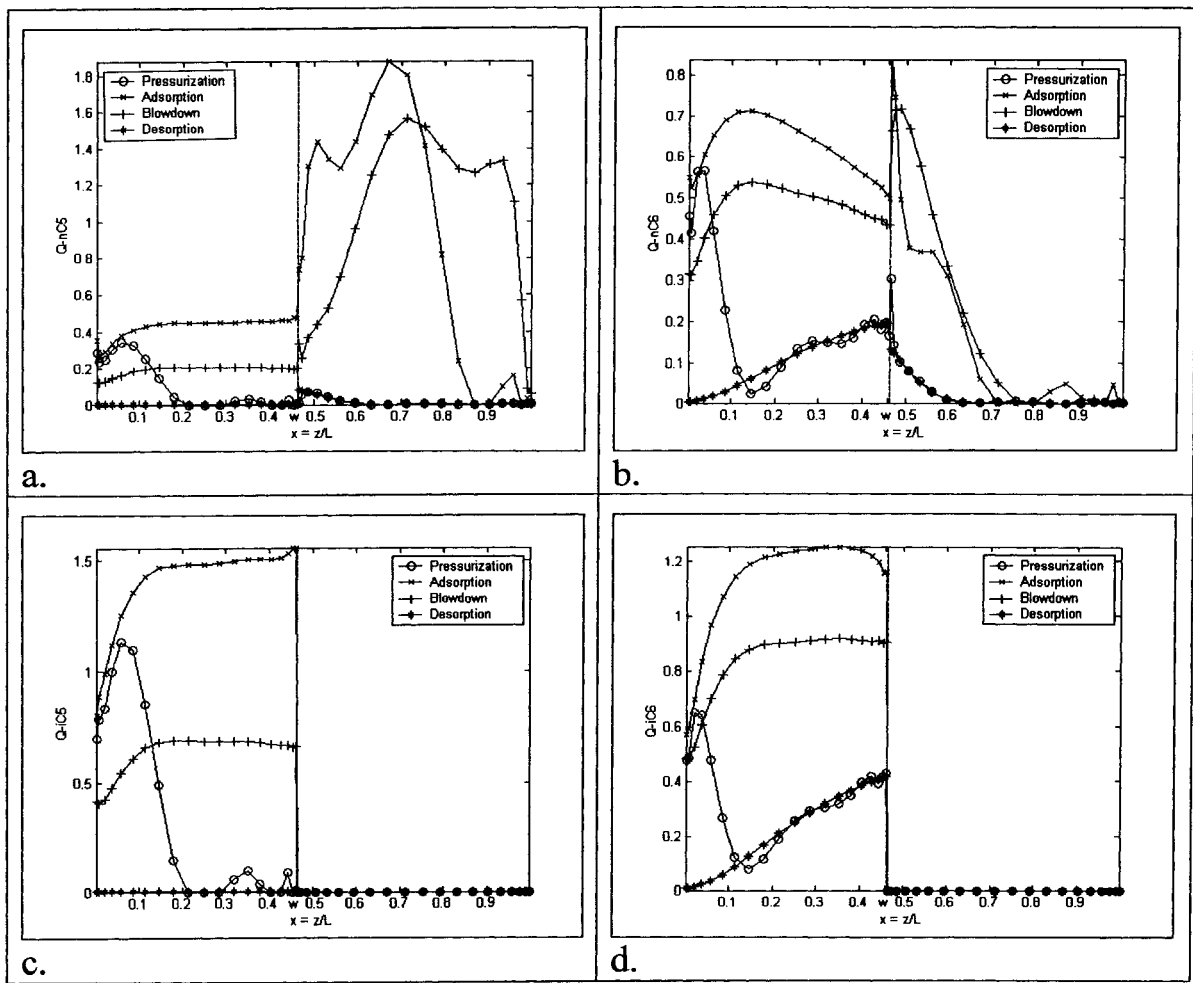


Figure 4.9: Solid phase capacitance profiles for reactive components in the PSARM bed at the end of cyclic steady state:

a.) n-C<sub>5</sub>,

b.) n-C<sub>6</sub>,

c.) i-C<sub>5</sub>,

d.) i-C<sub>6</sub>.

Parametric values are in Table 4.1. (Conventional PSARM unit/H<sub>2</sub> purge).



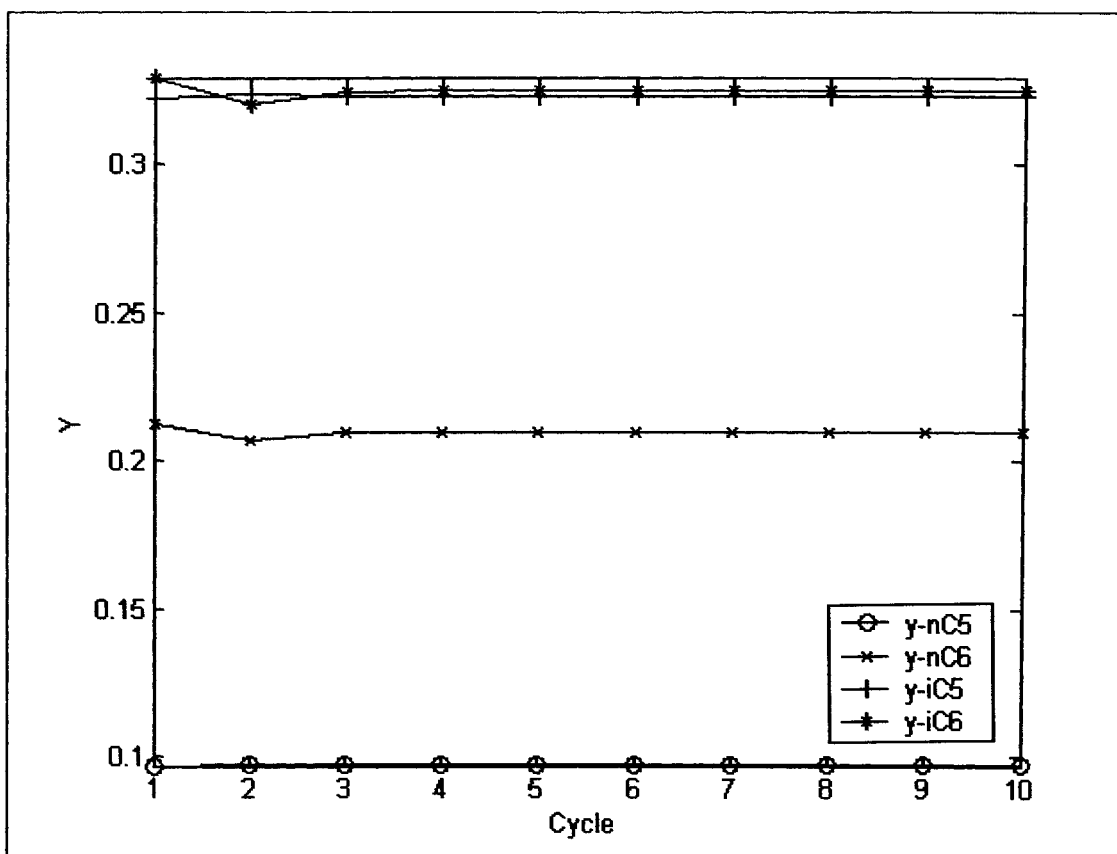


Figure 4.10: Approach to cyclic steady state, showing exit concentrations of reactants and products at end of Blowdown/Reaction step. Parametric values are in Table 4.1. (Conventional PSARM unit/H<sub>2</sub> purge).

Table 4.2: Percentage occupation for reactive components of the solid phase for both catalyst and adsorber sections (Conventional PSARM unit/H<sub>2</sub> purge).

Component	Pressurization		Adsorption		Blowdown		Desorption	
	Catalyst	Adsorber	Catalyst	Adsorber	Catalyst	Adsorber	Catalyst	Adsorber
n-C <sub>5</sub>	1.44	0.21	6.68	20.41	3.01	23.66	0.00	0.21
n-C <sub>6</sub>	6.32	1.40	21.55	9.87	16.46	13.71	3.58	1.25
i-C <sub>5</sub>	4.69	0.00	22.05	0.00	10.00	0.00	0.01	0.00
i-C <sub>6</sub>	10.42	0.00	39.20	0.00	28.93	0.00	7.47	0.00
Total	22.87	1.61	89.47	30.28	58.41	37.37	11.06	1.46

#### 4.7.1.2 Conventional PSARM Cyclic Process with Self Regeneration

Most of the discussion pertaining to the shape of the uptake curves obtained is performed in the previous section. In this section, we will focus on differences between uptakes obtained using pure hydrogen as a purge stream and those obtained by purging with a portion of the product stream.

Figure 4.11a illustrates the concentrations of reactive components at the end of the steady state reaction/pressurization step. The back-end concentration of  $i\text{-C}_5$  peaks-up to a value of 0.112. Similarly, for  $i\text{-C}_6$ , the concentration peaks up to a value of 0.103. These two peaks are direct resultants of purging with part of the product stream. The reactive components three dimensional concentration figures in Appendix F illustrate an increase in reactive components concentrations at the start of this step. These peaks are due to the simultaneous desorption of  $i\text{-C}_5$  and  $i\text{-C}_6$  and adsorption of  $n\text{-C}_5$  and  $n\text{-C}_6$ .

Figure 4.11b illustrates the concentrations of reactive components at the end of the steady state reaction/adsorption step. Concentrations of  $i\text{-C}_5$  and  $i\text{-C}_6$  peak to their highest values at the adsorption section due to hydrogen migration through the membrane. These peaks in products concentrations cause a drop in hydrogen concentration towards the end of the adsorber section. The drop in hydrogen concentration is illustrated in Figure 4.12. The noticeable increase in solid phase occupation of the adsorber section, over that reported by the hydrogen purge case, is due to purging with part of the product stream. The purge stream that contains amounts of  $i\text{-C}_5$  and  $i\text{-C}_6$  causes partial solid phase saturation at the reactor section of the vessel during desorption/reaction step. The partial saturation allows for a faster saturation of reactor section solid phase and consequently allows for a less residence time for reactive components in the reactor section. The lower residence time allows for passage of more amounts of reactive components through the adsorber section. The passage of higher amounts causes higher solid phase occupation.

Figure 4.11c illustrates the concentrations of reactive components at the end of the steady state blowdown/reaction step. The concentration profiles in this figure are similar to those generated in the previous section using hydrogen as purge stream.

Figure 4.11d illustrates the concentrations of reactive components at the end of the steady state desorption/reaction step. Reverse reactions take place at the front end of the reactor section in this step due to the high concentrations of  $i\text{-C}_5$  and  $i\text{-C}_6$  over  $n\text{-C}_5$  and  $n\text{-C}_6$  respectively.

Temperature profiles for all steps are illustrated in Figure 4.13. At the end of the reaction/pressurization step, a peak of 18 degrees is noticed at the reactor entrance. This peak is due to the rapid conversion of  $n\text{-C}_5$  to  $i\text{-C}_5$ . The high temperature profile towards the end of adsorber section is a continuation of the peak from the previous desorption/reaction step.

The temperature profile for the reactor section at the end of the reaction/adsorption step is similar to the one produced by the hydrogen purge case. For the adsorber section, a shift in temperature peak towards the end of the adsorber bed is noticed. This peak shift is due to the rapid saturation of the adsorber bed that is discussed earlier.

The temperature profile for the reactor section at the end of the blowdown/reaction step is also similar to the one produced by the hydrogen purge case. For the adsorber section, the lower temperature profile at the end of the bed is due to the blowdown of the high-temperature batches out of the vessel.

The lower reactor bed front temperature profiles at the end of desorption/reaction step, compared to hydrogen purge case, is due to the reverse chemical reaction taking effect at the entrance. The reverse chemical reaction is a direct result of the higher inlet concentrations of isoalkanes compared to normal alkanes. This is an expected result since we are purging with a portion of the product stream.

Figure 4.14 illustrates the velocity profiles at the end of each of the four steps. Velocity profiles are similar to those reported by the hydrogen purge case.

Solid phase capacitance profiles are illustrated in Figure 4.15. The total solid phase coverages of both reactor and adsorber sections are illustrated in Table 4.3. At the end of the reaction/pressurization step, the noticeable overall increase in the reactor section solid occupation for  $i\text{-C}_5$  and  $i\text{-C}_6$  is due to purging with a stream that contains amounts of these two components. Also, the noticeable increase in  $n\text{-C}_5$  concentration in the reactor section at the end

of the desorption/reaction step is attributed to the reverse chemical reaction taking place at this step. Due to the slow reaction kinetics for n-C<sub>6</sub>/i-C<sub>6</sub> pair, only a small increase is reported in n-C<sub>6</sub> solid phase occupation. The reverse chemical reaction is a direct result of purging with a stream containing only isoalkanes and hydrogen.

The exit concentrations of reactive components at the end of the blowdown/reaction step are plotted in Figure 4.16. It takes 7 cycles for this system to reach cyclic steady state.

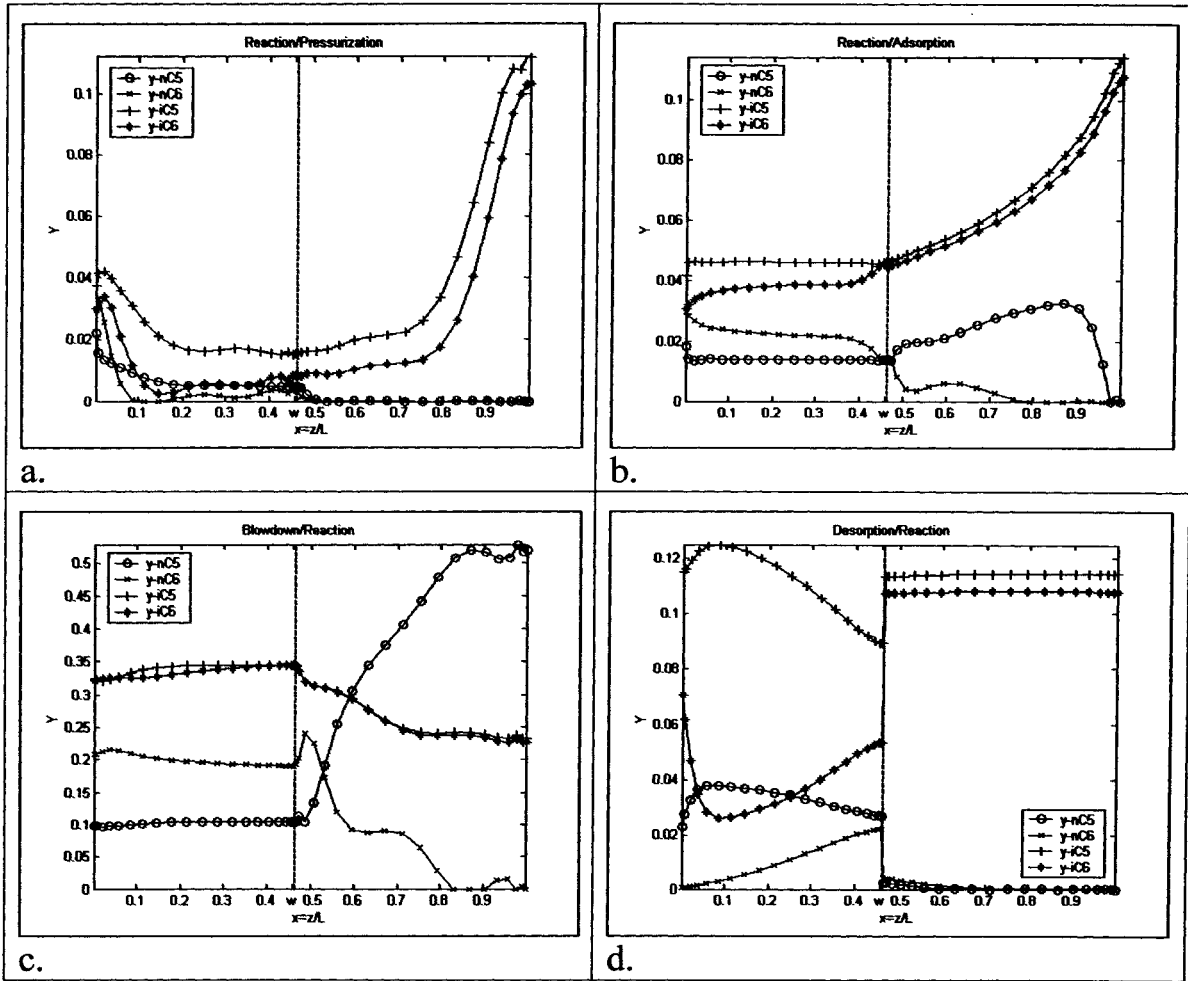


Figure 4.11: Gas phase concentration profiles for reactive components in the PSAR bed at the end of cyclic steady state:

- a.) reaction/pressurization
- b.) reaction/adsorption
- c.) blowdown/reaction,
- d.) desorption/reaction.

Parametric values are in Table 4.1. (Conventional PSARM unit/Self Regeneration).

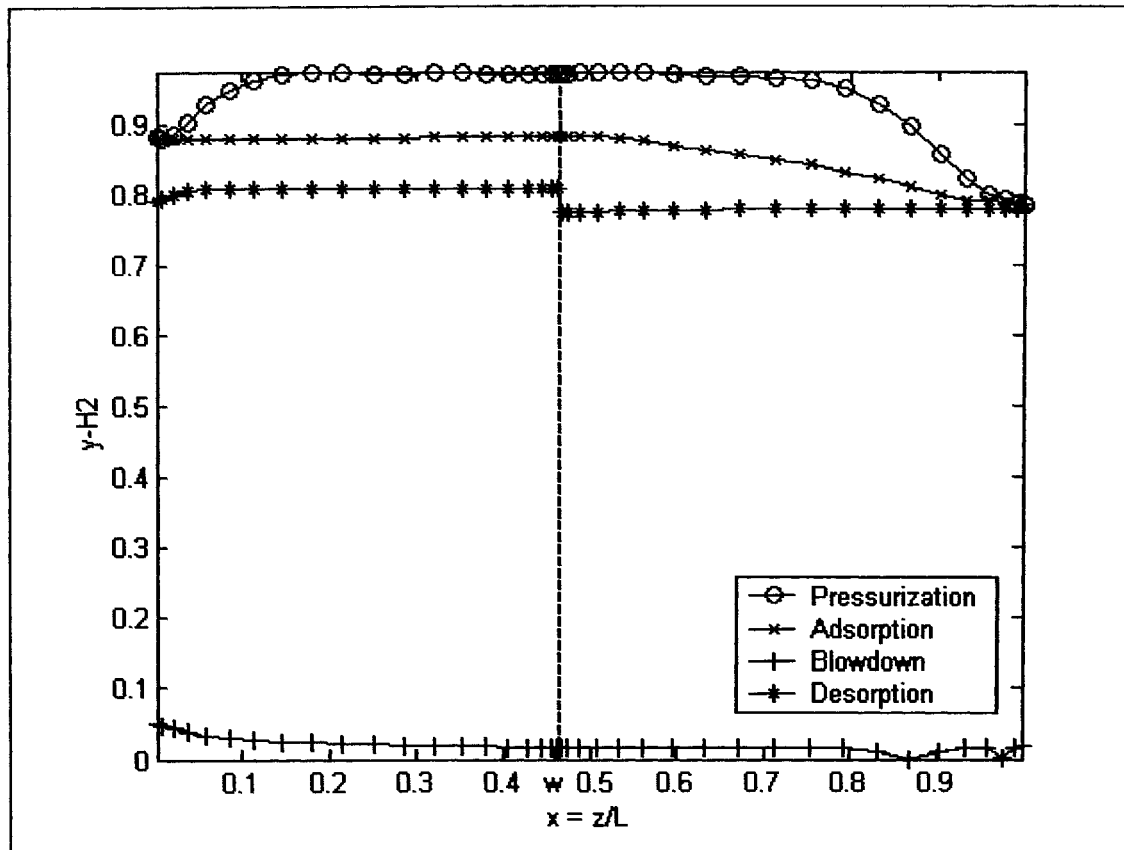


Figure 4.12: Gas phase concentration profiles for  $H_2$  in the PSARM bed at the end of cyclic steady state. Parametric values are in Table 4.1. (Conventional PSARM unit/Self Regeneration).

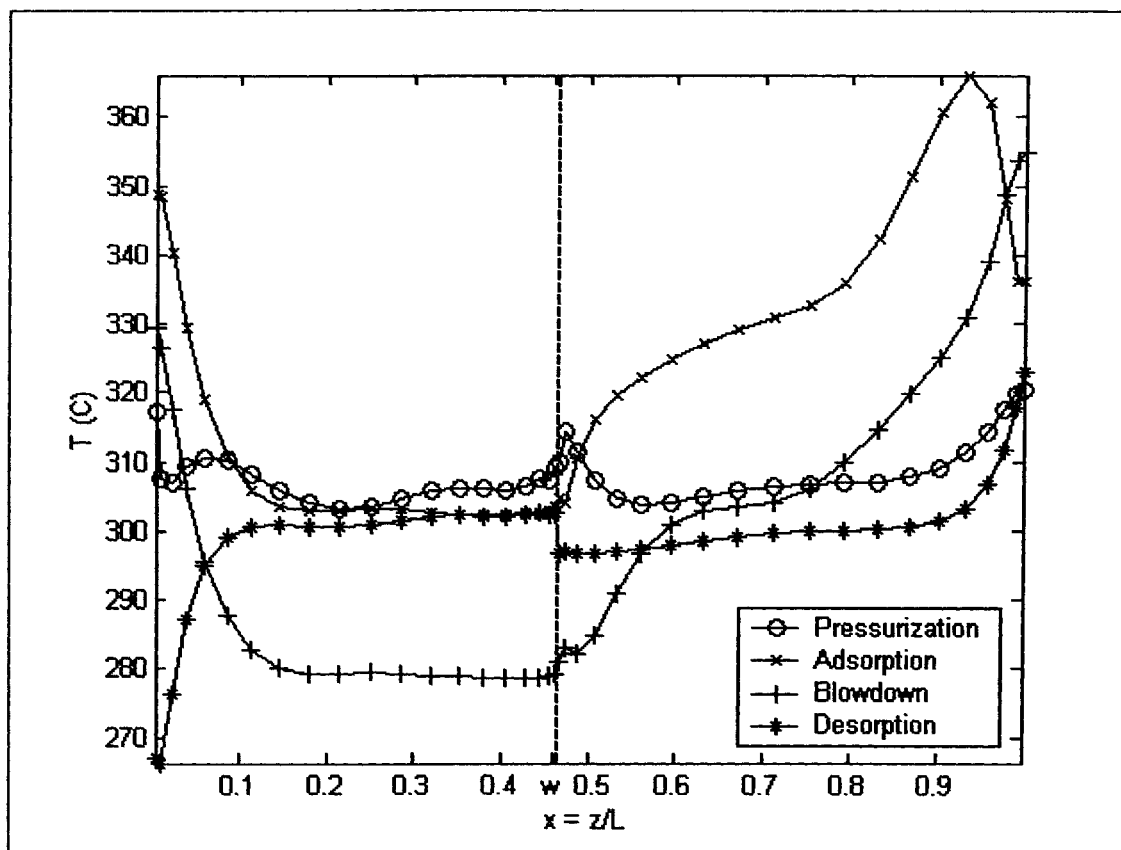


Figure 4.13: Temperature Profiles in the bed at the end of cyclic steady state. Parametric values are in Table 4.1. (Conventional PSARM unit/Self Regeneration).



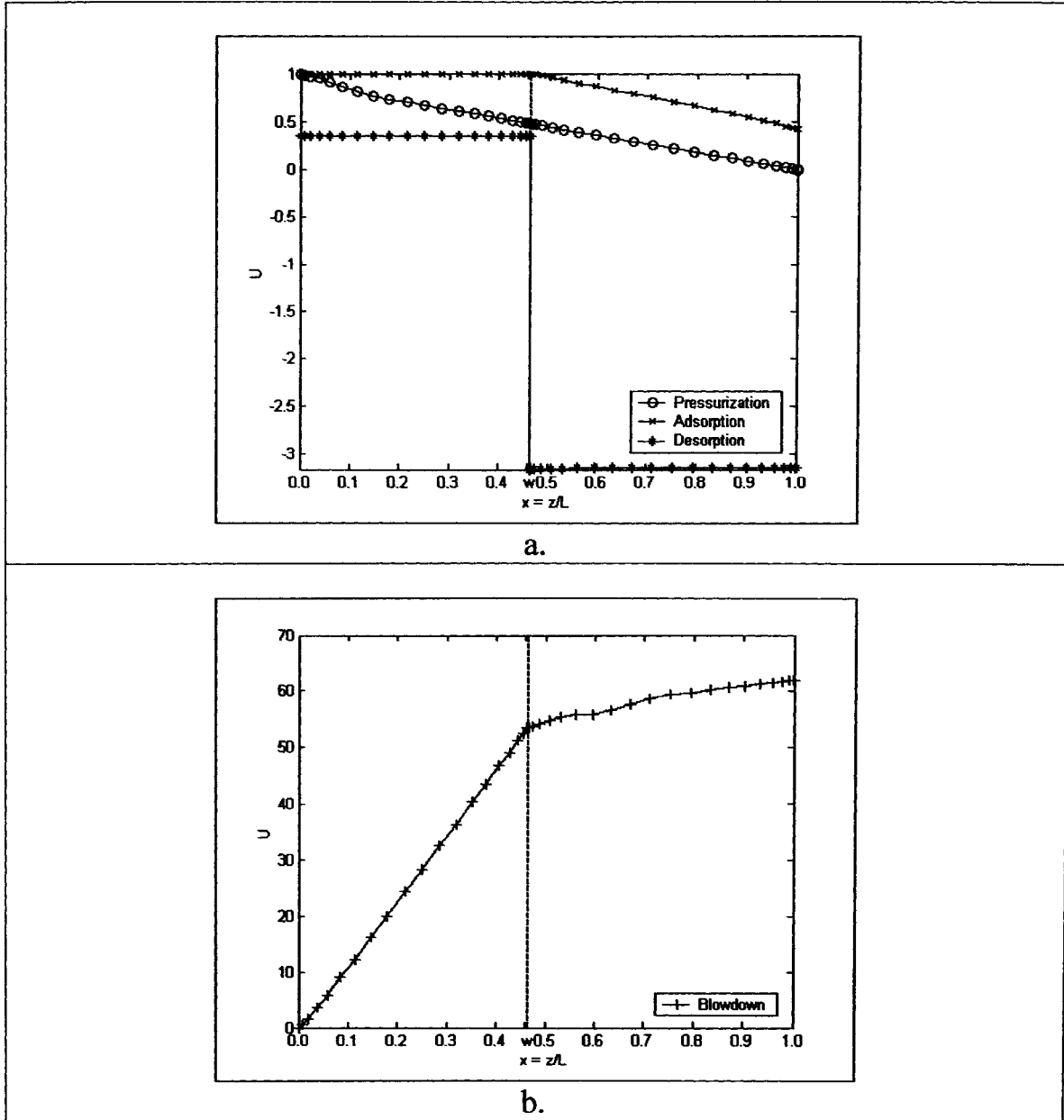


Figure 4.14: Velocity Profiles in the bed at the end of cyclic steady state:

- e. Pressurization, Adsorption and Desorption steps Profiles.
- f. Blowdown step profile.

Parametric values are in Table 4.1. (Conventional PSARM unit/Self Regeneration).

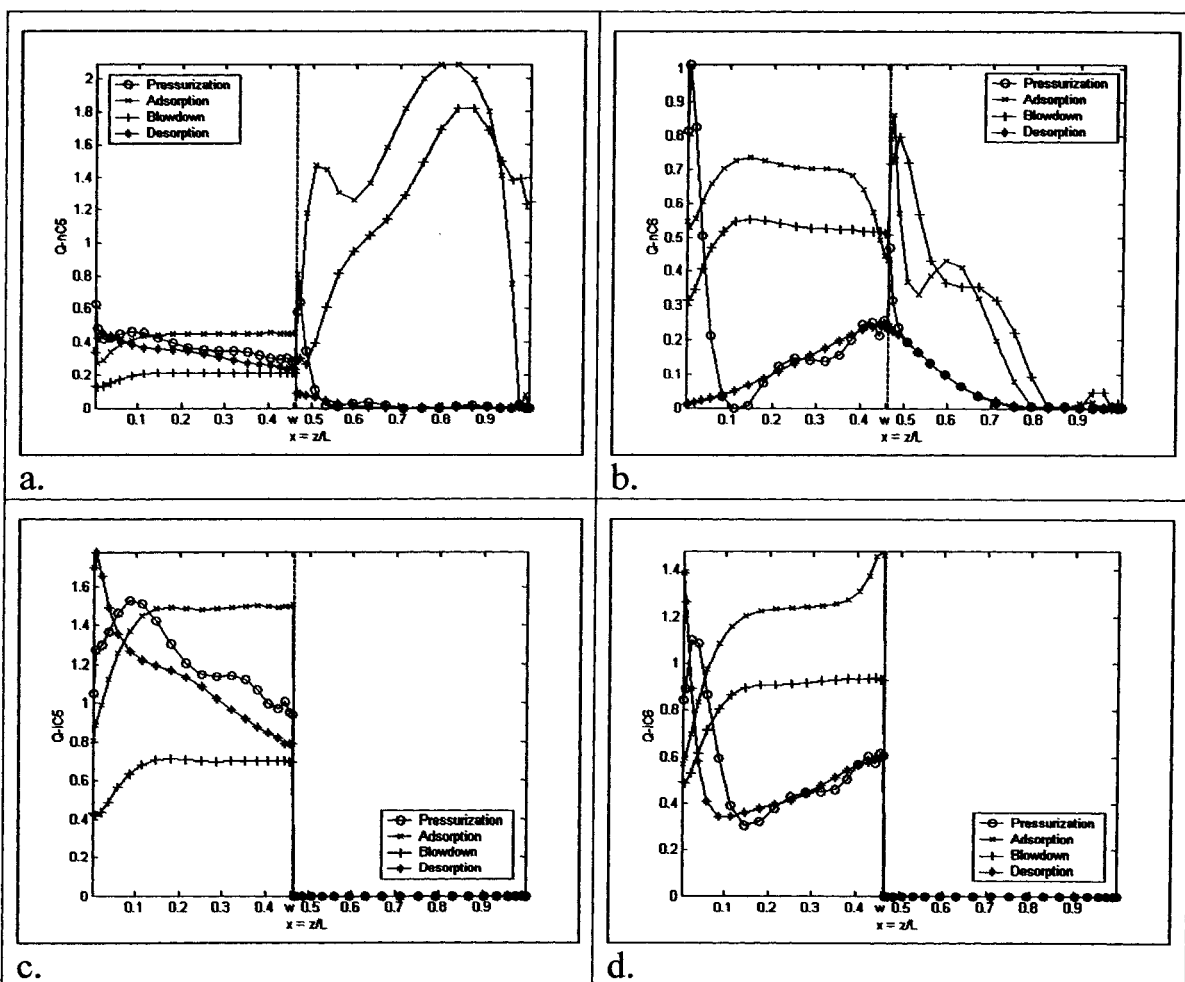


Figure 4.15: Solid phase capacitance profiles for reactive components in the PSAR bed at the end of cyclic steady state:

- a.)  $n-C_5$ ,
- b.)  $n-C_6$ ,
- c.)  $i-C_5$ ,
- d.)  $i-C_6$ .

Parametric values are in Table 4.1. (Conventional PSARM unit/Self Regeneration).

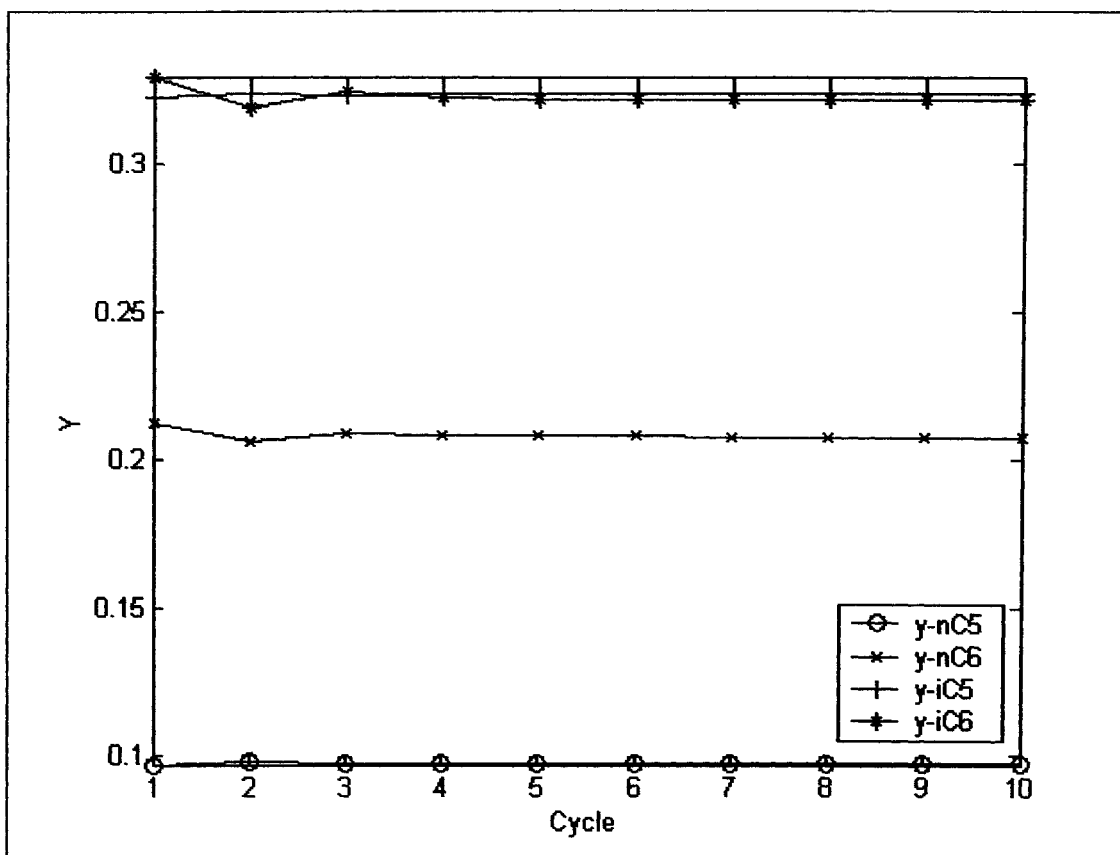


Figure 4.16: Approach to cyclic steady state, showing exit concentrations of reactants and products at end of Blowdown/Reaction step. Parametric values are in Table 4.1. (Conventional PSARM unit/Self Regeneration).

Table 4.3: Percentage Occupation for reactive components of the solid phase for both catalyst and adsorber sections (Conventional PSARM unit/Self Regeneration).

Component	Pressurization		Adsorption		Blowdown		Desorption	
	Catalyst	Adsorber	Catalyst	Adsorber	Catalyst	Adsorber	Catalyst	Adsorber
n-C <sub>5</sub>	5.85	0.91	6.67	32.57	3.11	26.67	5.13	0.29
n-C <sub>6</sub>	6.55	4.52	22.86	15.66	17.41	20.07	4.26	4.21
i-C <sub>5</sub>	19.07	0.00	22.04	0.00	10.30	0.00	17.26	0.00
i-C <sub>6</sub>	18.16	0.00	40.34	0.00	29.43	0.00	16.69	0.00
Total	49.64	5.43	91.91	48.23	60.25	46.74	43.33	4.49

#### 4.7.2 PSARM Cyclic Process with Waste Stream Recycled to feed

In this section, the effluent of the blowdown/reaction and desorption/reaction steps is combined with the fresh feed before entering the reaction section.

##### 4.7.2.1 PSARM Cyclic Process with Waste Stream Recycled to feed (Hydrogen Purge)

In this section, pure hydrogen is used as purge stream during desorption/reaction step. Most of the discussion pertaining to the shape of the uptake curves produced is performed in sections 4.7.1.1 and 4.7.1.2. In this section, we will focus on differences between uptakes obtained with conventional PSARM unit and those obtained with recycling waste stream to feed. In this section, pure hydrogen is used as purge stream.

Figures 4.17a and 4.17c illustrates the concentrations of reactive components at the end of the steady state reaction/pressurization and blowdown/reaction steps, respectively. Concentration profiles for these steps are similar to those produced by the conventional PSARM model.

Figure 4.17b illustrates the concentrations of reactive components at the end of the steady state reaction/adsorption step. The noticeable drop in n-C<sub>6</sub> conversion is due to the lower reactor section temperature compared to the conventional PSARM model.

Figure 4.17d illustrates the concentrations of reactive components at the end of the steady state desorption/reaction step. The figures follow the same profiles illustrated in conventional PSARM unit. However, those profiles are at lower concentrations than those reported by conventional PSARM units. The lower concentrations are due to the higher solid phase occupations in the previous reaction/adsorption step. Higher solid phase occupations cause higher velocities in the blowdown/reaction and desorption/reaction steps. Higher velocities push more amounts of reactive components out of the bed resulting in lower bed concentrations compared to conventional PSARM models.

Figure 4.18 illustrates the hydrogen profiles at the end of each of the steps for the last cycle. Hydrogen profiles produced with this model are very close to those produced with a conventional PSARM model.

Figure 4.19 illustrates the temperature profiles for all steps at the end of the steady state cycle. The reaction/pressurization, blowdown/reaction and desorption/reaction steps temperature profiles follow similar shapes to their respective counterparts from the conventional PSARM unit.

For the reaction/adsorption step, a lower peak is observed, in the adsorption section, than that produced by a conventional PSARM. This lower peak is a direct result of diluting fresh feed reactive components' concentrations with that of the recycle stream.

Capacitance profiles for each of the reactive components are illustrated in Figure 4.21. Also, the percentage relative solid phase occupation for each of the components is illustrated in table 4.4. An overall lower solid phase occupation is noticed in this model over the conventional PSAR model. The recycle of low reactive components' streams to the unit is the reason behind this low occupation.

The exit concentrations of reactive components at the end of the blowdown/reaction step are plotted in Figure 4.22. It takes 6 cycles for this system to reach cyclic steady state.

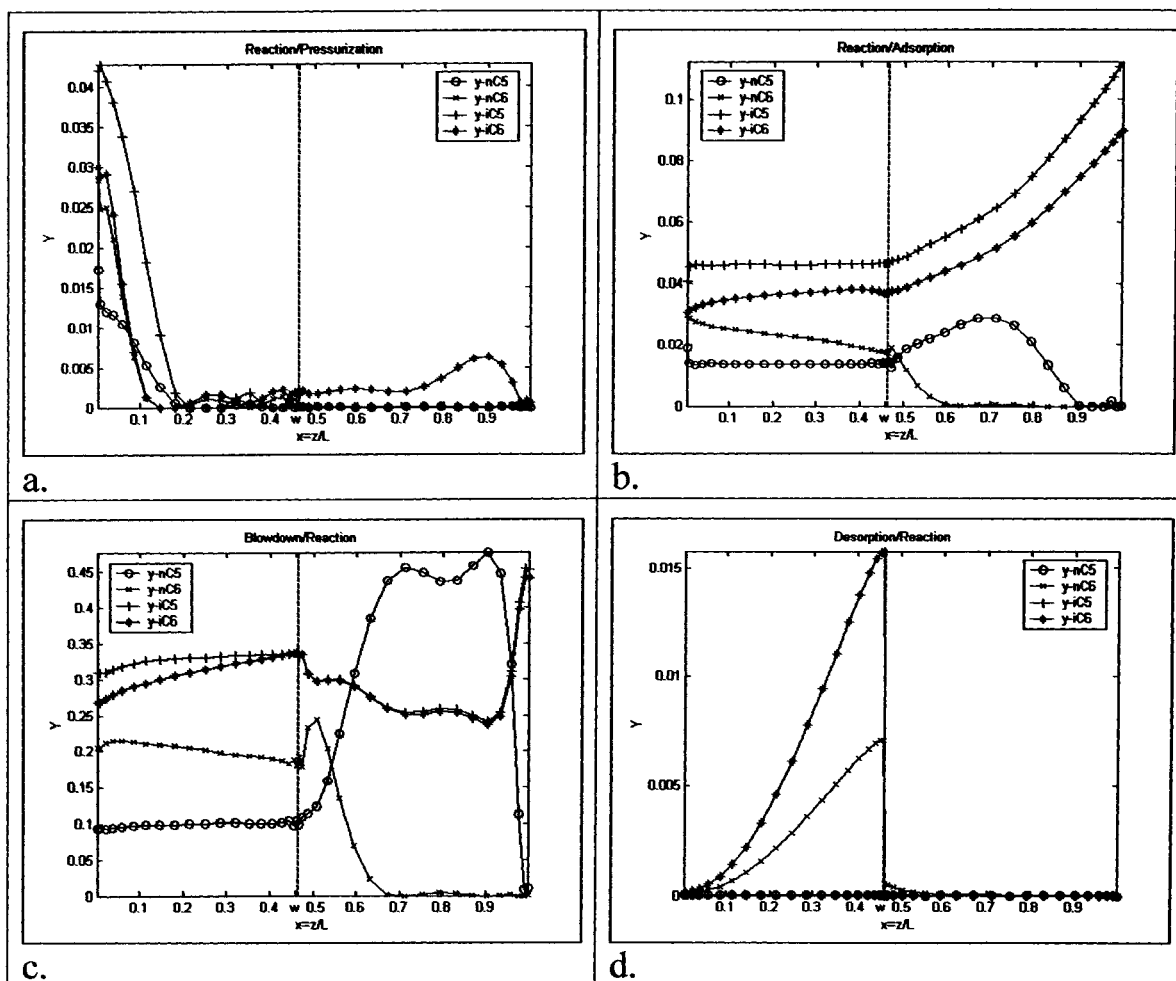


Figure 4.17: Gas phase concentration profiles for reactive components in the PSARM bed at the end of cyclic steady state:

- a.) reaction/pressurization,
- b.) reaction/adsorption,
- c.) blowdown/reaction,
- d.) desorption/reaction.

Parametric values are in Table 4.1. (PSARM with waste recycled to feed/ $H_2$  Purge).

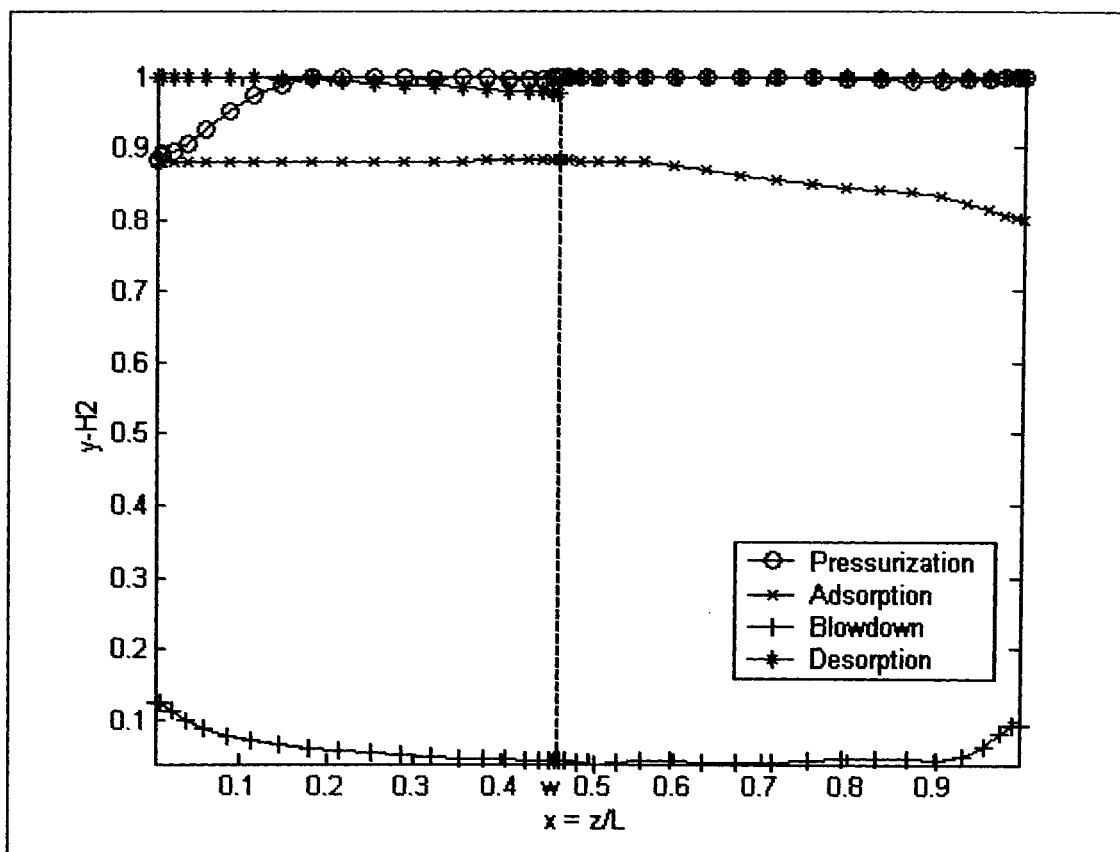


Figure 4.18: Gas phase concentration profiles for  $H_2$  in the PSARM bed at the end of cyclic steady state. Parametric values are in Table 4.1. (PSARM with waste recycled to feed/ $H_2$  Purge).



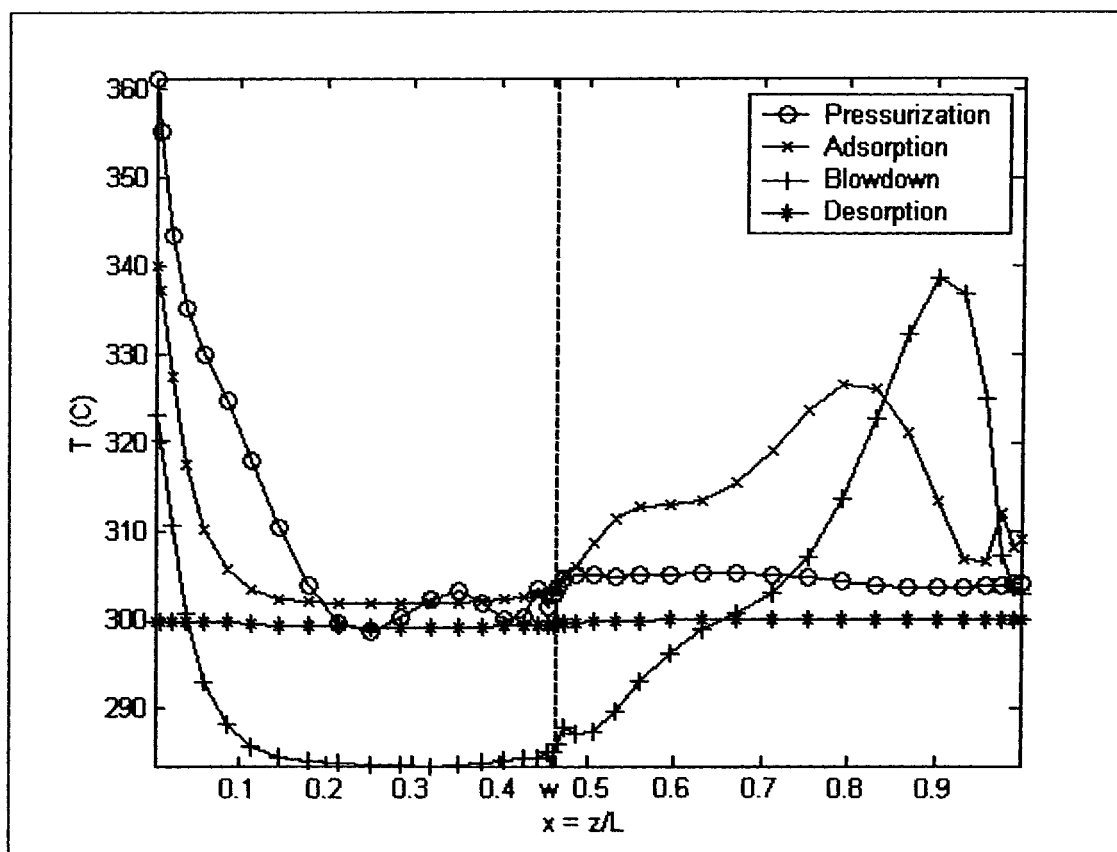


Figure 4.19: Temperature Profiles in the bed at the end of cyclic steady state. Parametric values are in Table 4.1. (PSARM with waste recycled to feed/ $H_2$  Purge).

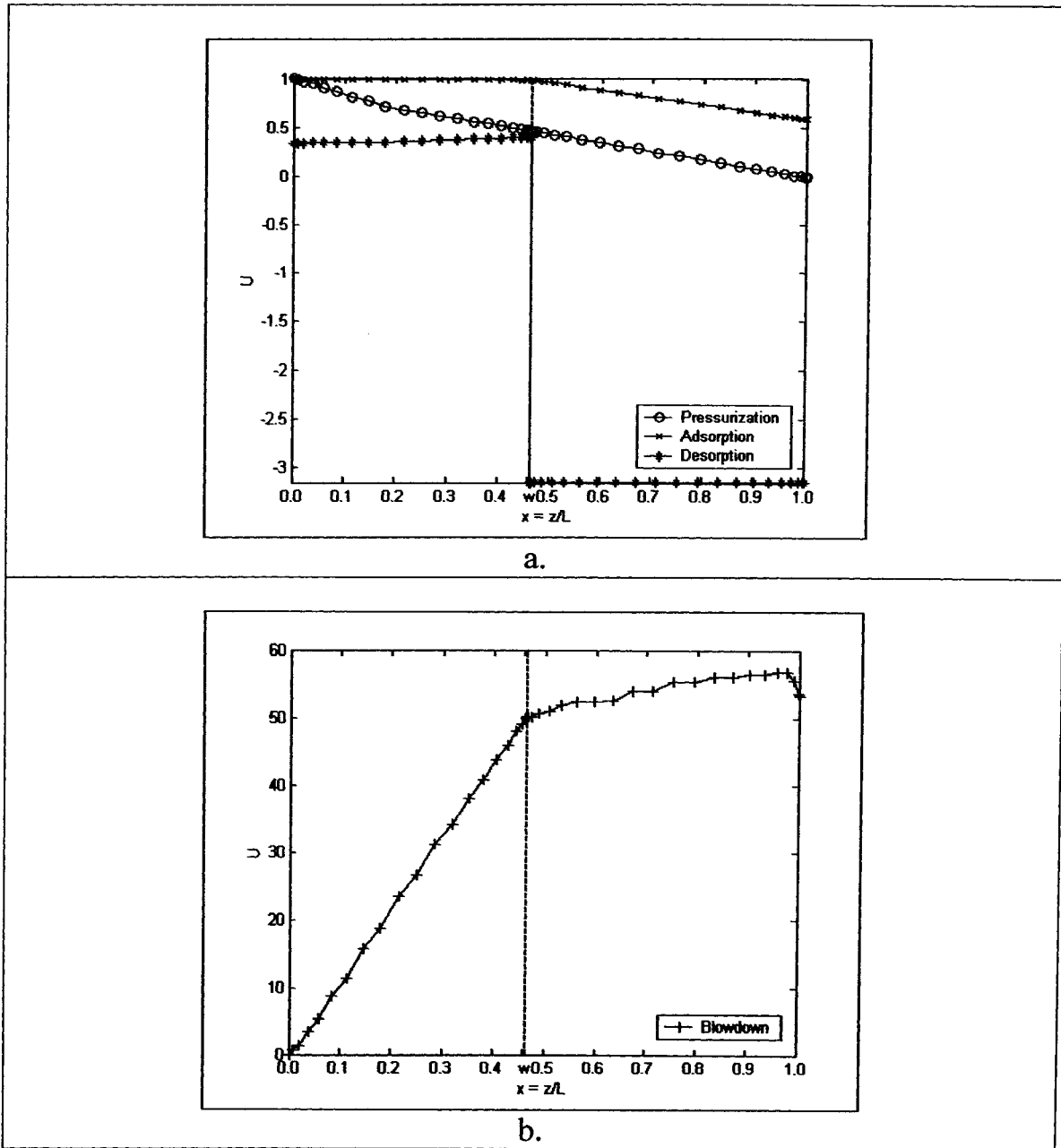


Figure 4.20: Velocity Profiles in the bed at the end of cyclic steady state:

- a. Pressurization, Adsorption and Desorption steps Profiles.
- b. Blowdown step profile.

Parametric values are in Table 4.1(PSARM with waste recycled to feed/ $H_2$  Purge).

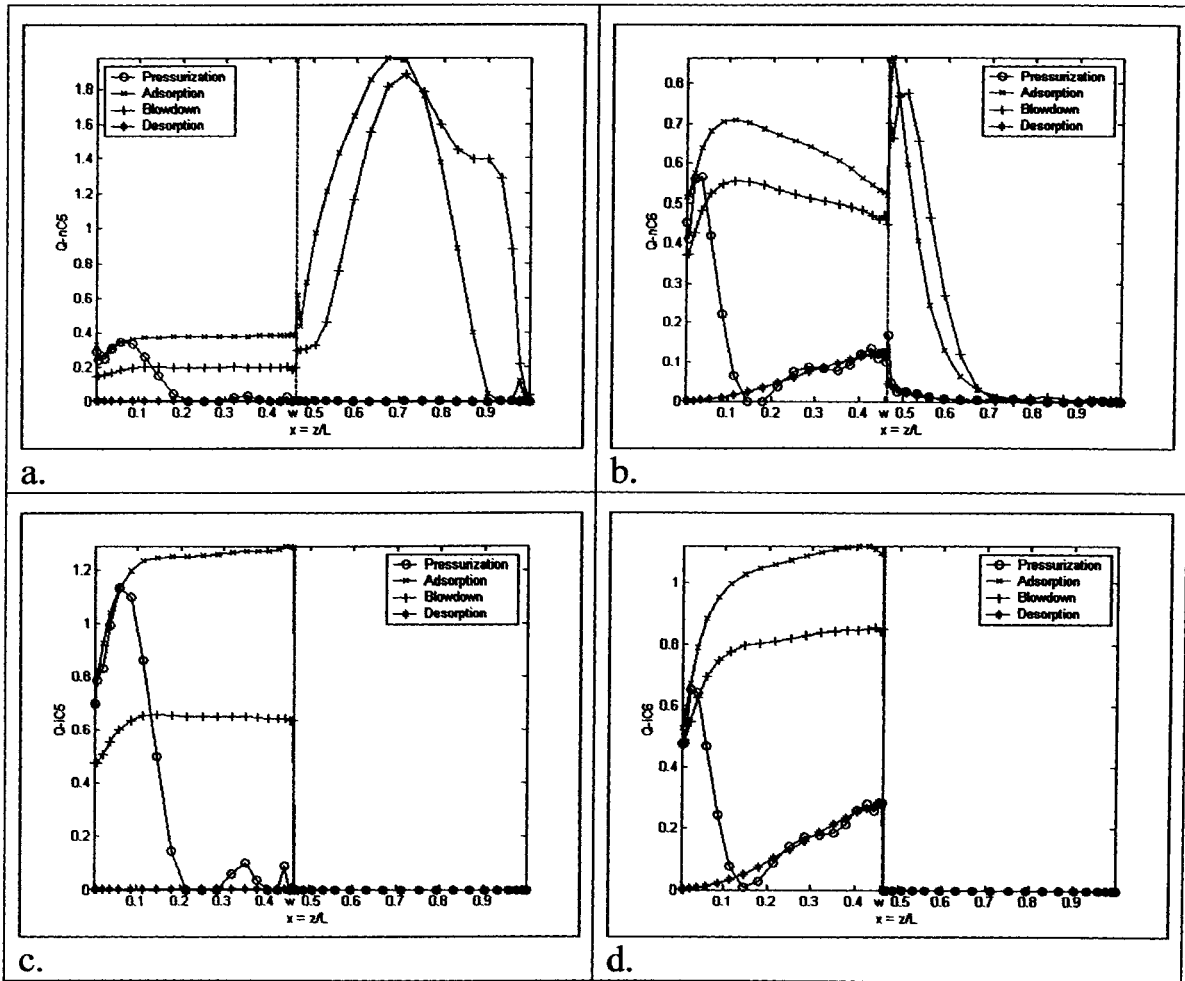


Figure 4.21: Solid phase capacitance profiles for reactive components in the PSAR bed at the end of cyclic steady state:

a.) n-C<sub>5</sub>,

b.) n-C<sub>6</sub>,

c.) i-C<sub>5</sub>,

d.) i-C<sub>6</sub>.

Parametric values are in Table 4.1. (PSARM with waste recycled to feed/H<sub>2</sub> Purge).

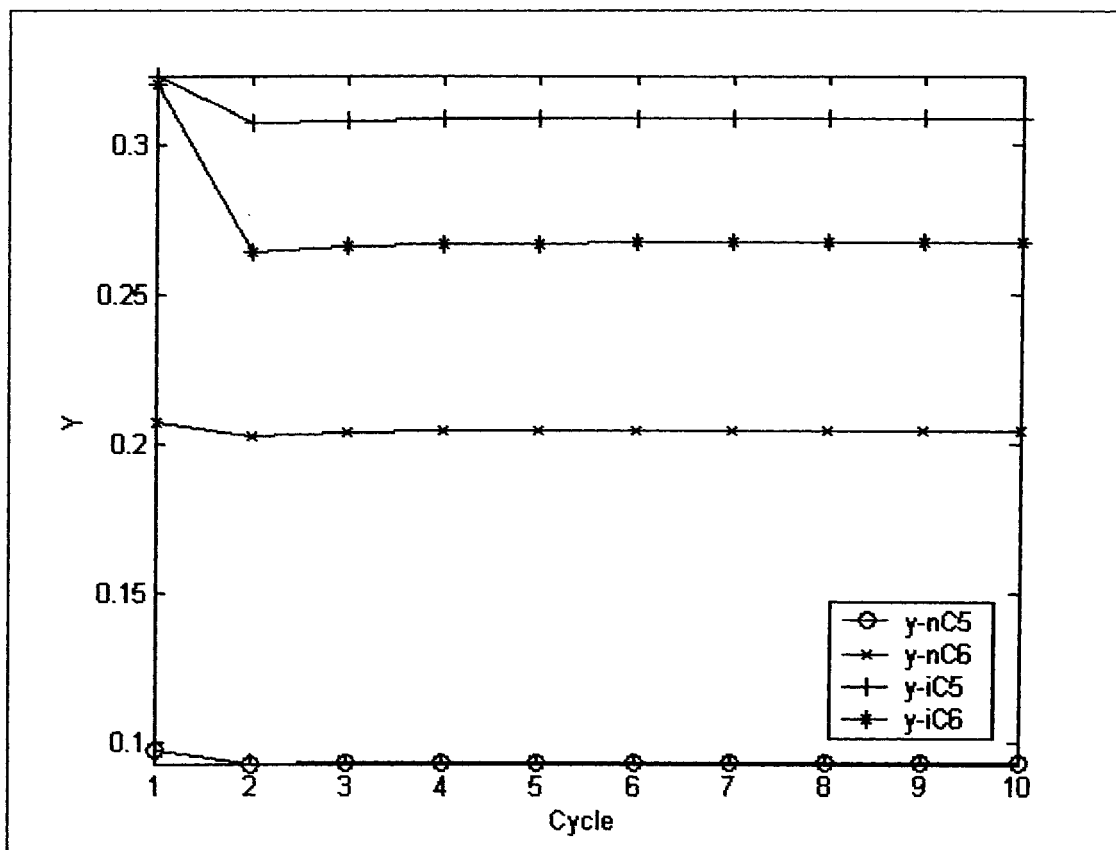


Figure 4.22: Approach to cyclic steady state, showing exit concentrations of reactants and products at end of Blowdown/Reaction step. Parametric values are in Table 4.1. (PSARM with waste recycled to feed/H<sub>2</sub> Purge).

Table 4.4: Percentage Occupation for reactive components of the solid phase for both catalyst and adsorber sections (PSARM with waste recycled to feed/H<sub>2</sub> Purge).

Component	Pressurization		Adsorption		Blowdown		Desorption	
	Catalyst	Adsorber	Catalyst	Adsorber	Catalyst	Adsorber	Catalyst	Adsorber
n-C <sub>5</sub>	4.27	0.83	5.69	23.65	2.96	26.16	0.00	0.00
n-C <sub>6</sub>	6.06	1.41	22.38	9.76	17.36	13.00	1.96	0.50
i-C <sub>5</sub>	13.88	0.00	18.86	0.00	9.82	0.00	0.00	0.00
i-C <sub>6</sub>	28.79	0.00	34.79	0.00	26.85	0.00	4.28	0.00
Total	53.00	2.24	81.05	33.41	56.99	39.16	6.24	0.50

#### 4.7.2.2 PSARM Cyclic Process with Waste Stream Recycled to feed (Self Regeneration)

In this section, a portion of the product stream is recycled as a purge stream during desorption/reaction step. Moreover, the effluents of blowdown/reaction and desorption/reaction steps are recycled back and combined with the feed before entering the vessel. As mentioned before, most of the discussion pertaining to the shape of the uptake curves produced is performed in sections 4.7.1.1 and 4.7.1.2. In this section, focus is drawn to differences between uptakes obtained from conventional PSARM unit with self-regeneration and those obtained from recycling waste stream to feed.

Figures 4.23a and 4.23c illustrate the concentrations of reactive components at the end of the steady state reaction/pressurization and blowdown/reaction steps, respectively. The components' profiles for these two steps are similar to the profiles produced in a conventional PSARM unit.

Figure 4.23b illustrated the concentrations of reactive components at the end of the steady state reaction/adsorption step. The higher  $i\text{-C}_5$  and  $i\text{-C}_6$  exit concentrations in this model, compared to conventional PSARM model are due to the lower adsorber section temperature.

Figure 4.23d illustrates the concentration of reactive components at the end of the steady state desorption/reaction step. The difference in concentration profiles between this model and the conventional PSARM model is attributed to the changing composition of the product stream flowing out of the vessel undergoing reaction/adsorption step. The changing composition is a direct result of recycling the waste stream to the vessel undergoing reaction/adsorption step.

Figure 4.24 illustrates the hydrogen concentration profiles at the end of each step. Reaction/pressurization, reaction/adsorption and blowdown/reaction profiles for this model are close to their counterparts from the conventional PSARM unit. The difference in desorption/reaction hydrogen concentration profiles in this model and the conventional PSARM model is due to recycling waste streams to the reaction/adsorption step. Recycling waste streams to reaction/adsorption step alters the time concentration curves of this step. Since part of the reaction/adsorption step product is used as purge stream, this purge stream composition is altered as a consequence.

Figure 4.25 illustrates the temperature profiles for all steps at the end of the steady state cycle. For the reaction/pressurization step, the reactor section temperature profile follows that of a conventional PSARM unit. The adsorber section temperature profile falls to a lower value due to lower inlet temperature of the previous desorption/reaction step. The lower temperature profile of the reaction/pressurization step continues in reaction/adsorption and reaction/desorption steps. The overall lower bed profile in all four steps is attributed to the addition of the hydrogen make up stream at the inlet of the vessel undergoing reaction/adsorption step. The make up hydrogen dilutes the concentration of reactive components resulting in a lower bed temperature profile.

Figure 4.27 illustrates the solid phase relative occupations for reactive components in all steps at the end of the cyclic steady state. Results of total coverage of the solid phase are illustrated in Table 4.4. The overall lower relative solid phase occupation, relative to conventional PSARM unit, is a direct result of the addition of the hydrogen makeup stream to the recycle stream directed to the vessel undergoing reaction/adsorption step.

The exit concentrations of reactive components at the end of the blowdown/reaction step are plotted in Figure 4.28. It takes 10 cycles for this system to approach cyclic steady state.

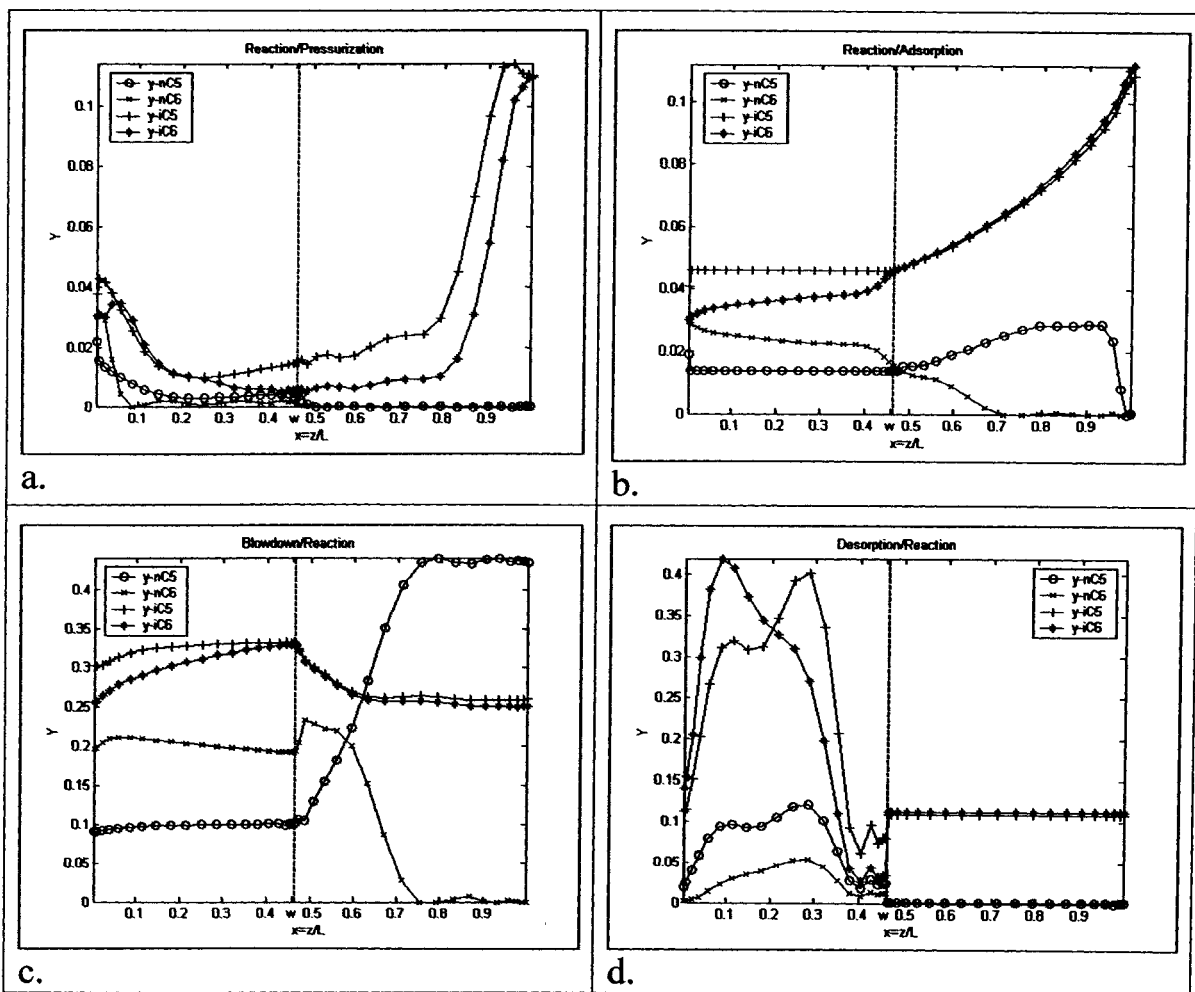


Figure 4.23: Gas phase concentration profiles for reactive components in the PSAR bed at the end of cyclic steady state:

a.) reaction/pressurization,

b.) reaction/adsorption,

c.) blowdown/reaction,

d.) desorption/reaction.

Parametric values are in Table 4.1. (PSARM with waste recycled to feed/self regeneration).



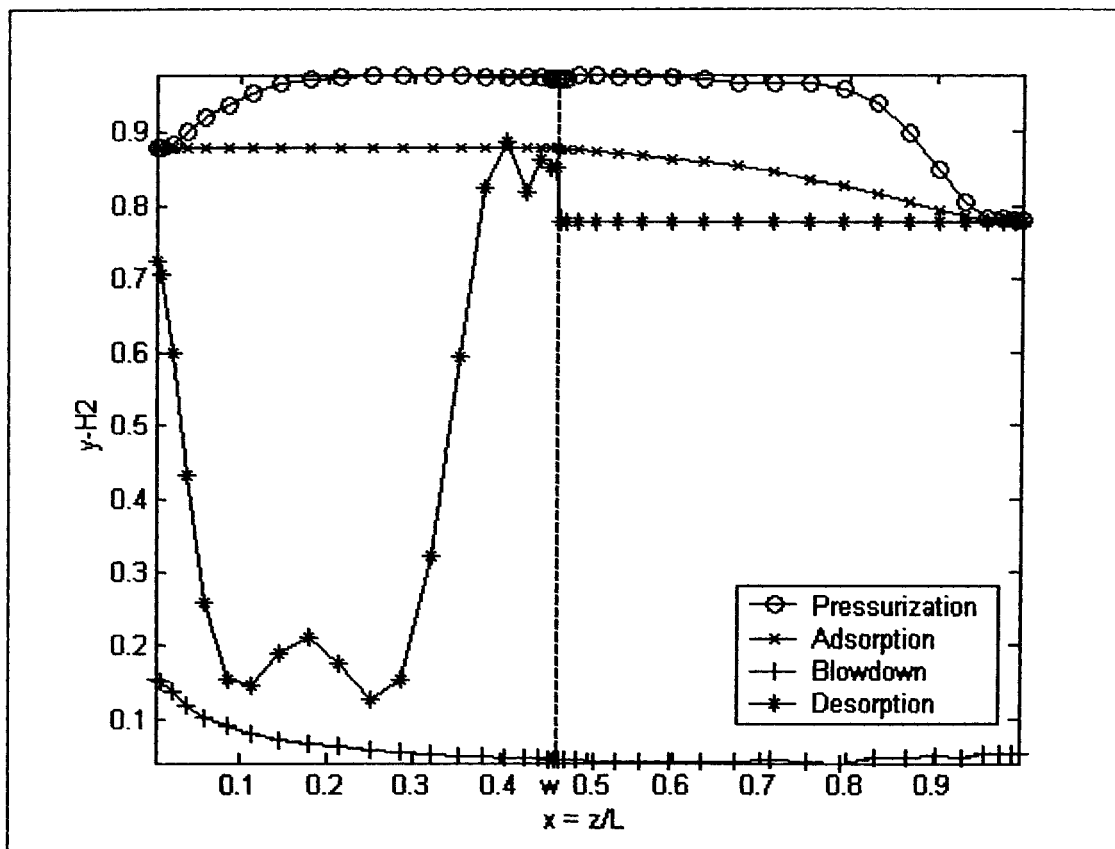


Figure 4.24: Gas phase concentration profiles for  $H_2$  in the PSARM bed at the end of cyclic steady state. Parametric values are in Table 4.1. (PSARM with waste recycled to feed/self regeneration).

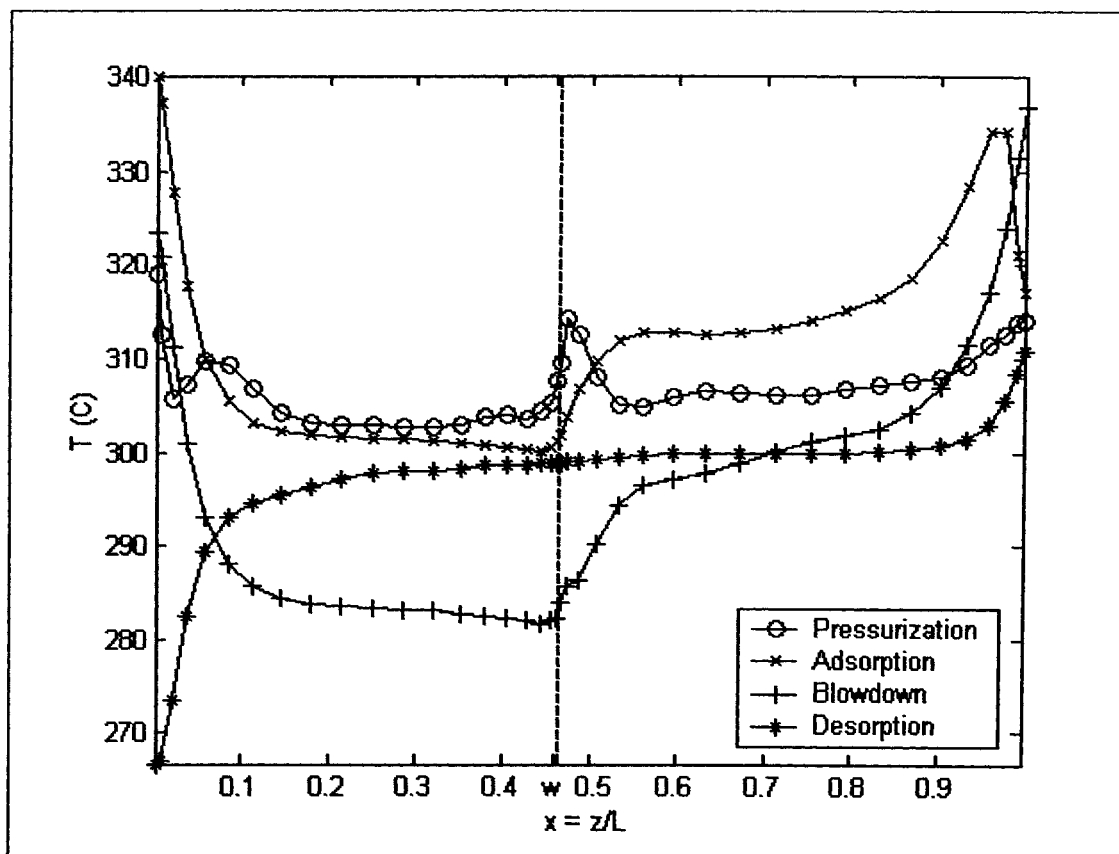


Figure 4.25: Temperature Profiles in the bed at the end of cyclic steady state. Parametric values are in Table 4.1. (PSARM with waste recycled to feed/self regeneration).

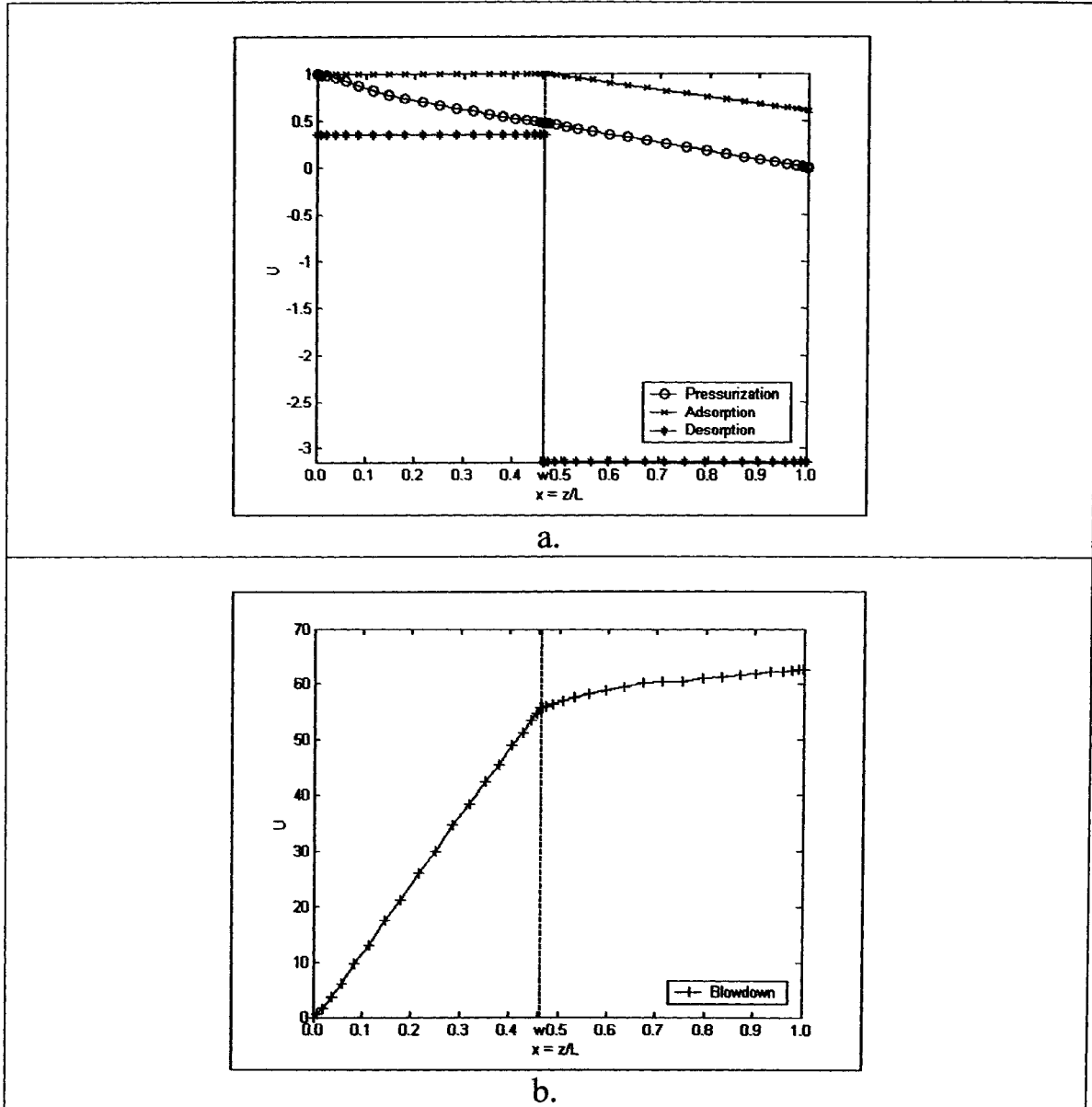


Figure 4.26: Velocity Profiles in the bed at the end of cyclic steady state:

a. Pressurization, Adsorption and Desorption steps Profiles.

b. Blowdown step profile.

Parametric values are in Table 4.1. (PSARM with waste recycled to feed/self regeneration)

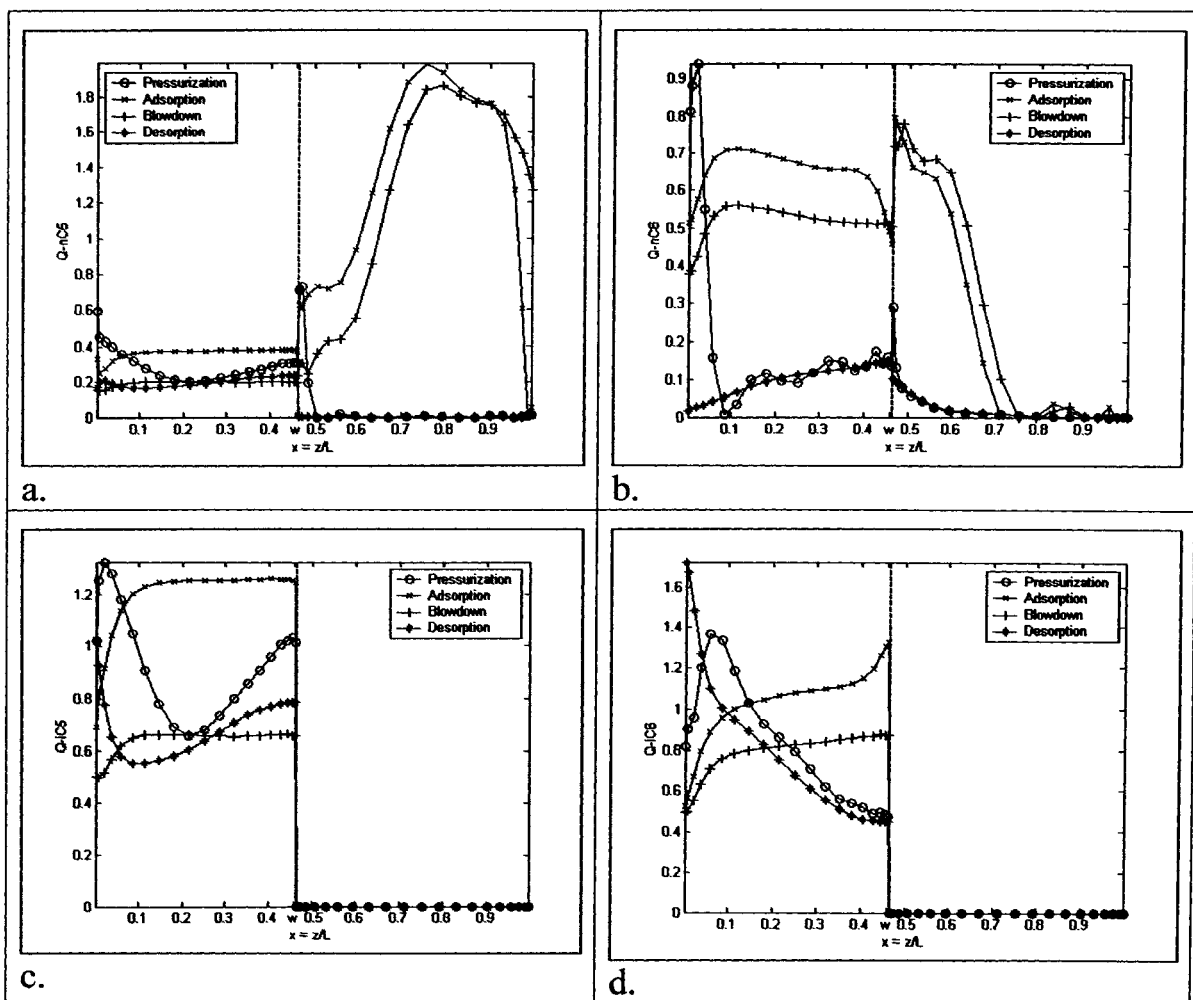


Figure 4.27: Solid phase capacitance profiles for reactive components in the PSAR bed at the end of cyclic steady state:

- a.)  $n-C_5$ ,
- b.)  $n-C_6$ ,
- c.)  $i-C_5$ ,
- d.)  $i-C_6$ .

Parametric values are in Table 4.1. (PSARM with waste recycled to feed/self regeneration).

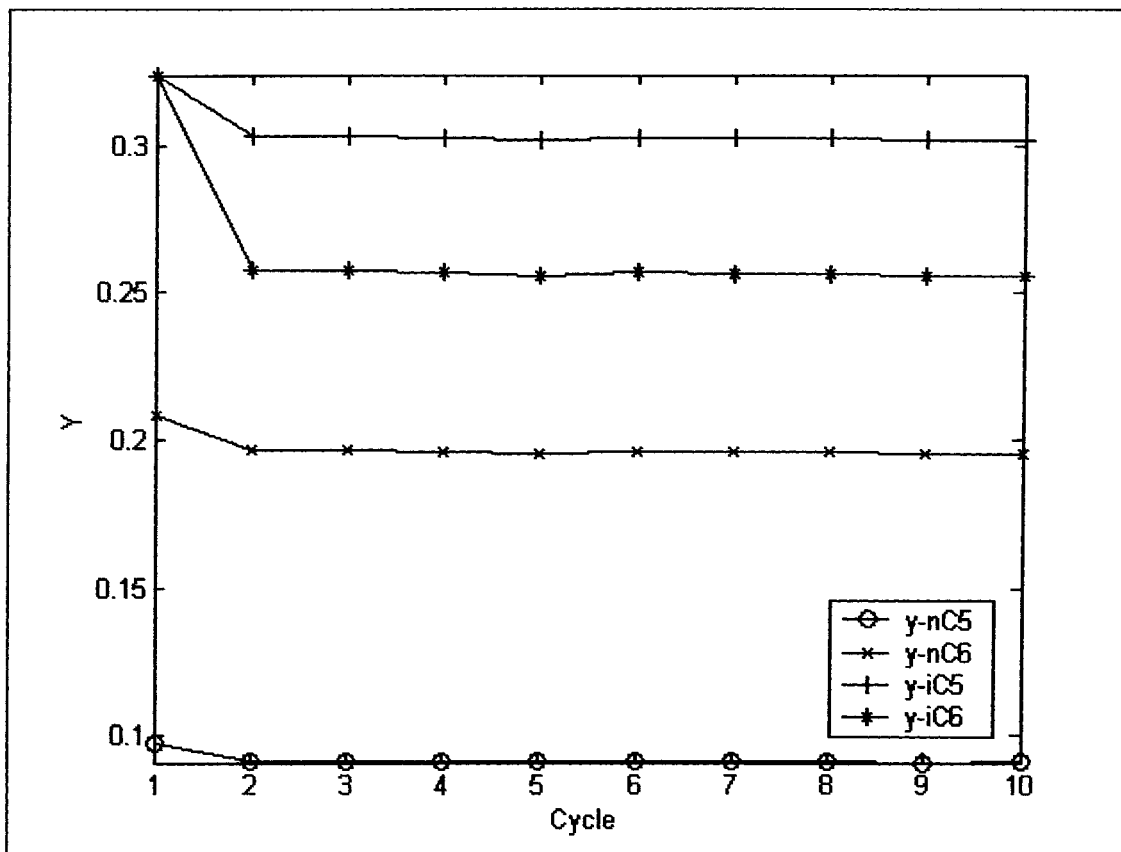


Figure 4.28: Approach to cyclic steady state, showing exit concentrations of reactants and products at end of Blowdown/Reaction step. Parametric values are in Table 4.1. (PSARM with waste recycled to feed/Self Regeneration).

Table 4.5: Percentage Occupation for reactive components of the solid phase for both catalyst and adsorber sections (PSARM with waste recycled to feed/Self Regeneration).

Component	Pressurization		Adsorption		Blowdown		Desorption	
	Catalyst	Adsorber	Catalyst	Adsorber	Catalyst	Adsorber	Catalyst	Adsorber
n-C <sub>5</sub>	4.27	0.60	5.69	29.70	3.02	27.27	3.07	0.04
n-C <sub>6</sub>	6.05	1.40	22.38	16.71	17.84	20.26	3.37	1.33
i-C <sub>5</sub>	13.88	0.00	18.80	0.00	9.99	0.00	10.38	0.00
i-C <sub>6</sub>	28.79	0.00	35.43	0.00	27.15	0.00	26.49	0.00
Total	52.99	2.00	82.30	46.41	58.00	47.53	43.30	1.37

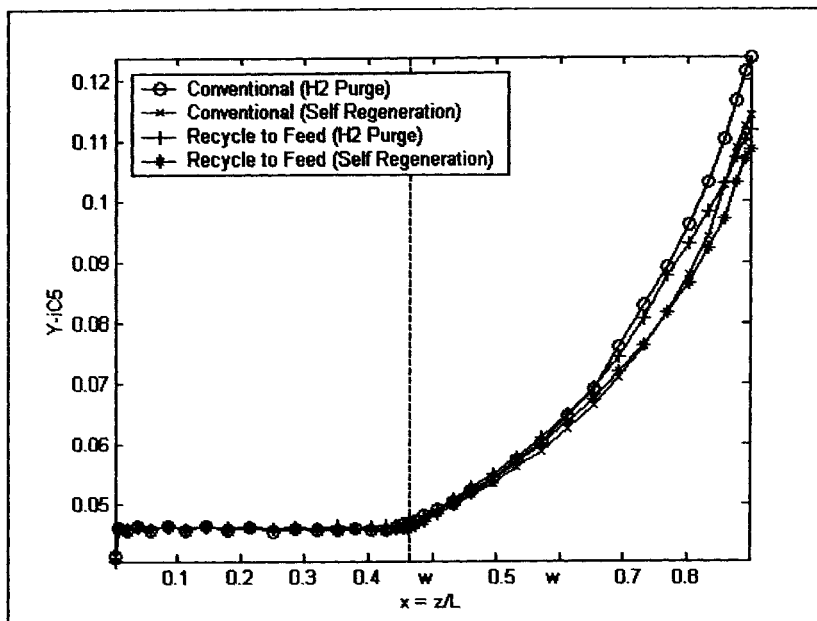
### 4.7.3 Overall Comparison of PSARM Systems

The same comparative analysis, performed in the previous, chapter is repeated in this chapter. Models are compared against each other to determine the best practical model. The full reaction/adsorption profiles, at the end of cyclic steady state, for i-C<sub>5</sub> are plotted in Figure 4.29a. Similar profiles for i-C<sub>6</sub> are plotted in Figure 4.29b. Values for exit concentrations of iso-pentane and iso-hexane, at the end of reaction/adsorption cyclic steady state are reported in Table 4.8.

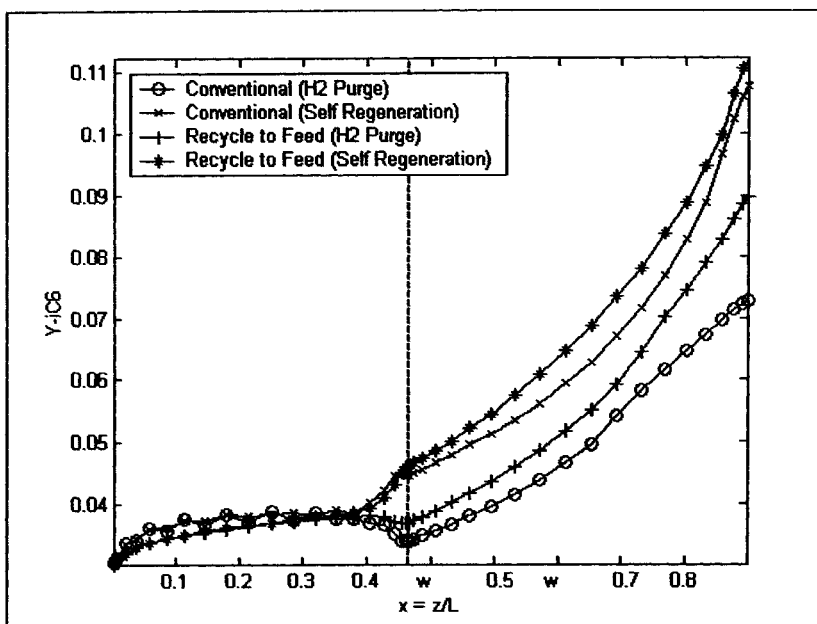
As illustrated in Figures 4.29a and 4.29b, the system that produces the highest concentrations of i-C<sub>5</sub> is the conventional system that uses hydrogen as purge stream. However, i-C<sub>5</sub> exit concentrations from all systems are very close to each other. The system that produces the highest concentrations of i-C<sub>6</sub> is the conventional PSARM system that uses part of the product stream as purge stream.

Table 4.8 illustrates the yield of conventional PSARM systems versus those recycling waste streams to feed. The yield of conventional PSARM system is 66.2%. The yield of systems that recycle their waste streams is 100%. If process yield is the evaluation criteria, the best system for the production of i-C<sub>5</sub> and i-C<sub>6</sub> is the one that recycles the waste stream and uses part of the product stream as purge stream.

It should also be noted that, in general, PSARM systems achieve cyclic steady state more rapidly than their counter PSAR systems.



a.



b.

Figure 4.29: Products' profiles for all models at the end of cyclic steady state reaction/adsorption step:

a.) i-C<sub>5</sub>

b.) i-C<sub>6</sub>



Table 4.6: Exit concentrations of iso-pentane and iso-hexane at the end of steady state cyclic reaction/adsorption step.

<b>Model</b>	<b>Isopentane Exit Molar Fraction</b>	<b>Isohexane Exit Molar Fraction</b>	<b>Yield</b>
Conventional PSARM (H <sub>2</sub> Purge)	0.1170	0.0852	66.2
Conventional PSARM (Self Regeneration)	0.1123	0.1134	66.2
PSARM with waste recycled to feed (H <sub>2</sub> Purge)	0.1118	0.0898	100
PSARM with waste recycled to feed (Self Regeneration)	0.1169	0.1220	100

## Nomenclature

$A_H$	heat of adsorption [cal/mol]
$B$	dimensionless adiabatic temperature rise [-] $= (-\Delta H_{ads})q_{A,ref} / (C_{ps}T_f)$
$c_T$	total gas concentration in the column [mol/cm <sup>3</sup> ]
$c_{Tf}$	total feed gas concentration [mol/cm <sup>3</sup> ]
$C_o$	total gas concentration in the column [mol/cm <sup>3</sup> ]
$C_T$	dimensionless total gas concentration in the column [-]
$C_{pg}$	heat capacity of the gas phase [J/(mol.K)]
$C_{ps}$	heat capacity of the adsorbent [J/(g.K)]
$Da_t$	true Damkohler number [-] = $\omega \frac{k_1 L}{u_f}$
$D_A$	pore diffusivity of component A [cm <sup>2</sup> /s]
$D_L$	axial mass dispersion coefficient [cm <sup>2</sup> /s]
$D_{pipe}$	membrane tube diameter
$d_C$	column diameter [cm]
$E_p$	membrane activation energy
$f_m$	membrane Phase Volume Fraction in Adsorber Section
$f_s$	solid Adsorbent Phase Volume Fraction in Adsorber Section
$h$	overall heat transfer coefficient [WAm <sup>2</sup> /K]
$(-\Delta H_{ads})$	isosteric heat of adsorption [J/mol]
$k$	membrane permeation coefficient
$k_o$	preexponential factor for membrane permeation coefficient
$k_{gl}$	global mass-transfer coefficient [cm/s]
$K_{ads}$	adsorption equilibrium constant [bar <sup>-1</sup> ] = $K_o \exp(-AH/R/T)$
$K_{C1}$	equilibrium reaction rate constant for nC <sub>5</sub> [-]
$K_{C2}$	equilibrium reaction rate constant for nC <sub>6</sub> [-]
$K_O$	limiting adsorption equilibrium constant [bar <sup>-1</sup> ]
$k_{1,1}$	forward reaction rate constant for nC <sub>5</sub> [cm <sup>3</sup> /g of cat/s]
$k_{1,2}$	forward reaction rate constant for nC <sub>6</sub> [cm <sup>3</sup> /g of cat/s]
$K_L$	axial bed thermal conductivity [W/(m.K)]
$L$	length of the PSA column [cm]
$n$	coefficient of Nitta et al. isotherm [-]
$N_f$	number of film mass-transfer units [-]

$N_w$	number of wall heat-transfer units [-] = $4hL/(d_c u_f C_{pg} c_{Tf} \varepsilon)$
$P$	total pressure in the column [bar]
$Pe$	mass Peclet number [-]
$Pe_H$	thermal Peclet number [-] = $u_f L C_{pg} c_{Tf} / K_L$
$P_H$	constant high pressure during adsorption step [bar]
$P_L$	constant low pressure during desorption step [bar]
$\langle q_A \rangle$	average adsorbed-phase concentration [mol/kg]
$q_{A,ref}$	adsorbed-phase concentration at equilibrium with $y_{Af}$ at $P_H$ and $T_f$ [mol/kg]
$q_{max}$	maximum adsorbed-phase concentration [mol/kg]
$Q_A$	dimensionless adsorbed-phase concentration [-] = $\langle q_A \rangle / q_{max}$
$R$	ideal gas constant [bar.cm <sup>3</sup> /mol.K]
$S$	Reactor Section Purge Velocity Ratio [-]
$t$	time [s]
$T$	column gas temperature [K]
$T_f$	feed gas temperature [K]
$\bar{T}$	dimensionless column gas temperature [-] = $(T - T_f) / T_f$
$u$	interstitial velocity [cm/s]
$u_f$	interstitial feed velocity [cm/s]
$u_p$	purge gas velocity [cm/s]
$U$	dimensionless interstitial velocity [-] = $u/u_f$
$V_1$	first PSARM Vessel
$V_2$	second PSARM Vessel
$V_3$	a container used to hold effluent of blowdown/reaction step.
$x$	dimensionless axial coordinate in the column [-] = $z/L$
$X_m$	membrane thickness
$y_A$	mole fraction of component A in the bulk phase in the column [-]
$y_{Af}$	mole fraction of component A in the feed [-]
$y_{Aj}$	mole fraction of component A in the bulk phase in bed i [-]
$y_{Bf}$	mole fraction of component B in the feed [-]
$y_{Bj}$	mole fraction of component B in the bulk phase in bed i [-]
$y_{AL}$	mole fraction of component A at the exit of the column [-]
$\langle y_{A2} \rangle$	average mole fraction of the sorbate in the pores of the adsorbent pellet in bed 2 [-]
$y_{A,eq}$	equilibrium mole fraction of component A for isomerization reaction [-]
$z$	axial coordinate in the column [cm]

## Greek Letters

$v_1$	dimensionless axial coordinate in the catalyst-bed region [-]
$v_2$	dimensionless axial coordinate in the adsorbent-bed region [-]
$\varepsilon_1$	bed void fraction [-]
$\varepsilon_2$	adsorbent void fraction [-]
$\zeta_H$	thermal capacity factor [-] = $(1 - \varepsilon_1 - \varepsilon_2)\rho_s C_{ps} / (\varepsilon_{Tf} C_{pg})$
$\zeta_m$	mass capacity factor [-]
$\mu_{H_2}$	permeation factor [-]
$\theta_{A,ref}$	coverage of adsorbent at $y_{Af}$ and $P_H$ [-]
$\rho_s$	apparent density of the adsorbent [g/cm <sup>3</sup> ]
$\tau$	dimensionless time [-] = $u_f t / L$
$\gamma_f$	dimensionless heat of adsorption [-] = $(-\Delta H_{ads}) / (RT_f)$

## Subscripts

A	n-pentane
B	n-hexane
C	i-hexane
D	n-hexane
f	Feed
I	inert (Nitrogen / Hydrogen)
m	membrane
P	purge
R	recycle
S	solid
T	total
1	reactor Section
2	adsorber Section

## CHAPTER 5

### CONCLUSIONS AND RECOMMENDATIONS

#### 5.1 CONCLUSIONS

Conversion, in chemical reaction processes, is often limited by chemical equilibrium. Moreover, the reactants-products separation section always follows the reactor section.

In both PSAR and PSARM models, a fixed bed is operated with a mixture of catalyst and adsorbent. In the PSARM model, a hydrogen membrane is added to partially separate hydrogen from the product stream.

In the present study, the system is modeled for reaction and separation of five components: n-pentane, n-hexane, iso-pentane, iso-hexane and hydrogen. Capacitance terms are added to the reactor section to model catalyst adsorption. Variable velocity profiles are modeled in the reactor section. Also, all models are developed as non-isothermal models.

A mathematical model describing the base case, consisting of a PSA unit, is developed. Results of the base case are compared to the results obtained by Silva and Rodrigues [78]. Results obtained are in fair agreement with the models developed by Silva and Rodrigues [78].

In this work, PSAR and PSARM units are packed with two separate layers of a Pd/Y zeolite catalyst and a 5A zeolite adsorbent. Moreover, a PSARM unit is equipped with a hydrogen membrane for separation of hydrogen. Flow sheet diagrams for both processes are developed. The proposed cyclic scheme, consisting of four steps, is similar to the basic Skarstrom scheme [80]. A minimum of two columns is needed for a continuous product withdrawal from these units.

Both PSAR and PSARM systems operated at a fresh feed temperature of 573K, a low pressure of 2 bars and a high pressure of 15 bars. The unit feed is introduced at a velocity of 0.5 cm/sec. The purge to feed ratio is 3.5.

Two models are developed for PSAR processes:

- The conventional PSAR process.
- PSAR with waste stream recycled to feed.

In each of the models, two purge conditions are investigated:

- Purging with pure hydrogen (hydrogen purge).
- Purging with a portion of the product stream (Self Regeneration).

Similar models are developed for the PSARM process.

Countercurrent blowdown and desorption is not used in this study due to the high concentrations of normal alkanes desorbing from the solid to the gas phase in the adsorber section. Once these normal alkanes reach the reactor section, they react rapidly to form products. Because of their high concentrations, the reaction releases enough energy to cause a large temperature peak at the reactor section adjacent to the interface region. This peak is enough to shift reactions from conversion to cracking region. To avoid this phenomena, cocurrent blowdown and desorption are used in this study.

The study revealed that models with recycle streams should be utilized to boost process yield. The yield of conventional models that make no use of recycle streams is 66.2%. The yield of models that make use of recycle streams is 100%. The best suitable system for both PSAR and PSARM processes is the one that recycles the waste to the feed stream and uses part of the product stream as a purge stream (recycle to feed with self regeneration).

The computer simulation code is developed using MatLab compiler language. MatLab is chosen over FORTRAN for its simplicity and robustness. MatLab is chosen over C for its comprehensive engineering applications library. In addition, MatLab offers a sophisticated yet simple to use graphical capabilities. All MatLab code is included in the accompanied CD.

## 5.2 RECOMMENDATIONS FOR FUTURE WORK

PSAR and PSARM processes involve several design parameters. Those design parameters include fresh feed conditions, catalyst/adsorbent types, recycle ratios, reactor/adsorber volumes etc. The investigation of those parameters and others is recommended in future work.

The models are developed for a process containing a mix of n/iso-pentane, n/ios-hexane and hydrogen. These models can be extended to accommodate multicomponent reactions and separations.

In present study, the length of the catalyst zone is determined using a reactor feed velocity of 0.5 cm/sec. A comprehensive study should be conducted to determine a suitable reactor size that will accommodate a range of feed velocities.

When simulating PSARM systems, some noise is noticed in integration routine output. This noise is then cleared out using standard filtering techniques. In future work, the number of internal nodes should be increased to eliminate the noise. The increase in internal nodes will increase integration execution time. Thus, faster machines should be chosen to perform future simulation runs.

A linear driving force is assumed in hydrogen diffusion through the membrane. A more realistic model that accounts for the change of hydrogen concentration through the membrane might reveal better results. Orthogonal collocation method could be used to solve such a model.

Heat effects due to hydrogen permeation are not studied in this model. Future work may include the study of hydrogen permeation heat effects.

Wall temperature is assumed constant throughout the models in this study. A more detailed heat balance incorporating wall effects and heat losses to the environment might reveal better results.

For simplicity, recycles are assumed to have a very fast response compared to the process response. Thus, a zero response time is assigned to recycle compressors and valves. This assumption can be verified through detailed modeling of recycle streams. Modeling of variable speed compressors is recommended due to the dynamic nature of the process.

Catalyst deactivation can be included in future models to test maximum unit operational time. The introduction of a deactivation model may introduce more stiffness to the model, which, consequently results in a considerable integration time. Thus faster machines are needed to simulate catalyst deactivation.

More detailed reaction kinetics can be included in future studies. These reaction kinetic models may include hydrocracking reactions that resemble a real reactor-operating mode.

The pure hydrogen produced from the membrane side can be utilized to boost hydrogen to hydrocarbon ratio of recycle streams. This is very crucial in recycling waste streams to the feed because it prevents cracking.

Currently, approximately two hours are needed to simulate two and half hours actual process cycle. The use of alternative simulation techniques should be investigated to bring simulation time to acceptable level.

This model can be linked to any process simulation package to extract more accurate thermodynamic information. In such a link, the model at hand will pass compositions and conditions of system components at any point from the feed to the recycle streams including column internal points. The process simulator will then compute thermodynamic properties including phase change during low temperature runs. This is very important in determining operational dew points. Reactors must run aside from their dew points conditions.

In these models, a purge stream split of 10% and 90% is used for reactor and PSA sections, respectively. Future models may consider the elevation of this split to 1% and 99% for reactor and PSA sections, respectively. A 100% purge stream through the PSA section may also be considered. However, in such a model, dispersion from the PSA section to reactor section should be modeled.

Counter current blowdown and desorption are not achievable in this study due to the high temperature peak encountered in the catalyst region adjacent to the interface. This temperature peak is a direct result of reacting a very high concentrations of normal alkanes leaving the adsorber section and entering the reactor section. The high normal alkanes concentration only last



for a small time interval. Future models can eliminate this high temperature peak through:

- Simulating cocurrent flow during this high normal alkanes concentration period and countercurrent flow after the pass of the high normal alkanes concentration period.
- The use a cooler in the interface region. This cooler will also eliminate the high temperature peak.
- Partial stepwise depressurization in different time intervals.

This type of modeling will not only allow for counter current blowdown and desorption, it will also allow for recycling waste streams directly to the PSA section of the PSAR and the PSARM units.

## References

1. Al-Juhani, Abdulhadi A., "Modeling and Simulation of a Combined Isomerization Reactor/Pressures Swing Adsorption Unit", M.S. thesis, King Fahd University of Petroleum & Minerals, May 2000.
2. Alpay, E., C. N. Kenney, and D. M. Scott, "Simulation of Rapid Pressure Swing Adsorption and Reaction Process," *Chem. Eng. Sci.*, 48, 3137 (1993).
3. Alpay, E., D. Chatsiriwech, L. S. Kershenbaum, C. P. Hull, and N. F. Kirby, "Combined Reaction and Separation by Pressure Swing Adsorption," *Chem. Eng. Sci.*, 49, 5845-5864 (1995).
4. Alpay, E., Y. S. Cheng, and L. S. Kershenbaum, "Simulation and Optimization of a Rapid Pressure Swing Reactor," *Comp. Chem. Eng.*, 22, S45-S52 (1998).
5. Aube, F. and H. Sapoundjiev, "Mathematical Model and Numerical Simulations of Catalytic Flow Reversal Reactors for Industrial Applications", *Comp. Chem. Eng.*, 24, 2623-2632 (2000).
6. Baltanas, Miguel A, Kristiaan K. Van Raemdonck, Gildert F. Froment, and Sergio R. Mohedas, "Fundamental Kinetic Modeling of Hydroisomerization and Hydrocracking on Nobel-Metal-Loaded Faujasites. 1. Rate Parameters for Hydroisomerization," *Ind. Eng. Chem. Res.*, 28, 899-910 (1989).
7. Barrer, R. M., and D. J. Clarke, "Diffusion of Some n-Paraffins in Zeolite A," *Trans. Faraday Soc.*, 69, 535-546 (1973).
8. Barrer, R. M. and J. W. Sutherland, "Inclusion complexes of faujasite with paraffins and permanent gases," Physical Chemistry Laboratories, Imperial College, London, 1956.
9. Bhatia, S., and K. Jothimurugesan, "Isomerization of n-Heptane over Nickel-Loaded Zeolite Catalysts," *Can. J. Chem. Eng.*, 62, 390 (1984).

10. Borse, G. J., *Numerical Methods with Matlab*, PWS Publishing Company, Boston, (1997).
11. Breck, D. W., *Zeolite Molecular Sieves*, John Wiley & Sons, New York, (1974).
12. Bryant, P., and A. J. Voorhies, "Hydroisomerization of n-Pentane over a Zeolite Catalyst," *AIChE J.*, 14(6), 852 (1968).
13. Bryant, P. and J. V. Spivey, "Hydroisomerization of n-C<sub>5</sub> and n-C<sub>6</sub> Mixtures on Zeolite Catalysts," *Ind. Eng. Chem. Proc. Des. Dev.*, 21(4), 750-760 (1982).
14. Cavalcant, C. L., M. Eic, D. M. Ruthven, and M. L. Occeli, "Diffusion of n-Paraffins in Offretite-Erionite Type Zeolite," *Zeolite*, 15, 293 (1995).
15. Chang, J. R., R. M. Jao, and T. B. Lin, "Light Naphtha Isomerization over Mordenite-Supported Ni-Pt Catalysts: Effect of Ni on the Performance for Pure Feed and Sulfur-Containing Feed," *J. Catal.*, 161, 222-229 (1996).
16. Chatsiriwech, D., E. Alpay, L. S. Kershenbaum, C. P. Hull, and N. F. Kirkby, "Enhancement of Catalytic Reaction by Pressure Swing Adsorption," *Catal. Today*, 20, 351 (1994).
17. Chihara, K., and M. Suzuki, "Simulation of Nonisothermal Pressure Swing Adsorption," *Chem. Eng. Japan*, 16 (1), 53 (1983).
18. Collins, J. J., "Air Separation by Adsorption," U.S. Patent No. 4,026,680 (1977).
19. Domerge, Bruno, "Advanced Recycle Paraffin Isomerization Technology," *Refining*, Spring 2001.
20. Douglas, J. M., "Periodic Reactor Operation," *Ind. Eng. Chem. Proc. Des. Dev.*, 6(1), 43-48 (1967).

21. Fajula, F., D. McQueen, B. H. Chiche, A. Auroux, C. Guimon, F. Fitoussi, and P. Schuiz, "A Multitechnique Characterization of the Acidity of Dealuminated Zeolite," *J. Catal.*, 161, 587-596 (1996).
22. Feng, Xianshe, "Pressure Swing Permeation: Novel Process for Gas Separation by Membranes", *AIChE Journal*, 46, 724-733 (2000).
23. Fogler, H. S., *Elements of Chemical Reaction Engineering*, Prentice Hall, New York, (1992).
24. Fujimoto, K., A. Zhang, I. Nakamura, and K. Aimoto, Isomerization of n-Pentane and Other Light Hydrocarbons on Hybrid Catalyst: Effect of Hydrogen Spillover," *Ind. Eng. Chem. Res.*, 34, 1074-1080 (1995).
25. Gary, J., "Total Isomerization Process," U.S. Patent 4,709,117 (1987).
26. Gates, B. C., and S. G. Ryu, "n-Hexane Conversion Catalyzed by Sulfated Zirconia and by Iron- and Manganese Promoted Sulfated Zirconia: Catalytic Activities and Reaction Network," *Ind. Eng. Chem. Res.*, 37, 1786-1792 (1998).
27. Glueckauf, E., "Formula for diffusion into spheres and their application to chromatography," *J. Chem. Soc.*, 51, 1540 (1955).
28. Goto, S., T. Tagawa, and T. Omiya, "Dehydrogenation of Cyclohexane in a PSA Reactor Using Hydrogen Occlusion Alloy," *Chem. Eng. Essays (Japan)*, 19(6), 978, (1993).
29. Han, C., and D. P. Harrison, "Simultaneous Shift Reaction and Carbon Dioxide Separation for the Direct Production of Hydrogen," *Chem. Eng. Sci.*, 49, 5875 (1994).
30. Hufton, R. J., and D. M. Ruthven, "Diffusion of Light Alkanes in Silicalite Studied by the Zero Length Column Method," *Ind. Eng. Chem. Res.*, 32, 2379 (1993).

31. Jothimurugesan, K. and S. Bhatia, "Isomerization of n-Hexane over Nickel-Loaded Zeolite Catalysts," *The Canadian Journal of Chemical Engineering*, 62, 390-397, June (1984).
32. Kadlec, R. H., and G. G. Vapordyan, "Periodic Chemical Processing System," U.S. Patent 5,254,368 (1993).
33. Karger, J., and D. M. Ruthven, *Diffusion in Zeolites and other Microporous Solids*, John Wiley, New York, (1992).
34. Kasab, John J., Sanjay Mehta and Warren E. Stewart, "Transport Modeling of Packed-Tube Reactors – IV: Steady-State Modeling with Intraparticle Gradients", *Chem. Eng. Sci.*, 55, 5783-5792 (2000).
35. Kesting, R. E. and A. K. Fritzsche, "Polymeric Gas Separation Membranes", John Wiley and Sons, 1<sup>st</sup> edition (1993).
36. Kirkby, N. F., and J. E. Morgan, "A Theoretical Investigation of Pressure Swing Reaction," *Trans. Inst. Chem. Eng.*, 72, 541 (1994).
37. Kodde, Adriaan J., Ymke S. Fokma, and Alfred Blik, "Selectivity Effects on Series Reactions by Reactant Storage and PSA Operation", *AIChE Journal*, 46, 2295-2304 (2000).
38. Kouwenhoven, H., and W. C. Langhout, "Shell's Hydroisomerization Process," *Chem. Eng. Prog.*, 67(4), 65-70(1971).
39. Kouwenhoven, H. W., in *"Molecular Sieves"*, eds. W. M. Meier and J. B. Uytterhoeven, Adv. Chem. Ser. 121, American Chemical Society, Washington, (1973).
40. Langmuir, I., "The Adsorption of Gases on Plane Surfaces of Glass, Mica, and Platinum," *J. Am. Chem. Soc.*, 40, 163 (1918).
41. LaPack, M. A. and P. F. Dupuis, "Dynamic Membrane Separation Process for Improved Selectivity," U.S. Patent No. 5,354,474 (1994).

42. Lee, I. D., and R. H. Kadlec, "Effects of Adsorbent and Catalyst Distributions in Pressure Swing Reactors," *AIChE Symp. Ser.*, 84, 167 (1989).
43. Lefevre, L., D. Dochain, S. Feyo de Azevedo and A. Magnus, "Optimal Selection of Orthogonal Polynomials Applied to the Integration of Chemical Reactor Equations by Collocation Methods", *Comp. Chem. Eng.*, 24, 2571-2588 (2000).
44. Li, K. and Tan Xiaoyao, "Mass Transfer and Chemical Reaction in Hollow-Fiber Membrane Reactors", *AIChE J.*, 47, 427-435 (2001).
45. Liu, Yujun, and James A. Ritter, "Pressure Swing Adsorption Cycles for Improved Solvent Vapor Enrichment", *AIChE Journal*, 46, 540-551 (2000).
46. Lu, Z. P., and A. E. Rodrigues, "Pressure Swing Adsorption Reactors: Simulation of Three-Step One-Bed Process," *AIChE J.*, 40, 1118 (1994).
47. Marriott, J. I., E. Sorensen and I. D. L. Bogle, "Detailed Mathematical Modeling of Membrane Modules", *Comp. Chem. Eng.*, 25 (2001) 692-700.
48. Minkinen, A., L. Mank, and S. Jullian, "Process for the Isomerization of  $C_5/C_6$  Normal Paraffins with Recycling of Normal Paraffins," U. S. Patent 5,233,120 (1993).
49. Morbidelli, M., M. Mazzotti, R. Baciochi, and G. Storti, "Vapor-Phase SMB Adsorptive Separation of Linear/Nonlinear Paraffins," *Ind. Eng. Chem. Res.*, 35, 2313 (1996).
50. Morbidelli, M., A. Servida, and G. Storti, "Simulation of Multicomponent Adsorption Bed- Model Analysis and Numerical Solution," *Ind. Eng. Chem. Fundam.*, 21, 123 (1982).

51. Morreale, Bryan D., Robert M. Enick, Badie I. Morsi, Bret H. Howard and Kurt S. Rothenberger, "Evaluation of High-Pressure, High Temperature Inorganic Hydrogen Membranes," U.S. Department of Energy, National Energy Technology Laboratory.
52. Nitta, Tomoshige, Takuo Shigetomi, Masayuki Kuro-Oka, and Takashi Katayama, "An Adsorption Isotherm of Multi-site Occupancy Model for Heterogeneous Surface," *J. Chem. Eng. Jpn.*, 17, 45-51 (1984).
53. Nitta, Tomoshige, Masayuki Kuro-Oka, and Takashi Katayama, "An Adsorption Isotherm of Multi-site Occupancy Model for Homogeneous Surface," *J. Chem. Eng. Jpn.*, 17, 39-45 (1984).
54. Park, Jong-Ho, Jong-Nam Kim, and Soon-Haeng Cho, "Performance Analysis of Four Bed H<sub>2</sub> PSA Process Using Layered Beds", *AIChE Journal*, 46, 790-802 (2000).
55. Perry, Robert H. and Don Green, "Perry's Chemical Engineers Handbook", McGraw-Hill, 6<sup>th</sup> edition, Singapore (1984).
56. Pines, H., K. Vetinskas, K. Assel. and I. Patieff, "Determination of Equilibrium Constants for Butanes and Pentanes," *J. Am. Chem. Soc.*, 67, 631 (1945).
57. Rajasree, R. and A. S. Moharir, "Simulation Based Synthesis, Design and Optimization of Pressure Swing Adsorption (PSA) Processes", *Comp. Chem. Eng.*, 24, 2493-2505 (2000).
58. Redlich, O., and D. L. Peterson, "Adsorption of Normal Paraffins by Molecular Sieves Type 5A," *Chem. Eng. Data*, 7(4), 570 (1962).
59. Ribeiro, F. R., *Nato Advanced Science Institute on Zeolites Science and Technology*, Alcabideche, Portugal. (1983).
60. Rice, Richard G. and Doung D. Do, "Applied Mathematics and Modeling for Chemical Engineers", John Wiley and Sons (1995).

61. Ruckenstein, E., A. S. Vaidynathan, and G. R. Youngquist, "Sorption in solids with bidisperse porous structures," *Chem. Eng. Sci.*, 26, 1305 (1971).
62. Runstraat, A., J. Grondelle, and R. A. Santen, "On the Temperature Dependence of the Arrhenius Activation Energy for Hydroisomerization Catalyzed by Pt/Mordenite," *J. Catal.*, 167, 460-463 (1997).
63. Runstraat, A., J. Kamp, P. Stobbelaar, J. Grondelle, S. Krijnen, and R. Santen, "Kinetics of Hydroisomerization of n-Hexane over Platinum Containing Zeolites," *J. Catal.*, 171, 77-84 (1997).
64. Runstraat, A., J. Grondelle, and R. Santen, "Microkinetics Modeling of the Hydroisomerization of n-Hexane," *Ind. Eng. Chem. Res.*, 36, 3116-3125 (1997).
65. Ruthven, D. M., and K. P. Loughlin, "The Adsorption and Diffusion of n-Butane in Linde 5A Molecular Sieve," *Chem. Eng. Sci.*, 26, 1145 (1971).
66. Ruthven, D. M., and K. F. Loughlin, "The Diffusional Resistance of Molecular Sieve Pellets," *Can. J. Chem. Eng.*, 28, 550 (1972).
67. Ruthven, D. M., and B. K. Kaul, "Adsorption of n-Hexane and Intermediate Molecular Weight Aromatic Hydrocarbons on LaY Zeolite," *Ind. Eng. Chem. Res.*, 35, 2060 (1996).
68. Ruthven, D. M., *Principles of Adsorption and Adsorption Process*, John Wiley & Sons, New York, (1984).
69. Ruthven, D. M., S. Farooq, and K. S. Knaebel, *Pressure Swing Adsorption*, VCH Publishers, New York, (1994).
70. Ruthven, D. M., M. M. Hassan, and N. S. Raghavan, "Numerical Simulation of a PSA System-Part I," *AIChE J.*, 31(3), 385-392 (1985).



71. Ruthven, D. M., and N. S. Rabgavan, "Numerical Simulation of a PSA System-Part III," *AIChEJ.*, 31(12), 1829 (1985).
72. Scott, K. and R. Hughes, "Industrial Membrane Separation Technology", Blackie Academic & Professional, 1<sup>st</sup> edition, (1996).
73. Shendalman, L. H., and J. E. Mitchell, "A Study of Heatless Adsorption in the Model System CO He," *Chem. Eng. Sci.*, 27, 1449-58 (1972).
74. Shin, H. S., and K. S. Knaebel, "An Experimental Study of Diffusion-Induced Separation of Gas Mixtures by Pressure Swing Adsorption," *AIChE J.*, 33, 654 (1987).
75. Silva, J. A., and A. E. Rodrigues, "Sorption and Diffusion of n-Pentane in Pellets of 5A Zeolite," *Ind. Eng. Chem. Res.*, 36, 493-500 (1997).
76. Silva, J. A., and A. E. Rodrigues, "Fixed-Bed Adsorption of n-Pentane/Isopentane Mixtures in Pellets of 5A Zeolite," *Ind. Eng. Chem. Res.*, 36, 3769-3777 (1997).
77. Silva, J. A., and A. E. Rodrigues. "Equilibrium and Kinetics of n-Hexane Sorption in Pellets of 5A Zeolite," *AIChE J.*, 43, 2524-2534 (1997).
78. Silva, J. A., and A. E. Rodrigues, "PSA Separation of n/iso-Paraffins Mixtures," presented at the 6<sup>th</sup> International Conference on Fundamentals of Adsorption, Ed. Francis Meulier, Paris, Ebevier (1998).
79. Sircar, S., B. T. Carvill, J. R. Hufton, and M. Anand, "Sorption-Enhanced Reaction Process," *AIChEJ.*, 42(10), 2765-2772 (1996).
80. Skarstrom, C. W., "Method and Apparatus for Fractionating Gaseous Mixtures by Adsorption," U.S. Patent No. 2,944,627 (1960).

81. Spivey, J., and P. Bryant, "Hydroisomerization of n-C<sub>5</sub> and n-C<sub>6</sub> Mixtures on Zeolite Catalysts," *Ind. Eng. Chem. Proc. Dev.*, 21 (4), 750-760 (1982).
82. Svoboda, Glenn D., Erik Vynckier, Birgit Dedrabandere, and Gilbert F. Froment, "Single-Event Rate Parameters for Paraffin Hydrocracking on a Pt/US-Y Zeolite," *Ind. Eng. Chem. Res.*, 34, 3793-3800 (1995).
83. Ueda, K., K. Haruna, and M. Inoue, "Process for Separating Gas," U.S. Patent No. 4,955,998 (1990).
84. Vaporciyan, G. G., and R. H. Kadlec, "Equilibrium Limited Periodic Separating Reactors," *AIChEJ.*, 33, 1334 (1987).
85. Vaporciyan, G. G., and R. H. Kadlec, "Periodic Separating Reactors: Experiments and Theory," *AIChE J.*, 3, 831 (1989).
86. Vavlitis, A. P., D. M. Ruthven, and K. F. Loughlin, "Sorption of n-Pentane, n-Octane, and n-Decane in 5A Zeolite Crystals," *Coll. Sci.*, 84(2), 526-531 (1981).
87. Wakao, N., and S. Kaguei, *Heat and Mass Transfer in Packed Beds*, Gordon and Breach Science Publishers, New York, (1982).
88. Wankat, Phillip C., "Rate Controlled Separations", Chapman & Hall, London (1994).
89. Weisz, P. B., in "Advances in Catalysis and Related Subjects," Vol. 13 (D. D. Eley, P. W. Selwood, and P. B. Weisz, Eds.), p. 157, Academic Press, London, (1962).
90. Yang, R. T., *Gas Separation by Adsorption Process*, Butterworth, Boston, (1987).
91. Zhang, Aihua, Ikusei Nakamura, Kohjiro Aimoto, and Kaoru Fujimoto, "Isomerization of n-Pentane and other Hydrocarbons on

Hybrid Catalyst. Effect of Hydrogen Spillover," *Ind. Eng. Chem. Res.*,  
34, 1074-1080 (1995).

## **APPENDICES**

## **APPENDIX A**

### **Three Dimensional Figures of the Conventional PSAR Unit with Hydrogen Purge**

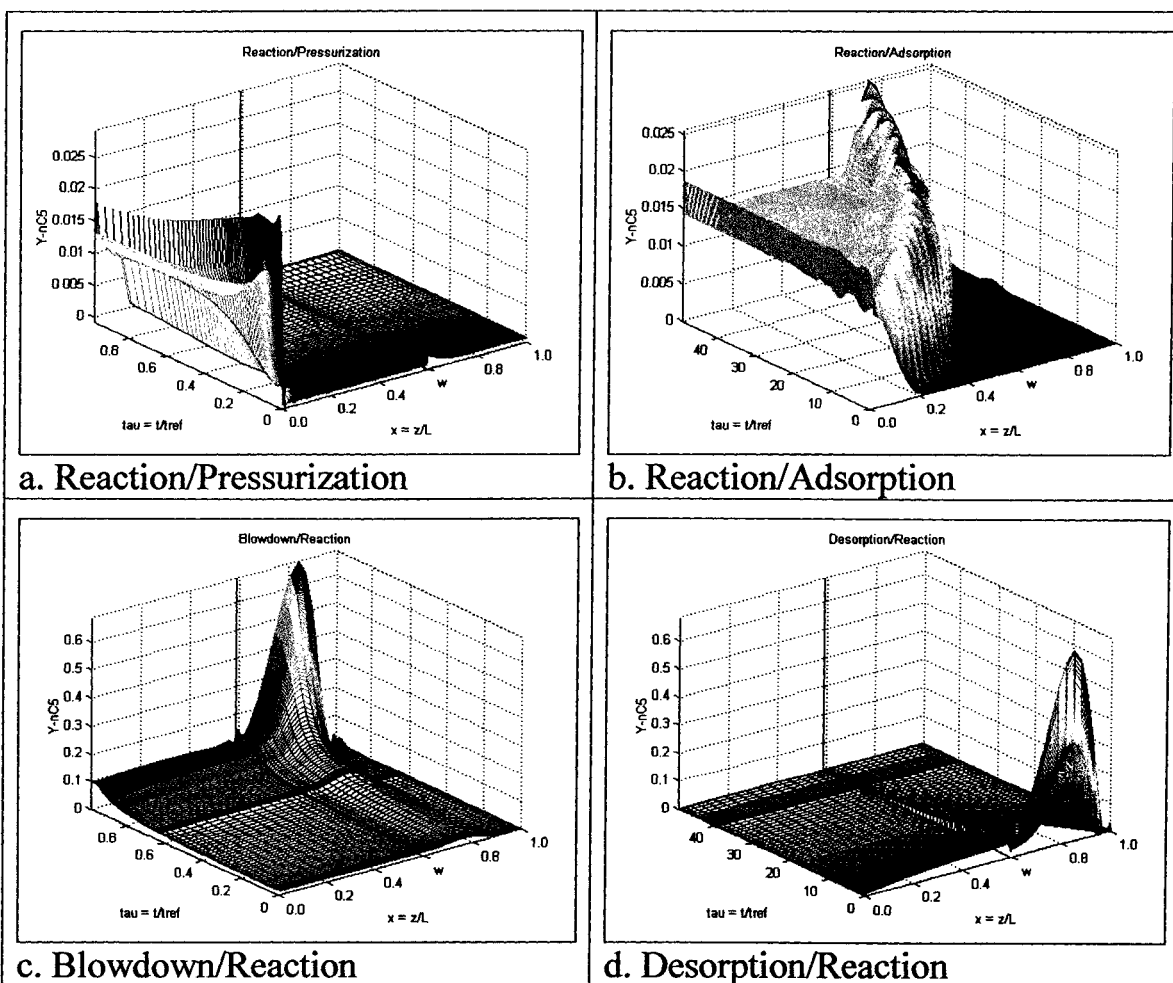


Figure A.1: Three dimensional drawing illustrating the transient and spatial change in  $n\text{-C}_5$  concentration with respect to time and axial distance for the four basic steps at the steady state cycle. (Conventional PSAR Unit/Hydrogen Purge)

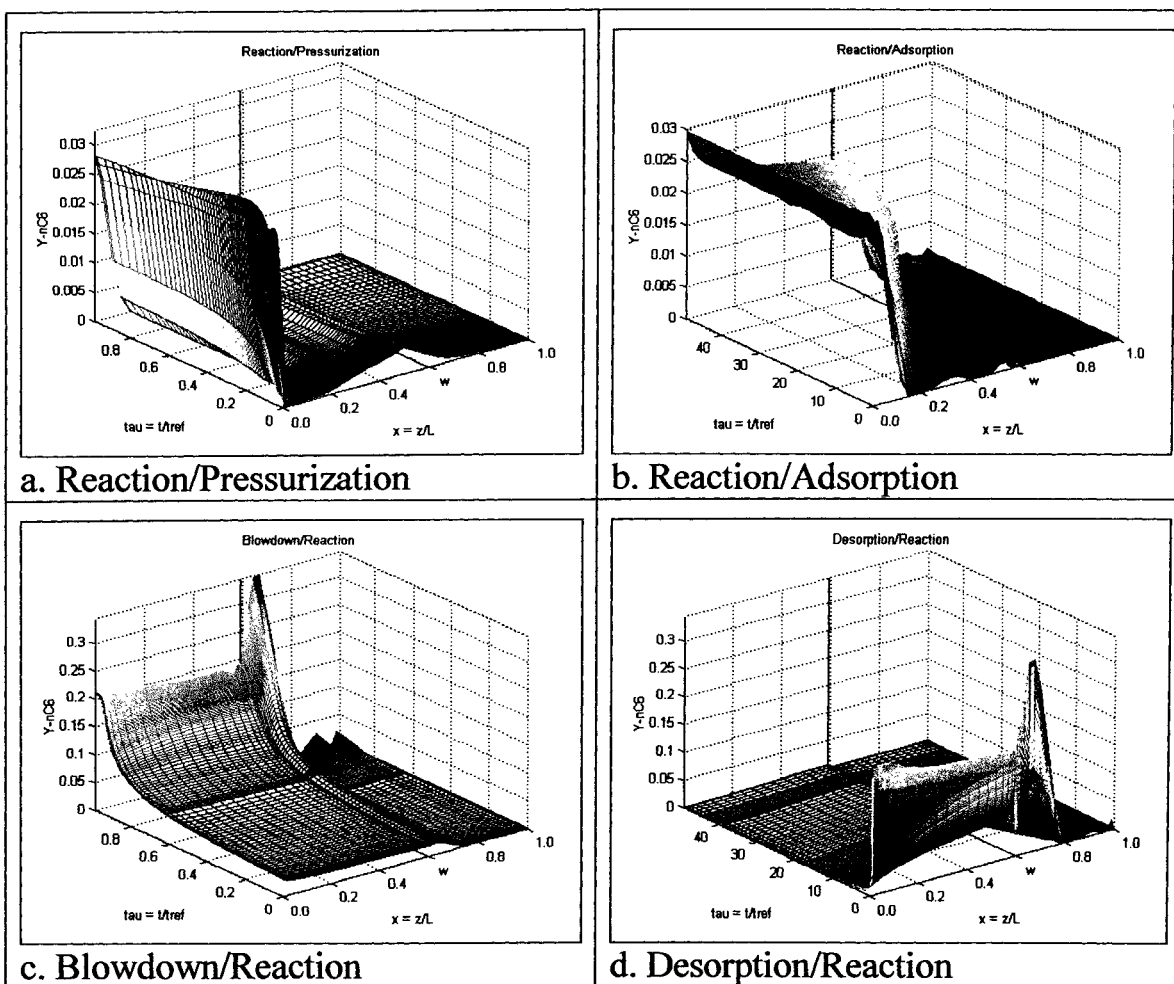


Figure A.2: Three dimensional drawing illustrating the transient and spatial change in n-C<sub>6</sub> concentration with respect to time and axial distance for the four basic steps at the steady state cycle. (Conventional PSAR Unit/Hydrogen Purge)

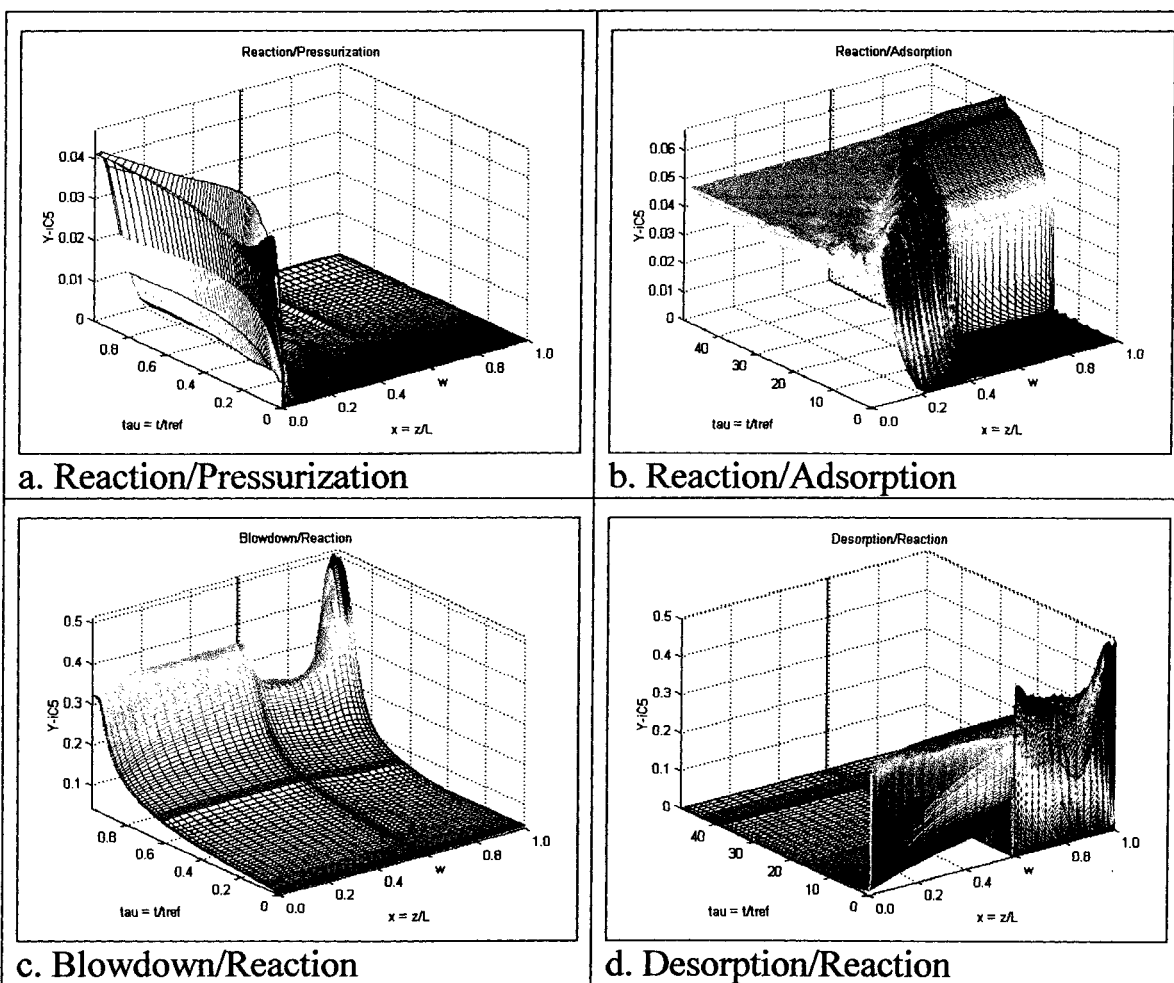


Figure A.3: Three dimensional drawing illustrating the transient and spatial change in  $i-C_5$  concentration with respect to time and axial distance for the four basic steps at the steady state cycle. (Conventional PSAR Unit/Hydrogen Purge)



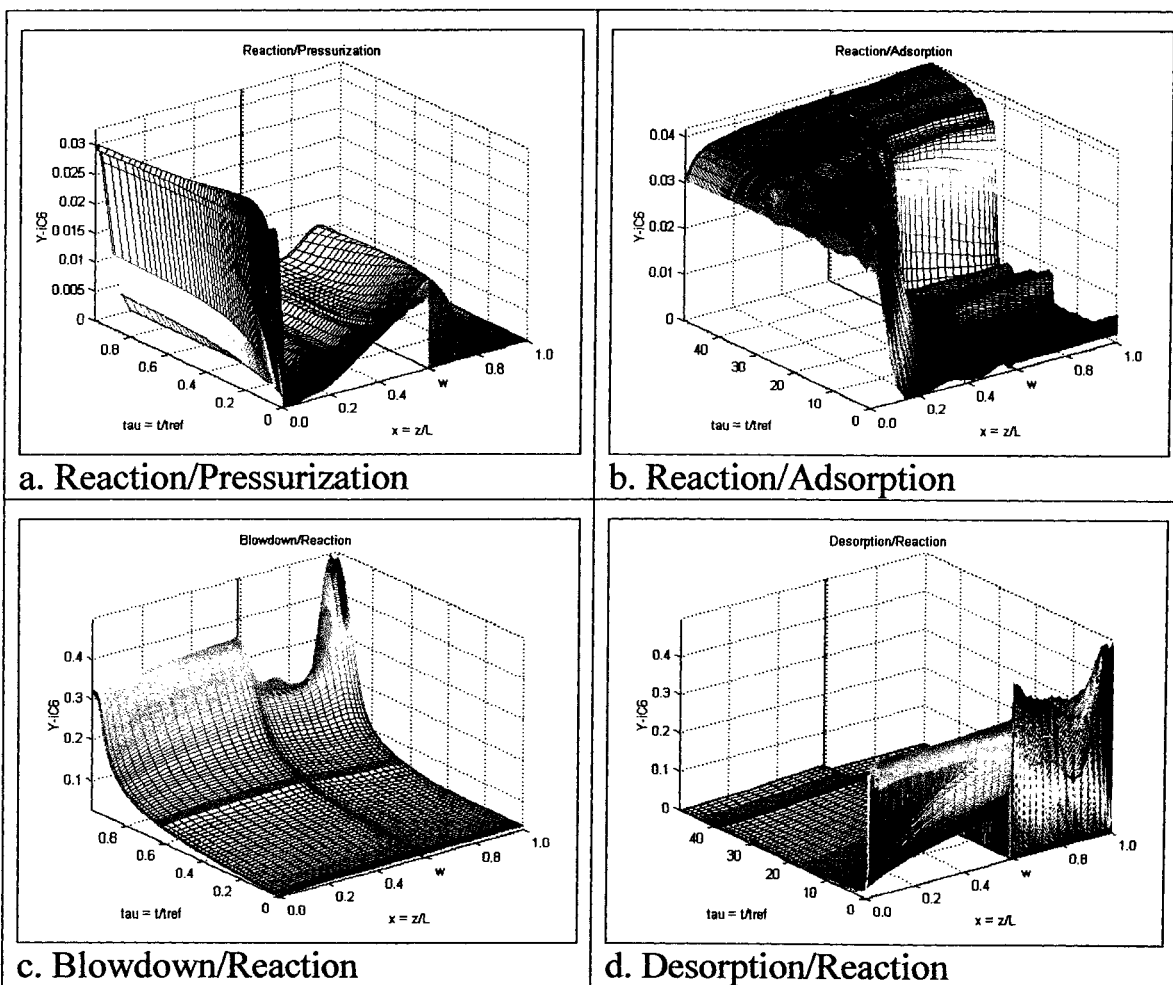


Figure A.4: Three dimensional drawing illustrating the transient and spatial change in  $i\text{-C}_6$  concentration with respect to time and axial distance for the four basic steps at the steady state cycle. (Conventional PSAR Unit/Hydrogen Purge)

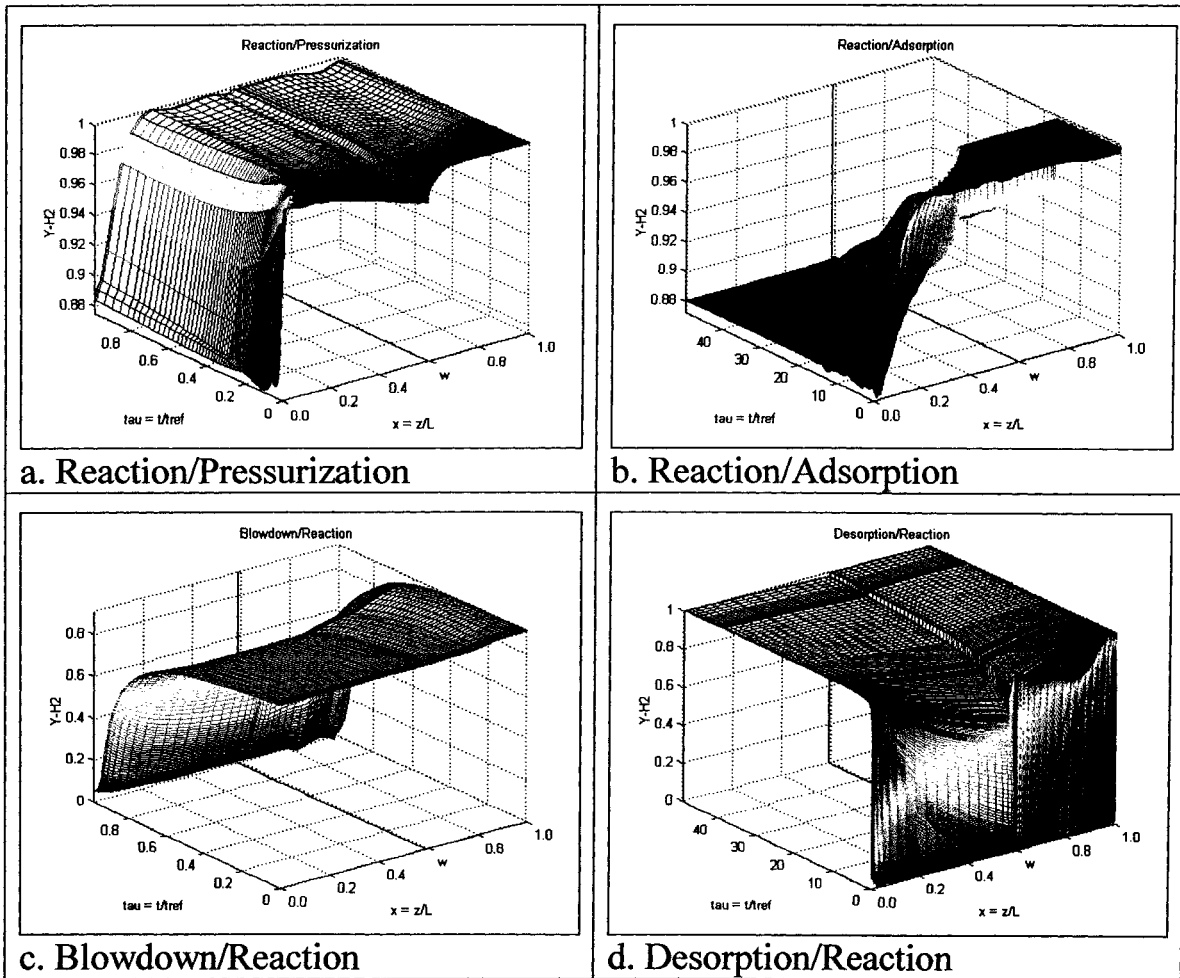
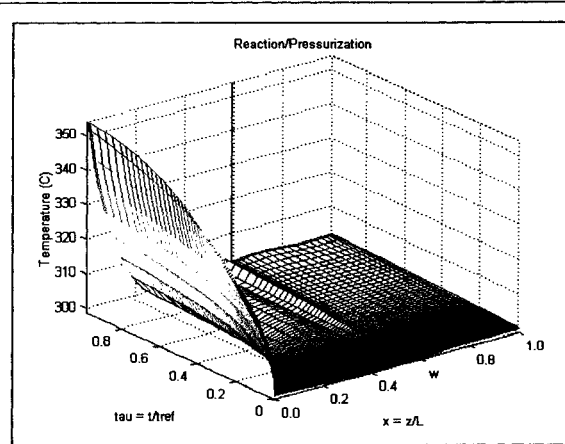
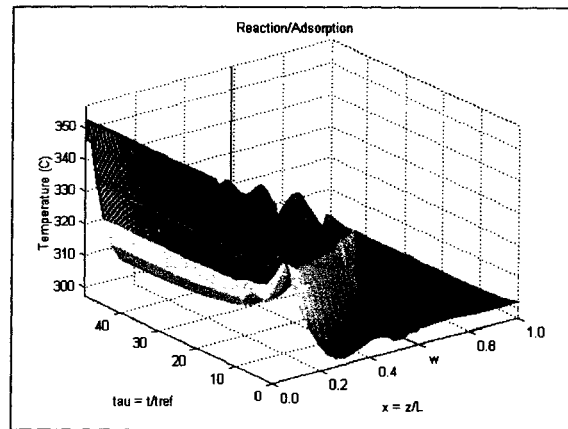


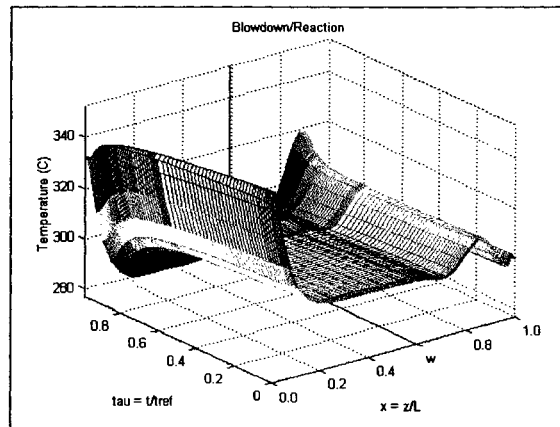
Figure A.5: Three dimensional drawing illustrating the transient and spatial change in  $H_2$  concentration with respect to time and axial distance for the four basic steps at the steady state cycle. (Conventional PSAR Unit/Hydrogen Purge)



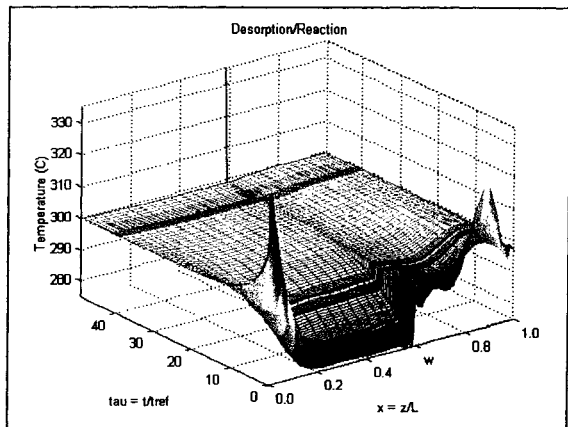
a. Reaction/Pressurization



b. Reaction/Adsorption



c. Blowdown/Reaction



d. Desorption/Reaction

Figure A.6: Three dimensional drawing illustrating the transient and spatial change in Temperature with respect to time and axial distance for the four basic steps at the steady state cycle. (Conventional PSAR Unit/Hydrogen Purge)

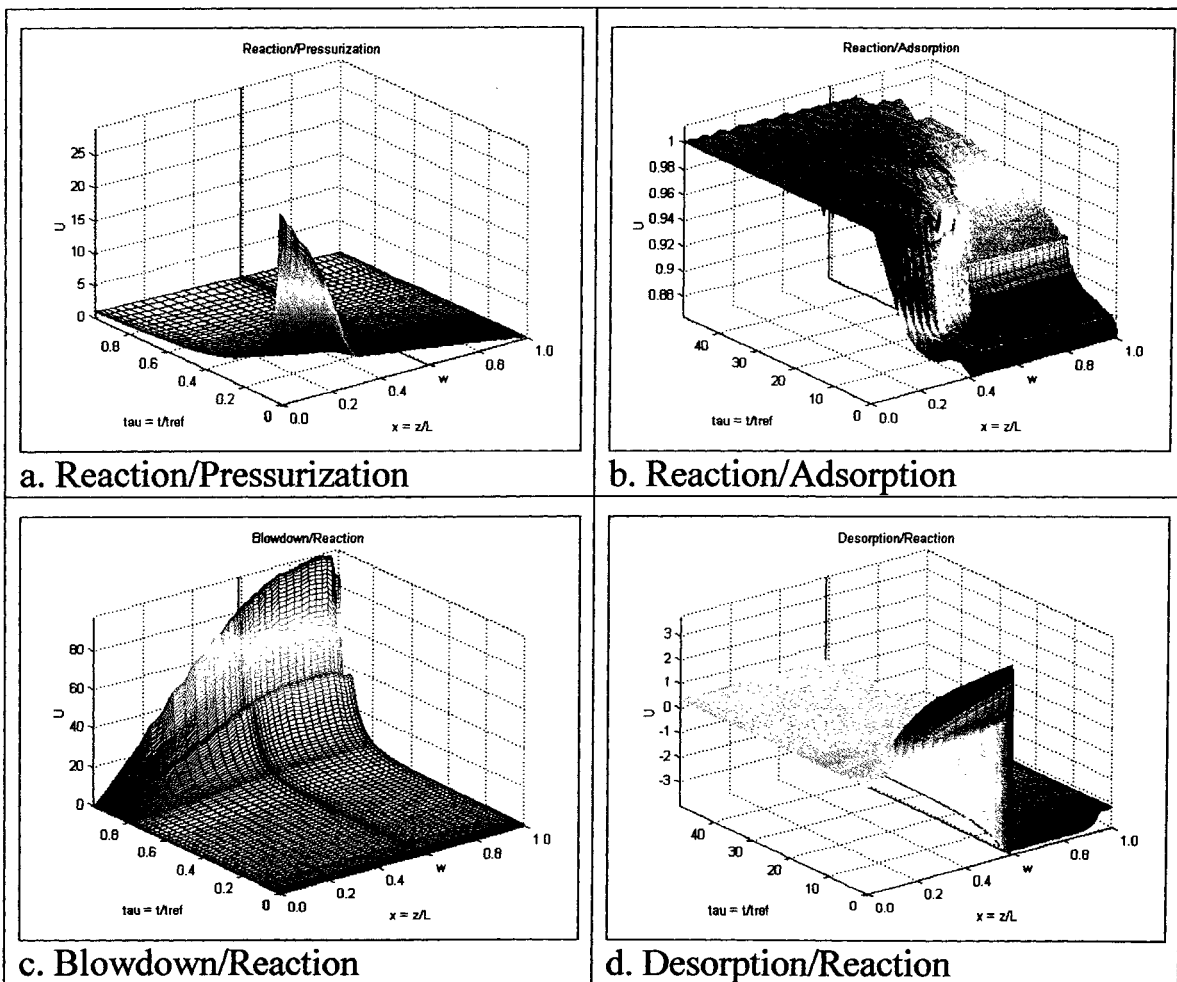


Figure A.7: Three dimensional drawing illustrating the transient and spatial change in Velocity with respect to time and axial distance for the four basic steps at the steady state cycle. (Conventional PSAR Unit/Hydrogen Purge)

## **APPENDIX B**

### **Three Dimensional Figures of the Conventional PSAR Unit with Self Regeneration**

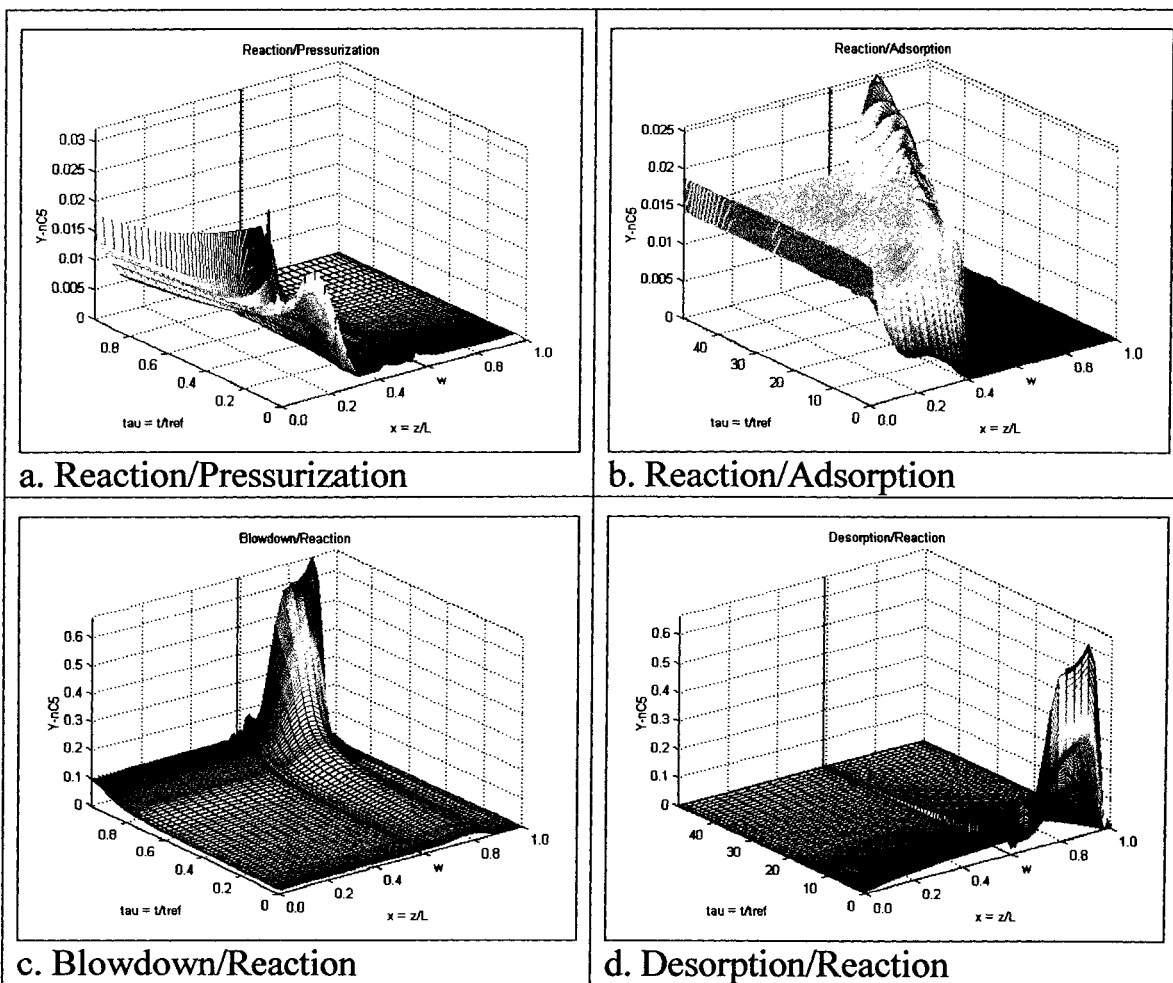


Figure B.1: Three dimensional drawing illustrating the transient and spatial change in n-C<sub>5</sub> concentration with respect to time and axial distance for the four basic steps at the steady state cycle. (Conventional PSAR Unit/Self Regeneration)

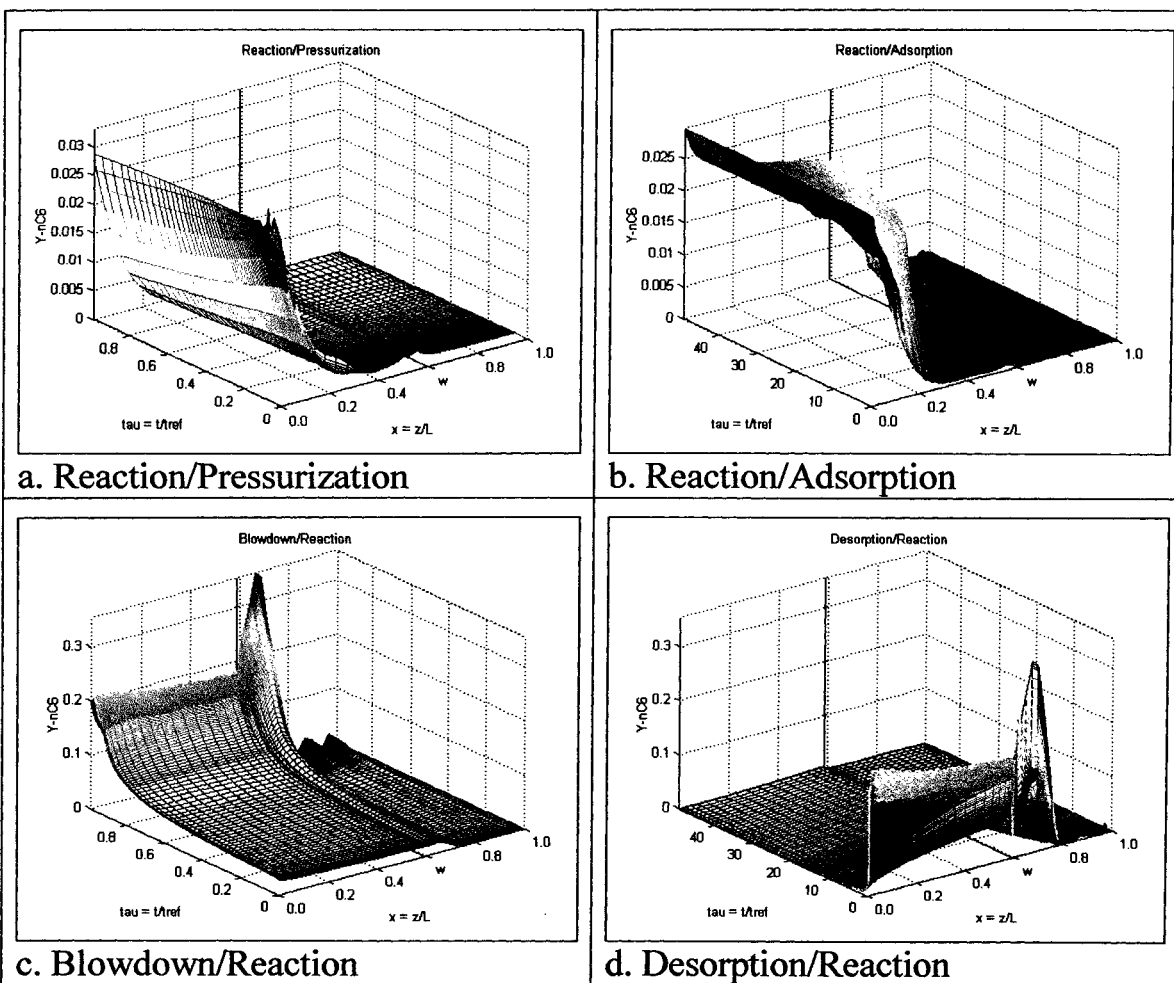


Figure B.2: Three dimensional drawing illustrating the transient and spatial change in n-C<sub>6</sub> concentration with respect to time and axial distance for the four basic steps at the steady state cycle. (Conventional PSAR Unit/Self Regeneration)

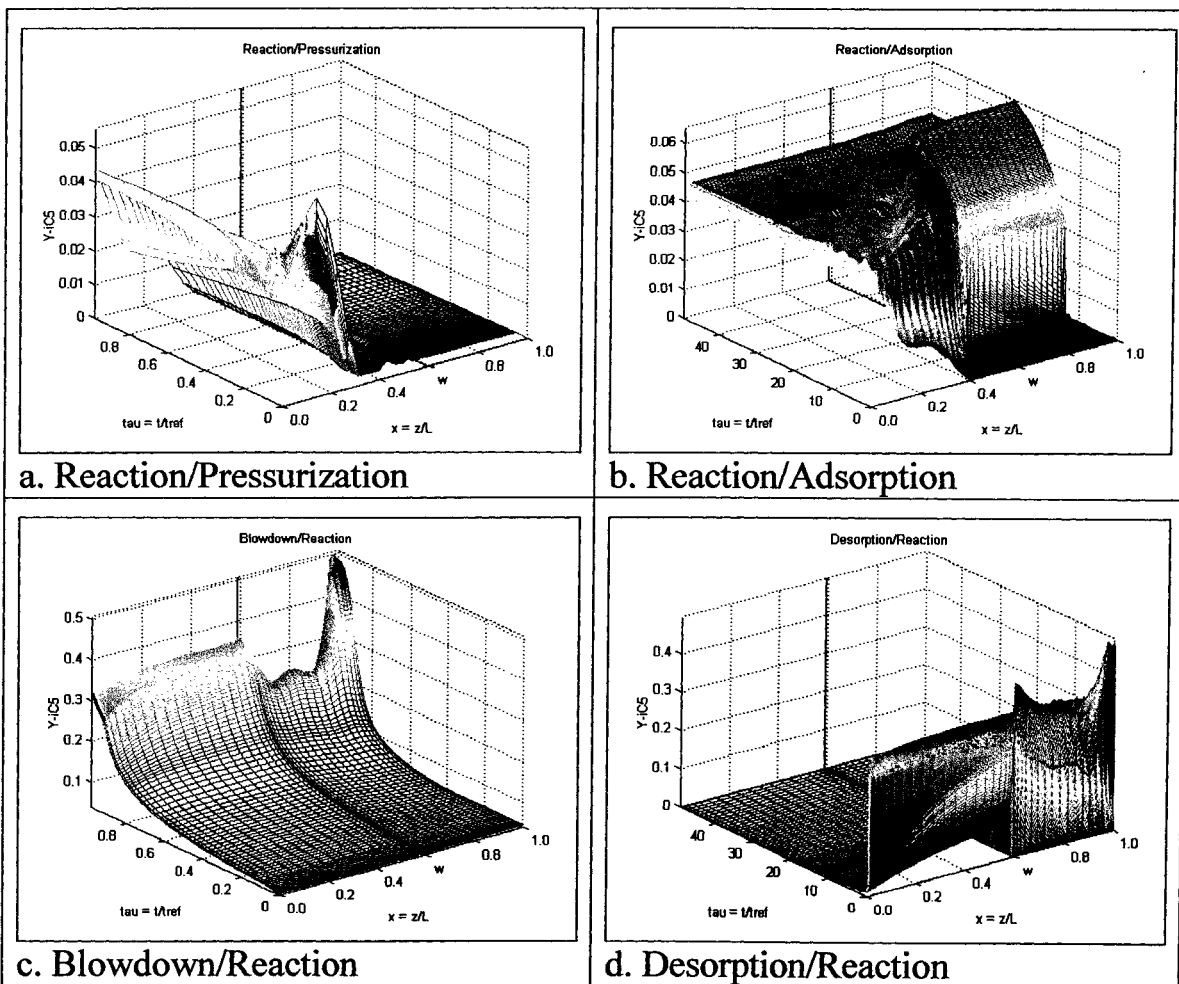
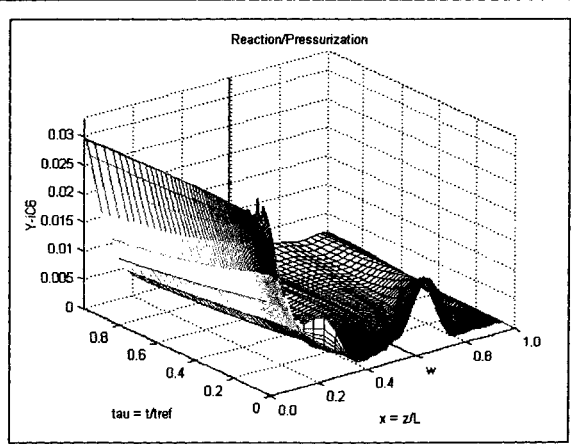
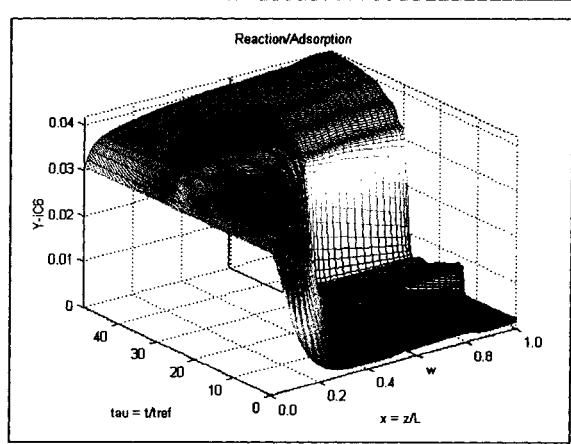


Figure B.3: Three dimensional drawing illustrating the transient and spatial change in  $i\text{-C}_5$  concentration with respect to time and axial distance for the four basic steps at the steady state cycle. (Conventional PSAR Unit/Self Regeneration)

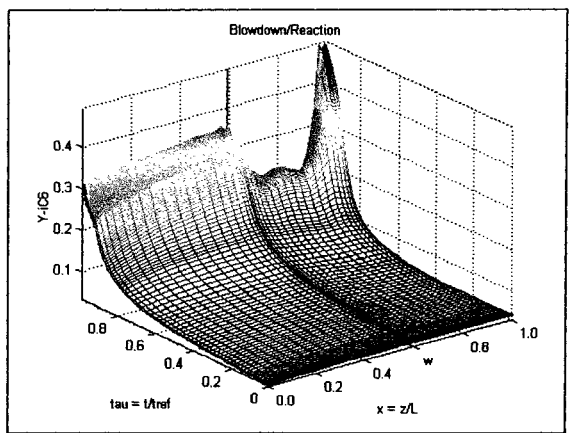




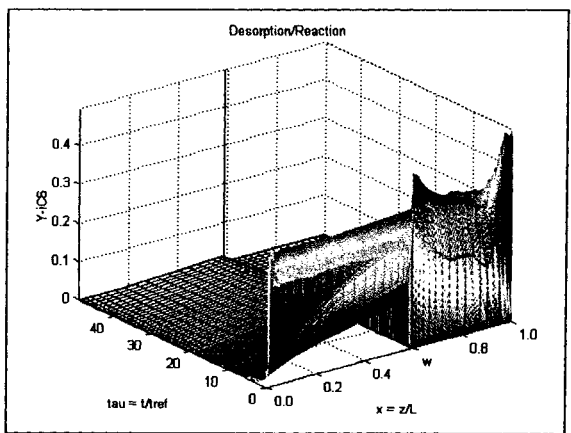
a. Reaction/Pressurization



b. Reaction/Adsorption



c. Blowdown/Reaction



d. Desorption/Reaction

Figure B.4: Three dimensional drawing illustrating the transient and spatial change in i-C<sub>6</sub> concentration with respect to time and axial distance for the four basic steps at the steady state cycle. (Conventional PSAR Unit/Self Regeneration)

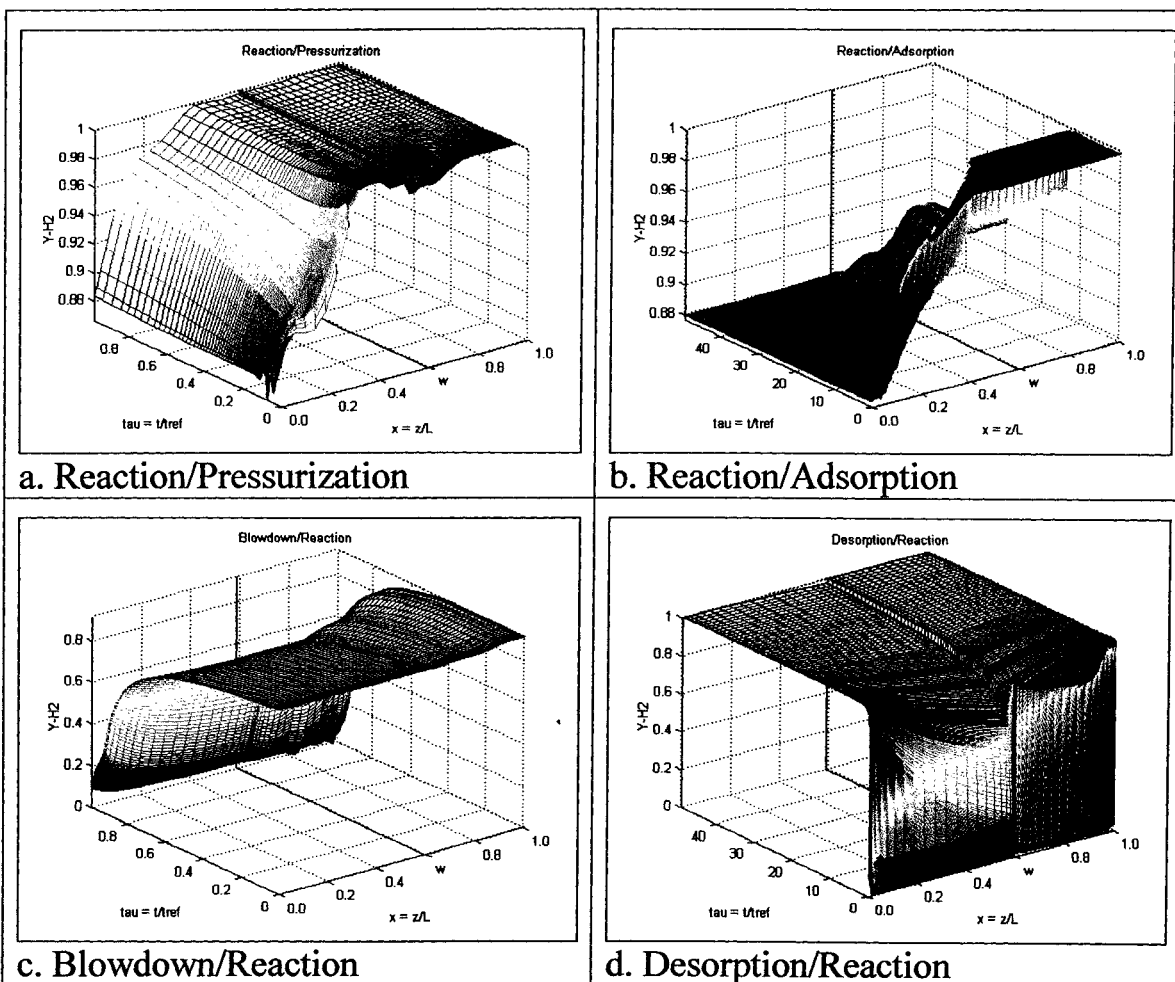


Figure B.5: Three dimensional drawing illustrating the transient and spatial change in  $H_2$  concentration with respect to time and axial distance for the four basic steps at the steady state cycle. (Conventional PSAR Unit/Self Regeneration)

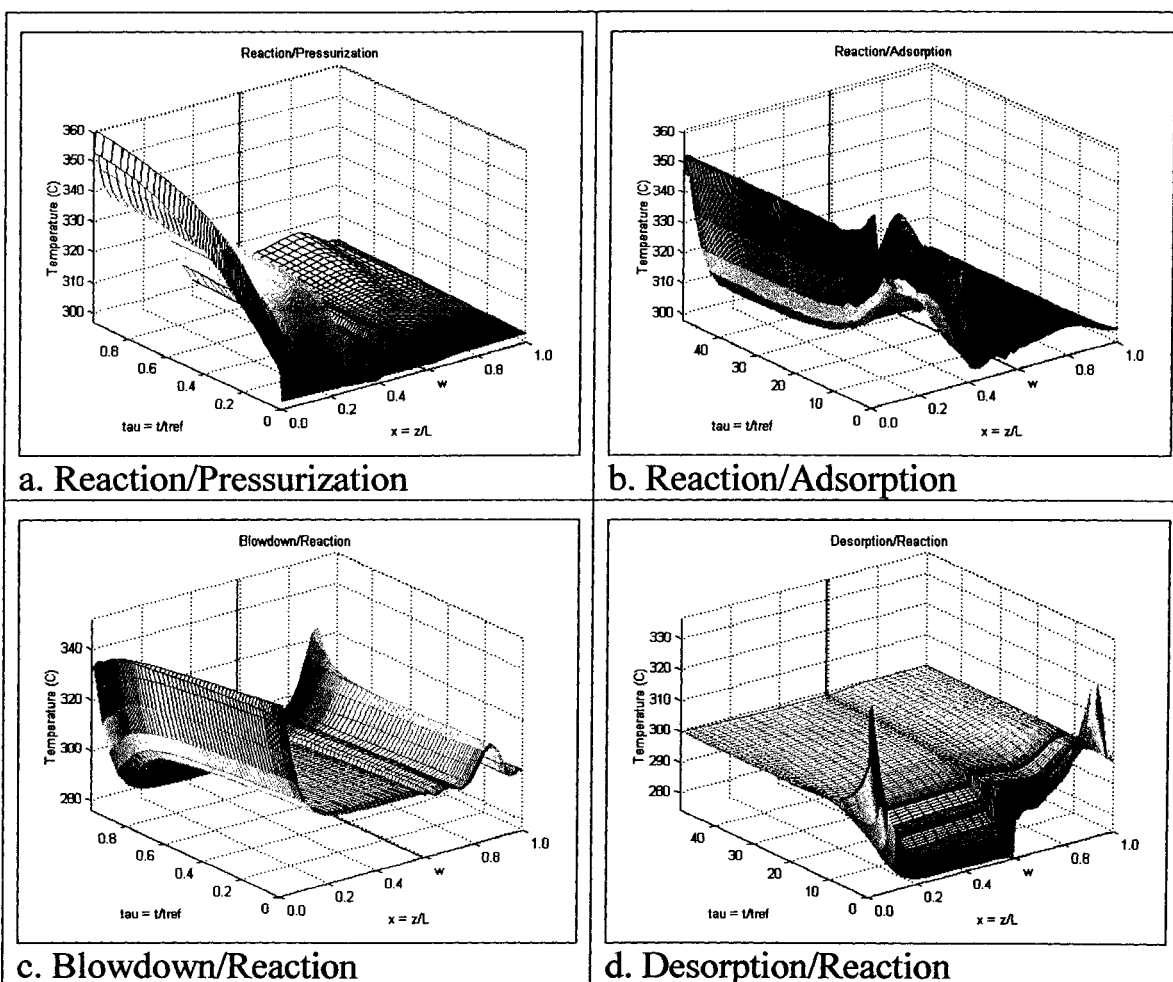


Figure B.6: Three dimensional drawing illustrating the transient and spatial change in Temperature with respect to time and axial distance for the four basic steps at the steady state cycle. (Conventional PSAR Unit/Self Regeneration)

## **APPENDIX C**

**Three Dimensional Figures of a PSAR Unit with Waste Recycled to Feed  
(Hydrogen Purge)**

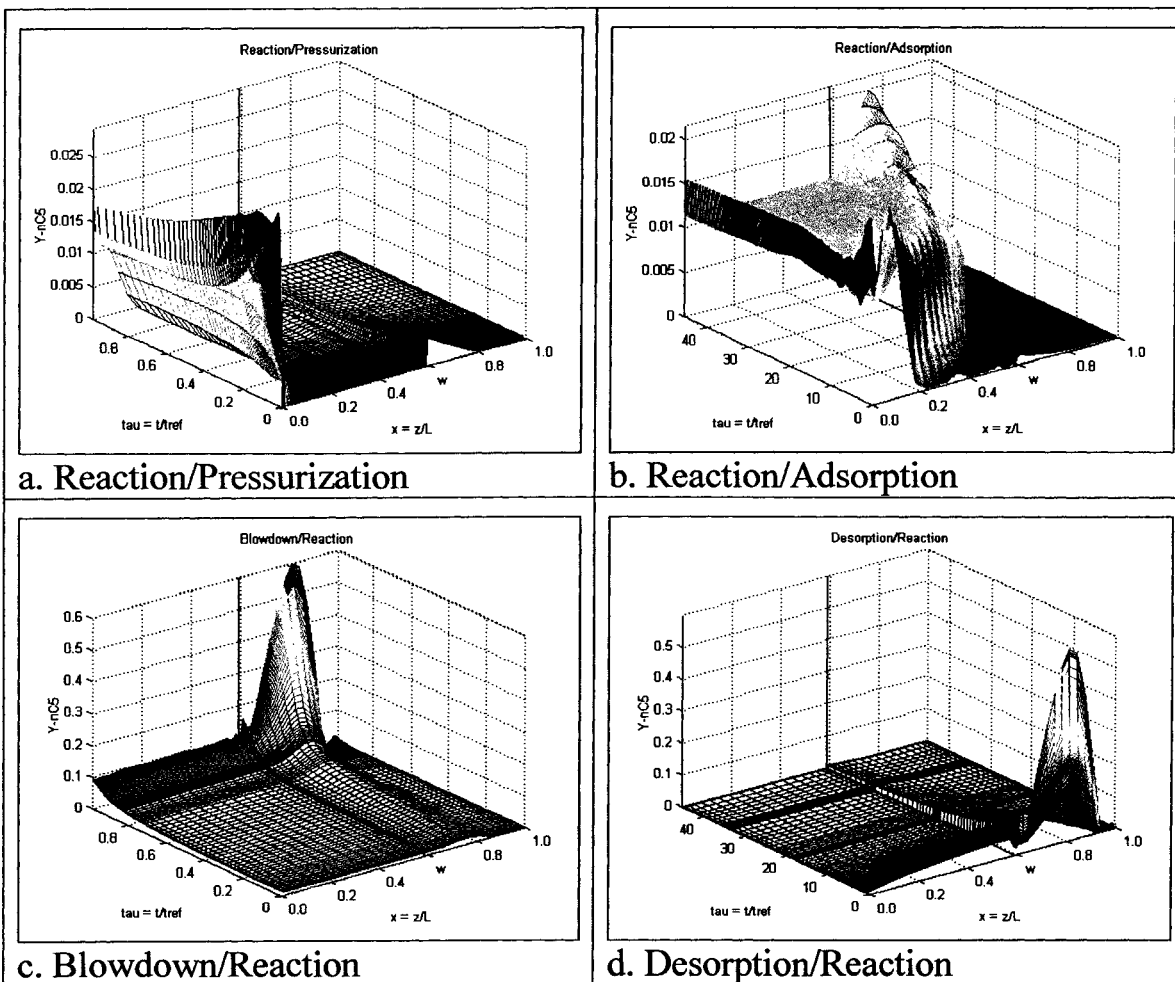


Figure C.1: Three dimensional drawing illustrating the transient and spatial change in  $n\text{-C}_5$  concentration with respect to time and axial distance for the four basic steps at the steady state cycle. (PSAR Unit with Waste Recycled to Feed/Hydrogen Purge)

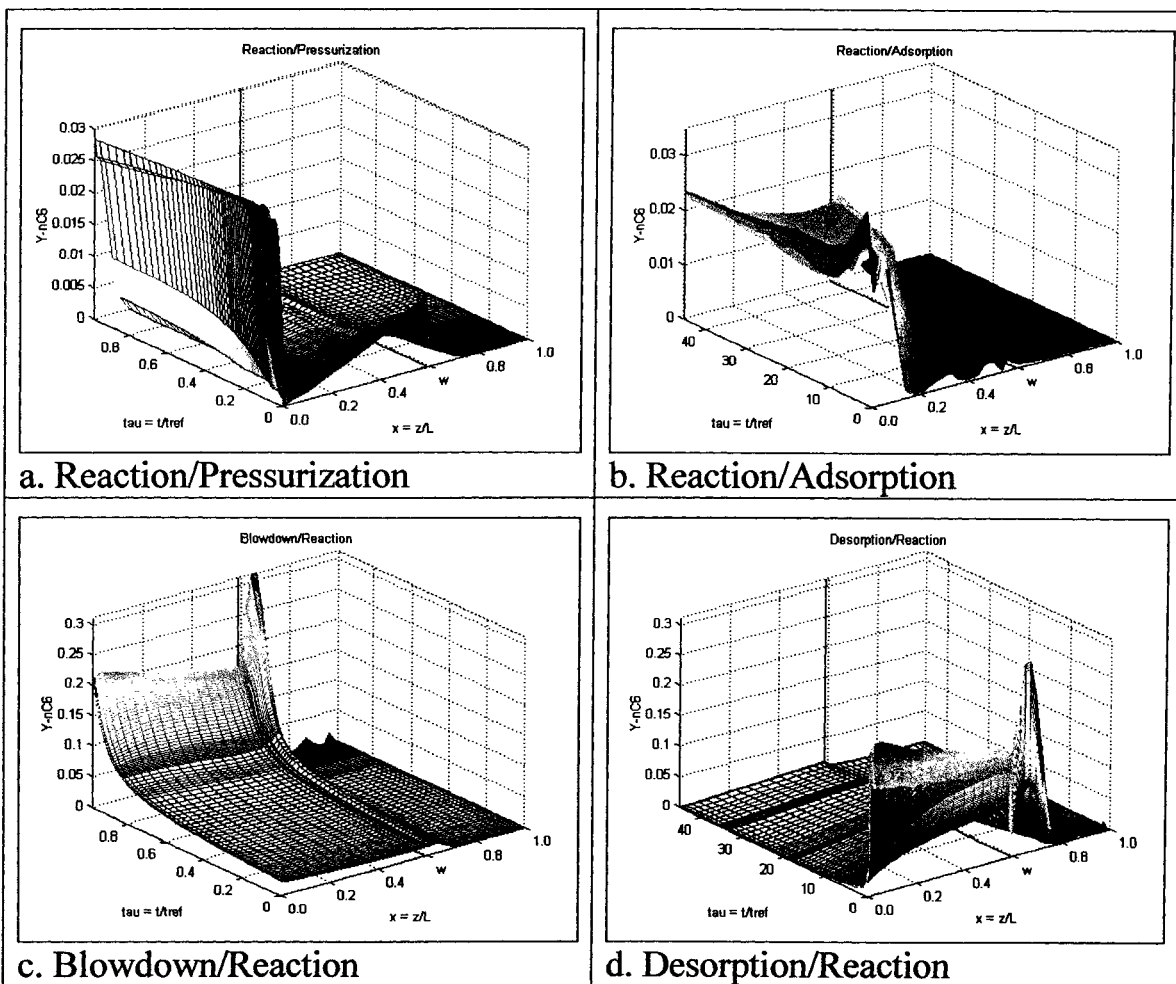


Figure C.2: Three dimensional drawing illustrating the transient and spatial change in  $n\text{-C}_6$  concentration with respect to time and axial distance for the four basic steps at the steady state cycle. (PSAR Unit with Waste Recycled to Feed/Hydrogen Purge)

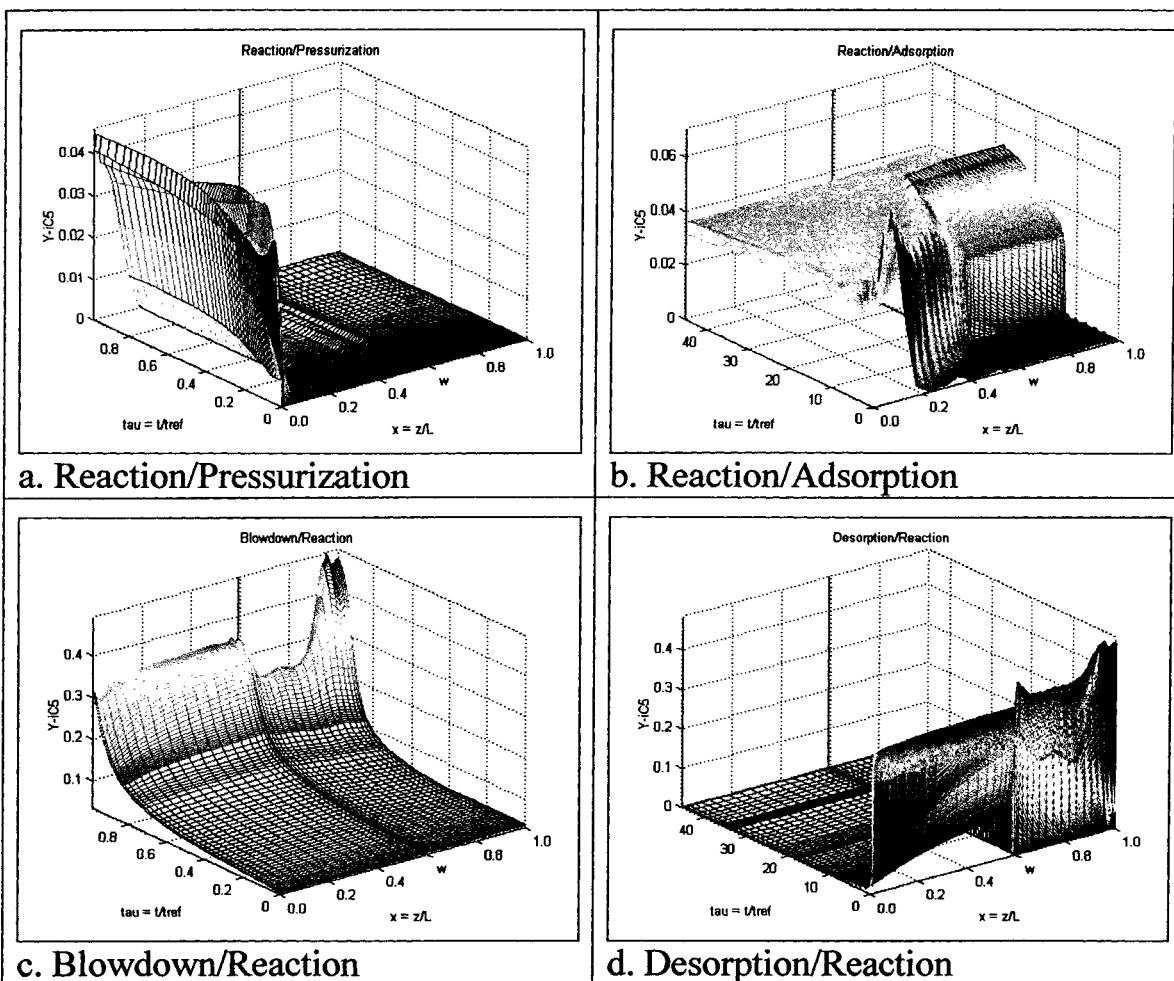


Figure C.3: Three dimensional drawing illustrating the transient and spatial change in  $i\text{-C}_5$  concentration with respect to time and axial distance for the four basic steps at the steady state cycle. (PSAR Unit with Waste Recycled to Feed/Hydrogen Purge)

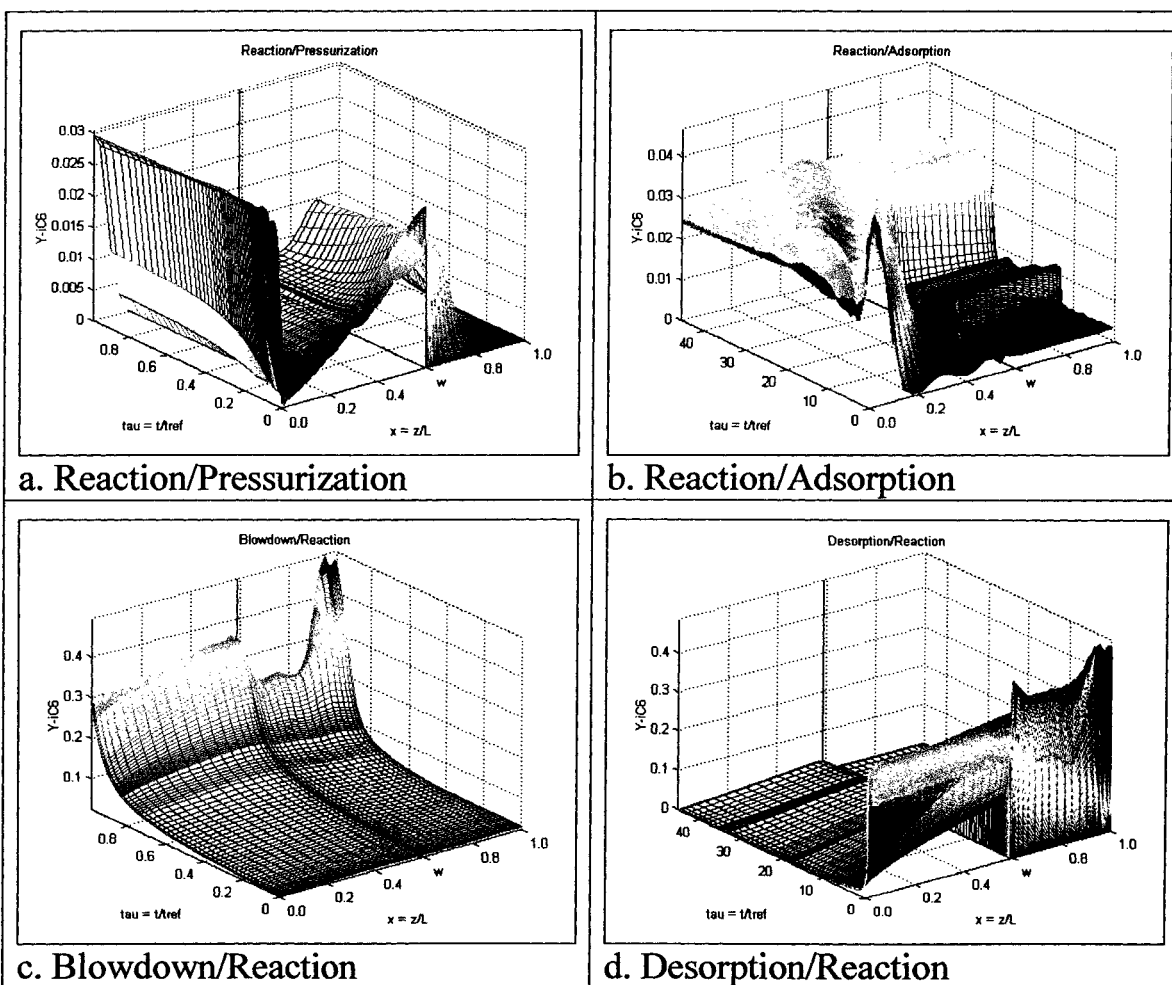


Figure C.4: Three dimensional drawing illustrating the transient and spatial change in  $i\text{-C}_6$  concentration with respect to time and axial distance for the four basic steps at the steady state cycle. (PSAR Unit with Waste Recycled to Feed/Hydrogen Purge)



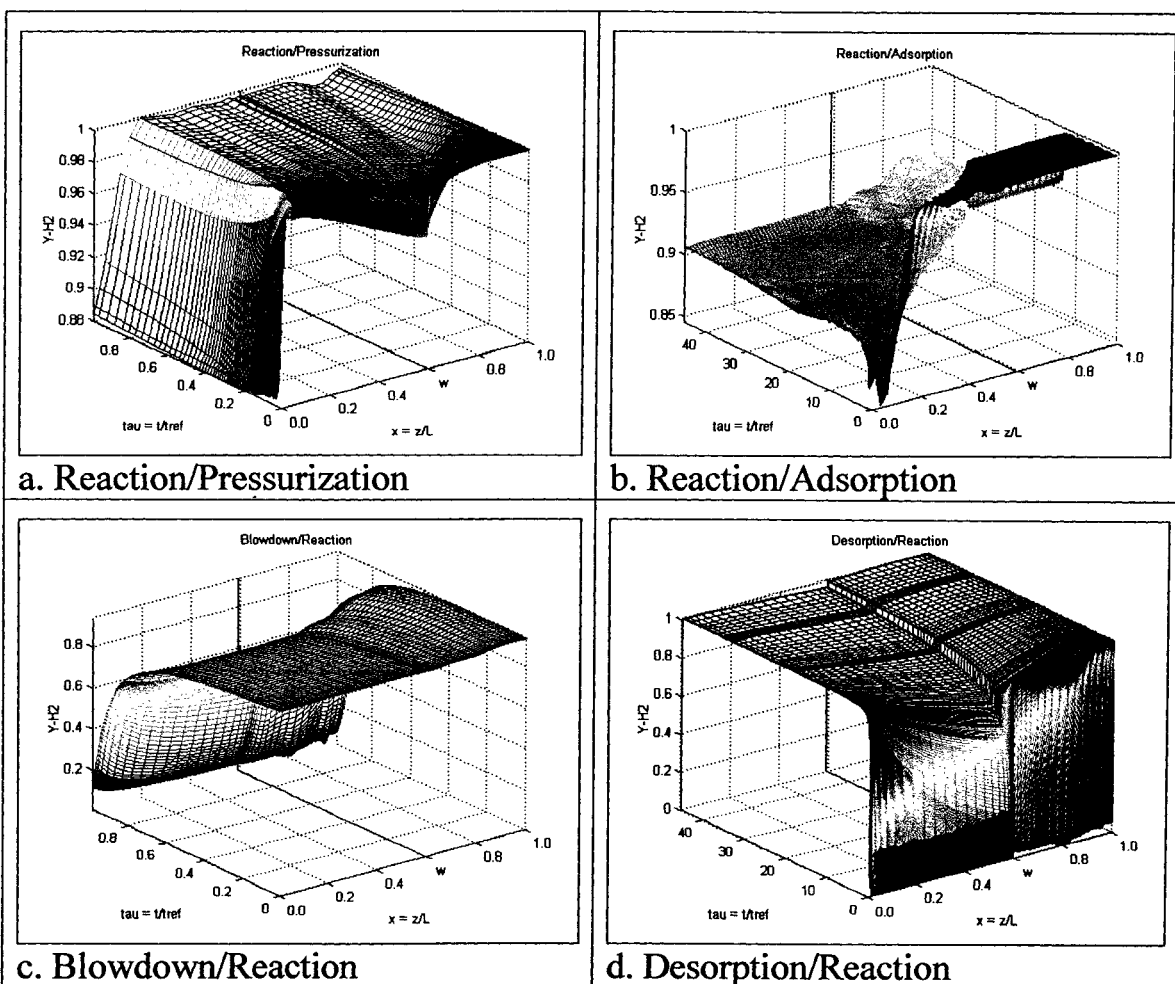


Figure C.5: Three dimensional drawing illustrating the transient and spatial change in  $H_2$  concentration with respect to time and axial distance for the four basic steps at the steady state cycle. (PSAR Unit with Waste Recycled to Feed/Hydrogen Purge)

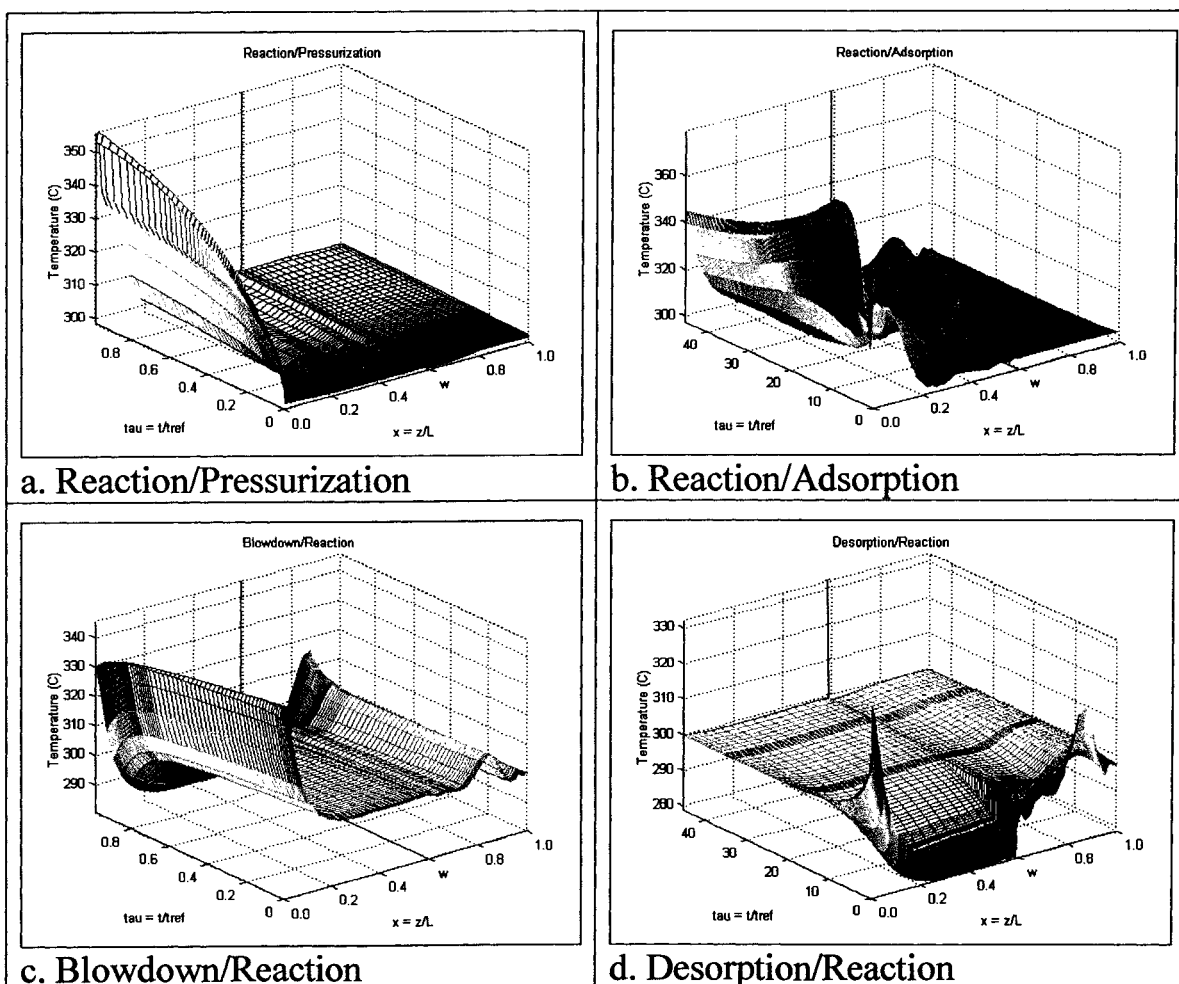


Figure C.6: Three dimensional drawing illustrating the transient and spatial change in Temperature with respect to time and axial distance for the four basic steps at the steady state cycle. (PSAR Unit with Waste Recycled to Feed/Hydrogen Purge)

## **APPENDIX D**

**Three Dimensional Figures of a PSAR Unit with Waste Recycled to Feed  
(Self Regeneration)**

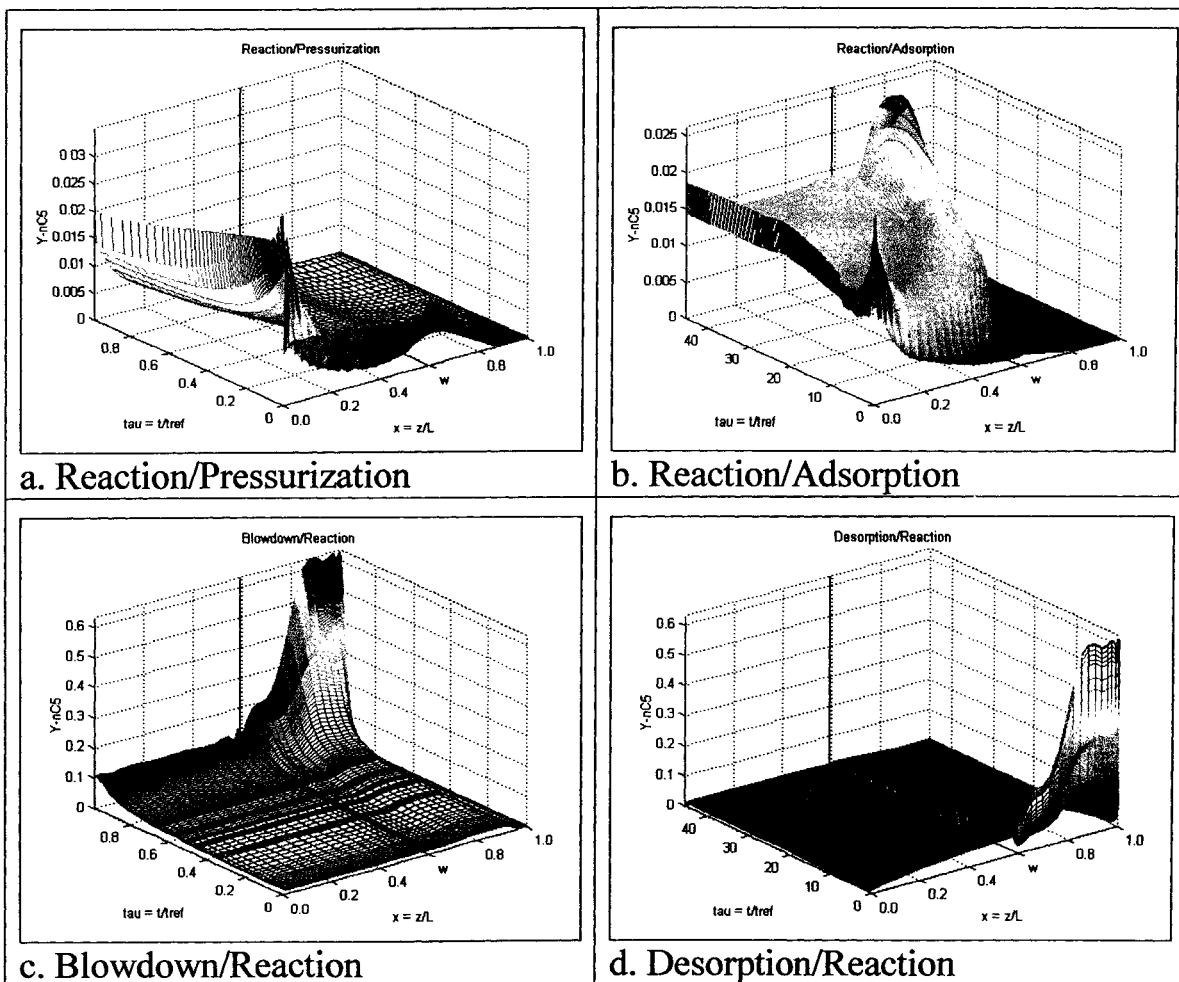


Figure D.1: Three dimensional drawing illustrating the transient and spatial change in n-C<sub>5</sub> concentration with respect to time and axial distance for the four basic steps at the steady state cycle. (PSAR Unit with Waste Recycled to Feed/Self Regeneration)

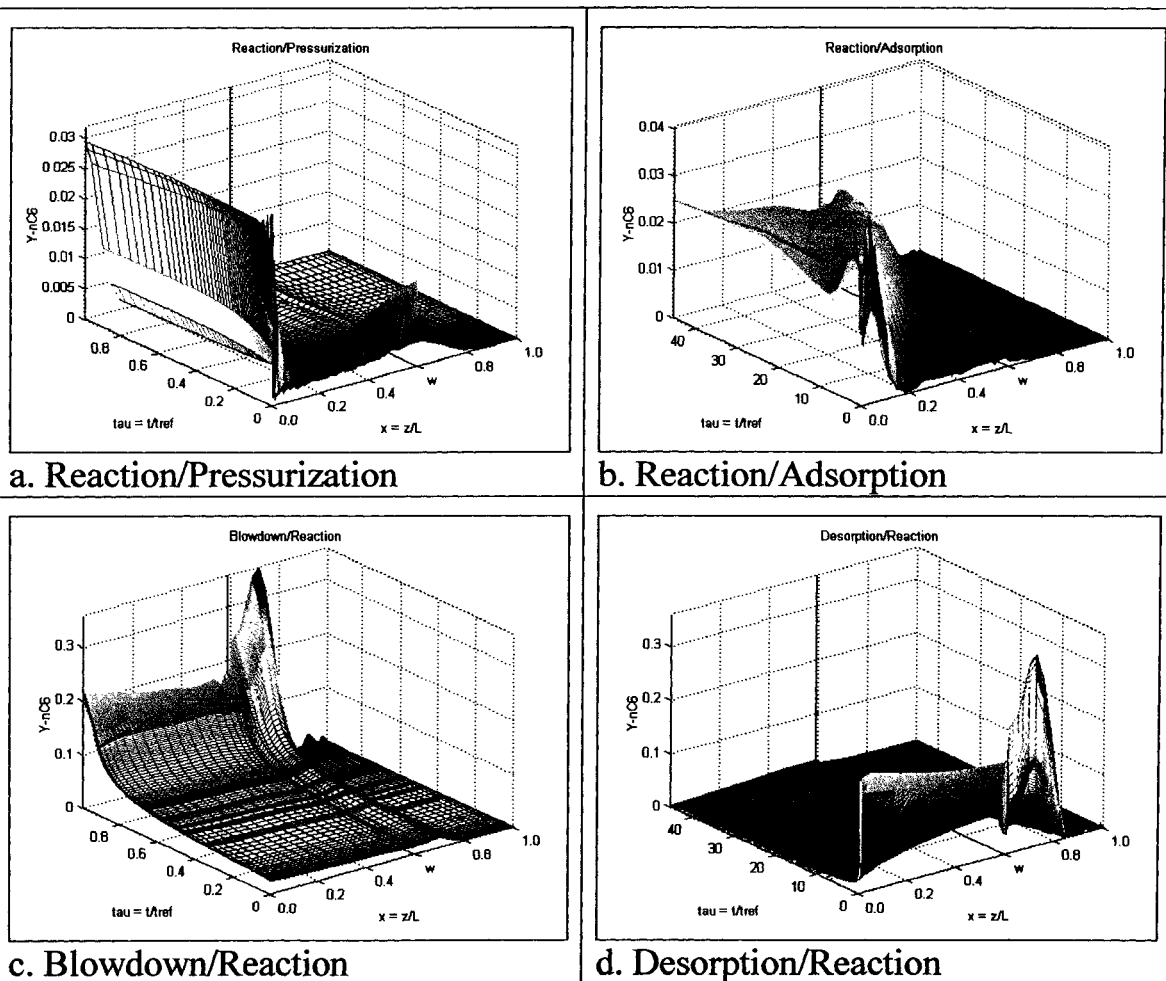


Figure D.2: Three dimensional drawing illustrating the transient and spatial change in  $n\text{-C}_6$  concentration with respect to time and axial distance for the four basic steps at the steady state cycle. (PSAR Unit with Waste Recycled to Feed/Self Regeneration)

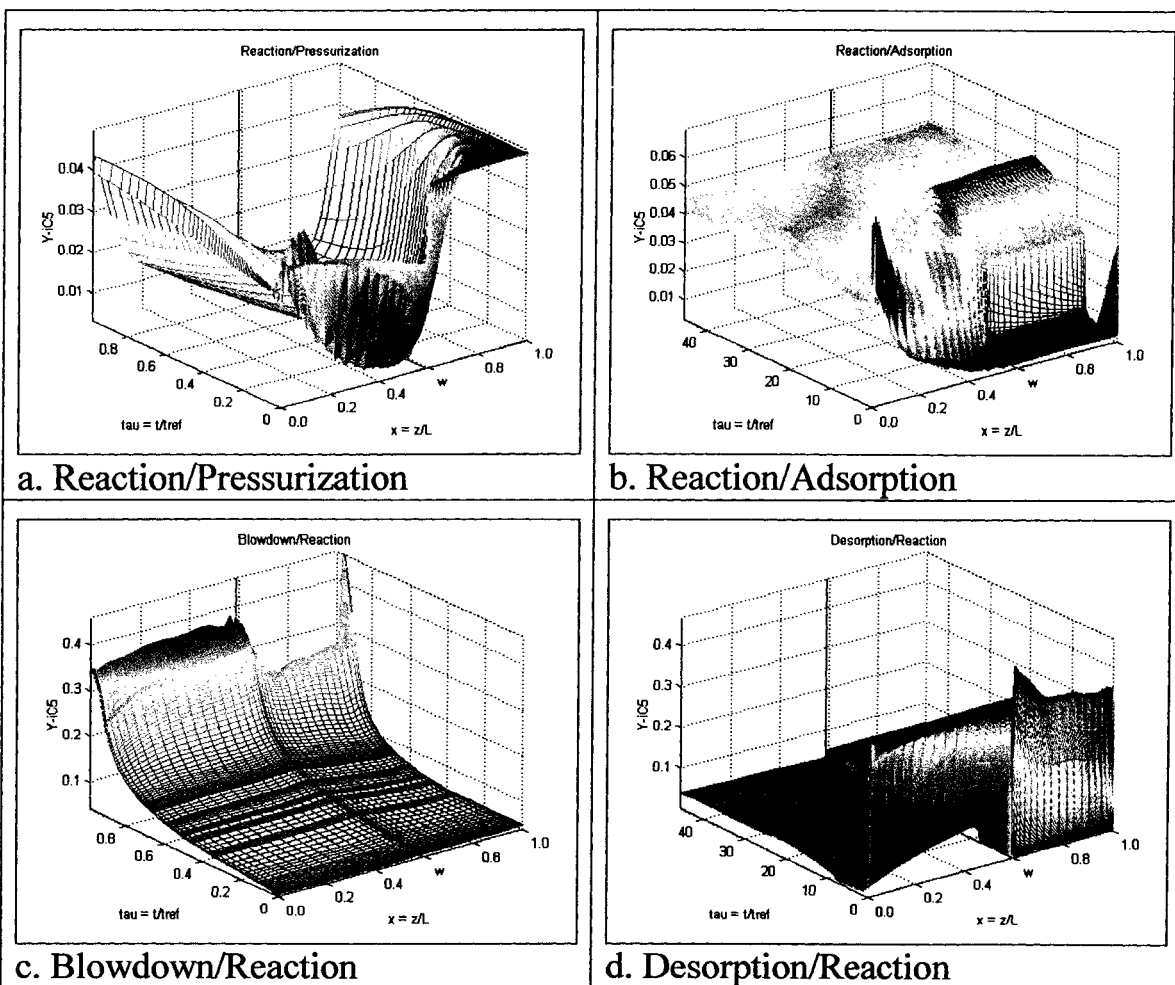


Figure D.3: Three dimensional drawing illustrating the transient and spatial change in  $i\text{-C}_5$  concentration with respect to time and axial distance for the four basic steps at the steady state cycle. (PSAR Unit with Waste Recycled to Feed/Self Regeneration)

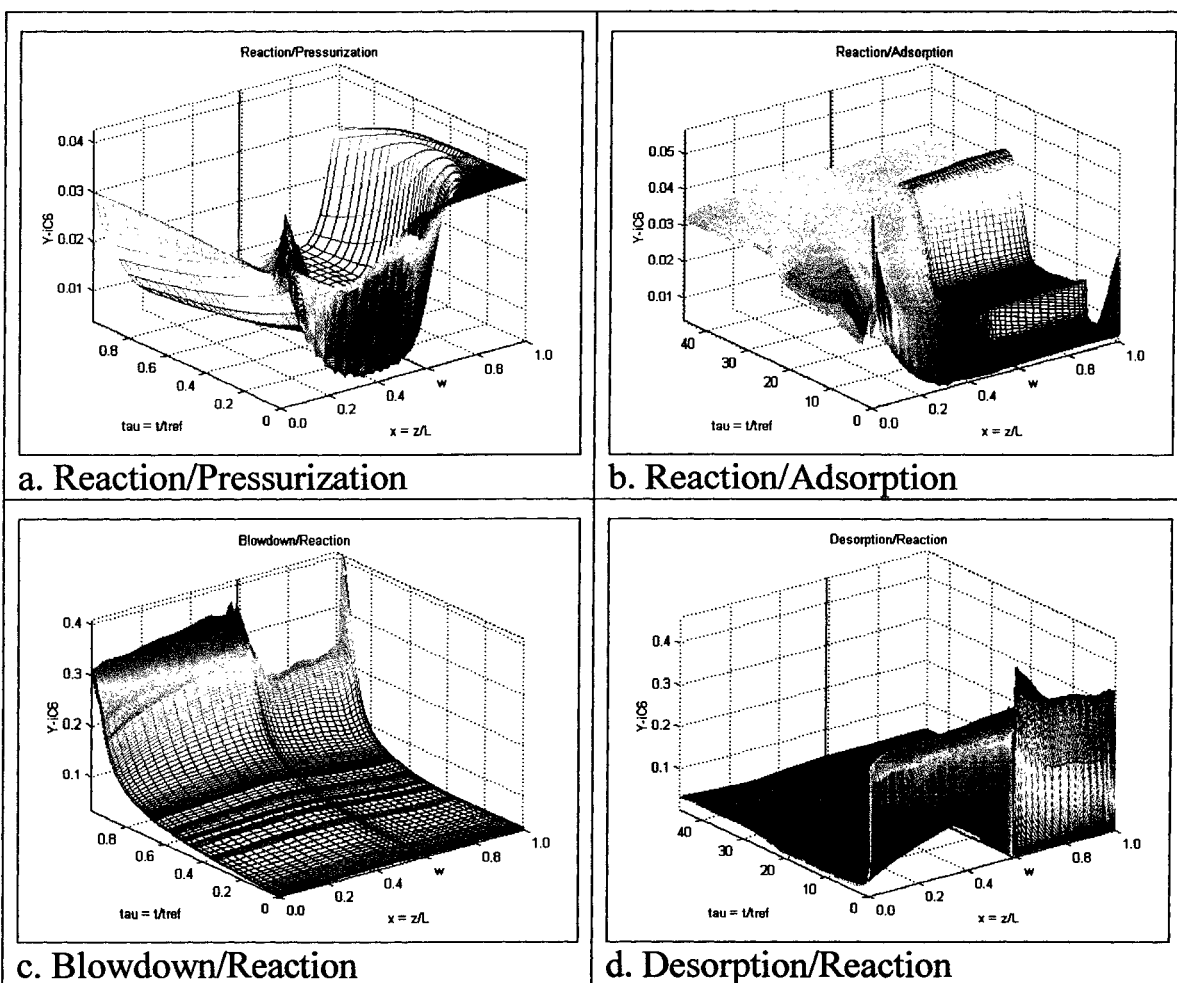


Figure D.4: Three dimensional drawing illustrating the transient and spatial change in  $i\text{-C}_6$  concentration with respect to time and axial distance for the four basic steps at the steady state cycle. (PSAR Unit with Waste Recycled to Feed/Self Regeneration)

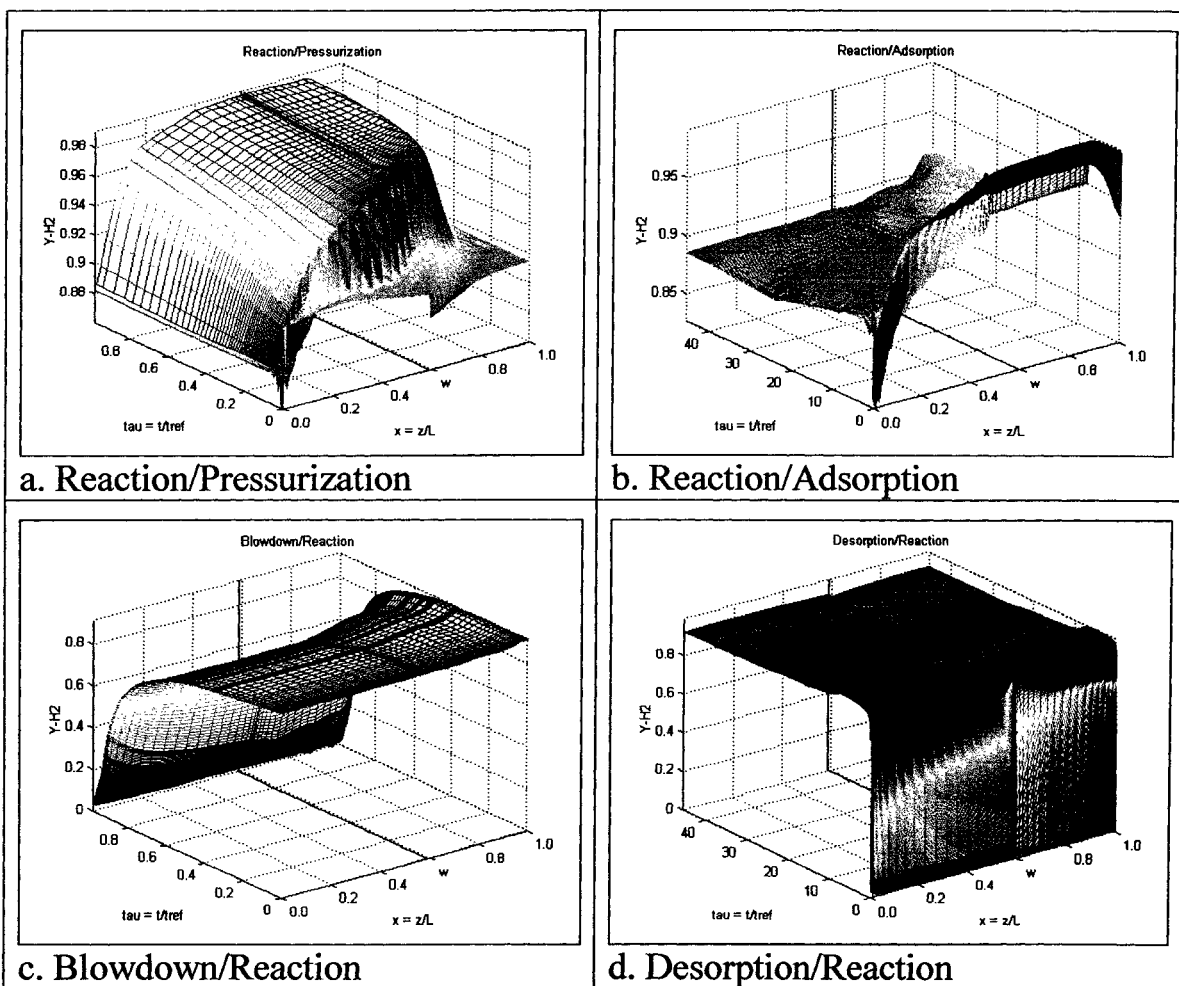


Figure D.5: Three dimensional drawing illustrating the transient and spatial change in  $H_2$  concentration with respect to time and axial distance for the four basic steps at the steady state cycle. (PSAR Unit with Waste Recycled to Feed/Self Regeneration)



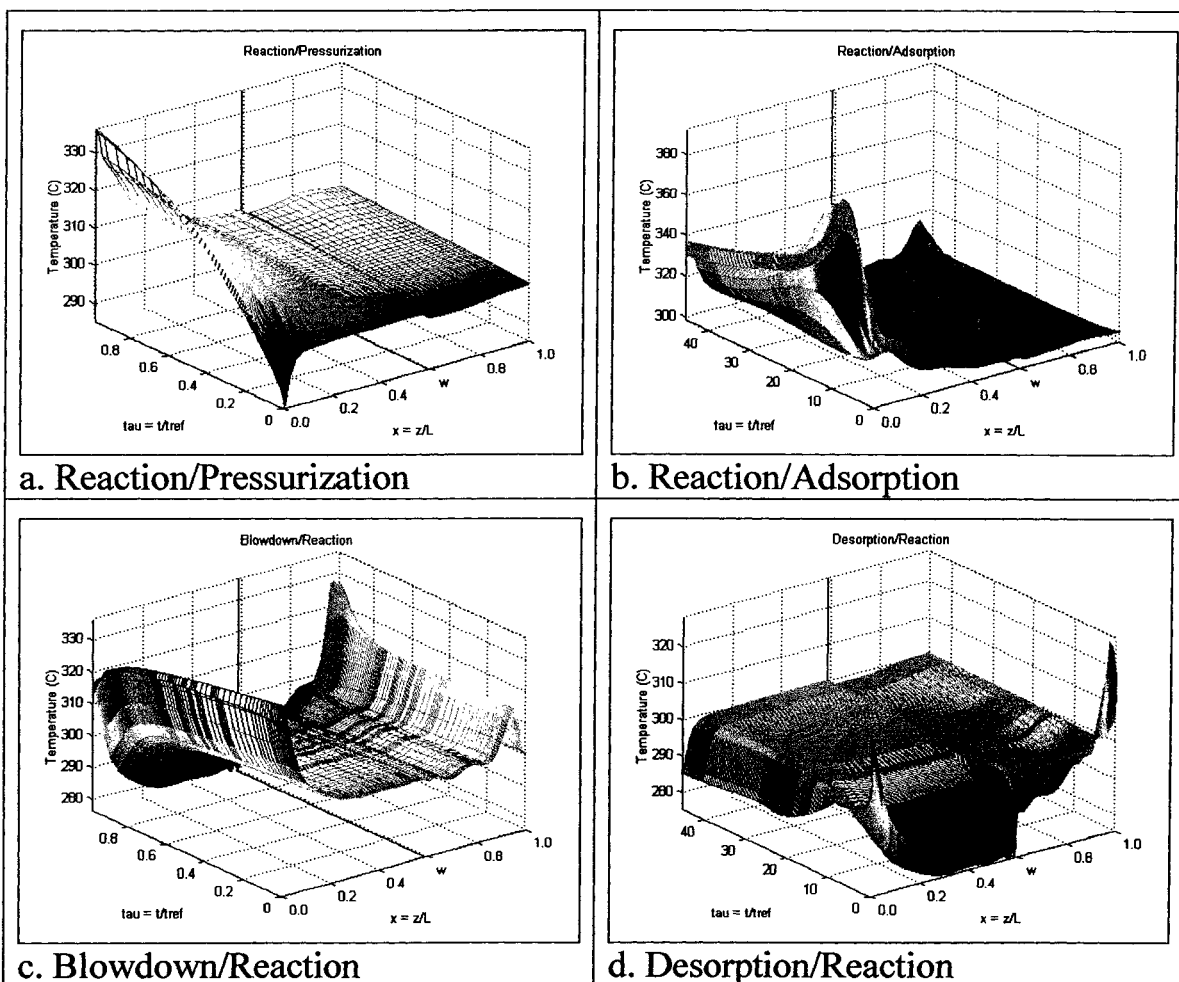


Figure D.6: Three dimensional drawing illustrating the transient and spatial change in Temperature with respect to time and axial distance for the four basic steps at the steady state cycle. (PSAR Unit with Waste Recycled to Feed/Self Regeneration)

## **APPENDIX E**

### **Three Dimensional Figures of a Conventional PSARM Unit With Hydrogen Purge**

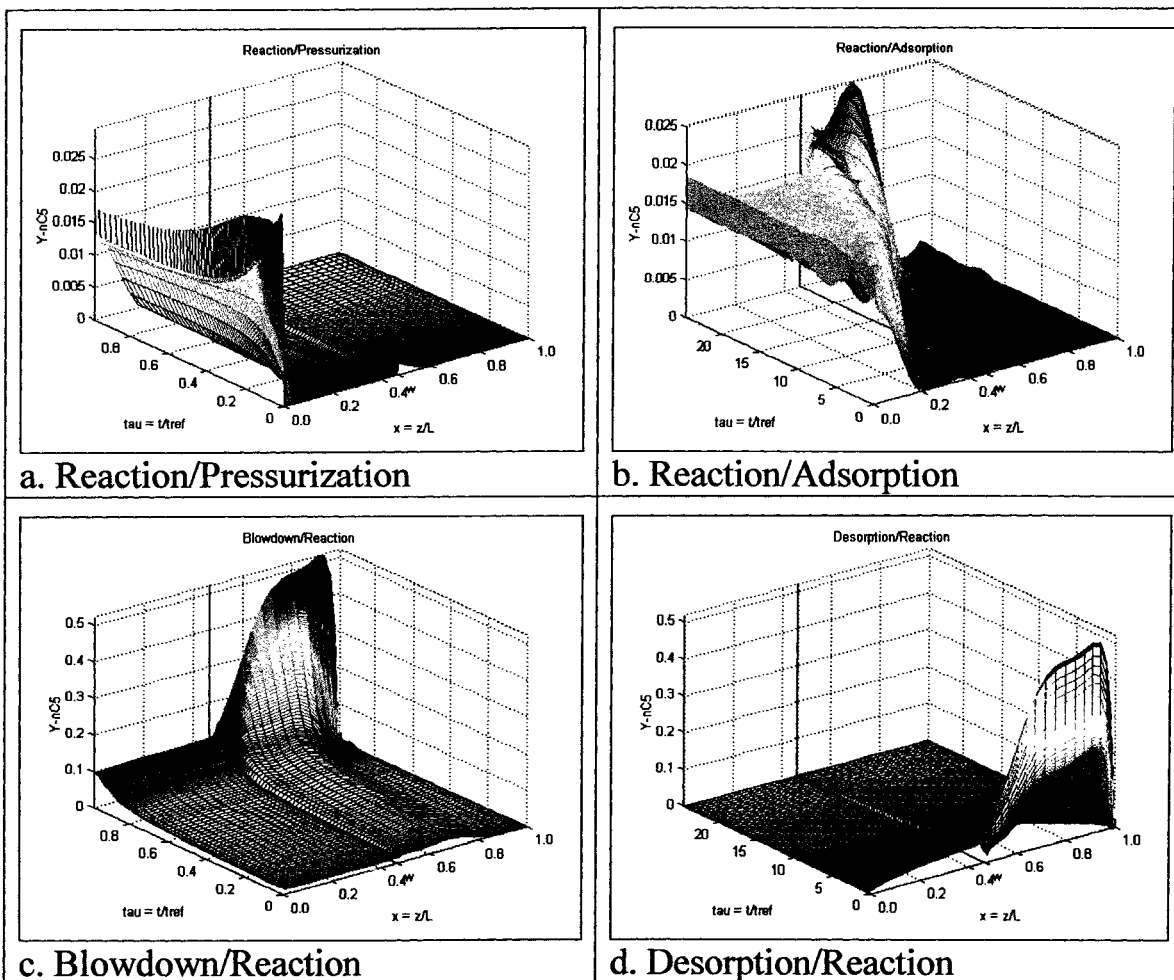


Figure E.1: Three dimensional drawing illustrating the transient and spatial change in  $n-C_5$  concentration with respect to time and axial distance for the four basic steps at the steady state cycle. (Conventional PSARM Unit/Hydrogen Purge)

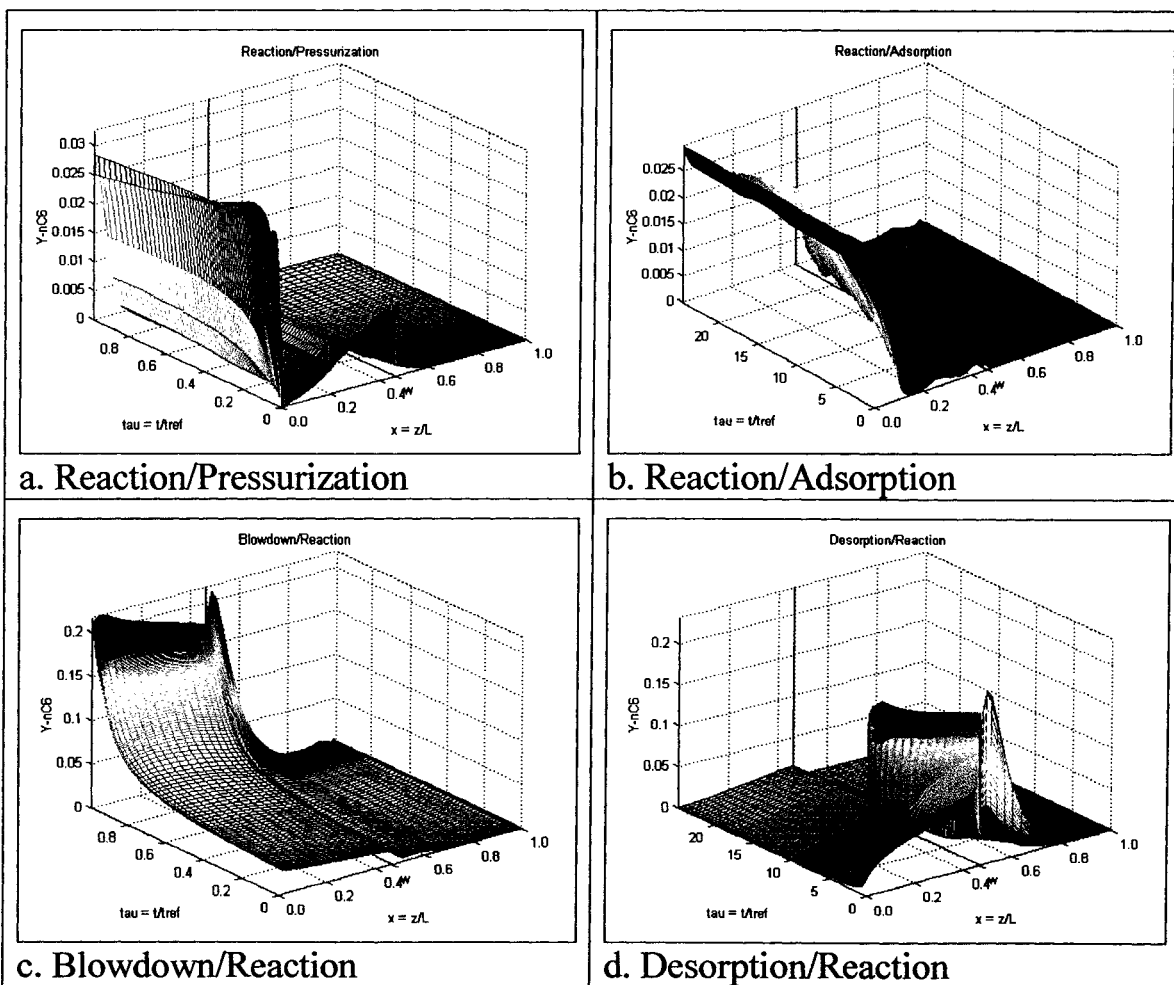


Figure E.2: Three dimensional drawing illustrating the transient and spatial change in n-C<sub>6</sub> concentration with respect to time and axial distance for the four basic steps at the steady state cycle. (Conventional PSARM Unit/Hydrogen Purge)

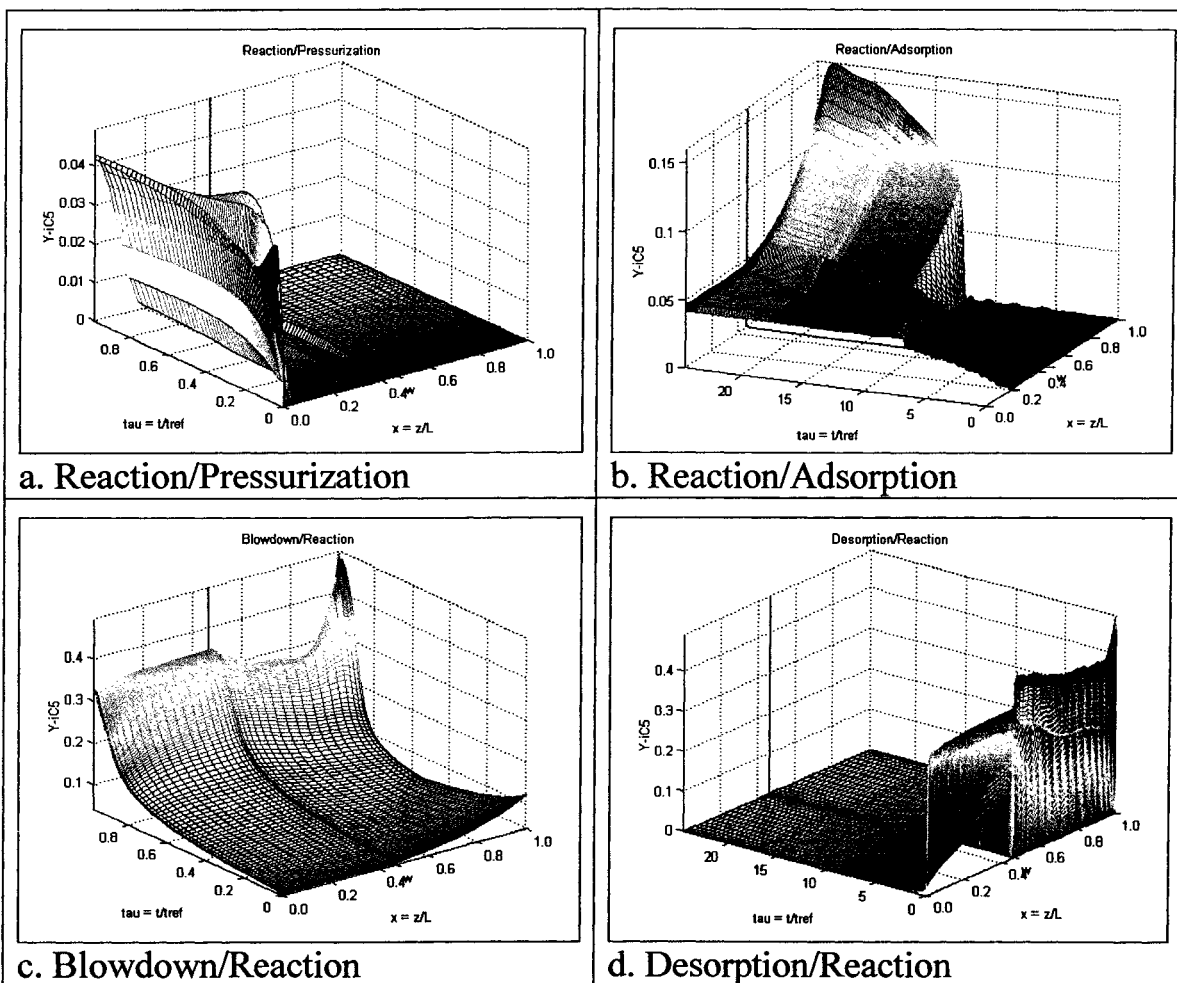


Figure E.3: Three dimensional drawing illustrating the transient and spatial change in  $i\text{-C}_5$  concentration with respect to time and axial distance for the four basic steps at the steady state cycle. (Conventional PSARM Unit/Hydrogen Purge)

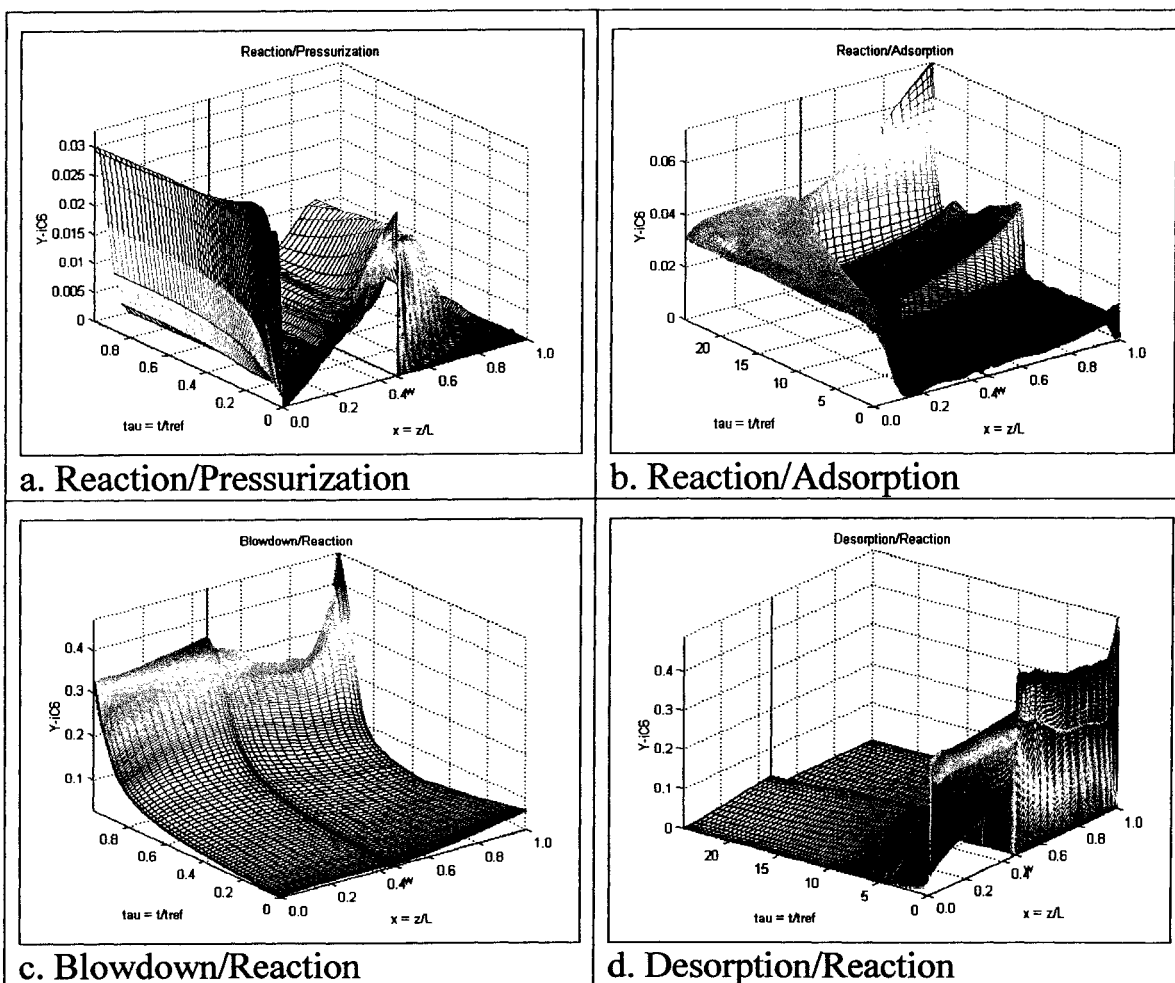


Figure E.4: Three dimensional drawing illustrating the transient and spatial change in  $i\text{-C}_6$  concentration with respect to time and axial distance for the four basic steps at the steady state cycle. (Conventional PSARM Unit/Hydrogen Purge)

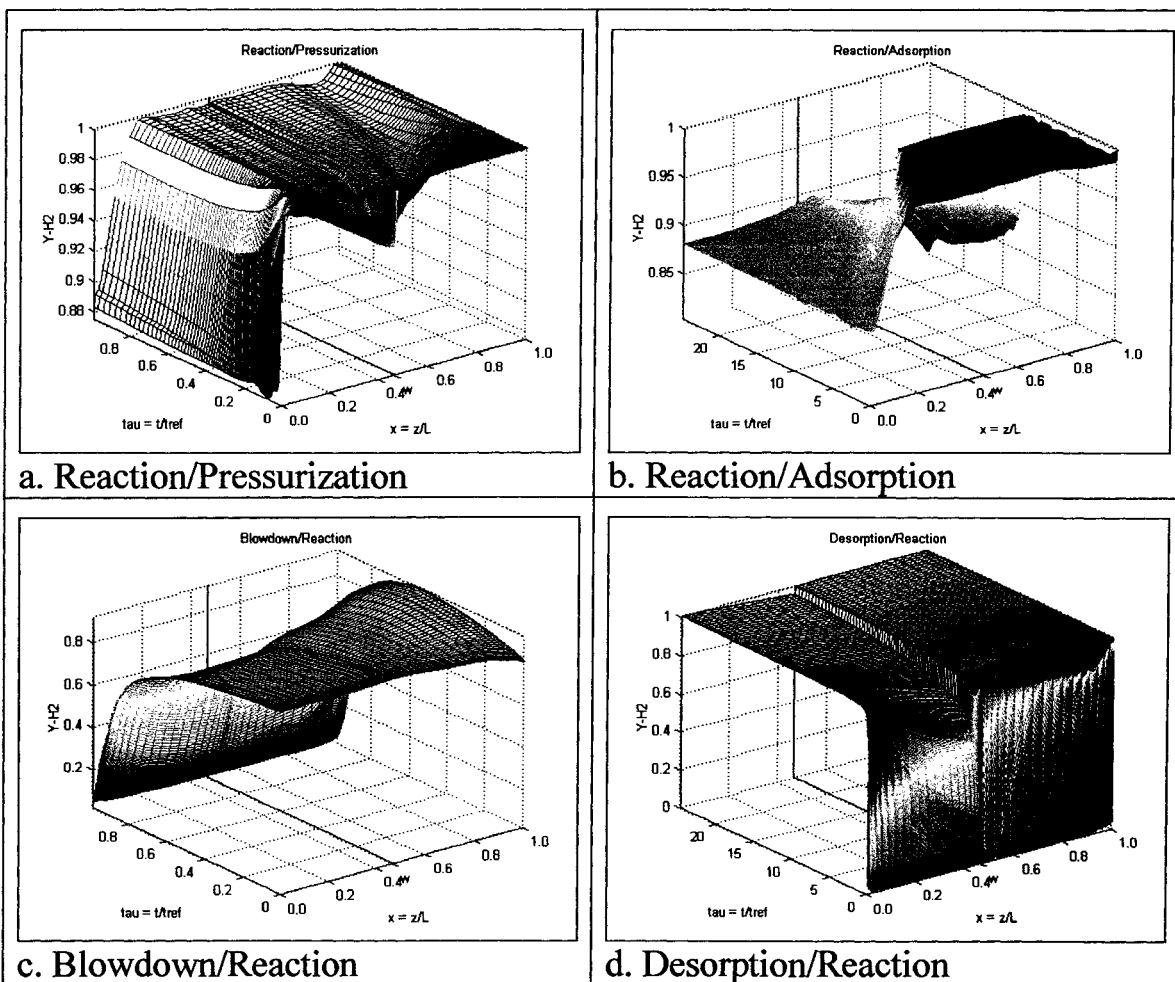
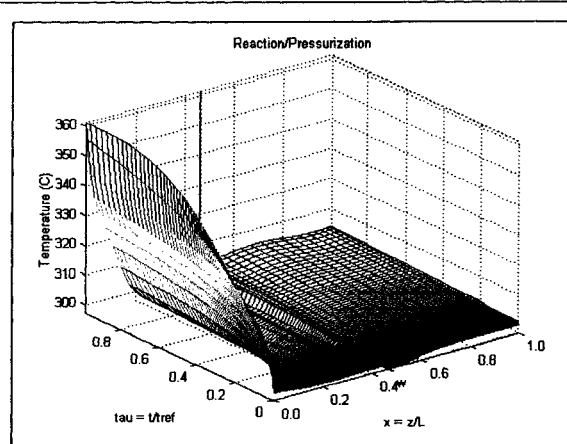
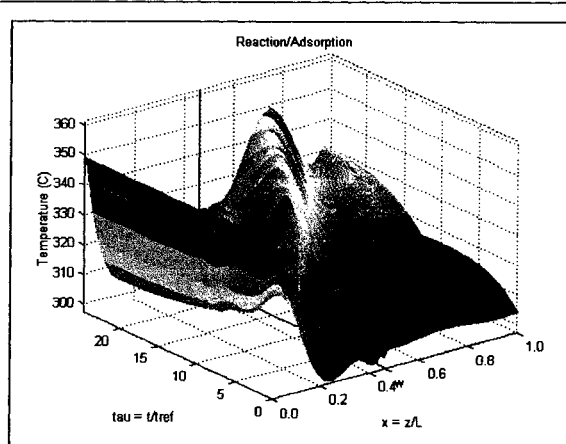


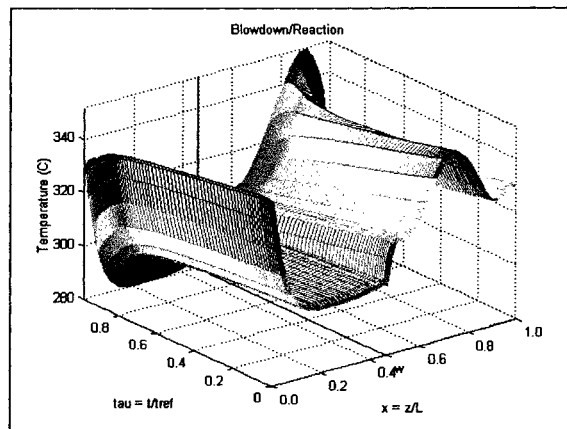
Figure E.5: Three dimensional drawing illustrating the transient and spatial change in  $H_2$  concentration with respect to time and axial distance for the four basic steps at the steady state cycle. (Conventional PSARM Unit/Hydrogen Purge)



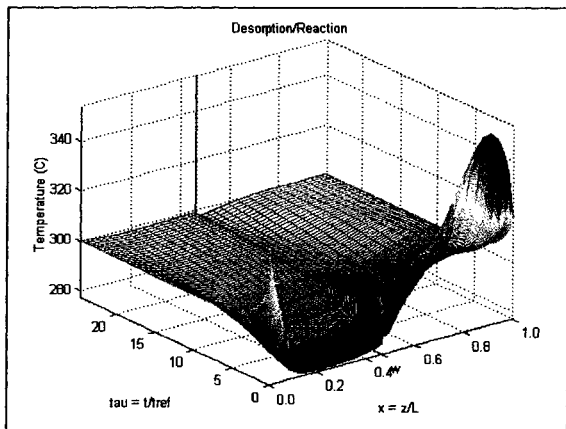
a. Reaction/Pressurization



b. Reaction/Adsorption



c. Blowdown/Reaction



d. Desorption/Reaction

Figure E.6: Three dimensional drawing illustrating the transient and spatial change in Temperature with respect to time and axial distance for the four basic steps at the steady state cycle. (Conventional PSARM Unit/Hydrogen Purge)



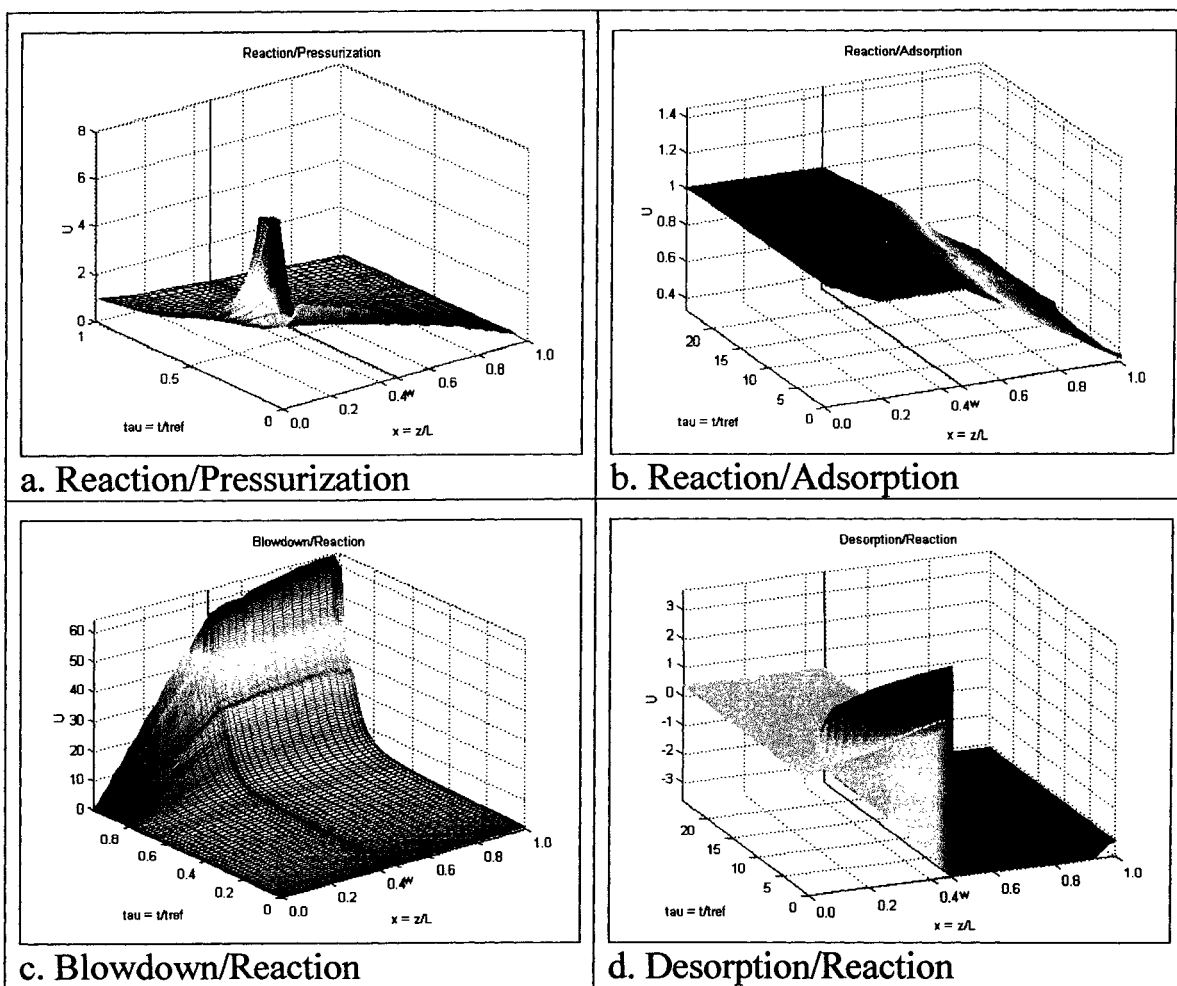


Figure E.7: Three dimensional drawing illustrating the transient and spatial change in Velocity with respect to time and axial distance for the four basic steps at the steady state cycle. (Conventional PSARM Unit/Hydrogen Purge)

## **APPENDIX F**

### **Three Dimensional Figures of a Conventional PSARM Unit (Self Regeneration)**

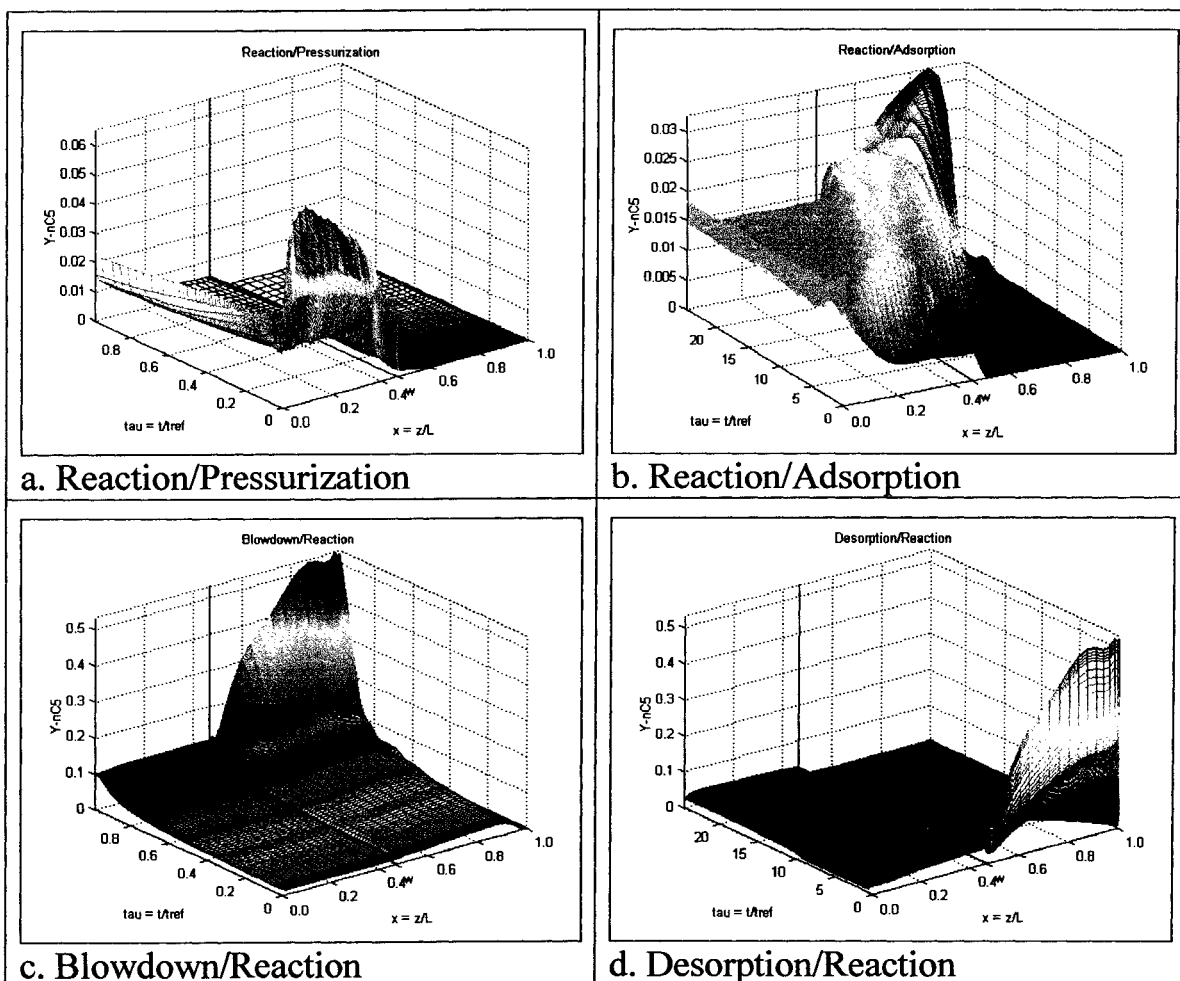


Figure F.1: Three dimensional drawing illustrating the transient and spatial change in  $n\text{-C}_5$  concentration with respect to time and axial distance for the four basic steps at the steady state cycle. (Conventional PSARM Unit/Self Regeneration)

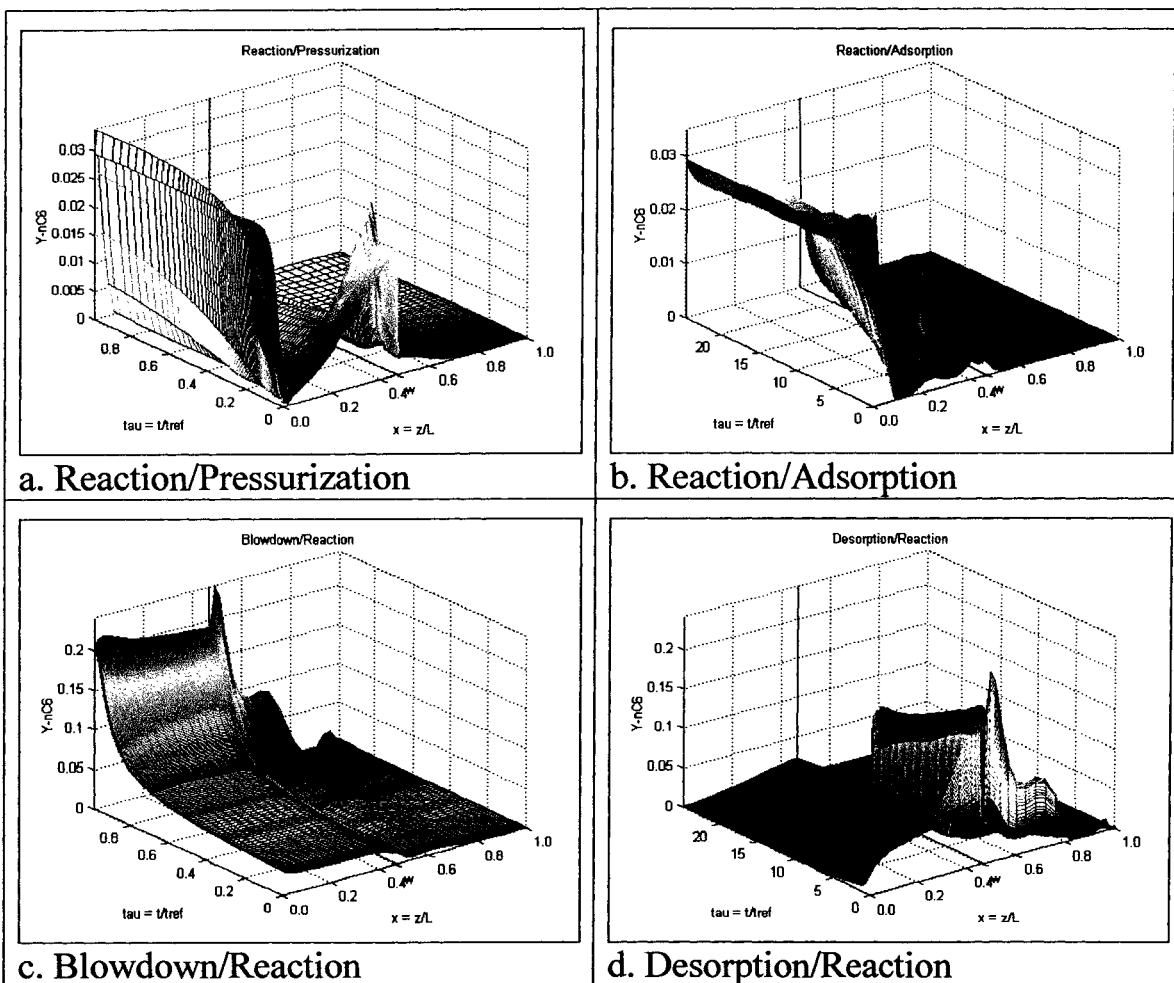


Figure F.2: Three dimensional drawing illustrating the transient and spatial change in n-C<sub>6</sub> concentration with respect to time and axial distance for the four basic steps at the steady state cycle. (Conventional PSARM Unit/Self Regeneration)

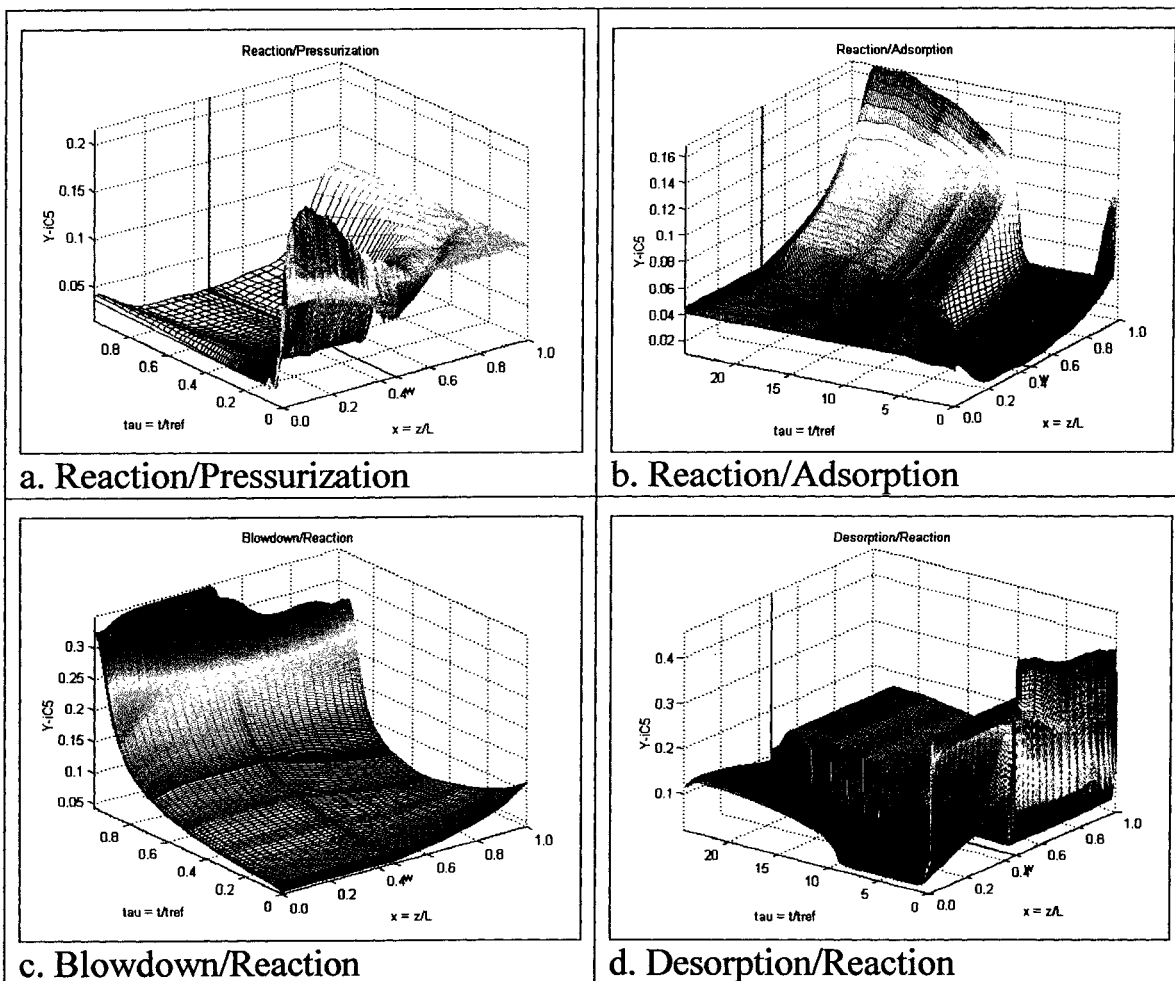


Figure F.3: Three dimensional drawing illustrating the transient and spatial change in i-C<sub>5</sub> concentration with respect to time and axial distance for the four basic steps at the steady state cycle. (Conventional PSARM Unit/Self Regeneration)

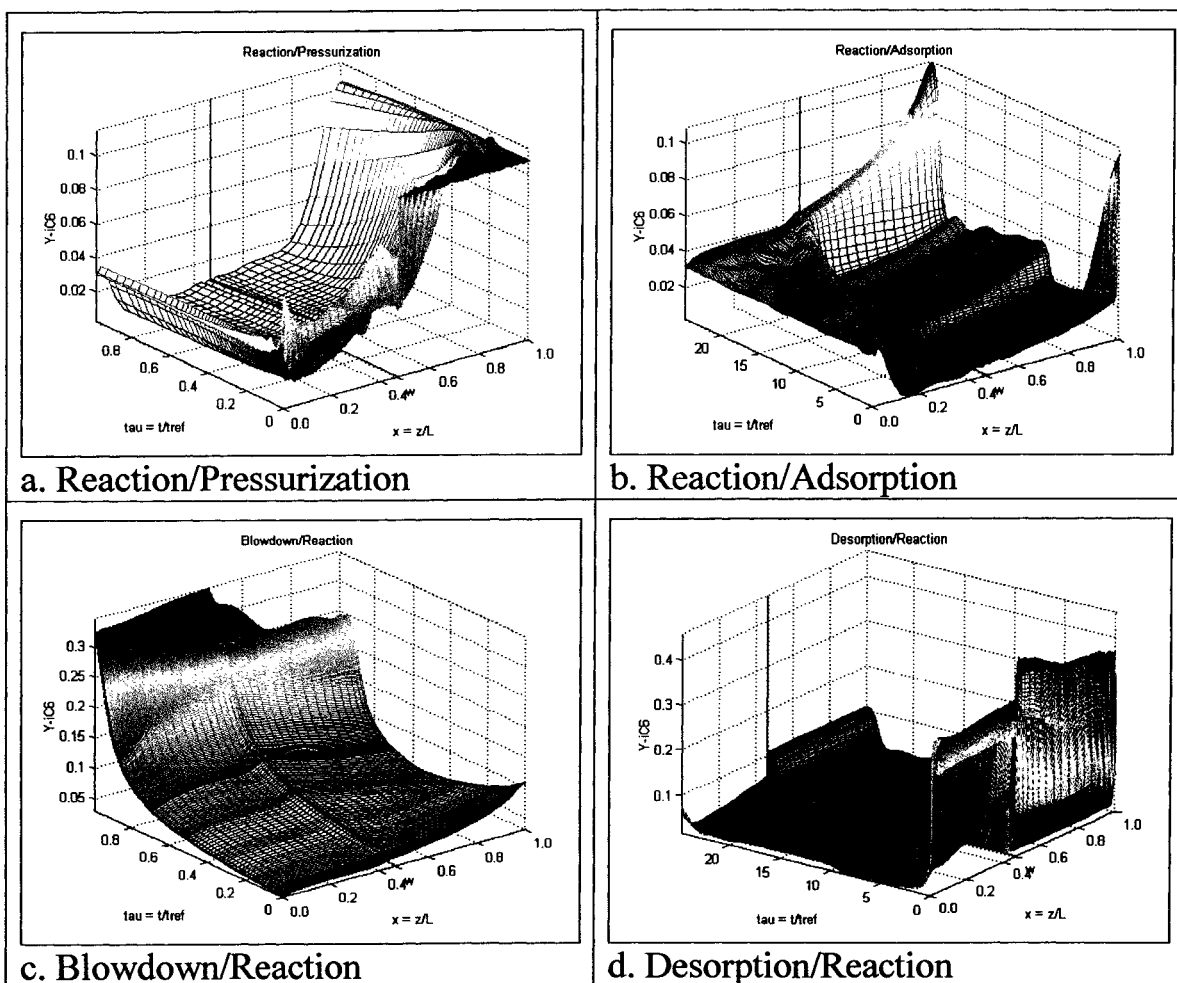


Figure F.4: Three dimensional drawing illustrating the transient and spatial change in  $i\text{-C}_6$  concentration with respect to time and axial distance for the four basic steps at the steady state cycle. (Conventional PSARM Unit/Self Regeneration)

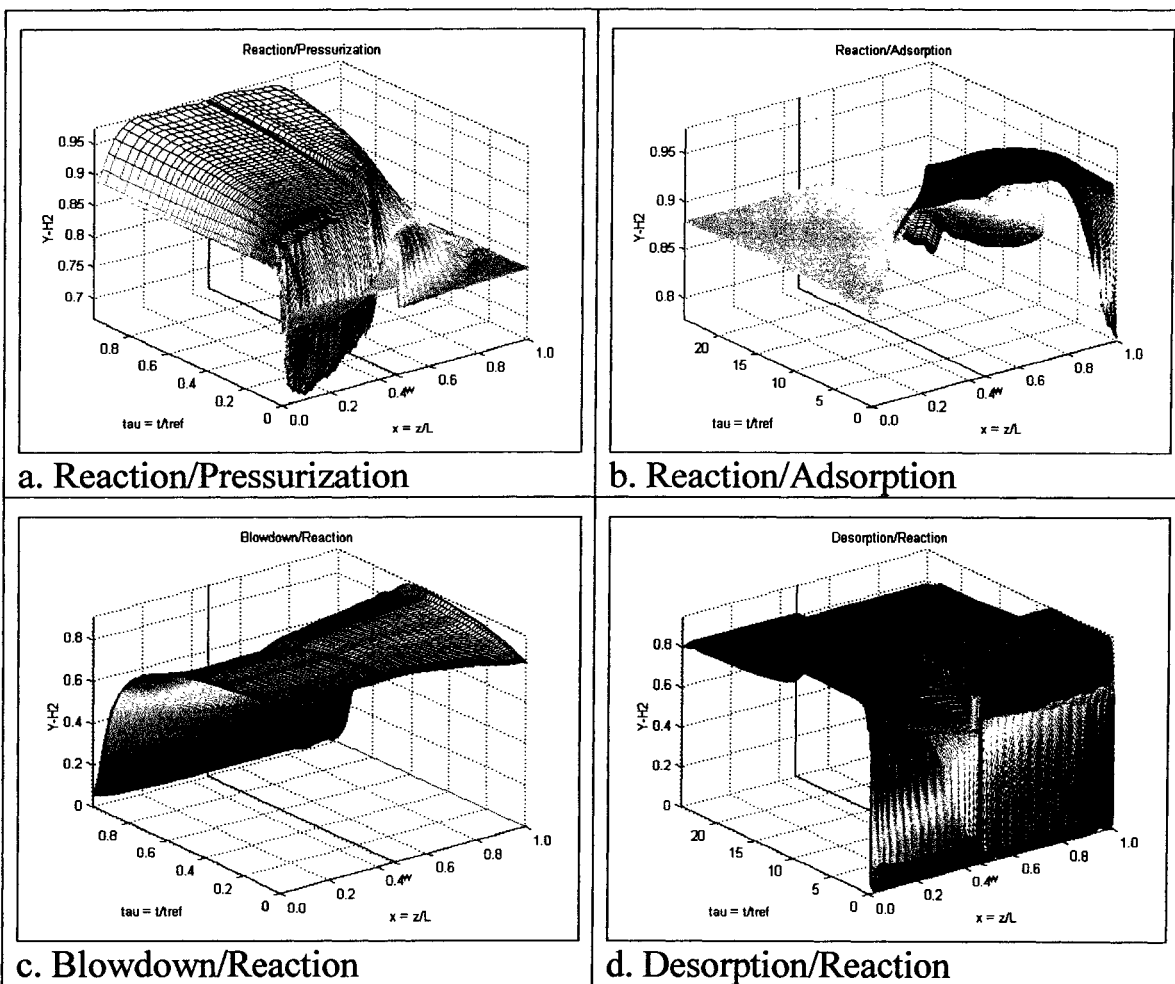


Figure F.5: Three dimensional drawing illustrating the transient and spatial change in  $H_2$  concentration with respect to time and axial distance for the four basic steps at the steady state cycle. (Conventional PSARM Unit/Self Regeneration)

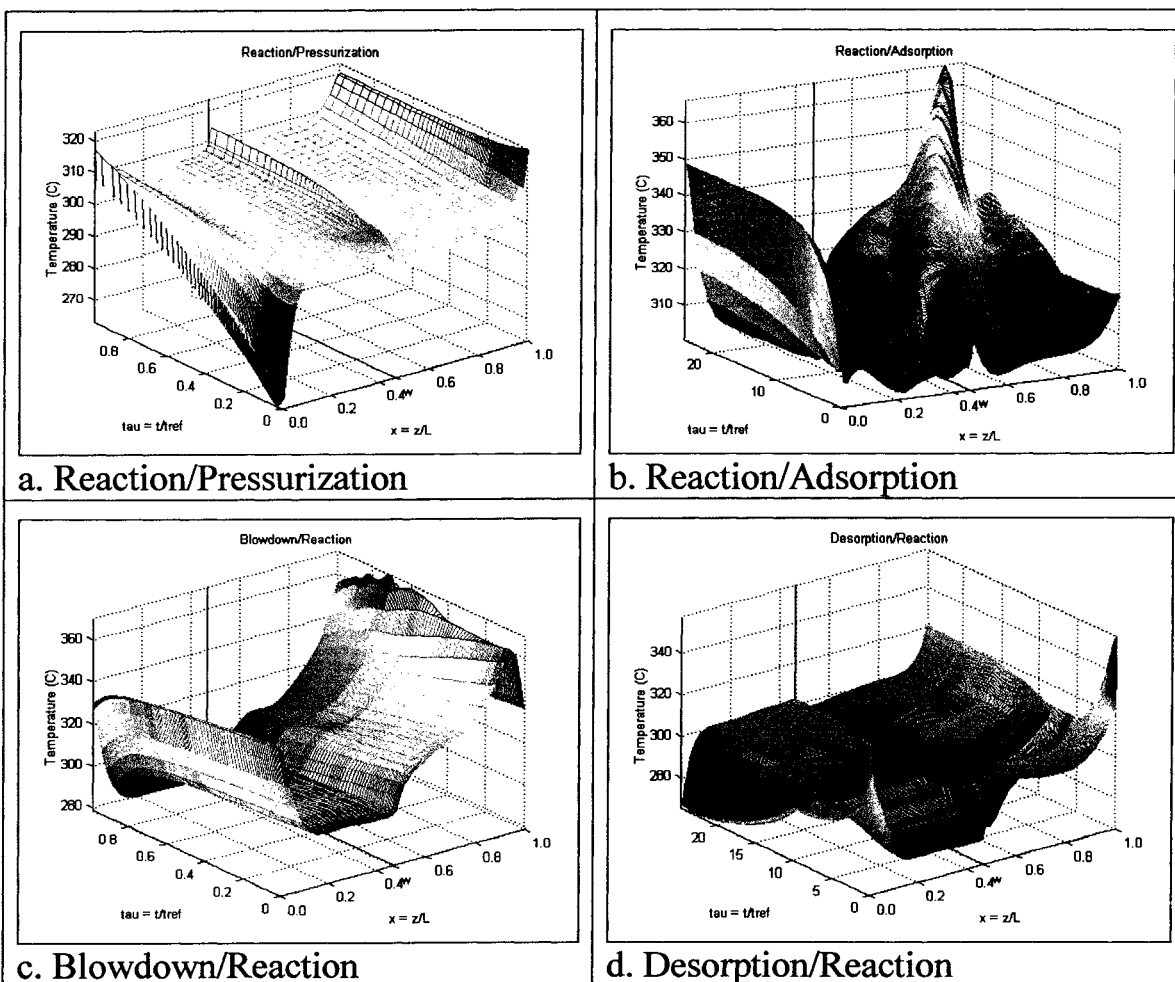


Figure F.6: Three dimensional drawing illustrating the transient and spatial change in Temperature with respect to time and axial distance for the four basic steps at the steady state cycle. (Conventional PSARM Unit/Self Regeneration)



## **APPENDIX G**

**Three Dimensional Figures of a PSAR Unit with Waste Recycled to Feed  
(Hydrogen Purge)**

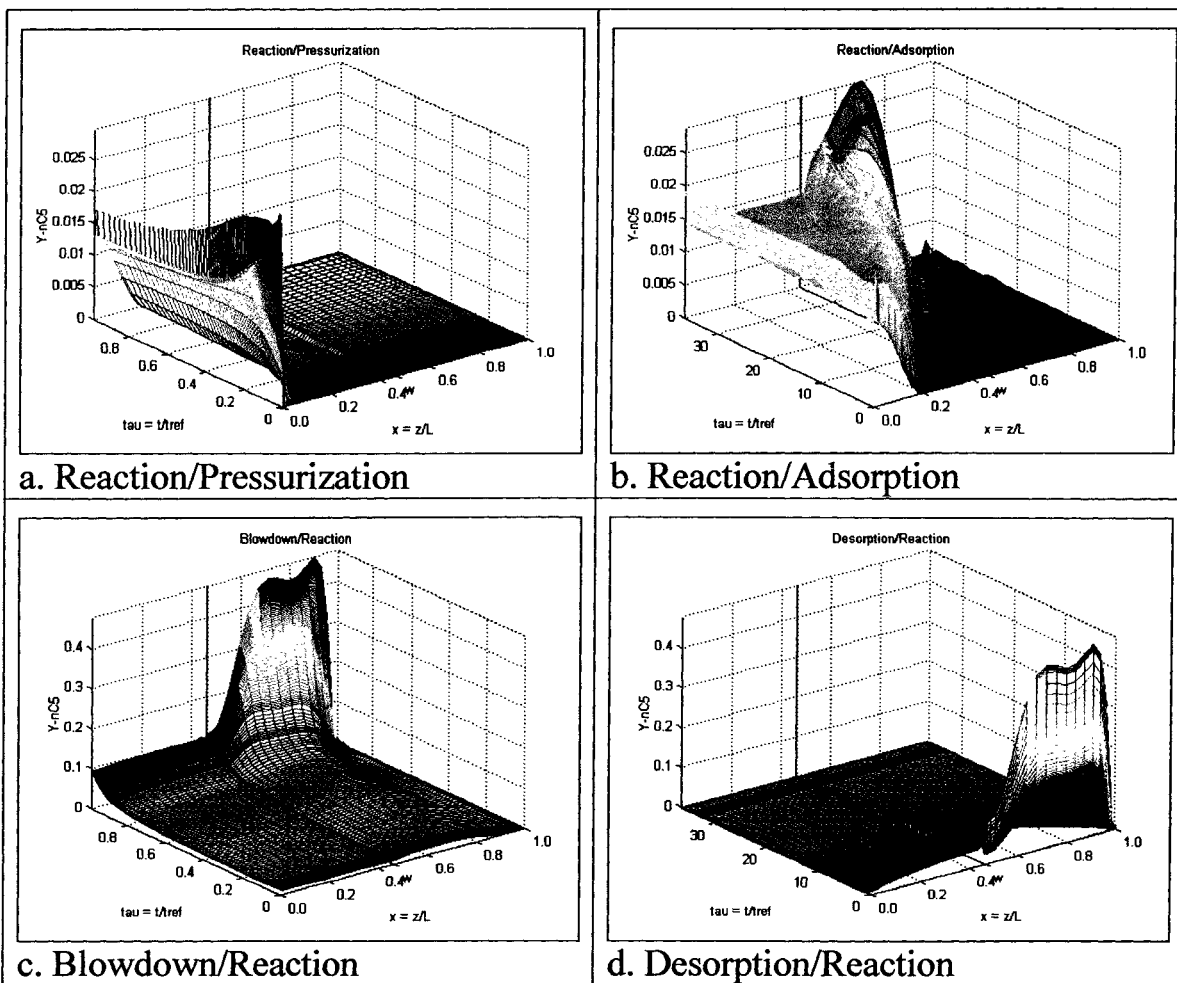


Figure G.1: Three dimensional drawing illustrating the transient and spatial change in  $n\text{-C}_5$  concentration with respect to time and axial distance for the four basic steps at the steady state cycle. (PSARM Unit with Waste Recycled to Feed/Hydrogen Purge)

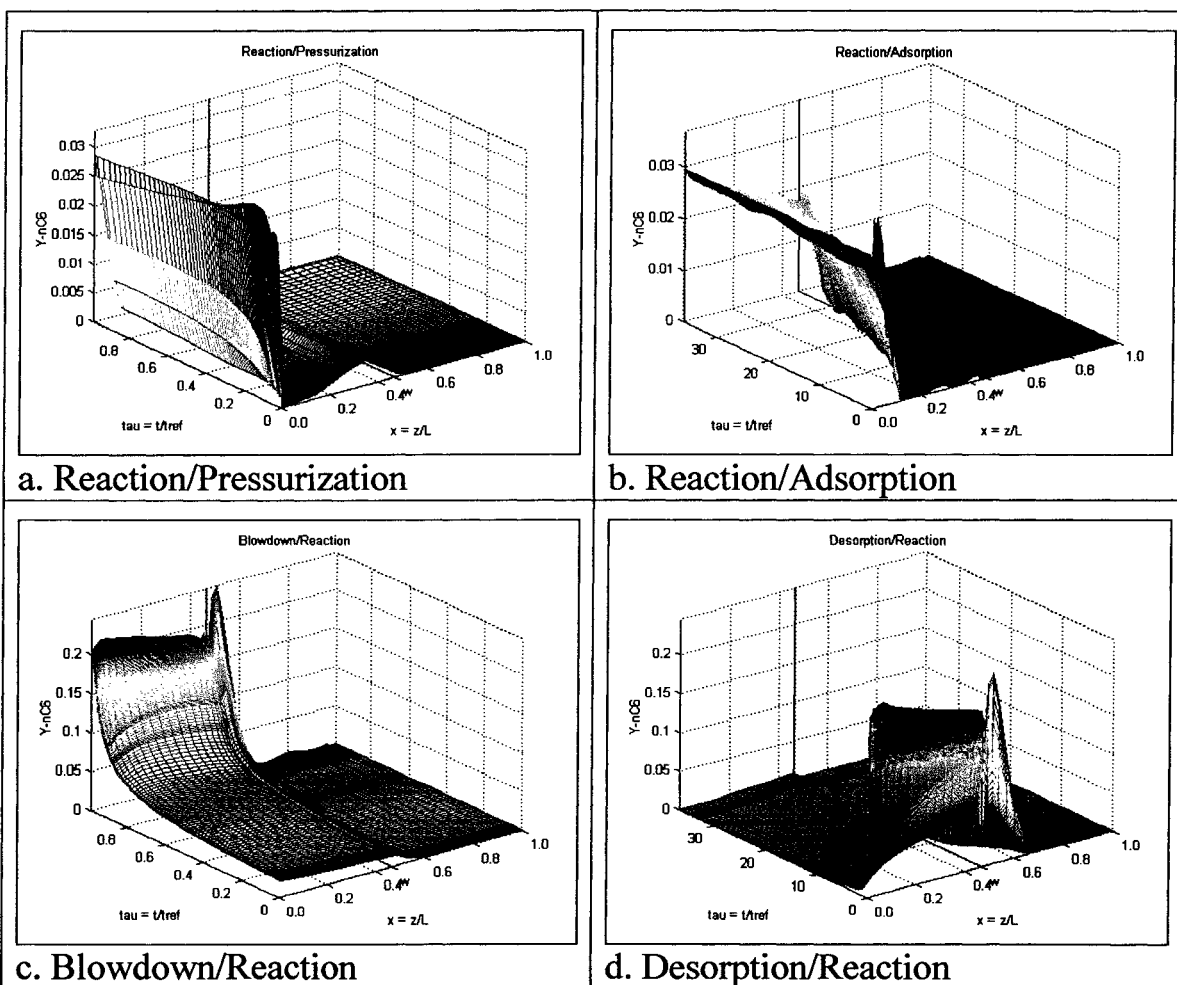


Figure G.2: Three dimensional drawing illustrating the transient and spatial change in  $n\text{-C}_6$  concentration with respect to time and axial distance for the four basic steps at the steady state cycle. (PSARM Unit with Waste Recycled to Feed/Hydrogen Purge)

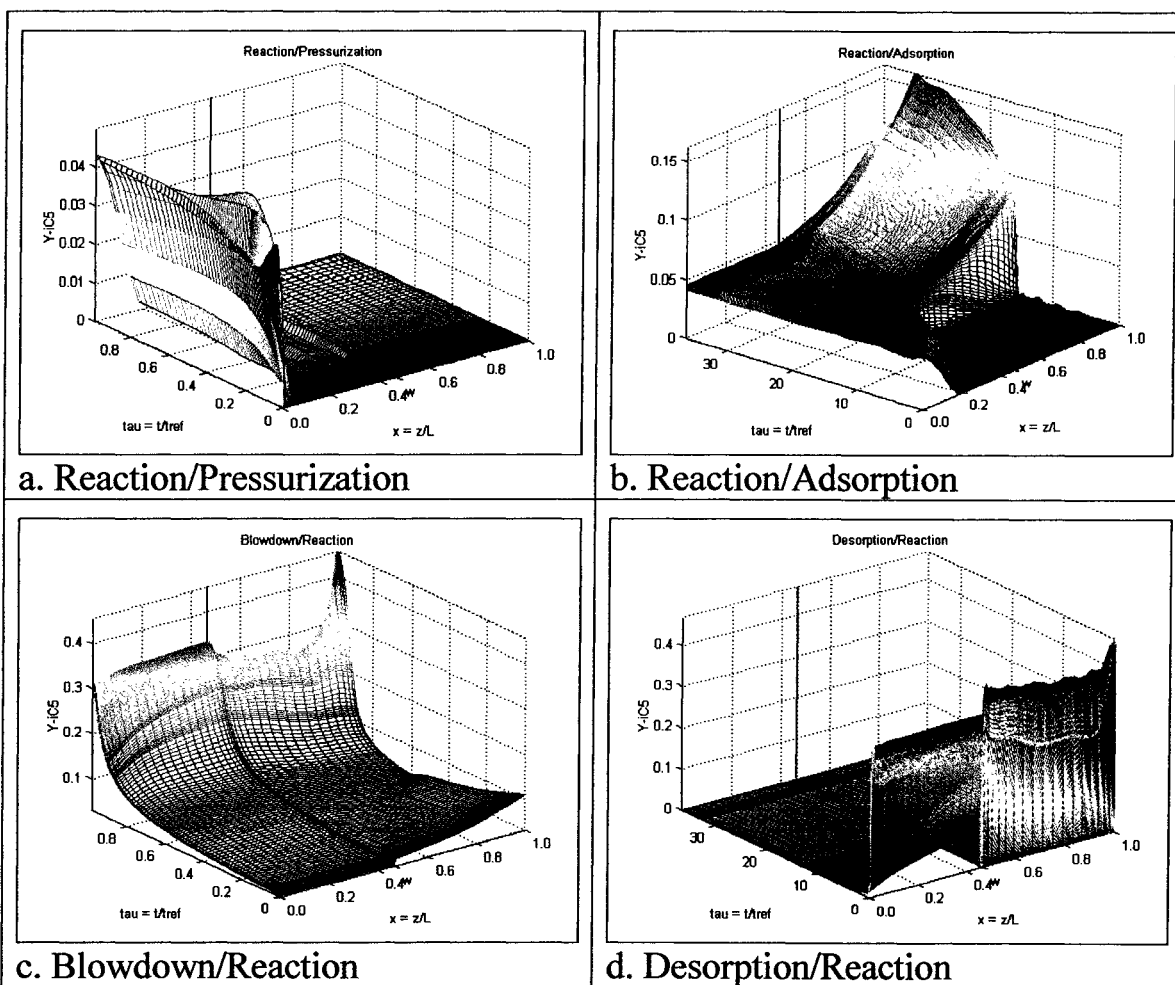


Figure G.3: Three dimensional drawing illustrating the transient and spatial change in  $i\text{-C}_5$  concentration with respect to time and axial distance for the four basic steps at the steady state cycle. (PSARM Unit with Waste Recycled to Feed/Hydrogen Purge)

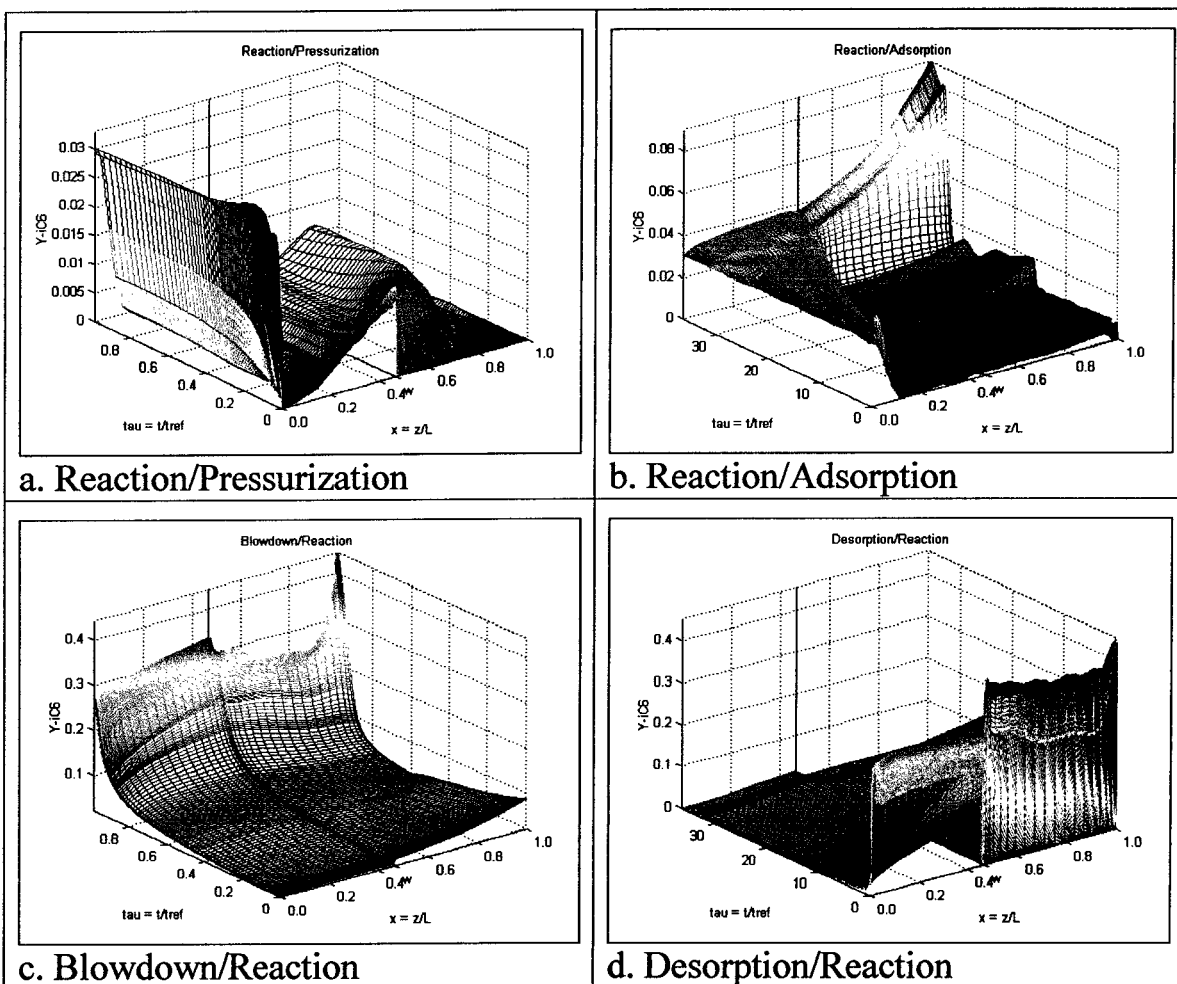


Figure G.4: Three dimensional drawing illustrating the transient and spatial change in  $i\text{-C}_6$  concentration with respect to time and axial distance for the four basic steps at the steady state cycle. (PSARM Unit with Waste Recycled to Feed/Hydrogen Purge)

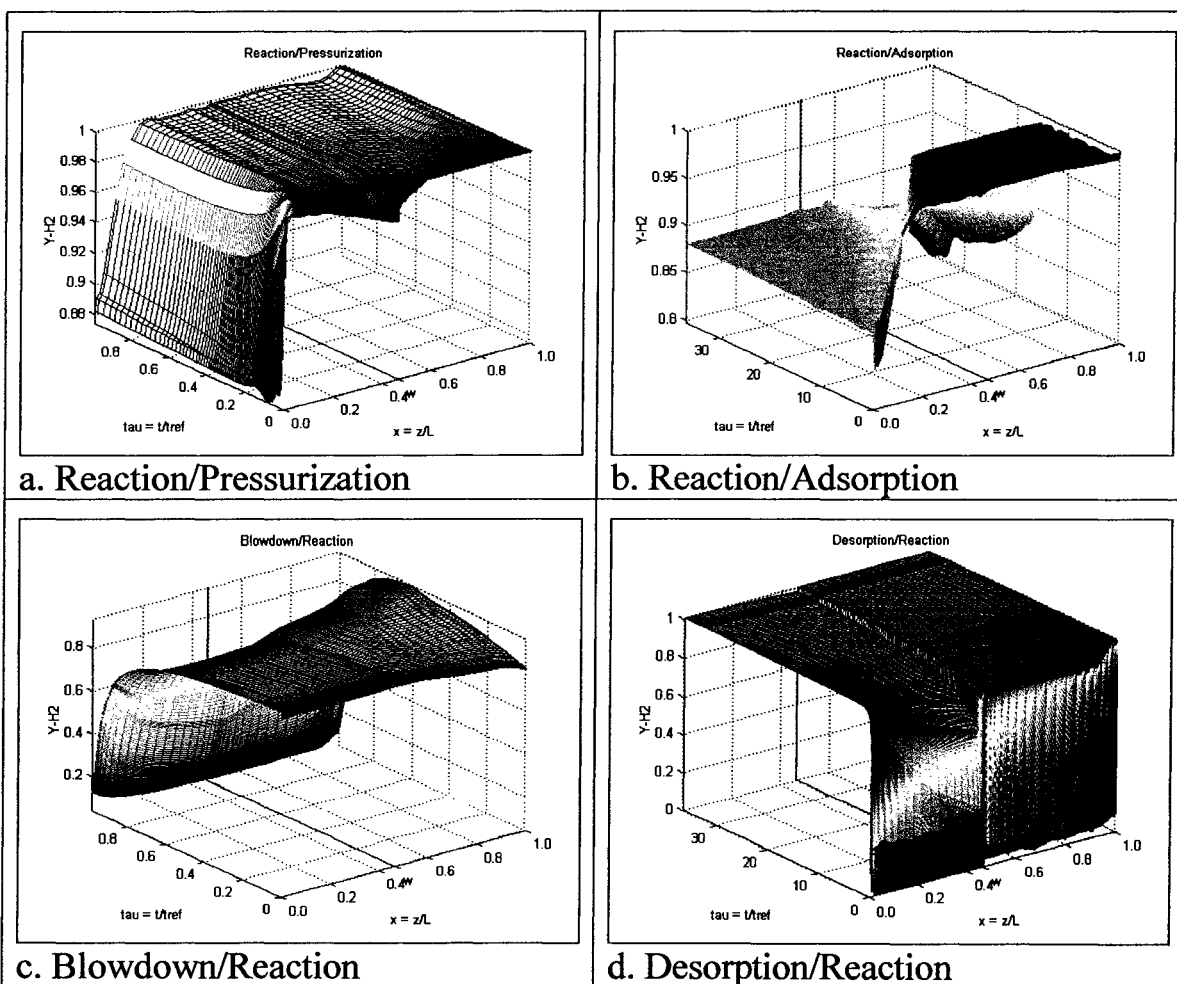


Figure G.5: Three dimensional drawing illustrating the transient and spatial change in  $H_2$  concentration with respect to time and axial distance for the four basic steps at the steady state cycle. (PSARM Unit with Waste Recycled to Feed/Hydrogen Purge)

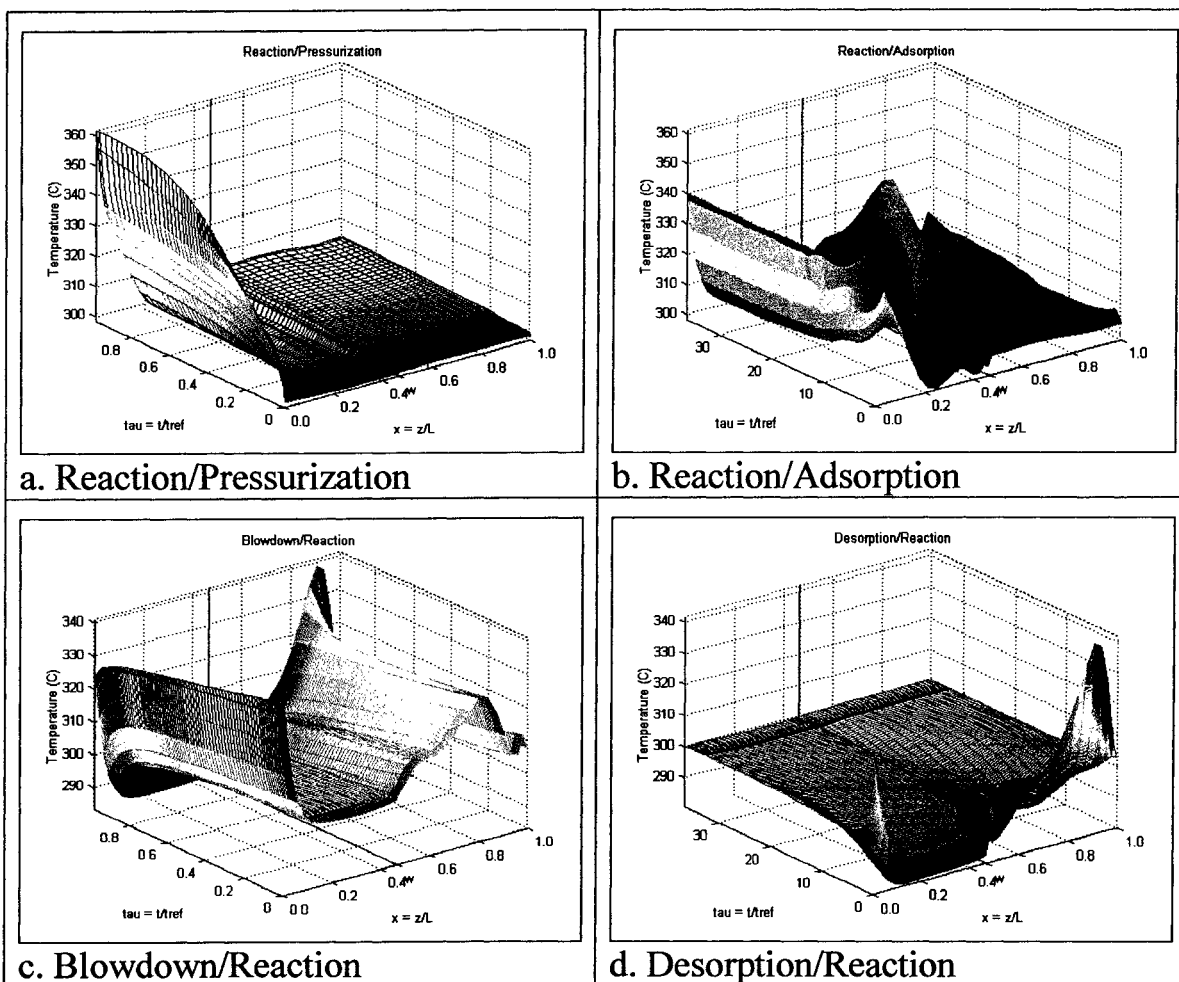


Figure G.6: Three dimensional drawing illustrating the transient and spatial change in Temperature with respect to time and axial distance for the four basic steps at the steady state cycle. (PSARM Unit with Waste Recycled to Feed/Hydrogen Purge)

## **APPENDIX H**

**Three Dimensional Figures of a PSARM Unit with Waste Recycled to Feed  
(Self Regeneration)**



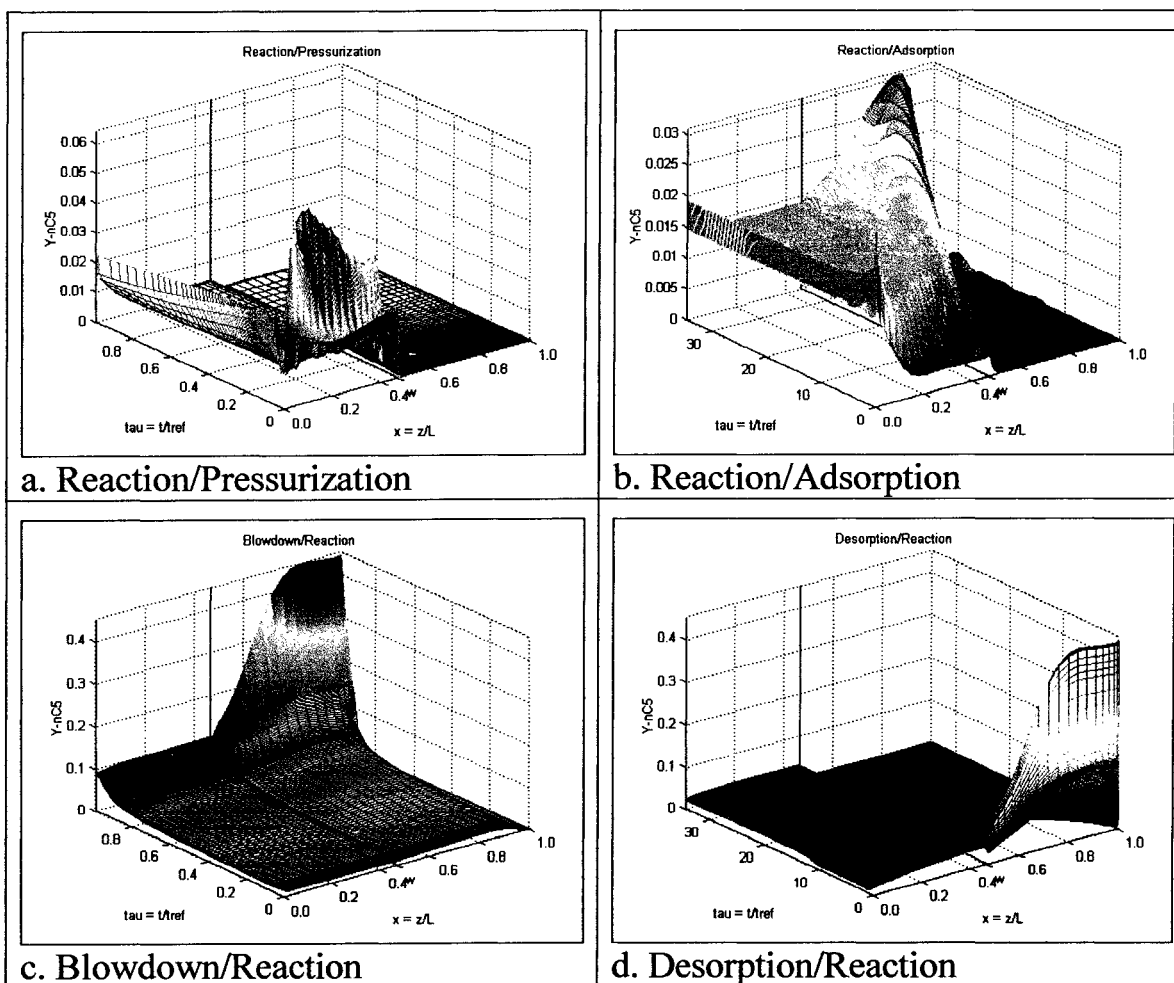


Figure H.1: Three dimensional drawing illustrating the transient and spatial change in n-C<sub>5</sub> concentration with respect to time and axial distance for the four basic steps at the steady state cycle. (PSARM Unit with Waste Recycled to Feed/Self Regeneration)

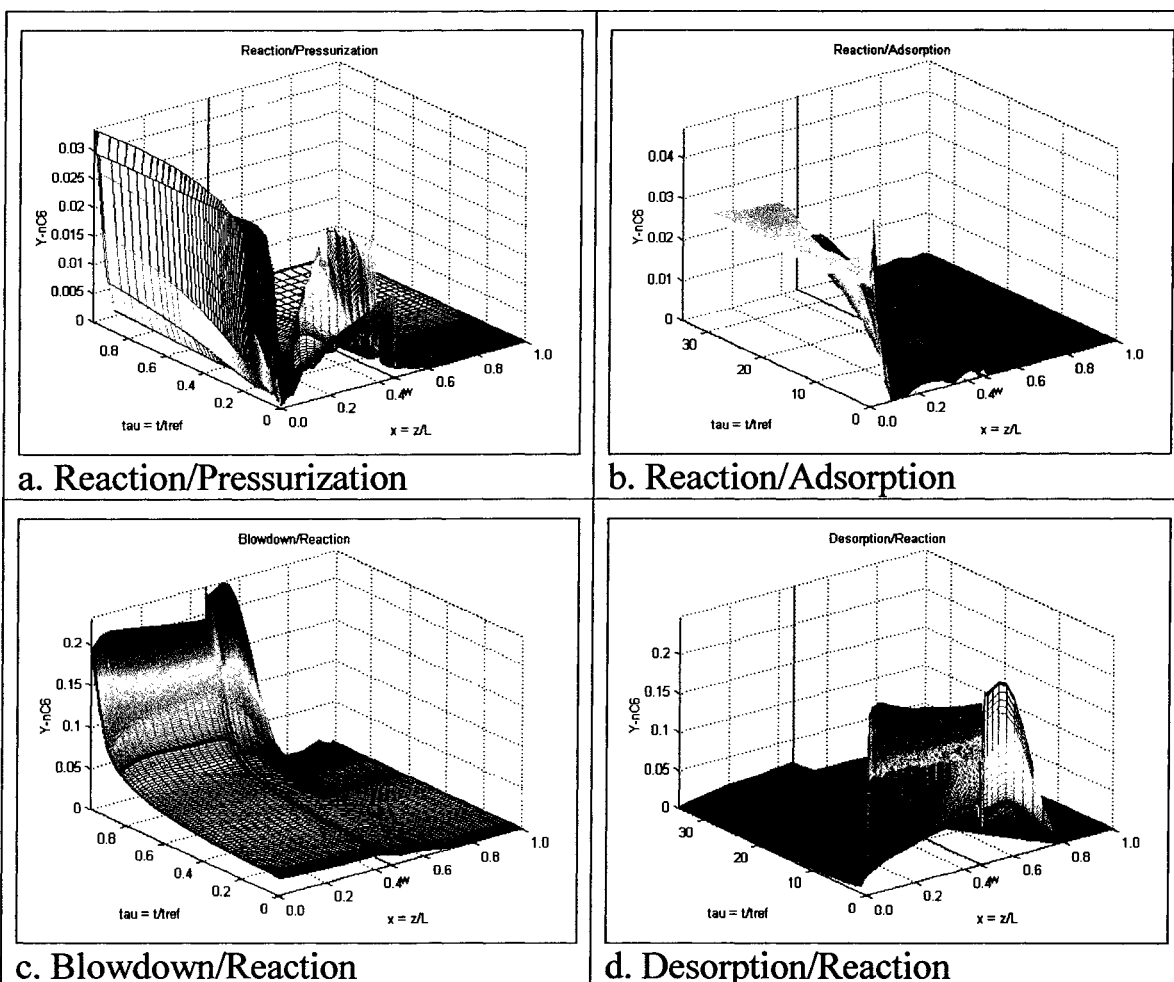


Figure H.2: Three dimensional drawing illustrating the transient and spatial change in n-C<sub>6</sub> concentration with respect to time and axial distance for the four basic steps at the steady state cycle. (PSARM Unit with Waste Recycled to Feed/Self Regeneration)

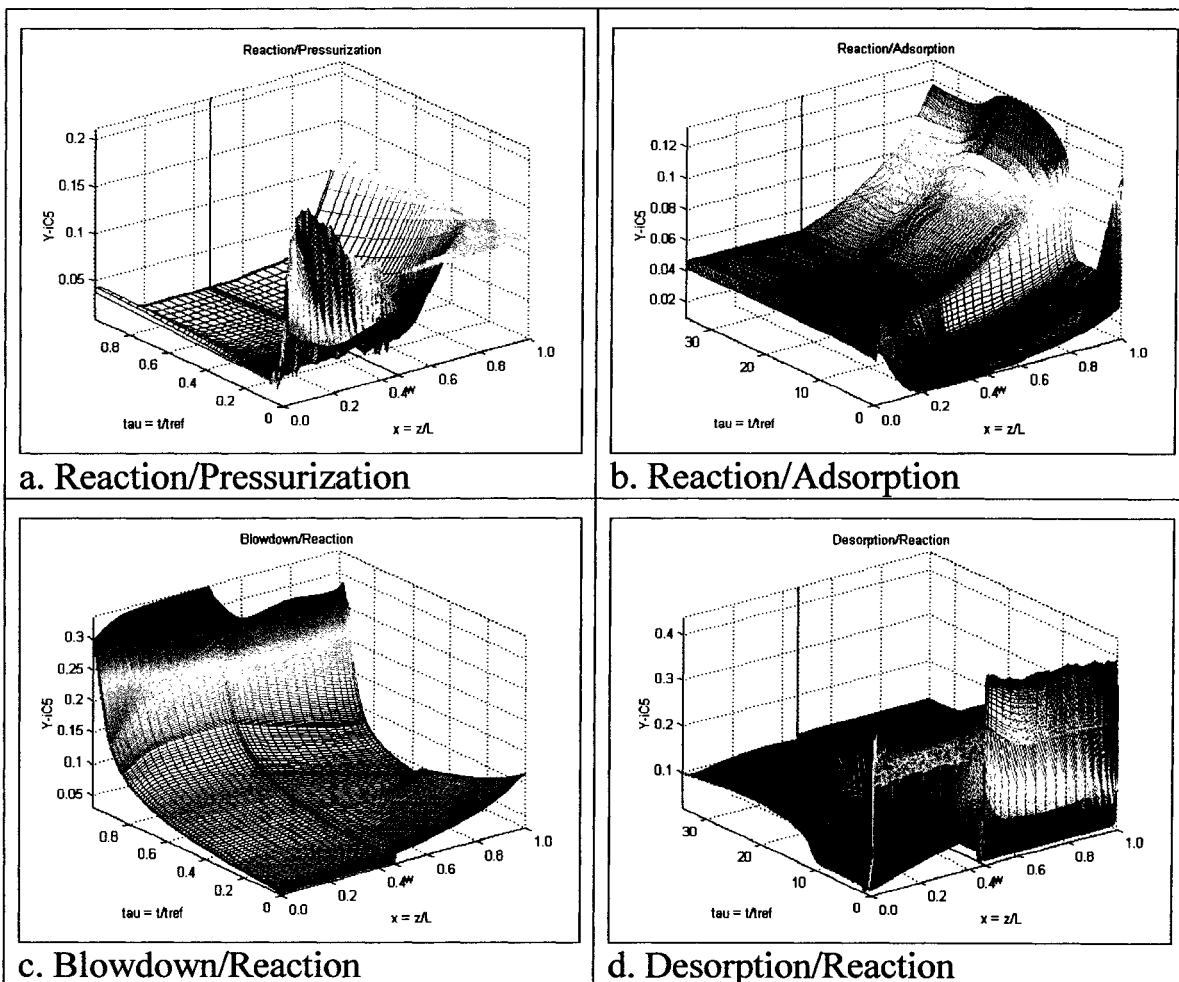


Figure H.3: Three dimensional drawing illustrating the transient and spatial change in  $i-C_5$  concentration with respect to time and axial distance for the four basic steps at the steady state cycle. (PSARM Unit with Waste Recycled to Feed/Self Regeneration)

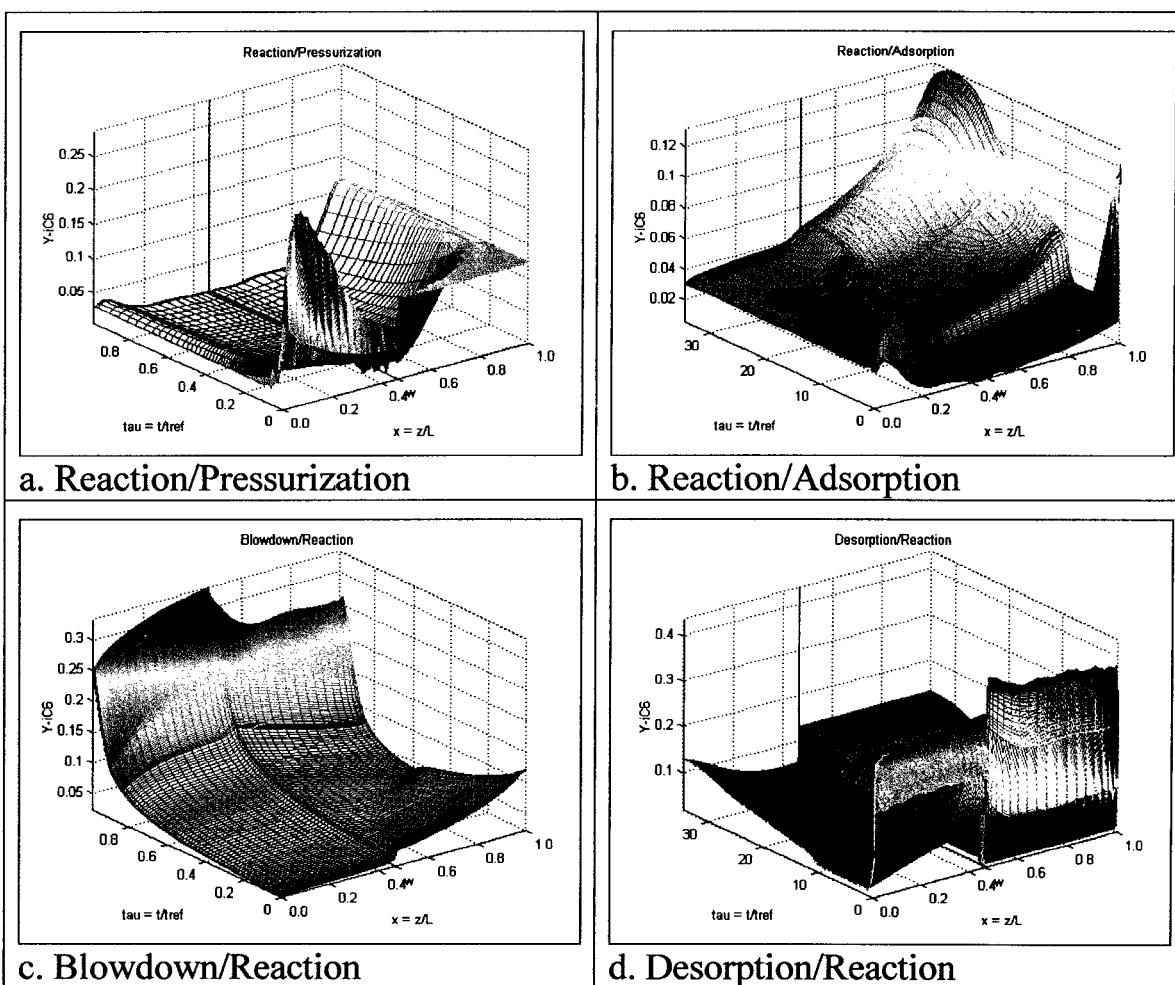


Figure H.4: Three dimensional drawing illustrating the transient and spatial change in  $i\text{-C}_6$  concentration with respect to time and axial distance for the four basic steps at the steady state cycle. (PSARM Unit with Waste Recycled to Feed/Self Regeneration)

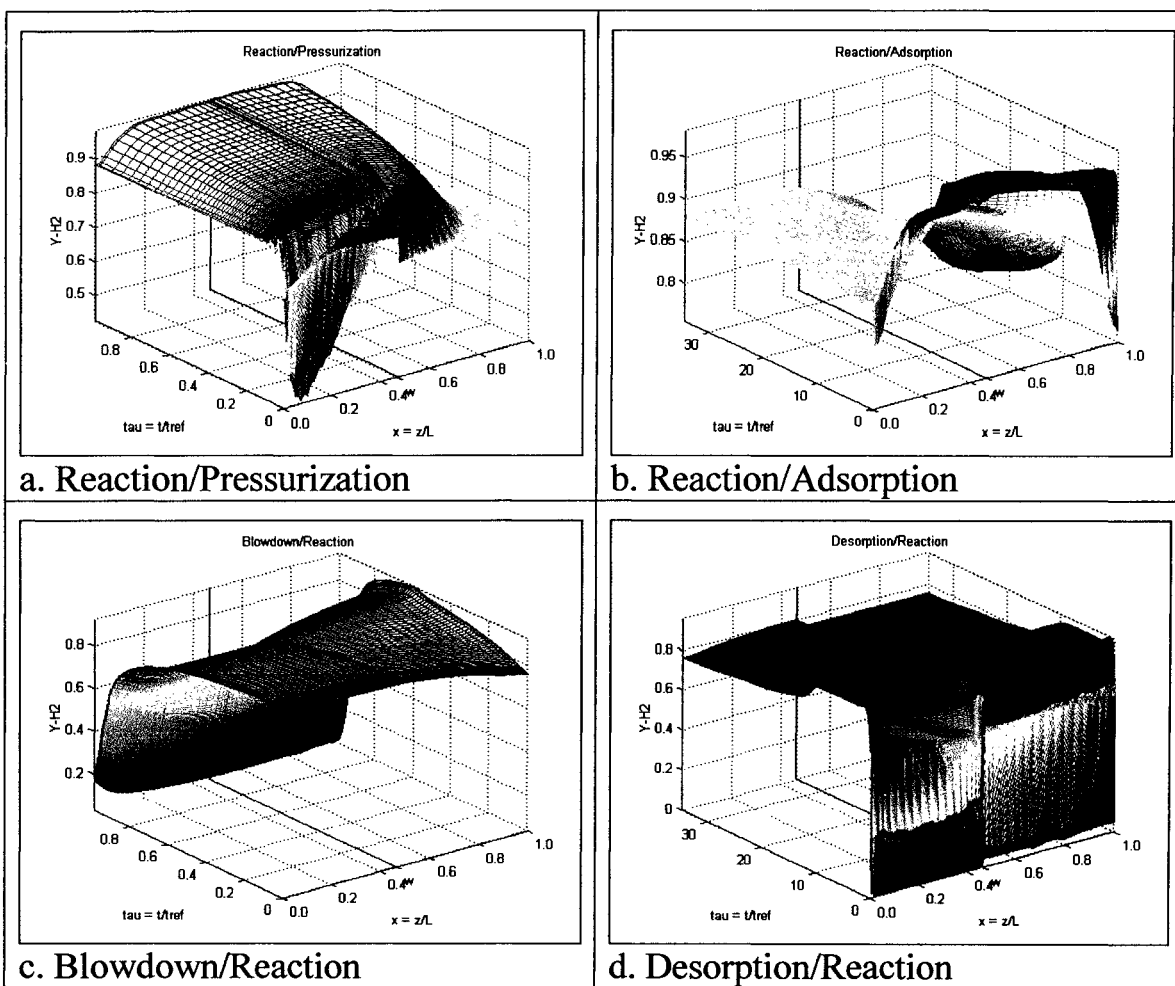


Figure H.5: Three dimensional drawing illustrating the transient and spatial change in  $H_2$  concentration with respect to time and axial distance for the four basic steps at the steady state cycle. (PSARM Unit with Waste Recycled to Feed/Self Regeneration)

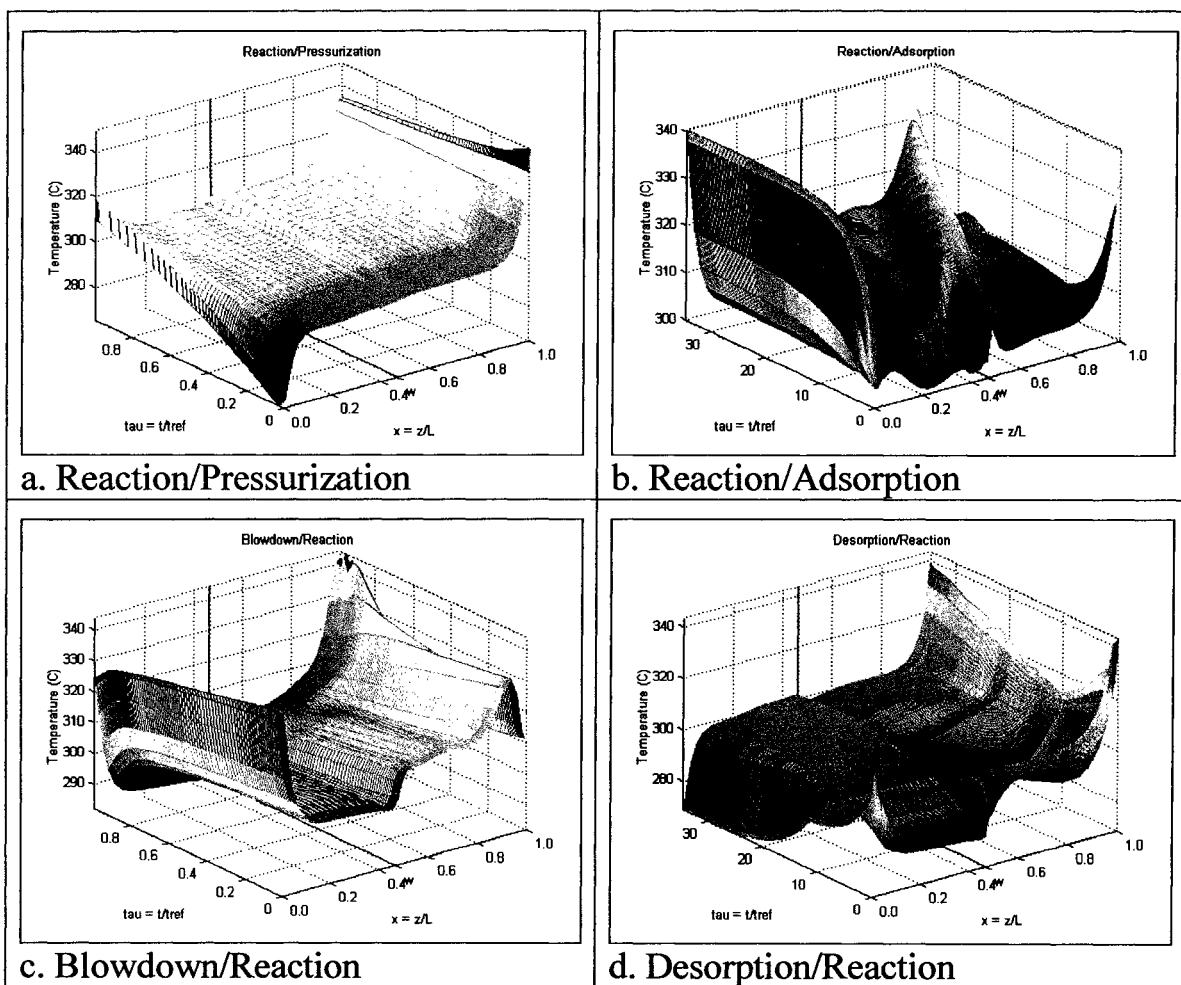


Figure H.6: Three dimensional drawing illustrating the transient and spatial change in Temperature with respect to time and axial distance for the four basic steps at the steady state cycle. (PSARM Unit with Waste Recycled to Feed/Self Regeneration)

## **VITA**

<b>Name</b>	<b>Tareg</b>
<b>Father's Name</b>	<b>Mohammed</b>
<b>Family Name</b>	<b>Al-Soudani</b>
<b>Date of Birth</b>	<b>January 19, 1973</b>
<b>Place of Birth</b>	<b>Khamees Mushait, Saudi Arabia</b>
<b>Nationality</b>	<b>Saudi</b>
<b>Educational Qualifications</b>	<b>B.Sc. Chemical Engineering (1995)</b> <b>King Fahd University of Petroleum &amp; Minerals</b> <b>Dhahran 31261, Kingdom of Saudi Arabia</b> <b>M.Sc. Chemical Engineering (2004)</b> <b>King Fahd University of Petroleum &amp; Minerals</b> <b>Dhahran 31261, Kingdom of Saudi Arabia</b>